UNIVERSITY *of*
TASMANIA
AUSTRALIA

Multi-View Stereopsis (MVS) from an Unmanned Aerial Vehicle (UAV) for natural landform mapping

by

Stephen John Harwin

BSurv (CompSci), MSc (Surv)

School of Land & Food

Submitted in fulfilment of the requirements for the Degree of Doctor of Philosophy

University of Tasmania
March, 2015

This thesis contains no material which has been accepted for a degree or diploma by the University or any other institution, except by way of background information and duly acknowledged in the thesis, and to the best of my knowledge and belief no material previously published or written by another person except where due acknowledgement is made in the text of the thesis, nor does the thesis contain any material that infringes copyright.

Stephen Harwin

27 March 2015

Statement of Co-Authorship

Statement of Co-Authorship

The following people and institutions contributed to the publication of the work undertaken as part of this thesis:

Stephen Harwin, School of Land and Food, University of Tasmania

Arko Lucieer, School of Land and Food, University of Tasmania

Jon Osborn, School of Land and Food, University of Tasmania

Author details and their roles:

Paper 1 (Chapter 2): Harwin (95%), Lucieer (5%)

All authors contributed to the idea and its development; Harwin performed all data processing, analysis, and writing; Lucieer contributed editorial and experimental design advice.

Conference Paper 1 (Chapter 3): Harwin (98%), Lucieer (2%)

All authors contributed to the idea and its development; Harwin performed all data processing, analysis, and writing; Lucieer contributed editorial advice.

Chapter 4: Harwin (90%), Lucieer (5%), Osborn (5%)

All authors contributed to the idea and its development; Harwin performed all data processing, analysis, and writing; Lucieer and Osborn contributed editorial and experimental design advice.

Chapter 5: Harwin (90%), Lucieer (5%), Osborn (5%)

All authors contributed to the idea and its development; Harwin performed all data processing, analysis, and writing; Lucieer and Osborn contributed editorial and experimental design advice.

Chapter 6: Harwin (95%), Lucieer (5%)

All authors contributed to the idea and its development; Harwin performed all data processing, analysis, and writing; Lucieer contributed editorial advice.

We the undersigned agree with the above stated "proportion of work undertake" for each of the above manuscripts contributing to this thesis:

Candidate: **Stephen Harwin** (27 March 2015)

Arko Lucieer (27 March 2015)

Jon Osborn (27 March 2015)

Statement regarding published work

Stephen Harwin

27 March 2015

Abstract

Unmanned aerial vehicles (UAVs) or drones have become a cost-effective tool for surveying and mapping. UAV photogrammetry using Multi-View Stereopsis (MVS), known as UAV-MVS, is a technique that combines photogrammetry and computer vision and is becoming increasingly popular for 3D reconstruction surveys. There is a need for rigorous accuracy assessment of 3D reconstructions using UAV-MVS. This thesis evaluates UAV survey design considerations (camera network, camera calibration, and ground control network) and assesses their impact on the accuracy of MVS point clouds. The aim of this thesis is to assess the accuracy of the UAV-MVS survey technique to better understand the scale of change that can be detected. The chosen application area is natural landform change, in this case of a section of sheltered coastline that is eroding at scales that are difficult to monitor from satellite or aerial photography. Quantifying the spatial and temporal scales of the erosion occurring along these often fragile sheltered coasts provides an insight into the response of the landscape to many different variables including sea level rise. The erosion is occurring at the decimetre and centimetre scale and UAV-MVS from low altitude (<40–50 m) can provide 3D point clouds with 1–6 points per cm^2. These point clouds are compared to an in situ verification dataset derived using a total station survey (σ ranging between 1 and 2 mm) to assess accuracy. Various UAV survey design and processing scenarios are compared to assess the impact of camera calibration method, image overlap, inclusion of oblique imagery, ground control survey precision and ground control point (GCP) distribution and density. The use of simulations to predict achievable accuracy is tested. Profiles are used to compare cross sections of the point clouds and visualise point density, accuracy and detected change. Dense point clouds are commonly converted to digital elevation models (DEMs) and differenced to detect and quantify change. The conversion process can introduce artefacts into the data through the interpolation and generalisation process. For this reason the change detection and quantification methods evaluated here are based on point cloud differencing and extracted shoreline comparison. Vegetation edge and erosion scarp edge are two shoreline proxies that are extracted and compared.

The results demonstrate that UAV-MVS point clouds of natural terrain can be accurate to < 5–6 mm when using precise control (σ = 1–2 mm) and 10–11 mm when using differential GPS equivalent control (σ = 22 mm). The flying height in these tests was ~20–25 m above terrain.

Comparisons of network simulations and empirical data demonstrate that a simulation

can be used to reliably predict object space accuracy for typical UAV operations, where ground control is being established using differential GPS (σ = 22 mm). However, simulation predictions are less reliable when the ground control is established using precise field survey methods (σ = 1–2 mm), with achieved accuracy lower than predicted precision. This is attributed to the influence of residual systematic errors in camera calibration.

The findings further demonstrate that 70–80% overlap nadir photography supplemented with oblique photography focussed on complex portions of the terrain provides the most accurate and complete 3D reconstructions of this coastal shoreline.

Point cloud differencing is an effective means of detecting and quantifying change. When extracting a proxy for shoreline at the fine-scale provided by UAV-MVS data, the scarp edge is more easily delineated than vegetation edge and provides a more accurate indication of shoreline position and associated change. The use of UAVs for surveying and monitoring can now be undertaken with confidence provided the design guidelines offered in this thesis are adhered to. The use of UAV-MVS to monitor centimetre-scale change along sheltered coastlines can provide the spatial and temporal resolution datasets needed to distinguish event-driven change from longer term trends.

Acknowledgements

Firstly, I thank my supervisors Dr Arko Lucieer, Dr Jon Osborn and Dr Christopher Watson.

I am grateful for the opportunity to work under the supervision of people with both knowledge and passion for the subject area. Both Arko and Jon provided guidance, knowledge, enthusiasm, patience and advice at all stages of the preparation of this thesis. Although I probably did not draw on Christopher's knowledge as much as I should have, he was always available when I required any guidance or advice.

I also thank Darren Turner and Matt Dell. I am indebted to both for providing technical expertise and advice.

Thank you to my mother Rose and step-father Les Wood for their unwavering support and guidance. I owe much of my enthusiasm for spatial science and geography to you both. Thanks also to my other family members, friends and colleagues.

Thank you to my three children, Amber, Noah and Leo. I know you have often wanted more of my time than I could give during this research endeavour and I am so grateful to have such amazing children who have been so very understanding.

Thank you to my partner Maria for everything. Your love, friendship and support are the foundation of my life. You let me run with this dream and supported and encouraged me at every stage of my PhD, sometimes that meant single parenting for weeks at a time while I went to the USA and to Antarctica. When I needed to immerse myself in research and parenting took a back seat for me, you took on all that you could and gave me the space I needed to get this thesis finished. Our love and friendship will endure anything after this I am sure.

Finally, I would like to dedicate this thesis to my father John Harwin, who passed away more than 30 years ago yet has influenced me and inspired me my whole life. I am my father's son and I know he would be proud of me for my efforts and my enthusiasm for spatial science. Thank you Dad.

Table of Contents

List of Tables

List of Figures

Glossary of Abbreviations

AGL Above Ground Level (AGL) is commonly used when referring to aircraft flying height.

ALS and LiDAR Airborne Laser Scanning/Scanner (ALS) includes Light detection and ranging (LiDAR) and involves using airborne laser measurements to derive 3D data.

DEM Digital Elevation Models (DEMs) are based on data sampled on a regular grid (matrix/lattice) of height values (ground height with vegetation removed). No other information is stored. There is usually only one height value possible for each horizontal position (i.e. each pixel/cell) and these data models are therefore referred to as 2.5D. This allows a DEM to be stored as a simple raster/image.

DSM Digital Surface Models (DSMs) are based on surface height data values. In GIS this is usually data that is sampled on a regular grid (matrix/lattice). Any object/surface (e.g. buildings, vegetation) can be represented, not just bare terrain. DSMs in this thesis refer to the upper most surface of topography as seen on an aerial photograph or detected from the first-return pulse of a laser scanner (Newby, 2012).

DTM Digital Terrain Models (DTMs) are based on a grid of regularly spaced, bare terrain (topography) height values. They may contain other information about the terrain surface (e.g. ridge lines, spot heights, troughs, coast/shore lines, drainage lines, faults, peaks, pits, passes, etc.)

GCP Ground Control Point (GCP) is a known point that is directly measured or surveyed for spatial georeferencing of spatial data (Newby, 2012).

GIS Geographic Information System (GIS) is software used to create, visualise, edit and analyse geographical information.

GNSS, GPS and DGPS Modern receivers are GNSS (global navigation satellite system) receivers meaning that they augment the United States' GPS (Global Positioning System) positioning with other satellite navigation system data including the Russian Federation's GLONASS (GLObal NAvigation Satellite System), the European Union's Galileo system, the Chinese BeiDou system, Japan's Quasi-

Zenith Satellite System (QZSS) and India's IRNSS (Indian Regional Navigation Satellite System). Not all these systems are fully operational but GNSS receivers are capable of improving their position based on the additional data when available. The systems used in this thesis are only using the GPS satellites and therefore GPS and DGPS (differential GPS) are the terminology used to describe data captured with satellite positioning systems, the latter uses a base/rover configuration with the base at a known point to provide differential correction of the rover position.

GSD Ground Sample Distance (GSD) is the distance between image/raster pixel centres or pixel size, measured in object space (ground) units.

IMU Inertial Measurement Unit (IMU) provides data on the orientation (pitch, role, heading and other information) of a moving system.

MVS Multi-View Stereopsis (MVS) combines the fields of photogrammetry with computer vision algorithms to reconstruct 3D objects as dense 3D point clouds based on photography.

N Value Geoid-ellipsoid separation value.

OTJ self-calibration "On-the-job" self-calibration, referring to the estimation of camera calibration coefficients as part of the bundle adjustment undertaken in Structure-from-Motion (see below) processing.

RMSE Root Mean Squared Error (RMSE) is the square root of the mean/average of the square of all of the error (or residuals, i.e. the difference between actual value and predicted value).

RTK Real Time Kinematic (RTK) is a technique that improves GPS/GNSS positions using differential corrections broadcast via a telemetry link.

SfM Structure-from-Motion (SfM) using matched features in multiple images of an object to derive camera position and pose, camera distortion parameters and a sparse 3D point cloud.

SIFT The Scale Invariant Feature Transform (SIFT) operator developed by Lowe (2004) provides a robust scale-invariant description of features in a scene/images that can be for feature comparison and image matching.

TLS Terrestrial Laser Scanning/Scanner (TLS) involves using terrestrial laser measurements to derive 3D data.

TIN or Mesh Triangular Irregular Networks (TINs) based on irregular sampled data and Delaunay triangulation (mathematically equivalent to Thiessen, Dirichlet, Voronoi and perhaps other eponymous tessellation processes producing TINs). A TIN are often referred to as a mesh. They can represent any 3D object (Newby, 2012).

UAV Unmanned Aerial Vehicle (UAV, Unmanned Aircraft or Drone) is an aircraft that is controlled by a remote pilot or on-board systems.

UAS Unmanned Aircraft System (UAS) is the UAV and all associated support equipment (ground control station, communication, telemetry and data links, navigation equipment and on-board sensors).

UTM The Universal Transverse Mercator (UTM) system divides the earth up into 60 six degree wide longitude zones. Each zone is projected to a grid coordinate system using the secant transverse Mercator projection.

VP Verification Point (VP) is a known point that is directly measured or surveyed that provides verification of the accuracy and precision of spatial georeferencing of spatial data.

VTOL Vertical Take-Off and Landing (VTOL) is a term used to describe aircraft that are capable of taking off and landing vertically.

1 | Introduction

1.1 Background

1.1.1 Monitoring landscape change

Landscape change is a process that can occur over millennia or within moments and these changes can be minuscule or vast. To quantify and monitor change a scientist needs to choose the tool that best suits the scale of change (Anderson and Gaston, 2013). When monitoring change a key aim of terrain mapping is for the measurement of the object to be repeatable in each epoch dataset (Fraser, 2013). From a spatial sciences perspective the accuracy and resolution requirements are fundamental considerations when determining the most appropriate data capture method for an application. Accuracy is needed to ensure data collected at an epoch is reliably mapped to a real-world coordinate system. For reliable comparison all epochs must be accurately georeferenced to the same coordinate system or coregistered. When differences are detected there needs to be a clear understanding of the likelihood that those differences are actual change as opposed to differences introduced due to inaccuracy and imprecision in the measurements (Lu et al., 2004). For measurements derived from imaging sensors the pixel resolution of that imagery adds an additional layer of uncertainty as each pixel is a square (or rectangle) that represents the combined reflectance of what is in that instantaneous field of view with a single colour or digital number (Cracknell, 1998). The goal is therefore to ensure the resolution of the captured imagery provides sufficient detail to be able to distinguish what is important for a particular application. The temporal resolution is the other aspect of resolution that is fundamental in change monitoring. The magnitude of change that can be measured is directly linked to the accuracy and pixel resolution of the datasets in the time series. The temporal resolution dictates how well the trajectory and dynamics of that change is mapped (Coppin et al., 2004).

Remote sensing via satellite-borne sensors offers pixel resolutions of 30 cm at best (DigitalGlobe, 2015). Aerial photographs commonly provide resolutions of ~10 cm. These platforms provide large extent datasets that can be used to monitor magnitudes of change greater than the resolution of the image pixels they produce. The timing of data collection is dictated by satellite trajectory or aircraft availability, and of course the weather. Accurate mapping of changes that are small is difficult or impossible at

the resolutions available with these sensors.

The use of unmanned aerial vehicles (UAVs) or drones in remote sensing, surveying and mapping has become commonplace in recent years (Colomina and Molina, 2014; Remondino et al., 2011; Nex and Remondino, 2013). The potential for very high temporal and spatial resolution coupled with the low cost of deployment has driven a rapid expansion of the industry and has huge potential in the future (Anderson and Gaston, 2013). Multi-view stereopsis (MVS) combines the fields of photogrammetry with computer vision algorithms and when coupled with UAV platforms provides close-range airborne photogrammetry on-demand. UAV surveys that use MVS techniques based on images from consumer-grade cameras and low-cost lightweight on-board positioning and navigation systems to generate 3D point cloud representations of natural and man-made subjects is known as UAV-MVS and is a branch of UAV photogrammetry (Eisenbeiss, 2009). UAV-MVS has the potential to revolutionise mapping and monitoring. The accuracy and viability of this technique for mapping natural landforms and landform changes is the focus of this research thesis.

Mapping coastal erosion is one monitoring application that will benefit from the UAV-MVS technique. The rate of change of coastal erosion in sheltered waterways may be less than 10–20 cm per year which is much less than the rate of erosion seen along ocean beaches and exposed soft sediment shorelines. Prahalad et al. (2014) suggests that, in order to distinguish episodic changes from more gradual change, monitoring erosion along these sheltered waterways requires high accuracy and high spatial and temporal resolution data. Events such as king tides that coincide with unfavourable wind direction can expose fragile shores to wind waves. Monitoring small changes can provide insight into how mean sea level rise impacts coastal morphology (Mitasova et al., 2004). Traditional monitoring via photogrammetry or topographic and bathymetric surveys may not provide the temporal and spatial resolution necessary to adequately define the cause of the erosion (Splinter et al., 2013; Rovere et al., 2014). The impacts of sea level rise associated with climate change require accurate monitoring of fragile coasts to document coastal change and assess the effects of any mitigation efforts. Pre- and post-event mapping is possible with UAVs, and UAV-MVS has the potential to offer 3D datasets with spatial resolutions higher than 1–3 cm and accurate to ~1 cm. Splinter et al. (2013) suggests intense sampling (monthly or less) at key sites is needed to adequately capture variability. These high resolution and high accuracy time series captured from UAV can provide insight into the causes of gradual and episodic erosion that until now may not have been visible and may not have been monitored frequently enough to determine what events might be causing annual and decadal erosion along

sheltered coastlines.

An alternative to UAVs is to use ground based measurements. Techniques exist to extrapolate point data into interpolated topographically continuous data layers, however, the accuracy of these approximations is dictated by the chosen data model (raster, TIN, 3D mesh), the interpolation method and the density of sample points, which in turn is limited by the constraints of the data capture survey method (e.g., total station detail surveys and profiling, point soil samples and target tracking). Ground-based sensors, such as terrestrial laser scanners can provide dense spatial coverage of small areas (<1 ha). However, these scanners are expensive and they are limited by the line of sight of the sensor and therefore multiple scan positions are required to avoid occlusion. UAVs, due to their top-down view angle and manoeuvrability, can overcome some of the occlusion problems. UAVs can fill the scale gap between ground-based measurements, and satellite and manned aircraft remote sensing. The resolutions achievable from low flying UAVs have the potential to provide surveyors, scientists and land managers with datasets at temporal and spatial scales that previously would have required expensive and time-consuming data capture missions.

Photogrammetry has been the discipline responsible for the creation of topographical maps since the late 1800s (Wolf, 1983). Photogrammetry has traditionally been based on stereovision or stereopsis, the ability to perceive 3D from a stereo pair of photographs. Analogue photogrammetry provided a map maker with a 3D view from which they could create contour maps and detailed topographic data. Digital photogrammetry provided this capability via a computer and drastically improved efficiently. In recent decades, robotics has given rise to the field of computer vision, which builds onto the principles of photogrammetry combined with advances in feature detection and automated image matching to derive 3D structure from overlapping photography taken from multiple angles. MVS uses Structure-from-Motion (SfM) to derive camera position and orientation (and optionally camera distortion) and 3D model coordinates via a bundle adjustment (Snavely et al., 2007; Snavely, 2010; Lowe, 2004; Furukawa and Ponce, 2007). The tools for deriving 3D reconstructions from image sets have matured into commercial software packages, and in the last five years the use of MVS has become common for a range of applications including landform change monitoring (erosion, landslides, gullies, and glaciers) (James et al., 2013; Kaiser et al., 2014; Eltner et al., 2013; Mancini et al., 2013; D'Oleire-Oltmanns et al., 2012; Harwin and Lucieer, 2012b; Frankenberger et al., 2008; Carvajal et al., 2011; Westoby et al., 2012; Dietrich, 2014; Genchi et al., 2015; Lucieer et al., 2013; Niethammer et al., 2010), geological and mine mapping (geological structure mapping, stockpile and landfill mapping, deformation monitoring) (Vasuki

et al., 2013; Previtali et al., 2014; Naumann et al., 2014; Bemis et al., 2014) archaeology and urban mapping (Eisenbeiss, 2008; Verhoeven, 2011; Doneus et al., 2011; Stal et al., 2014; Remondino et al., 2011; Tampubolon and Reinhardt, 2014; Nex and Remondino, 2013; Tahar, 2012; Irschara et al., 2010; Barazzetti et al., 2010; Remondino and El-Hakim, 2009; Wefelscheid et al., 2011), disaster mapping (Wu et al., 2013) and crop monitoring (agriculture and forestry) (Wallace et al., 2012; Turner et al., 2011; Pierzchala et al., 2014).

UAVs for environmental remote sensing as a monitoring tool can now map change at temporal and spatial scales that may shed new light on the key questions we face relating to anthropomorphic impacts on our planet and the changes that are taking place. UAVs provide a means of mapping before and after key events, and the potential for change monitoring at these spatial and temporal scales is yet to be fully realised. Provided the datasets have minimal distortion and can be georeferenced or coregistered accurately, the insights the time series might provide into the drivers and impacts of those changes may prove invaluable.

1.1.2 UAVs for terrain mapping

Military and civilian use of UAVs has proliferated in the last decade. The technology that underpins unmanned flight including control/positioning systems, motors, batteries, construction materials (e.g., carton fibre, lightweight alloys) have advanced rapidly. The cost of early systems was high and much of the technology was therefore confined to the military. The availability of affordable platforms has been augmented by advances in sensor technology. Lightweight cameras, thermal, multispectral and hyperspectral sensors, RADAR systems, and LiDAR systems have been developed that can be integrated into a UAV platform and used to generate very high resolution datasets (Wallace et al., 2012; Turner et al., 2011; Lucieer et al., 2014; Kelcey and Lucieer, 2012; Berni et al., 2009a; Berni et al., 2009b; Laliberte et al., 2011; Lin et al., 2011; Zarco-Tejada et al., 2012; Zarco-Tejada et al., 2009; Leuschen et al., 2014).

UAVs offer ease of deployment and low cost of operation allowing for more frequent missions focusing in fine detail on the areas of interest. The choice of unmanned aircraft is important. Fixed-wing UAVs can be restrictive in their flight path design and, therefore, are usually flown using traditional 2D photogrammetric strip and block flight paths. Recent advances in multi-rotor technology have provided vertical take-off and landing (VTOL) UAVs that are stable, manoeuvrable, and capable of navigating com-

plex 3D flight paths. Currently, micro-UAVs (<5 kg) can fly 5–10 minutes carrying a payload, although flight time is increasing as new designs emerge and battery technology improves. Micro-UAVs are not the ideal tool for mapping large areas, particularly in Australia where altitude and line of sight restrictions do not allow high-altitude or long-range UAV flights without a lengthy approval process. Multiple flights are required for UAV-MVS surveys of more than 1–3 ha. Not all UAVs are well suited to UAV-MVS terrain mapping from low altitude. The aircraft dynamics and manoeuvrability of multi-rotor UAVs means that they can fly the complex flight paths needed to avoid occlusion when mapping complex terrain. A number of studies have mapped terrain from below 50 m above ground level (AGL) using these aircraft (Eltner et al., 2013; Lucieer et al., 2013; Mancini et al., 2013; Lucieer et al., 2011a; Harwin and Lucieer, 2012b; Carvajal et al., 2011; Neitzel and Klonowski, 2011). Others flew at a range of heights (Niethammer et al., 2012; Niethammer et al., 2010; D'Oleire-Oltmanns et al., 2012; Flener et al., 2013; Pierzchala et al., 2014; Naumann et al., 2014). Other UAV aircraft have been used such as RC helicopters (Flener et al., 2013; Stefanik et al., 2011) and fixed-wing UAVs (D'Oleire-Oltmanns et al., 2012).

Typical multi-rotor and fixed-wing UAVs used for civilian and scientific applications have payload restrictions and in the majority of cases metric cameras are too heavy for UAV photogrammetry, particularly for use with micro-UAVs. These typically heavy photogrammetric cameras are engineered to provide the performance and stability necessary for high accuracy metrology. This restriction has resulted in the use of non-metric consumer grade cameras not designed and manufactured for photogrammetric accuracy and as a result they exhibit much greater magnitudes of distortion and instability (Fraser et al., 1995; Fraser, 2013; Remondino and Fraser, 2006; James and Quinton, 2014). "Prosumer" or consumer-grade digital SLR cameras are often used, ideally with a fixed focal length prime lens, as these tend to suffer less from stability issues (Fraser, 2013). The interior orientation instability of these consumer-grade cameras needs to be recognised. Overcoming some of the limitations imposed by relying on non-metric cameras can be achieved relatively easily with a self-calibrating bundle adjustment (Fraser, 2013). "On-the-job" self-calibration is commonly used to solve for camera distortion using the same set of imagery as that used to the derive the model (e.g. Naumann et al., 2014; Pierzchala et al., 2014; Fonstad et al., 2013; Mancini et al., 2013; Lucieer et al., 2011a; Lucieer et al., 2013; Rosnell and Honkavaara, 2012; Harwin and Lucieer, 2012b; Niethammer et al., 2010; Niethammer et al., 2012). In on-the-job self-calibration the camera model is specific to that image set, the network geometry may not have been designed with camera calibration in mind, and the resulting model may contain

deformations (Fraser, 2013; Remondino and Fraser, 2006; James and Quinton, 2014). A pre-calibration using imagery of a target field from a similar flying height to the planned survey can provide more reusable calibration coefficients. This method has been used in a number of UAV-related studies (e.g. Carvajal et al., 2011; Eltner et al., 2013; D'Oleire-Oltmanns et al., 2012). Checkerboard calibration is a third method that has been employed (e.g. Flener et al., 2013; Stefanik et al., 2011). Several studies have compared camera calibration options (Strecha et al., 2008; Rosnell and Honkavaara, 2012; Vallet et al., 2011), and argued that the impact of camera calibration method on the accuracy of MVS point clouds requires more research.

The low-cost UAV data capture allows for high levels of redundancy and UAV-MVS is well-suited to unstructured image acquisition (Mancini et al., 2013). This may allow for more ad-hoc UAV flight paths and a less strict adherence to flight planning protocols. A well-defined image acquisition design is a prerequisite of traditional photogrammetry from manned aircraft (Mancini et al., 2013). For topological mapping of large areas the timing of these missions is usually dictated by budget and logistical constraints rather than monitoring requirements. Similarly, in industrial metrology and close-range photogrammetry camera network design is a critical step and the expense of undertaking the metrology is often coupled with shutting down and perhaps dismantling the target object. The driver for this intensive planning stage is the need to understand the impact of measurement uncertainty on resulting model accuracy. In aerial and close-range photogrammetry, camera network design and ground control distribution and density is managed with tried and tested protocols and carefully defined formulae (Wolf, 1983; Abdel-Aziz and Karara, 1971; Abdel-Aziz, 1974; Abdel-Aziz, 1982). Simulation can be used to test photogrammetric camera network design and estimate the accuracy of results based on measurement uncertainty estimates. Simulation has not been used extensively for the evaluation of UAV-MVS 3D reconstruction accuracy and in the assessment of GCP layout scenarios (e.g. Rosnell and Honkavaara, 2012; James and Robson, 2014).

Accurate georeferencing is a key step in the UAV-MVS process. Survey design must consider ground control point (GCP) density and distribution, and the method of GCP survey. The impact of varying the number of GCPs has not been addressed in many studies (Tahar, 2013; Rosnell and Honkavaara, 2012). Both these studies measured the GCP positions with differential GNSS (Global Navigation Satellite Systems) or differential GPS (DGPS) surveys and Tahar (2013) assessed error based on check point comparisons, whereas Rosnell and Honkavaara (2012) compared a point cloud from a traditional photogrammetric survey to the UAV survey results. The use of differential GNSS or DGPS for the control survey is common in UAV terrain mapping studies (Nau-

mann et al., 2014; Pierzchala et al., 2014; Westoby et al., 2012; Fonstad et al., 2013; Mancini et al., 2013; Flener et al., 2013; Lucieer et al., 2011a; Lucieer et al., 2013; Rosnell and Honkavaara, 2012; Harwin and Lucieer, 2012b; Niethammer et al., 2010; Niethammer et al., 2012; Carvajal et al., 2011; James et al., 2013). Some have assessed accuracy by comparing check points derived from various techniques, such as DGPS/GNSS surveyed check points (Rosnell and Honkavaara, 2012; Carvajal et al., 2011; Mancini et al., 2013), and to LiDAR or terrestrial laser scanning (Strecha et al., 2008; Vallet et al., 2011; James and Robson, 2012; Flener et al., 2013; Westoby et al., 2012). The comparison of SfM/MVS derived products to total station surveyed check points has been investigated (Tahar and Ahmad, 2011; Harwin and Lucieer, 2012b; Eltner et al., 2013), however, a UAV terrain mapping accuracy assessment using a rigorous precise total station survey of those check points (and the GCPs) is required to validate the UAV-MVS survey technique.

In the context of monitoring terrain change at scales of a few centimetres the MVS survey technique has significant potential. A number of recent studies have investigated using MVS for coastal erosion monitoring. James et al. (2013), James and Robson (2012) and Westoby et al. (2012) used MVS from terrestrial imagery and Casella et al. (2014) and Mancini et al. (2013) used multi-rotor UAVs. Both of these UAV-MVS studies used GNSS/GPS GCPs and did not achieve decimetre accuracy. Similar studies looked at landslides (Lucieer et al., 2013; Carvajal et al., 2011; Niethammer et al., 2012), gully and soil erosion (D'Oleire-Oltmanns et al., 2012; Eltner et al., 2013; Eisenbeiss, 2009; Hugenholtz et al., 2013; Frankenberger et al., 2008) and river monitoring (Flener et al., 2013). No studies have used precise total station surveying techniques to assess accuracy and place uncertainty bounds on change measurements.

UAV-MVS combines the best of both aerial and close-range photogrammetric disciplines with advanced computer vision algorithms and powerful computing hardware. The challenge faced, as UAV photogrammetry proliferates, is defining how photogrammetric principles apply when the platform provides a means of capturing data in ways that are taking close-range photogrammetric techniques into the air. The availability of on-demand UAV imagery coupled with increased computer power and commercial MVS processing offers spatial scientists, surveyors, land managers, and scientists with unprecedented access to 3D representations of the environment. From a surveying and photogrammetry perspective the level of distortion and the achievable accuracy of UAV-MVS datasets are fundamental research considerations, particularly if the goal is to discern change.

1.2 Problems and Objectives

1.2.1 Problem Statement

Coastal erosion that is occurring at the centimetre scale can gradually undermine coastlines and increase the vulnerability of coastlines to major erosion events. Even small erosion events may impact fragile ecosystems and may have repercussions for infrastructure (Ranasinghe et al., 2011). Landowners, councils and governments require monitoring that accurately captures the state of the terrain over time in key indicator areas at centimetre scale in order to be able to detect and quantify change. UAV-MVS surveys can be undertaken at low cost before and after key events and at regular intervals to provide insight into how and why those coasts are changing. The erosion is happening at spatial and temporal scales that satellite and manned aerial systems cannot achieve within operational cost constraints. The terrain often has complex 3D features such as overhangs that 2.5D datasets derived from nadir photography fail to represent. The sparse datasets produced using traditional ground based measurements are insufficient for detailed change monitoring, and modern systems such as terrestrial laser scanners are too expensive to deploy for most environmental monitoring applications. UAV-MVS fills the scale gap and can provide very detailed 3D terrain maps on-demand. The techniques and technology are new and there are still many unknowns.

The erosion and accretion of ocean beaches is a well-understood phenomenon. Coastlines along sheltered waterways are not part of that system and the erosion may not recover. The erosion is gradual and often impacts fragile ecosystems such as salt marshes. Erosion along these coasts has increased over recent years and is a potential climate change indicator. For accurate erosion monitoring, and in other similar applications, there is a need for UAV survey design guidelines and clear workflows that avoid inaccuracies, put bounds on uncertainty, and ensure robust, repeatable outputs. From an operational perspective, image overlap, inclusion of oblique imagery, occlusion minimisation, lens calibration, and ground control survey method are key design considerations when planning a UAV survey. Investigation is needed into the impact of these UAV survey design choices on the accuracy of derived 3D point clouds and terrain models to ensure change detection reliability.

1.2.2 Aim

The aim of this thesis is to assess the accuracy of the UAV-MVS survey technique to better understand the scale of change that can be detected. The work focuses on the impact of operational choices on 3D point cloud accuracy and completeness with the goal of providing high resolution and high accuracy datasets for change monitoring applications like coastal monitoring. The specific objectives of the research are:

Objective 1

Assess how accurately an area of natural terrain can be mapped using UAV-MVS; specifically to:

- evaluate the impact of camera network design decisions relating to image overlap and oblique imagery inclusion on 3D model accuracy and completeness;
- assess the sensitivity of the UAV-MVS process to camera calibration procedures; and
- assess the impact of ground control density and survey accuracy on georeferencing accuracy.

Objective 2

Develop operational guidelines for making UAV survey design decisions; specifically to:

- investigate the relationship between GCP density, GCP survey precision, camera calibration method and camera network design; and
- assess the influence of GCP quality on point cloud accuracy.

Objective 3

Detect differences between UAV-MVS point clouds and quantify change; specifically to:

- compare accurately georeferenced point clouds from different UAV-MVS surveys of an eroding coastal site;

- measure point cloud separation as a means of monitoring coastal erosion;
- visually assess 3D surface generation options as an alternative to point clouds for change detection;
- visualise point cloud difference to ascertain whether actual change is represented; and
- assess shoreline definition options in the context of change monitoring.

1.3 Thesis structure

The structure of this thesis is by publication, and therefore Chapters 2–6 comprise publications that have been published in peer-refereed literature (Chapters 2 and 3) or prepared for submission to international peer-reviewed journals (Chapters 4–6). The research objectives are addressed by each of the publications as illustrated in Figure 1.1. Each chapter separately addresses the relevant literature and includes detailed methods, results, discussions and conclusions. Chapters 4–6 include a background theory section at the start of the methods. Given the cross-disciplinary nature of this thesis, the background sections have been included to provide the reader with relevant theory, and a summary of the literature and current knowledge. The reader may not be familiar with discipline specific theory and it will help place each chapter in context. A conclusion chapter (Chapter 7) summarises the overall outcomes and contributions of the thesis in context of the objectives and provides an overview of limitations and future work.

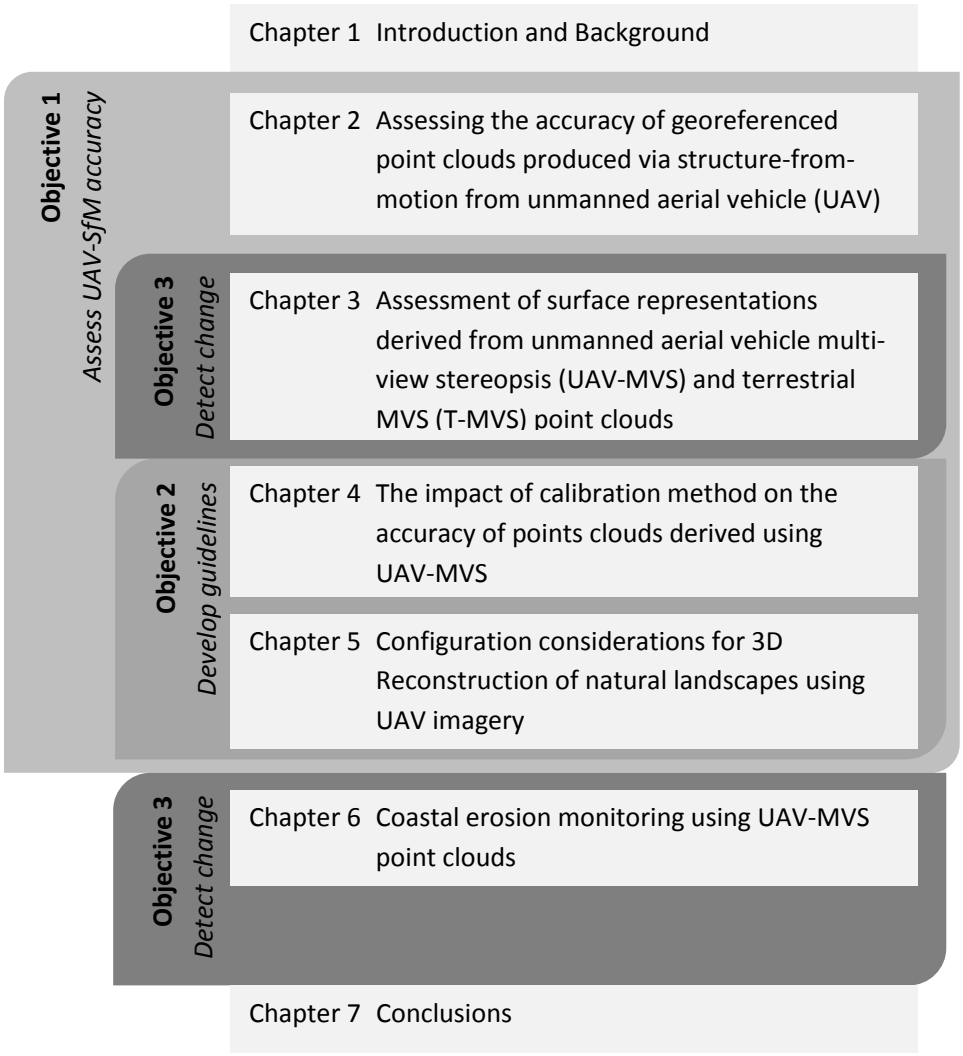

Figure 1.1: Structure of thesis, research objectives and chapters.

2 | Assessing the accuracy of georeferenced point clouds produced via multi-view stereopsis (MVS) from Unmanned Aerial Vehicle (UAV) imagery

Chapter 2 focuses on the assessment of accuracy of UAV-MVS point clouds produced using open source tools. The work comprising this chapter is published in the peer-reviewed *Remote Sensing* (Harwin and Lucieer, 2012b).

Abstract

Sensor miniaturisation, improved battery technology and the availability of low-cost yet advanced Unmanned Aerial Vehicles (UAV) have provided new opportunities for environmental remote sensing. The UAV provides a platform for close-range aerial photography. Detailed imagery captured from micro-UAV can produce dense point clouds using multi-view stereopsis (MVS) techniques combining photogrammetry and computer vision. This study applies MVS techniques to imagery acquired from a multi-rotor micro-UAV of a natural coastal site in southeastern Tasmania, Australia. A very dense point cloud (<1–3 cm point spacing) is produced in an arbitrary coordinate system using full resolution imagery, whereas other studies usually downsample the original imagery. The point cloud is sparse in areas of complex vegetation and where surfaces have a homogeneous texture. Ground control points collected with Differential Global Positioning System (DGPS) are identified and used for georeferencing via a Helmert transformation. This study compared georeferenced point clouds to a total station survey in order to assess and quantify their geometric accuracy. The results indicate that a georeferenced point cloud accurate to 25–40 mm can be obtained from imagery acquired from ~50 m. UAV-based image capture provides the spatial and temporal resolution required to map and monitor natural landscapes. This paper assesses the accuracy of the generated point clouds based on field survey points. Based on our key findings we conclude that sub-decimetre terrain change (in this case coastal erosion) can be monitored.

2.1 Introduction

Remote sensing technology has improved a great deal in recent decades and the miniaturisation of sensors and positioning systems has paved the way for the use of Unmanned Aerial Vehicles (UAVs) for a wide range of environmental remote sensing applications (Laliberte et al., 2010; Coulter et al., 2011). The use of UAVs for non-military applications has only become possible in more recent times as these miniaturised systems have become affordable for research and commercial entities (Chao et al., 2010). UAVs are now a viable alternative for collecting remote sensing data for a wide range of practical applications. The miniaturisation and commercialisation of sensors, positioning systems, and UAV hardware provide scientists with a means to overcome some of the limitations of satellite imagery and aerial photography, namely spatial and temporal resolution. The datasets produced by UAV remote sensing are at such high detail that characteristics of the landscape can be mapped that are simply not distinguishable at the lower resolutions generally obtainable via manned aircraft (~10–100 cm) and satellite systems (>50 cm). Furthermore, the ease of deployment and low running costs of these UAV systems allows for frequent missions providing very high spatial and temporal resolution datasets on-demand (Laliberte et al., 2010).

Recent advances in computer vision include multi-view stereopsis (MVS) techniques (Furukawa and Ponce, 2007), which can derive 3D structure from overlapping photography taken from multiple angles. Recent studies (Neitzel and Klonowski, 2011; Rosnell and Honkavaara, 2012; Turner et al., 2011; Dandois and Ellis, 2010; Lucieer et al., 2011a) have successfully adopted MVS to derive dense point clouds from UAV photography. Creating an accurately georeferenced point cloud using these methods will be referred to as UAV-MVS as it combines photogrammetric and computer vision techniques to process the UAV data.

2.1.1 Structure from Motion - Photogrammetry meets computer vision

The UAV-MVS process yields a 3D point cloud similar to that produced using active sensors such as LiDAR and interferometric RADAR and the point density of the cloud is a function of the image resolution and camera object separation. The 3D point cloud is a good data structure for storing complex surface structure and a digital surface model (DSM) can be generated to represent the captured surface. This complexity is not usually well represented in a digital elevation model (DEM) as these are commonly

2.5D datasets, i.e., there is only one Z-value at each 2D coordinate (x,y) (Monserrat and Crosetto, 2008). An advantage of UAV-borne sensors is the ability to acquire data from close range at multiple viewing angles (i.e., nadir and oblique). A nadir view commonly used in photogrammetry results in more occlusion and detail can be missed. "The central theme of photogrammetry is accuracy" (Hartley and Mundy, 1993), and the techniques used in this field for deriving 3D coordinates are well-established and robust. Technological advances have improved the efficiency and automation of these accurate established techniques. Robotics and computer vision have also advanced significantly in recent decades. The achievement of human-level capability for information extraction from image data being the theme of this field (Hartley and Mundy, 1993).

3D reconstruction from imagery relies on the extraction of image correspondences. In recent years both fields have sought to improve automated image matching. Matched feature points in overlapping photography enable the derivation of 3D coordinates as point clouds. In computer vision this is done through a process known as Structure-from-Motion (SfM) that incorporates multi-view stereopsis (MVS) techniques to derive camera position and orientation and 3D model coordinates. The success of MVS via the feature matching process is hindered by untextured surfaces, occlusions, illumination changes and acquisition geometry (Remondino and El-Hakim, 2006). Of the recent advancements in this area, the Scale Invariant Feature Transform (SIFT) operator (Lowe, 2004) has proven to be one of the most robust to large image variations (Remondino and El-Hakim, 2006; Juan and Gwun, 2009). A number of alternatives to SIFT exist such as Gradient Location and Orientation Histogram (GLOH)(Mikolajczyk and Schmid, 2004), Speeded Up Robust Features (SURF)(Bay et al., 2006), LDAHash(Strecha et al., 2011) and Principal Component Analysis (PCA)–SIFT(Ke and Sukthankar, 2004), however, each of which aim to achieve essentially the same result.

Advances such as SIFT have allowed MVS 3D reconstruction systems to solve for the orientation of the camera and derive 3D positions of the feature surface points using bundle block adjustment techniques. As outlined in Triggs et al. (1999), the theory and methods for bundle adjustment have been around for a long time. A number of software solutions exist that perform the bundle adjustment required to solve the camera parameters (including image orientation) and generate a 3D point cloud of a scene, they include Bundler(Snavely, 2010) (Snavely et al., 2006; Snavely et al., 2007), Microsoft Photosynth[1], Agisoft PhotoScan[2] and PhotoModeler[3]. These tools are optimised for

[1] `https://photosynth.net/`
[2] `http://www.agisoft.com/`
[3] `http://www.photomodeler.com/`

consumer-grade cameras with an uncalibrated focal length and close-range imagery acquired from different view angles. The density of the point clouds created is a function of the number of unambiguous point matches found. Generally, the density is quite sparse, which is adequate for the purpose of basic 3D modelling and tourism photo collection management. To increase the density it is necessary to revisit the images and use the knowledge of camera parameters to extract more points. Multi-view stereo techniques such as patch-based multi-view stereo (PMVS2)[4] and cluster multi-view stereo (CMVS)[5]) take the output from a standard bundle adjustment and perform a match, expand, filter approach to densify the original sparse point cloud (Furukawa and Ponce, 2010; Furukawa and Ponce, 2007). This point cloud densification is usually done using the down-sampled imagery (<3 Megapixels) in order to reduce computing overhead.

In this paper we propose a modified workflow so that full-size images can be used in PMVS2 resulting in much denser and more accurate point clouds. Seitz et al. (2006) compares over one hundred MVS algorithms[6] and this approach outperforms most other algorithms (although the objects were not natural landscapes). Strecha et al. (2008) used LiDAR reference data to compare the Furukawa and Ponce (2007) approach to the Strecha and Fransens (2004) and Strecha et al. (2006) approaches and their results favoured the Furukawa and Ponce (2007) algorithm for completeness and relative accuracy. A number of alternative MVS approaches have been developed such as Semi-Global Matching (SGM) (Hirschmüller, 2005; Hirschmüller, 2008), Plane-sweep strategies (Baillard and Zisserman, 2000), and the MVS pipeline developed by Vu et al. (2011), some of these are now also freely available and may be evaluated in a future study. The PMVS2 software is open source, it integrates easily with Bundler, and creates a very dense and accurate point cloud. Whilst SfM and MVS were not designed for environmental monitoring and modelling nor intended for UAV imagery, these techniques are proving to be well suited to UAV data capture as they combine images from multiple angles and varying overlap. The low UAV flying height also improves feature definition as the technique can capture complex shapes allowing for the representation of features such as hollows and overhangs.

2.1.2 UAVs for 3D Reconstruction of Natural Landscapes

The use of UAVs for 3D reconstruction and point cloud generation via aerial imagery has been considered in the past, particularly in recent years (Eisenbeiss and Sauerbier,

[4] http://www.di.ens.fr/pmvs/
[5] http://www.di.ens.fr/cmvs/
[6] http://vision.middlebury.edu/mview/

2011; Neitzel and Klonowski, 2011; Küng et al., 2011; Vallet et al., 2011; Rosnell and Honkavaara, 2012; Dandois and Ellis, 2010; Lucieer et al., 2011a; Turner et al., 2011). These studies usually focussed on assessing the accuracy of similar techniques, however, this manuscript presents the first attempt to quantify the accuracy of the whole UAV-MVS close-range data capture and georeferencing process applied to a natural landscape based on a comparison with total station survey data. Eisenbeiss and Sauerbier (2011) examined the use of UAVs in archaeological applications. They employed a more traditional photogrammetric approach to obtaining 3D data (DSM and ortho-images) from UAV photography. Neitzel and Klonowski (2011) compared a number of web services and software packages that "automatically generate 3D points from arbitrary image configurations" (Neitzel and Klonowski, 2011). Whilst the accuracy assessment performed in Neitzel and Klonowski (2011) provided some insight into the comparative accuracy of the successfully generated point clouds they were not able to derive a general rule or prediction of accuracy due mainly to their uncertainty relating to the influence of topography on the point clouds produced. The images used were down-sampled from 12 Megapixels to 3 Megapixels and only PMVS2 and Photoscan produced point clouds dense enough (~90 and ~110 points per m^2 respectively) to see the ground control points (GCPs) across the entire study site (a relatively flat parking lot with few GCPs). Küng et al. (2011) used Pix4D[7] to generate and compare georeferenced DEMs and orthmosiacs based on UAV GPS camera positions (geotags) and GCPs measured using DGPS and identified in the captured imagery. They flew at 130–900 m over non-natural sites and found that the accuracy of the geotagging was 2–8 m and the GCP method was accurate to 5–20 cm. The accuracy was strongly influenced by the resolution of the imagery and the texture and terrain in the scene (Küng et al., 2011). Vallet et al. (2011) compared georeferenced DTMs produced from LiDAR, Pix4D and NGATE[8]. The UAV flew at 100–150 m over a semi-natural scene containing 12 GCPs measured using static DGPS. The results suggest 10–15 cm accuracy is achievable when flying at 150 m. Rosnell et al. (2011) looked at imaging conditions in different seasons and how the point cloud generation performed. They chose more natural sites, however, they focussed on a comparison between a 1 m resolution DEM resampled from a relatively sparse Photosynth point cloud (2–3 points per m^2) and a detailed terrain produced using NGATE. The photography was captured from an altitude of 110–130 m and it is unclear how the GCPs were found in the imagery. Hirschmüller (2011) briefly discussed the use of Bundler and SGM with UAV imagery and provided a qualitative accuracy assessment. Dandois and Ellis (2010) focussed on vegetation structure mapping and chose to use

[7] `https://pix4d.com/`
[8] SOCET SET® Module: `http://www.socetgxp.com/docs/products/modules/ss_ngate.pdf`

GCPs from photography and DEMs resulting in poor georeferencing precision. They compared their tree height estimates from point clouds to LiDAR methods and found that DTMs produced using SfM techniques suffered from inaccuracy due to the complex canopy structure resulting in poor ground point extraction. The canopy surface was well represented and compared well to the LiDAR equivalent. Lucieer et al. (2011a) used the UAV-MVS technique to create point clouds of complex terrain with 1–2 cm point spacing. The 1 cm resolution DEMs generated were used to derive terrain derivatives such as topographic wetness index. Turner et al. (2011) used the Bundler to create DSMs from point clouds with an estimated accuracy of ~10 cm. The derived transformations were then applied to the matched SIFT feature locations in each image to allow georectified image mosaics to be created.

2.1.3 Georeferenced Point Clouds and Reference Data

The point cloud generated by UAV-MVS is generally in an arbitrary reference frame and needs to be registered to a real-world coordinate system. This is achieved by identifying key features in the point cloud that can be matched to known real world coordinates. In natural environments GCPs that stand out are not often available. The solution is to distribute highly visible targets. Once the coordinates for feature points have been established and matched (manually or automatically) a 3D Helmert transformation (with seven parameters: three translations, three rotations and one scale) can be used to transform the point cloud from an arbitrary reference frame into a real-world coordinate reference frame. The georeferenced point clouds produced need to be compared to reference data. The use of a total station survey to accurately map a set of reference points around the study area is an accepted method of obtaining "ground truth". Walker and Willgoose (2006) assessed the accuracy of their total station data using error propagation theory and found that uncertainty in position is ~1 cm and uncertainty in elevation is ~2 cm. Shrestha et al. (1999) used traditional surveying techniques to acquire profiles to assess the accuracy of LiDAR; Töyrä et al. (2003) used total station elevation data to assess LiDAR; and Farah et al. (2008) used total station data to assess the accuracy of DEMs derived from GPS. In a number of these studies the Root Mean Squared Error (RMSE) for each dimension and the total RMSE have been used as accuracy metrics. There are other possible metrics such as the mean difference, standard deviation, correlation length, minimum/maximum difference and bias (Walker and Willgoose, 2006; Hodgson and Bresnahan, 2004; Vaaja et al., 2011). The RMSE is a recognised and relatively easily understood proxy for answering this question when the "ground truth" dataset is a set of distributed points rather than a continuous

"truth" surface.

This study seeks to evaluate the accuracy of the UAV-MVS point cloud generated from imagery of a natural environment, namely a section of protected coastline. This accuracy assessment will by compare georeferenced point clouds to a total station and differential GPS (DGPS) survey. The site was chosen due to the fact that it is gradually eroding and this erosion may serve as an indicator for climate change. The erosion on this protected section of coastline is subtle and may not be visible via traditional aerial and satellite change detection techniques. We aim to use the UAV-MVS technique to generate dense and accurate 3D point clouds of this site and detect and quantify change over time. This investigation into the accuracy of UAV-MVS is the first step in a series of investigations into the application of these systems and processes to hyperspatial and hypertemporal earth observation and environmental monitoring using UAVs. To reliably quantify change we must first verify that the technique is sufficiently accurate to allow subtle (sub-decimetre) changes to be detected and measured. This accuracy assessment will serve to validate our GCP georeferencing process and quantify the uncertainty in the absolute position of the point cloud. We hypothesize that sub-decimetre change can be monitored using the UAV-MVS process.

2.2 Methods

2.2.1 Study Area

The site chosen for this study is a 100 m section of coast in a sheltered estuary in southeast Tasmania, Australia (Figure 2.1). The site was selected to evaluate the suitability of the UAV-MVS technique to fine-scale change detection. The southern end of the site is a salt marsh and the remainder contains grasses along an erosion scarp with intermittent scrub bush (Figure 2.2).

2.2.2 Hardware

The TerraLuma UAV used for this study is based on the OktoKopter platform (Mikrokopter, 2012). The OktoKopter is an electric, multi-rotor system with an approximate payload limit of 1 kg. When carrying a full payload the flight time is approximately 6 minutes, which is more than enough to capture UAV-MVS imagery for a ~1–2 ha area. The on-board GPS and navigation sensors provide 5–10 m positional accuracy and the on-board

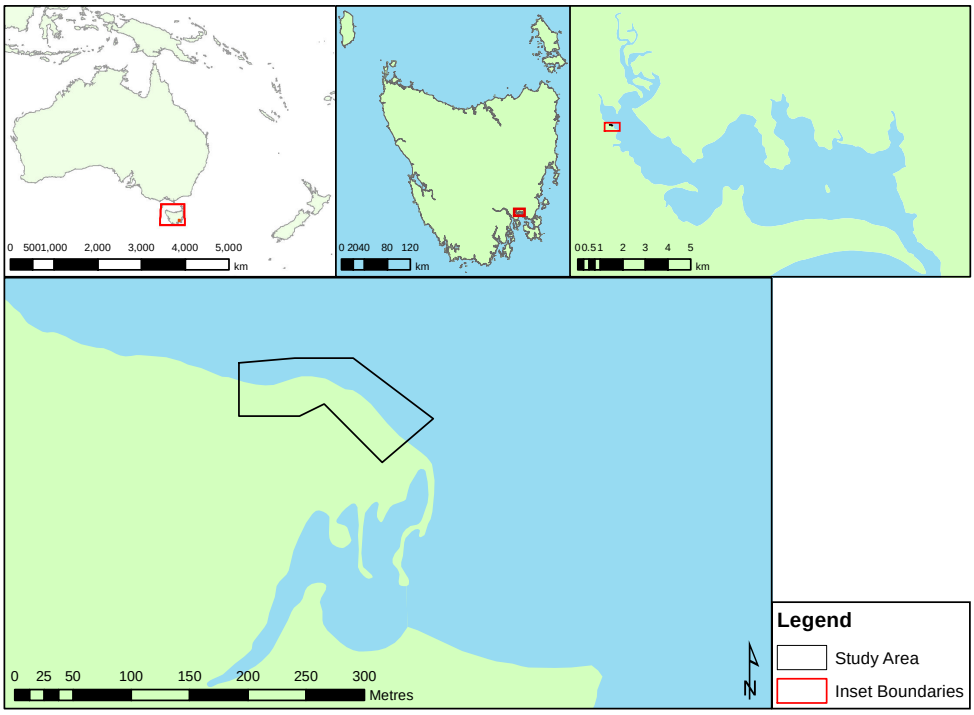

Figure 2.1: Coastal monitoring site in an estuary in southeast Tasmania.

Figure 2.2: Images of the site (the first two are taken looking east, the third is taken looking west). The first image shows a ~2 m high erosion scarp and the second shows the much smaller 5–10 cm scarp. The third image shows that this section of coast is representative of the area.

computer is able to navigate the UAV to pre-defined GPS waypoints. The OktoKopter has a stabilised camera mount that can carry different sensors. To create UAV-MVS point clouds a standard digital camera can provide imagery with sufficient resolution. We have chosen the Canon 550D digital SLR camera as it has excellent image quality and a lightweight body. The focus of the lens is fixed to infinity, the ISO is set to 200, and the aperture is fixed to $f3.5$ resulting in a minimum shutter speed of $1/2000^{\text{th}}$ of a second. These settings reduce motion blur. The camera is triggered once per second (1 Hz) by the OktoKopter's flight controller acquisition interval. This frequency provides a great deal of overlap (70–95%) and redundant photography (over 300 photos per flight).

A Leica Viva real-time kinematic dual-frequency differential GPS (RTK DGPS) was

used to survey the GCPs for UAV-MVS point cloud georeferencing. A Leica Total Station (TC407) was also used to survey the GCPs and create a reference dataset for accuracy assessment.

2.2.3 Data Collection

For accurate georeferencing of the UAV imagery accurate GCP coordinates are required. We distributed around 90 orange circular flat disks, ~10 cm in diameter, across the study site at a spacing of ~3–5 m. Initially traffic cones (witches hats) were used for GCPs, however the exact centre and height reference were difficult to establish when surveying the GCPs. These disks were our first attempt at ground control and this study was partially set up to assess if their small size was potentially reducing georeferencing accuracy. To evaluate an alternative 21 larger 22 cm pizza trays have been used. A hole was drilled in the centre of each tray. A 3 cm wide rim of was painted on each tray in colours designed to allow automated unique identification (since the datasets used for this study were captured the colour has been reconsidered and the trays now have an orange rim). For future studies we are considering custom made cones that may provide better centre point matching once point clouds have been extracted.

The larger trays were distributed along the two sides of the study area at intervals of ~6 m. Figure 2.7 shows the layout of the GCP trays and disks. We carried out both an RTK DGPS survey and an additional total station survey (with the prism mounted on a pole) to provide a reference dataset of GCP coordinates for all trays and disks. The orthometric height obtained from the total station survey was converted to an ellipsoid height by subtracting a geoid-ellispoid separation value (or N value) of 3.256 m (derived using AUSGeoid09 Geoid-Ellispoid Separation Interpolation[9]. These GCPs were surveyed using RTK DGPS which were compared to total station coordinates to gauge the accuracy of the GCP survey technique. The UAV was deployed at a flying height of 30–50 m above ground level (AGL) capturing a photograph every second. The first flight captured nadir photography and the second flight captured oblique photography with the camera tilted to approximately 45°. The captured photos were screened and a subset of clear (i.e., not blurred) photos of the area were selected for the UAV-MVS process.

[9] `http://www.ga.gov.au/ausgeoid/nvalcomp.jsp`

2.2.4 UAV-MVS

The first stage in the UAV-MVS process is feature extraction. Automated methods rely on features that can be distinguished, described, and matched in multiple views of a scene. This is done using the method described in Snavely et al. (2006) and Snavely et al. (2007) whereby a least squares bundle adjustment is performed based on the matching of SIFT features from down-sampled versions of the images. Lowe (2004) describes the SIFT process as follows. A 128 element SIFT feature vector (or invariant descriptor vector) is created for each interest point in the image that is determined to be invariant to scale and orientation. The vector describes a chosen stable keypoint and is designed to reduce the effects of illumination and shape distortion. A database of these keypoints is then created and the matching process exhaustively compares each feature from a new image to all features in the database. Candidates are chosen based on Euclidean distance of their feature vectors using a nearest neighbour algorithm. A typical image can contain thousands of SIFT keypoints (Lowe, 2004; Farenzena et al., 2010).

The matching of these features across overlapping photography produces a sparse set of 3D coordinates of the surface features, the position and orientation of the camera, and radial distortion parameters for each photograph. These outputs from the bundle adjustment are based on the lower resolution images. The PMVS2 software can be used to "fill in" or "densify" the point cloud (Furukawa and Ponce, 2007) however, this is usually done using the down-sampled imagery rather than the original full resolution imagery, which potentially reduces the density and accuracy of the final point cloud.

Our UAV-MVS process improves the densification by utilising the full resolution imagery in the PMVS2 process. As portrayed in Figure 2.5, the process extracts SIFT features (in fact "SIFTFast"[10] features) from a reduced resolution dataset and performs the bundle adjustment to retrieve a sparse point cloud and camera parameters. We then transform the coordinates of the sparse point cloud and the camera coordinates to match their equivalent values for the full resolution imagery, i.e., essentially scaling up the coordinate system. The radial distortion of the full resolution images is removed and these images are then processed with PVMS2 resulting in a dense set of 3D coordinates, including point normals. To evaluate the point derivation performance increase and assess the increase in computation time PMVS2 was run on down-sampled imagery and full resolution imagery. The point cloud produced (see example point cloud from the full resolution imagery in Figure 2.3) is in an arbitrary reference frame and must be

[10] `http://sourceforge.net/projects/libsift/`

transformed into a real-world coordinate system via a Helmert transformation.

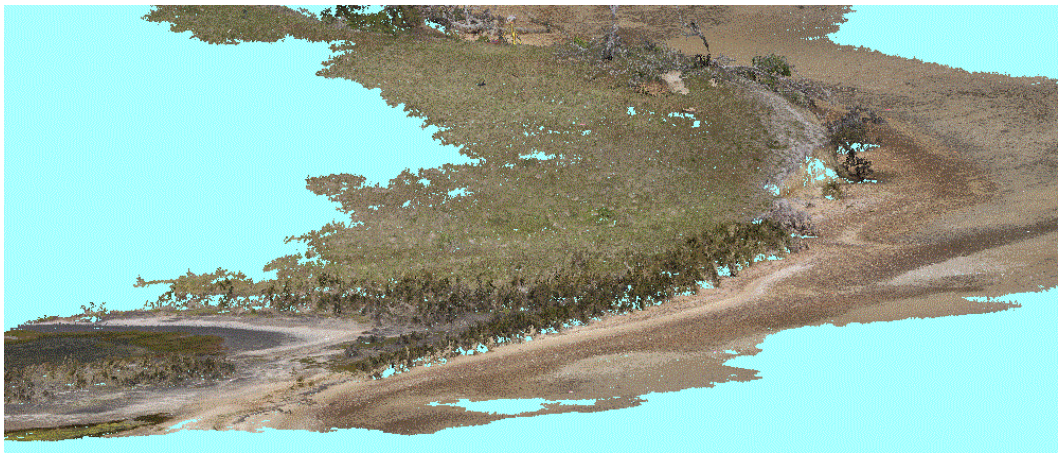

Figure 2.3: A dense UAV-MVS point cloud after PMVS2 processing with full resolution imagery. The majority of the surface is represented in the cloud at <1–3 cm point spacing. The patches with no points are either scrub bush or tussock grass. The erosion scarp is usually bare earth (see Figure 2.2) and is well represented in the cloud.

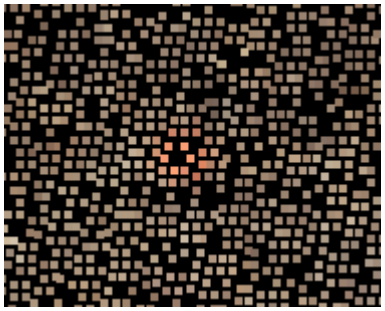

(a) A small ~10 cm orange GCP disk. The orange points can be extracted from the cloud by applying a colour threshold. These disks do not result in clusters with many points when flying at ~50 m, larger disks or cones are now considered more suitable unless flying lower or for terrestrial MVS.

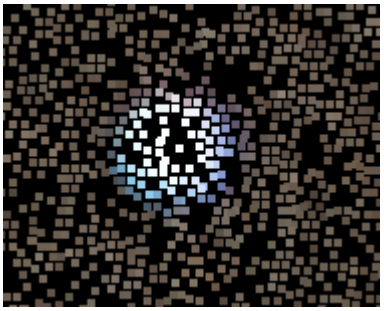

(b) A large 22 cm GCP tray. The GCP tray clusters were manually extracted from the point cloud due to their varying colour. Future studies will ensure these GCP trays (or cones) are designed and painted so that they result in dense clusters of many points and can be found automatically.

Figure 2.4: GCP Clusters in the point cloud used for georeferencing by matching cluster centres to GCP locations.

The georeferencing of the point cloud can be done in a number of ways. The simplest and least accurate method is direct georeferencing. This is done by geotagging the photography using the navigation-grade GPS on-board the UAV with approximate GPS locations of the time-synchronised camera at the moment of capture. These coordinates are then used to calculate the Helmert transformation parameters by matching the camera coordinates in the arbitrary reference frame to the corresponding GPS locations. The second method, which shall be referred to as "semi-automatic GCP georeferencing" (portrayed in Figure 2.6), analyses the colour attributes of the points in the point cloud and ex-

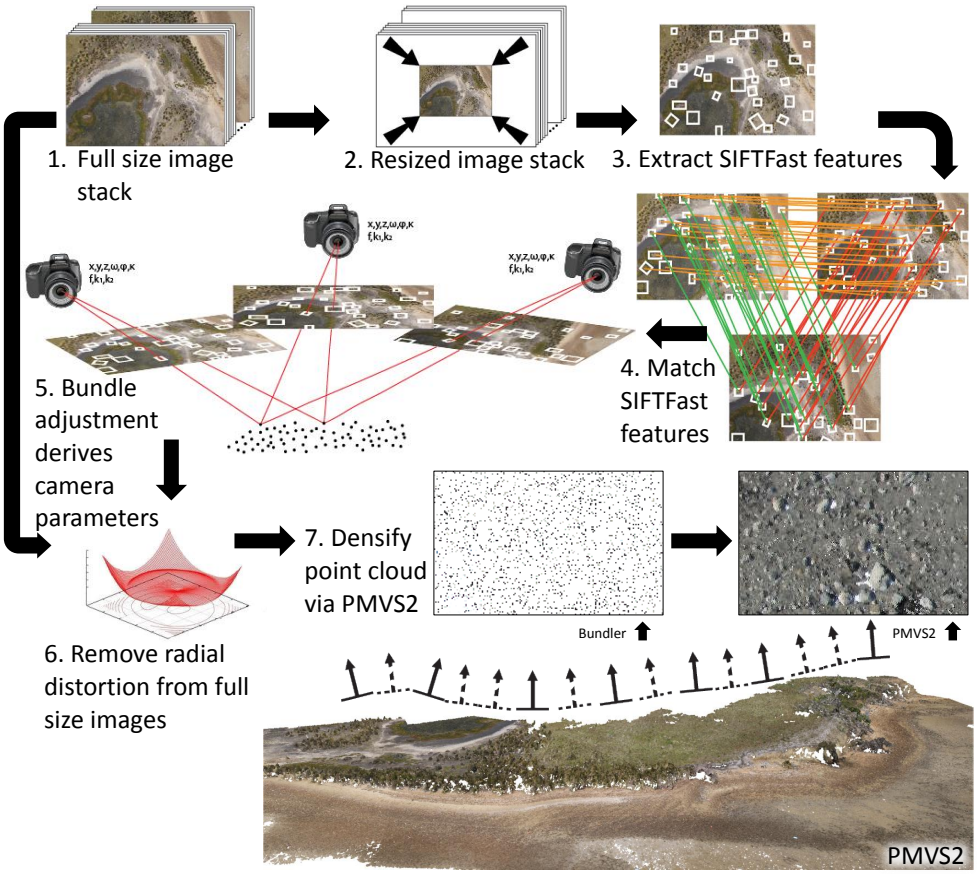

Figure 2.5: The UAV-MVS point cloud generation process. The key difference from the standard work flow is at Step 6 where the full resolution imagery is undistorted and provided to PMVS2 for point cloud densification.

tracts the point subsets that match the colour of the orange GCP disks. This colour is based on a threshold collected from a selection of images of the disks (i.e., disks are located in a random set of images and a colour picker is used to calculate an RGB average for the disks). The threshold is applied to the Euclidean distance for each point in RGB colour space to find points that match the disk colour. When all disk points are extracted, the reference points for the point clusters (an example of which is shown in Figure 2.4(a)) need to be determined to identify the centre coordinate for each disk. An alternative approach may be to use least squares template matching (Zhang et al., 2005b; Zhang et al., 2003; Kocaman et al., 2006) or ellipse fitting (Hanley, 2001) to determine corresponding GCP locations in multiple images and then compute 3D centre point coordinates in the arbitrary coordinate system based points in the cloud (found using cluster extraction) and their matched feature descriptor vectors (containing corresponding image coordinates). This has not been attempted here and is being considered for future studies. The automated extraction of GCP clusters has potential, particularly

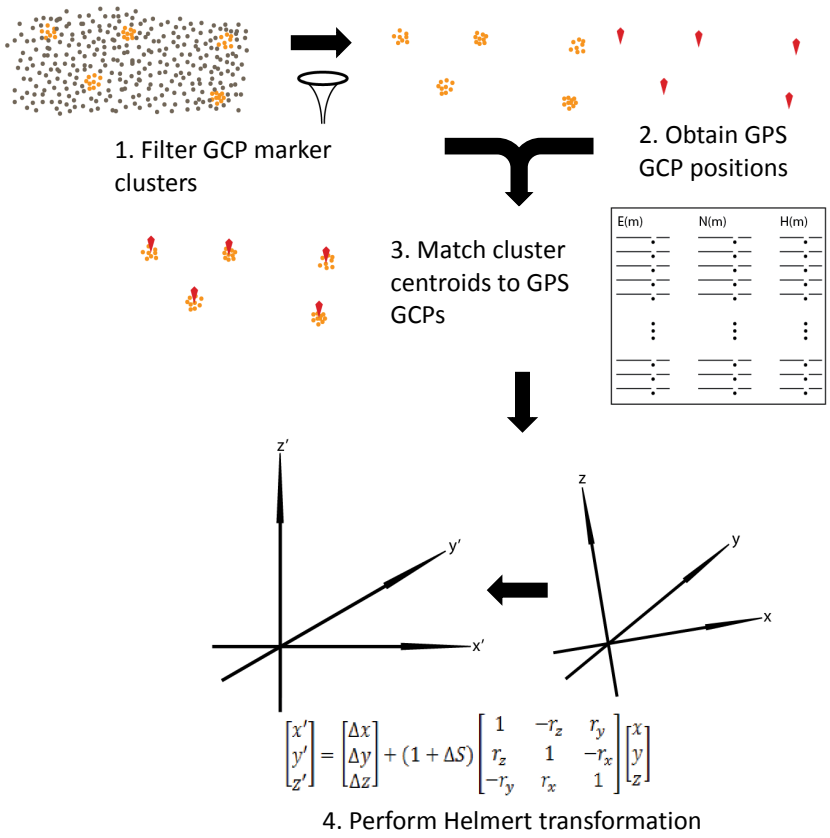

Figure 2.6: The UAV-MVS georeferencing process. The filter in Step 1 can either be manual or automatic. The match in Step 3 could either be based on cluster centoid or cluster mean. In Step 4 a Helmert transformation is derived for transforming the point cloud or generated DSMs.

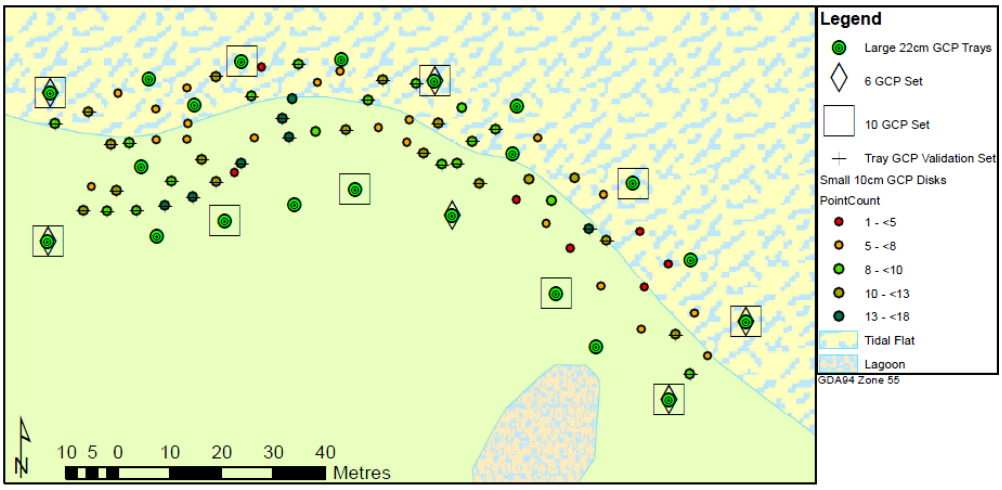

Figure 2.7: Map of GCP layout. The trays are mainly along the edge of the study area and a number are placed toward the central portion. This distribution is considered favourable to accurate georeferencing. The smaller GCP disks are spread throughout the study area.

if GCP target design is improved further. The approach will therefore be used here to evaluate its feasibility and the resulting centre location determination accuracy.

The GCP cluster centre could either be (a) the centroid of the cluster based on its bounding box, or (b) the mean coordinate from the set of coordinates in the cluster. Both are strongly influenced by the cluster shape and the spatial distribution of the cluster points. To transform the point cloud into real world scale, the cluster centres are matched to their corresponding GCP coordinates to calculate the Helmert transformation parameters. This is done by deriving an initial Helmert Transformation based on the navigation grade on-board GPS positions for the time synchronised camera locations matched to the Bundler derived camera positions to locate the point cloud to an accuracy of ~5–10 m. The GCP cluster centroids can be matched to the corresponding GCP positions by finding the closest GCP position to each cluster (when GCPs are not sufficiently dispersed this process may need to be done manually).

A third method, which shall be referred to as "manual GCP georeferencing", produces the transformation parameters based on manually selected point clusters representing the large GCP trays (see Figure 2.4(b)). The Helmert transformation derived from the large GCP trays can be validated against the cluster centres for the automatically extracted orange GCP disks. As with the automated approach the cluster centres are calculated and matched to the GCP positions.

2.2.5 Accuracy Assessment

The accuracy of the GPS GCP survey impacts on the subsequent transformation, therefore the GPS survey is compared to the total station survey results. The initial assessment relates to the choice of mean or centroid cluster centre. To assess the effect of the cluster centre derivation method on the derived transformations, the 12 best centroid-based and 12 best mean-based transformation results are compared (those with a RMSE of less than 40 mm). Subsequently, an assessment of the layout and number of GCP clusters used to derive the Helmert transformation is conducted by evaluating the results from a number of scenarios (Scenario 1, 2 and 3). In each scenario the transformed cluster centre locations of the validation disks are compared to the GCP reference coordinates (total station data). The validation set is a subset of GCPs not used to derive the transformation.

The first and second scenarios use a set of GCP clusters extracted manually from the

large trays, i.e., manual GCP georeferencing. All 21 GCP trays are used for the initial transformation derivation. To assess the effect of the number of GCPs on the accuracy of the transformation, ten and six GCP trays distributed across the area are used (see Figure 2.7). Ideally, the reference dataset would be a continuous coverage over the entire study area, unfortunately this is not available at sufficient accuracy and precision in the study area to allow us to compare with UAV-MVS point clouds. For validation a set of orange disk GCP clusters made up of eight or more points will be used to derive a set of cluster centres. This validation set (see Figure 2.7) will be transformed using each version of the Helmert transformation derived from the 21, 10, and 6 GCP tray sets respectively. The results will then be compared.

In the first scenario (Scenario 1), only total station coordinates for the GCP trays are used in the Helmert transformation and then its accuracy is assessed against the total station coordinates of the GCP disks. This provides a "best case" accuracy, even though the additional time required to undertake a total station survey may not be viable for most cases. If required, the total station could use tripod mounted prisms instead of pole mounted prism to further improve the accuracy of the GCP survey. The second scenario (Scenario 2) uses the RTK DGPS tray coordinates for manual GCP georeferencing and the transformed GCP disk cluster centres are compared to the total station GCP coordinates.

The third scenario (Scenario 3) assesses the accuracy of our semi-automatic georeferenced UAV-MVS technique. The small orange disk GCPs are automatically extracted from the point cloud and the cluster centres are used to derive a Helmert transformation by matching cluster centres to DGPS GCPs (i.e., semi-automatic GCP georeferencing). The number of points per disk cluster and GCP disk layout are examined and six sets of disk GCPs are chosen to examine the effect of GCP density and distribution, and the impact of cluster point count on accuracy. The GCP disk layout and the effect of poor orange point cluster extraction (i.e., a low number of points in the cluster) can then be evaluated. Similar to the first scenario these sets are used to derive Helmert transformations which are applied to validation sets of GCP cluster centres, one validation set being automatically selected GCP disks and the other being manual extracted trays. Both validation sets are evaluated to assess whether the semi-automatic cluster extraction or manual cluster selection processes have a systematic influence on accuracy. After transformation the resulting cluster centre coordinates are compared. By changing the distribution and number of GCP disks used to derive the transformation the optimal number of GCPs and the optimal GCP layout can be evaluated and the minimum number of points in a cluster required to achieve accurate georeferencing can

be determined.

2.3 Results and Discussion

The data collection and processing methods described are the proposed technique for future change monitoring studies, hence there is a need for a clear understanding of the geometric accuracy of the UAV-MVS point clouds. Our georeferencing technique relies on accurate and sufficient ground control and RTK DGPS is the most time efficient means of surveying GCPs. The accuracy of the total station survey is within +/-10–15 mm in both horizontal and vertical components with respect to fixed control. When these coordinates are compared to the RTK DGPS coordinates they are typically +/-17 mm apart and always less than 26 mm horizontally and less than 40 mm vertically. These results correspond with the standard deviations reported by the GPS.

There were three UAV flights flown over the site on the 30th of November 2010, two flights for nadir photography and one flight for oblique photography. Almost 1000 photographs were taken and from this large set a subset of 105 photographs were chosen based on image clarity and content. These images were down-sampled (5184x3456 pixels $\Rightarrow$ 2000x1333 pixels) and processed by Bundler. An initial point cloud containing approximately 230,000 points was extracted (including points for each of the 105 camera locations). The Bundler output was prepared for use with PMVS2 (including transforming the parameters to suit full resolution imagery). The full resolution images were radially undistorted using the calculated coefficients and PMVS2 was run to produce a dense point cloud. The resulting point cloud contained over seven million points. The processing time was 26 hr 43 min 54 sec (or 96,234 sec) on a Dell PowerEdge R815 with four AMD Opteron processors (32 cores at 2.2 GHz), 256 GB of RAM, and 15K RPM SAS drives. The PMVS2 processing time was 11 hr 34 min 3 sec (or 41,643 sec). The resulting point spacing was <1–3 cm. When PMVS2 was run on the down-sampled imagery the resulting point clouds had only ~1.3 million points (or a ~5–15 cm point spacing) and the PMVS2 processing time was 1 hr 33 min 15 sec (or 5595 sec). The use of full resolution imagery in PMVS2 results in 5 times more points in ~11 times the processing time.

The colour matching parameters for orange GCP disks were determined and 67 GCP disk clusters were extracted. The cloud was manually processed to extract 21 GCP tray clusters. Figure 2.7 shows the layout of the GCP trays and disks.

2.3.1 Cluster Centres - Centroid or Mean?

The initial question relates to the choice of cluster centre calculation, i.e., the choice between centroid and mean. If we consider the 24 GCP disk cluster set transformations with a total RMSE of less than 4 mm and analyse the mean RMSE for the "centroid" derived results versus the "mean" derived results (as portrayed in Table 2.1) there is evidence to favour the mean over the centroid if the overall RMSE (i.e., ENH_{RMSE} or combined Easting, Northing and Height Root Mean Squared Error) is used as the main accuracy metric, however, there is only a 1.1 mm difference. The other accuracy metrics shown are Easting RMSE (E_{RMSE}); Northing RMSE (N_{RMSE}); Height RMSE (H_{RMSE}); and combined Easting and Northing RMSE (EN_{RMSE}).

Table 2.1: RMSE errors (in millimetres) for Means vs Centroids. Height is the least accurate dimension. The Easting and Northing error or horizontal position error is higher for the mean based transformations. This is important for GCP matching and georeferencing accuracy, therefore the centroid based transformation is the favoured method for determining cluster centre.

	E_{RMSE}	N_{RMSE}	H_{RMSE}	EN_{RMSE}	ENH_{RMSE}
Centroid based transformations	15.2	14.4	53.1	14.8	34.4
Mean based transformations	18.0	15.4	49.0	16.7	33.5

These cluster points are filtered based on colour and proximity. If the filter has identified more coloured points on one side of a disk than the other, then the mean will be biased to one side. The centroid, on the other hand, is based on the bounding box of all pixels in a cluster, which is less influenced by the distribution of points within the bounding box. Both methods result in a poor centre calculation when points are only found on one side of a disk and not the other, so perhaps a measure of shape would help highlight good GCP cluster candidates in future studies. As discussed, template matching and ellipse fitting may be alternatives worth considering. The centroid option results in a better EN_{RMSE} and less favourable H_{RMSE} with a 4 mm difference, which impacts on the overall accuracy (i.e., ENH_{RMSE}). The disks are flat and usually placed so that they are reasonably level, therefore the variation in height across the disk should be much less than the variation in horizontal position. The control is captured using DGPS and the predicted accuracy for height measurements is usually ~4 cm, this is an order of magnitude more than the cluster point height difference (~4 mm) seen between the two cluster centre options in that dimension. Based on these considerations the centroid of the clusters will be used to define cluster centre as it is more robust to poor cluster point distribution and it results in a more accurate horizontal position of the disk centres.

2.3.2 Automated GCP Disk Cluster Extraction performance

Figure 2.8 provides a histogram of frequency distribution cluster point counts along with the mean, median and standard deviation of those counts. These results indicate that the majority of clusters contain between five and 13 points, with eight being the average. More than half the clusters contain more than eight points. The scenarios discussed below will compare the effect of using only clusters with more than eight points versus allowing clusters with six or more points to be used.

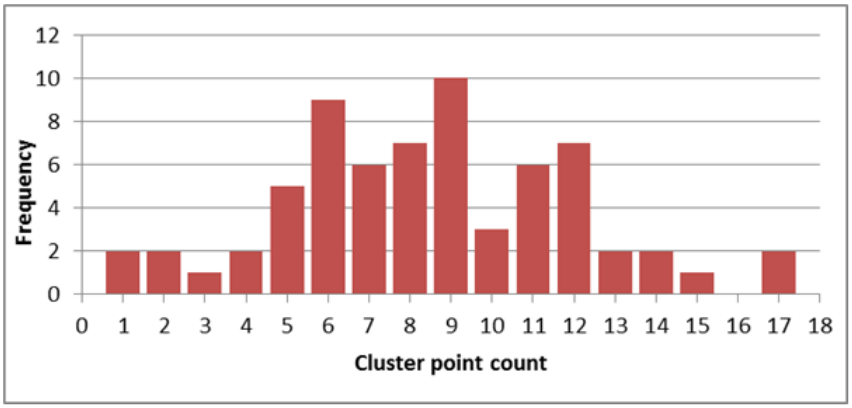

Figure 2.8: A histogram of the number of automatically extracted points per cluster representing each of the orange disks. The mean is 8.5 points per cluster, the median is 8 and the standard deviation is 3.5.

To estimate the accuracy of the georeferenced point clouds and to evaluate the effect on accuracy of GCP layout for scenarios 1 and 2, the Helmert transformations are compared using the RMSE derived from the comparison of the reference total station dataset to the 34 transformed GCP disk cluster centres (i.e., those with eight or more points in a cluster, see GCP tray validation set in Figure 2.7).

2.3.3 Scenario 1 and 2

Scenario 1 tests the accuracy of the georeferenced point cloud based on the manually selected GCP tray clusters Helmert transformation (Table 2.2) and a total station GCP survey. Scenario 2 uses the manually selected GCP tray clusters Helmert transformation (Table 2.3) and a DGPS GCP survey for the accuracy assessment. The comparative accuracy of the three transformation outcomes for the two scenarios is summarised in Table 2.4 and Table 2.5. The distribution and orientation of these errors were visualised in 3D in Eonfusion[11] allowing the visual assessment of the X, Y, and Z components of

[11] `https://www.echoview.com/`

the error. Two example views are shown in Figure 2.9 for the residuals for the GCP disks transformed using the tray centroid transformation for all 21 trays (Figure 2.9(a)) and for 6 trays (Figure 2.9(b)).

The higher accuracy total station survey of the GCP trays was expected to result in a more accurate transformation, however, the GPS survey surprisingly showed a slightly higher accuracy (7 mm difference in ENH_{RMSE}). The EN_{RMSE} is lower in all three GPS-based transformations (approximately 0.5 mm more accurate). The H_{RMSE} is driving the overall accuracy down, similar to what occurred in the cluster centre centroid versus mean comparison. The error estimates for each of the DGPS GCP derived Helmert transformation parameters (Table 2.3) are slightly better than the error estimates for each of the total station GCP derived Helmert transformation parameters (Table 2.2). The differences are small, however, as can be seen in the 3D residual portrayals (Figure 2.9), these slight differences and the often major differences in the parameter values can affect the transformation results by millimetres. Figure 2.9(a) and Figure 2.9(b) show that removing the majority of the GCPs from the transformation has a significant impact on the error in the central portion of the transformed point cloud. This region coincides with the portion of the site with most topographic relief. In both scenarios, the number of GCPs used has a major impact on the accuracy. The size of the error doubles in each case, from <35 mm to >75 mm in scenario 1 and <30 mm to >65 mm in scenario 2; and finally to ~140 mm and ~130 mm respectively when only 6 GCPs are used.

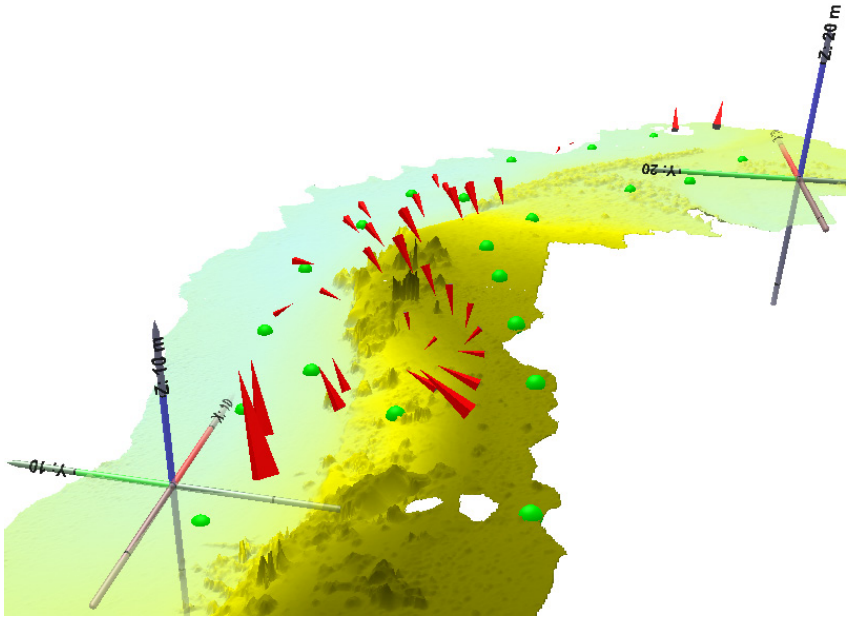

(a) The 21 tray set (i.e., All trays). The largest horizontal residuals of ~25 cm occur at either end of the study area (vertically the largest residuals are as high as ~40 cm) whilst the majority of the residuals are ~14 cm. The smallest residuals occur on the beach.

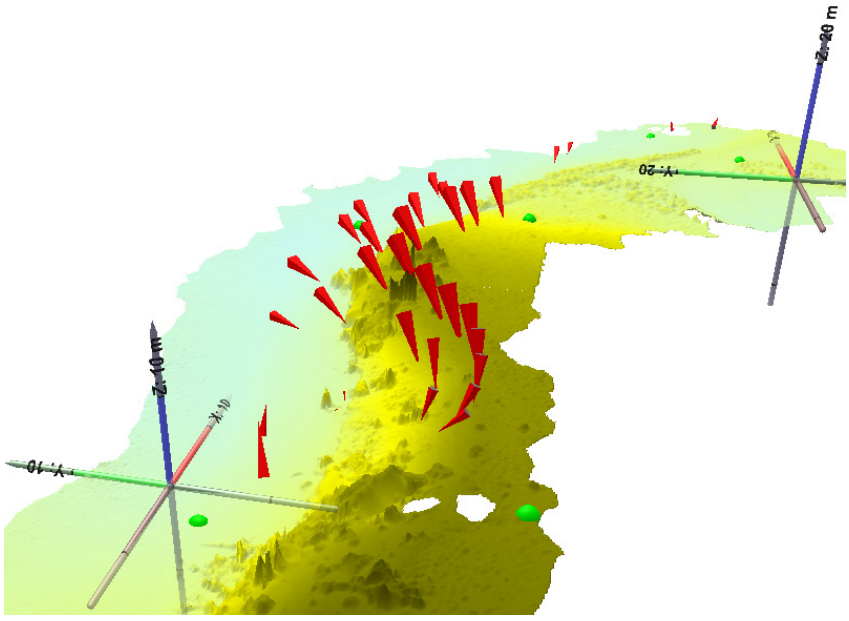

(b) The 6 tray set. The largest residuals of ~-31 cm occur in the central portion of the study area near the steep scarp whilst the majority of the residuals are ~-14 cm. Again, the smallest residuals occur on the beach.

Figure 2.9: Eonfusion screen captures of 3D residuals for the validation GCP set (red arrows of residuals for each GCP are scaled by a factor of 20). The underlying surface model is derived from the UAV-MVS point clouds (the two holes in the foreground are due to dead scrub bushes resulting in no points). The view angle is from the west looking down on the site.

Table 2.2: Scenario 1 Helmert transformation results (translation parameters are in metres, rotation parameters are in degrees and accuracies are in millimetres). Only total station coordinates for the GCP trays are used in this Scenario its accuracy is assessed against the total station coordinates of the GCP disks.

Description	Tx	+/-	Ty	+/-	Tz	+/-	Rx	+/-	Ry	+/-	Rz	+/-	Scale	+/-
All trays	536154.565	61.1	5262637.035	98.2	30.916	68.6	-6.216	1.1	-18.8783	2.5	-32.9718	0.9	9.4409	8.2
10 trays	536154.522	108.6	5262636.977	169.9	30.837	118.6	34.6250	1.9	9.4528	4.3	-73.8128	1.4	9.4383	13.4
6 trays	536154.401	154.2	5262636.794	244.2	30.6975	165.2	3.2108	2.5	-3.1168	6.2	-48.6806	1.9	9.4352	17.8

Table 2.3: Scenario 2 Helmert transformation results (translation parameters are in metres, rotation parameters are in degrees and accuracies are in millimetres). This scenario uses the RTK DGPS tray coordinates for manual GCP georeferencing and compares the transformed GCP disk cluster centres to the total station GCP coordinates.

Description	Tx	+/-	Ty	+/-	Tz	+/-	Rx	+/-	Ry	+/-	Rz	+/-	Scale	+/-
All trays	536154.554	60.7	5262637.027	97.6	30.947	68.1	-56.4816	1.1	-31.4445	2.5	-32.9719	0.9	9.4415	8.1
10 trays	536154.511	108.1	5262636.970	169.1	30.870	118.1	-40.7732	1.8	3.1694	4.3	-42.3968	1.4	9.4389	13.4
6 trays	536154.392	152.8	5262636.792	242.0	30.732	163.7	3.2107	2.5	-3.1168	6.1	-48.6806	1.9	9.4358	17.6

Table 2.4: Scenario 1 result for manually selected tray transformation validation against total station GCP disks (accuracies in millimetres). Total station coordinates for the GCP trays are assessed against the total station coordinates of the GCP disks.

Description	GCP Count	Test Count	E_{RMSE}	N_{RMSE}	H_{RMSE}	EN_{RMSE}	ENH_{RMSE}
All trays	21	34	28.1	18.7	49.2	23.4	34.4
10 trays	10	34	67.5	43.8	102.9	55.6	75.4
6 trays	6	34	143.0	97.0	171.0	120.0	140.4

Table 2.5: Scenario 2 result for manually selected tray transformation validation against DGPS GCP disks (accuracies in millimetres). In this scenario RTK DGPS tray coordinates are used to transform GCP disk cluster centres. These are assessed against the total station GCP coordinates.

Description	GCP Count	Test Count	E_{RMSE}	N_{RMSE}	H_{RMSE}	EN_{RMSE}	ENH_{RMSE}
All trays	21	34	36.8	19.6	21.0	28.2	27.0
10 trays	10	34	76.9	43.8	73.6	60.3	66.5
6 trays	6	34	153.2	97.5	143.7	125.3	133.7

2.3.4 Scenario 3

The question that arises from the previous scenarios relates to an optimal GCP distribution and number of GCPs. Scenario 3 was developed to evaluate GCP layout and the success of automated orange disk cluster extraction. For this scenario, a number of GCP disk subsets were used to derive transformations via semi-automated georeferencing and the results compared to two validation sets, i.e., the GCP tray dataset and the set of the GCP disks that were not used to derive the transformation and that had a cluster point count of eight or more.

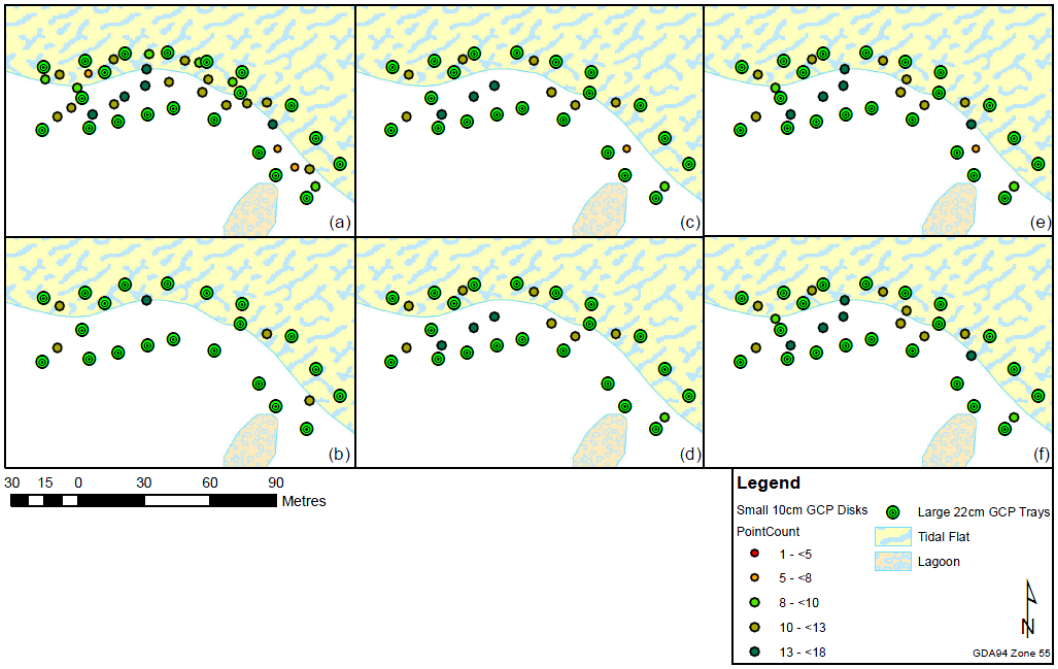

Figure 2.10: GCP disk layouts, (a) Dense GCP coverage; (b) Very sparse GCP coverage; (c) GCPs along edge (≥6 cluster points); (d) GCPs along edge (≥8 cluster points); (e) GCPs along edge and within (≥6 cluster points); (f) GCPs along edge and within (≥8 cluster points). The disk distribution suffers when GCPs are removed due to low point counts.

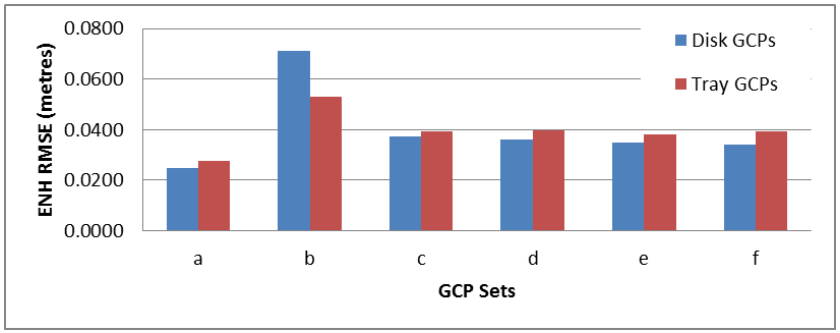

Figure 2.11: Comparison of RMSE for each of the automatically extracted GCP disk cluster transformations assessed against remaining GCP disks (blue) and GCP trays (red). Set (a) (27 GCPs) performs the best due to the distribution and density of control. Set (b) (5 GCPs) performed poorly as expected. The remaining sets show mixed results, the differences between sets (c) and (d) and sets (e) and (f) are not definitive. This may suggest the number of GCPs is more important than avoiding clusters with only six or seven points.

Table 2.6: Scenario 3 Helmert transformation results (translation parameters are in metres, rotation parameters are in degrees and accuracies are in millimetres). In this scenario, the small orange disk GCPs are automatically extracted from the point cloud and the cluster centres are used to derive a Helmert transformation by matching cluster centres to DGPS GCPs.

Description	Tx	+/-	Ty	+/-	Tz	+/-	Rx	+/-	Ry	+/-	Rz	+/-	Scale	+/-
Dense GCP coverage	536154.462	39.3	5262636.876	73.4	30.905	46.4	-6.2140	0.8	-18.8730	2.0	-58.1048	0.6	9.4474	5.9
Very sparse GCP coverage	536154.393	94.9	5262636.718	193.5	30.812	104.6	0.0695	1.8	-0.0215	5.4	-45.5388	1.4	9.4445	13.1
GCPs along edge (≥6 cluster points)	536154.484	64.5	5262636.881	117.0	30.935	73.9	-15.6391	1.3	9.4484	3.3	-36.1137	1.0	9.4451	9.7
GCPs along edge (≥8 cluster points)	536154.483	68.4	5262636.875	125.5	30.941	79.1	0.0689	1.4	-0.0236	3.5	-39.2554	1.2	9.4465	11.0
GCPs along edge and within (≥6 cluster points)	536154.468	50.9	5262636.866	96.1	30.928	59.4	12.6356	1.0	-6.3064	2.7	-26.6889	0.8	9.4479	7.7
GCPs along edge and within (≥8 cluster points)	536154.466	53.0	5262636.860	101.7	30.934	62.1	-12.4972	1.1	-6.3063	2.8	-58.1050	0.9	9.4495	8.5

Table 2.7: Result for automatically extracted GCP disk cluster transformation (based on subsets of GCP disks) validated against GCP disks (accuracies in millimetres), see Figure 2.10 for mapped distributions.

Description	Map	GCP Count	Test Count	E_{RMSE}	N_{RMSE}	H_{RMSE}	EN_{RMSE}	ENH_{RMSE}
Dense GCP coverage	a	27	13	15.2	3.0	40.0	9.1	24.8
Very sparse GCP coverage	b	5	31	87.9	77.6	38.7	82.7	71.3
GCPs along edge (≥6 cluster points)	c	12	24	15.5	1.3	63.1	8.4	37.5
GCPs along edge (≥8 cluster points)	d	11	24	9.6	1.7	61.7	5.7	36.1
GCPs along edge and within (≥6 cluster points)	e	16	21	6.6	2.8	59.9	4.7	34.8
GCPs along edge and within (≥8 cluster points)	f	15	21	0.7	1.3	59.1	1.0	34.1

Table 2.8: Result for manually extracted GCP tray cluster transformation (based on subsets of GCP disks) validated against manually extracted GCP trays (accuracies in millimetres), see Figure 2.10 for mapped distributions.

Description	Map	GCP Count	Test Count	E_{RMSE}	N_{RMSE}	H_{RMSE}	EN_{RMSE}	ENH_{RMSE}
Dense GCP coverage	a	27	21	8.1	22.6	41.0	15.4	27.5
Very sparse GCP coverage	b	5	21	64.8	47.7	44.0	56.3	53.0
GCPs along edge (≥6 cluster points)	c	12	21	6.3	25.4	62.9	15.9	39.3
GCPs along edge (≥8 cluster points)	d	11	21	13.8	28.9	61.0	21.3	39.8
GCPs along edge and within (≥6 cluster points)	e	16	21	17.0	22.8	59.7	19.9	38.2
GCPs along edge and within (≥8 cluster points)	f	15	21	24.6	24.5	58.5	24.5	39.3

Figure 2.10 portrays the chosen GCP sets and the number of points in the clusters. Table 2.6 provides the derived Helmert transformation results, this set of transformations was applied to the two validation sets. Table 2.7 compares the validation sets of the transformed GCP disk cluster centres to the corresponding total station coordinates of the validation GCPs. Similarly, Table 2.8 compares the transformed centres of the manually selected tray clusters to the reference data validation GCPs. Figure 2.11 compares the RMSE of the two validation scenarios. The resulting transformed validation sets show that the automatically extracted disk clusters provide a better georeferencing accuracy, the maximum ENH_{RMSE} is approximately <5 mm in all sets except set (b) (Figure 2.11); this effect is similar to the results seen in the other scenarios. The choice of cluster extraction method (manual or semi-automatic) has a systematic impact on accuracy. The impact of cluster density and distribution can therefore be evaluated by examining either validation set result.

The dense coverage set (a) contains 27 clusters all made up of more than six points evenly distributed throughout the study area. As expected, this transformation performs the best of all the cases (an ENH_{RMSE} of ~25 mm and ~28 mm when validated against GCP disks and trays respectively). In this set the GCPs are both within and along the edges of the study area. In contrast, the results relating to set (b) are relatively poor (ENH_{RMSE} of ~71 mm and ~53 mm respectively). Again, this is to be expected since only five GCPs were used to derive the transformation. This result highlights the need for sufficient, well distributed control. The accuracy obtained by UAV-MVS when properly controlled is, in fact, within the magnitude of accuracy achievable by RTK DGPS.

The four remaining GCP sets test the effect of fewer GCPs where set (c) and set (e) contain a cluster with six points whereas sets (d) and (f) also have an additional four GCPs in the central portion of the study area. In some cases the removal of the six point cluster improves accuracy (Table 2.7) whereas in others it reduces accuracy (Table 2.8). The disk validation set shows a more accurate result, particularly in the horizontal dimension. The height dimension is the major contributor to the overall error. Set (f) using disk validation is by far the most accurate of these three options in the horizontal dimensions (EN_{RMSE} of 1 mm) and the H_{RMSE} is 59 mm which is similar to other H_{RMSE} values for the other four sets. Removing disks with relatively few points (<8) might improve the overall accuracy, however, this reduction will result in fewer available GCP clusters to contribute to the transformation, which could ultimately lead to a poorer fit of the transformation model. Due to this potential impact, and due to the less than definitive results, it may be better to allow these six point clusters to remain

in the transformation derivation. In addition, the shape of the cluster may need to be measured to help rank the clusters and discard those that are not circular enough in shape. The size and colour of GCP targets is important. The ~10 cm disks often result in GCP disk clusters of fewer than eight points, this is influenced by both the disk size and by the height of surrounding vegetation and other occluding surfaces. The accuracy of the cluster centre calculation is therefore affected. The larger 22 cm trays with a higher percentage of painted surface area might provide more accurate cluster representations in the generated point cloud.

2.3.5 GCP Distribution

The georefencing accuracy is strongly influenced by GCP distribution and to a lesser degree by the cluster centre to GCP match. Based on this assessment the best distribution of GCPs is evenly distributed throughout the focus area with a spacing of one fifth to one tenth the UAV flying height (AGL). The terrain variation is important and GCPs should be closer together in steeper terrain. The GCP targets should be clearly visible at the chosen flying height, camera resolution and focal length (>10 cm in diameter for a 40–50 m flying height with the Canon 550D), and they should be visibly different in colour to the surrounding landscape.

2.3.6 Applications and Limitations

SfM was developed mainly for 3D reconstruction of buildings and other objects from overlapping photography. Examples include modelling tourist destinations captured by hundreds of people who made their photos available on community Internet sites and modelling from photographs and video footage for applications such as architecture, archaeology, robotics and computer graphics. UAV-MVS point clouds have a great deal of potential due to their high point density. This results in an extremely detailed record of the surface at the time of data capture. A major limitation of the process is that the point clouds generated by the UAV-MVS do not represent areas in the landscape where vegetation is dense and complex (such as dead or dry bush with many overlapping branches) and when the surface has a homogeneous texture (e.g., water or a tin roof). These features do not provide the visible attributes needed for algorithms such as SIFT (Lowe, 2004) and pixel-wise dense matching MVS algorithms (Furukawa and Ponce, 2010; Furukawa and Ponce, 2007). Techniques are emerging that may overcome these problems (Lu et al., 2011; Mičušík and Košecká, 2010).

Natural environments present a range of complexities, including variable vegetation cover, strong topographic relief and variability in texture. Future studies will need to assess the impact of these complexities on the accuracy of the generated point clouds as landscape snapshots. Unlike LiDAR, the technique is not well suited to penetrating vegetation and, therefore, in vegetated areas it may not produce an accurate DEM when applying ground filtering algorithms (Dandois and Ellis, 2010; Remondino and El-Hakim, 2006). In applications where the ground is not the focus, the point clouds can provide a very detailed picture of the surface/terrain. The technique is well suited to canopy monitoring, particularly when combined with LiDAR derived DEMs. Furthermore, in areas where vegetation is sparse, such as along the coast, on mine sites, and on farm land the technique offers affordable hyperspatial and hypertemporal data.

2.4 Conclusion

This study presented an assessment of the accuracy and applicability of point clouds derived by structure-from-motion (MVS) based on Unmanned Aerial Vehicle (UAV) photography for natural landscape mapping and monitoring. The UAV-MVS technique generates dense point clouds (1–3 cm point spacing) of natural environments using MVS techniques to process imagery captured from a micro-UAV and georeferences the derived point cloud using Differential Global Positioning System (DGPS) surveys of ground control points (GCPs). In general, the use of UAV-MVS for 3D surface reconstruction and monitoring of natural landscapes has a lot of potential. There have been previous studies that have looked at assessing the accuracy of similar techniques, however, this is the first attempt to quantify the accuracy of the whole data capture and georeferencing process applied to a natural landscape. We developed new additions to existing SfM workflows that allow for full resolution imagery to be used instead of down-sampled imagery, resulting in denser point clouds (~80% increase in point density for an 87% increase in processing time based on 12 Mega-pixel versus 3 Mega-pixel imagery). We present a case study of UAV-MVS point clouds for a natural coastal area in southeastern Tasmania, Australia. Accurate and dense 3D point clouds are required to quantify the impact of erosion events on the coastline. The main objective of this study was to test the geometric accuracy of the point clouds based on Real-Time Kinematic (RTK) DGPS and total station surveys of GCPs. We found that, when flying at 40–50 m, an accuracy of 2.5–4 cm can be achieved provided sufficient, clearly visible GCPs are distributed evenly throughout the study area, and the flight planning ensures a high degree of overlap (70–95%) between images. The accuracy obtained by UAV-MVS when prop-

erly controlled is, in fact, within the magnitude of accuracy achievable by DGPS. In this study the distribution and number of GCP disks used to derive the transformation was varied to assess the optimal GCP layout, the number of GCPs, and the best methods for automated GCP extraction. The use of RTK DGPS to survey the ground control compared favourably to the total station survey results. The estimated accuracy of the total station data is ~1 cm in position and ~2 cm in elevation compared to DGPS accuracy of ~2.5 cm and ~4 cm in position and elevation respectively. Semi-automatic GCP point cluster extraction where clusters have greater than six points can allow a cluster centroid to be calculated. When GCP targets are well placed, large (>10 cm in diameter) and visibly different in colour to the surrounding landscape, this cluster extraction will be more successful. Future studies will investigate improving GCP design and matching. Semi-automatic cluster extraction enables georeferencing to sufficient accuracy such that sub-decimetre terrain change can be detected and monitored. Assessing the accuracy of these point clouds was an essential first step towards proving the viability of the UAV-MVS technique for fine-scale landform change monitoring. In particular coastal erosion monitoring requires sub-decimetre dense and accurate 3D point clouds. Fine scale change mapping cannot be achieved to sufficient spatial and temporal resolution with traditional airborne surveys and satellite sensors. The study site used in this paper will be monitored in the future to assess whether subtle coastal erosion in a sheltered estuary can be used as a climate change indicator. The MVS technique used fails to find sufficient features for matching in areas of complex vegetation and where surfaces have a homogeneous texture, these result in gaps or sparse areas in the point cloud. The technique does not penetrate dense vegetation and the resulting point cloud contains very few ground points beneath vegetation. Despite these limitations, the techniques have great potential in a wide range of application areas beyond coastal monitoring, including mining, agriculture and habitat mapping, and this accuracy assessment will serve to solidify the viability of the process.

Acknowledgements

We would like to thank Darren Turner for his technical and logistical support and UAV training and Dr. Christopher Watson for his help in undertaking the total station survey. Thank you to Myriax for the scholarship license to the Eonfusion nD spatial analysis package. In addition, we would like to give thanks and appreciation to the following people who have made their algorithms and software available: Noah Snavely and the Bundler development team; David Lowe (SIFT); the libsift team (SIFTFast);

and Yasutuka Furukawa and Jean Ponce (multi-view stereopsis algorithms: PMVS2 and CMVS). Without that generosity this research would not have progressed to this point.

Thesis context

At the time of this initial research (2010) the open source tools for SfM and MVS were only just being investigated for use with UAV imagery and the accuracy and reliability of the derived georeferenced point clouds needed to be assessed. This chapter sought to provide that assessment by comparing UAV-MVS survey data to total station verification points. The next stage in evaluating the technique for high resolution, high accuracy change detection was to ascertain whether to compare point cloud data or whether to convert these very large datasets to the triangulated mesh data structure. The comparison undertaken in Chapter 3 sought to provide insight into the two main options, namely triangulated mesh and Poisson surface reconstruction (Kazhdan et al., 2006). Chapter 2 also showed that the assessment of accuracy would require a much more precise comparison in order to properly assess accuracy and the impact of camera calibration method and other design choices on the derived 3D reconstructions. This lead to the experimental design used in Chapter 4 and Chapter 5.

3 | Assessment of surface representations derived from unmanned aerial vehicle multi-view stereopsis (UAV-MVS) and terrestrial multi-view stereopsis (T-MVS) point clouds

Chapter 3 focuses on the comparison of two surface representations derived from UAV-MVS and terrestrial MVS point clouds. The work comprising this chapter is published in the Proceedings of ISPRS2012 (Harwin and Lucieer, 2012a) with the original title: "An accuracy assessment of georeferenced point clouds produced via multi-view stereo techniques applied to imagery acquired via unmanned aerial vehicle". The only addition to the text is the aim and objectives statement at the end of the introduction.

Abstract

Low-cost Unmanned Aerial Vehicles (UAVs) are becoming viable environmental remote sensing tools. Sensor and battery technology is expanding the data capture opportunities. The UAV, as a close range remote sensing platform, can capture high resolution photography on-demand. This imagery can be used to produce dense point clouds using Structure-from-Motion (SfM) and multi-view stereopsis (MVS) techniques combining computer vision and photogrammetry. This study examines point clouds produced using MVS techniques applied to UAV and terrestrial photography. A multi-rotor micro UAV acquired aerial imagery from a altitude of approximately 30-40 m. The point clouds produced are extremely dense (<1-3 cm point spacing) and provide a detailed record of the surface in the study area, a 70 m section of sheltered coastline in southeast Tasmania. Areas with little surface texture were not well captured, similarly, areas with complex geometry such as grass tussocks and woody scrub were not well mapped. The process fails to penetrate vegetation, but extracts very detailed terrain in unvegetated areas. Initially the point clouds are in an arbitrary coordinate system and need to be georeferenced. A Helmert transformation is applied based on matching ground control points (GCPs) identified in the point clouds to GCPs surveyed with differential GPS. These point clouds can be used, alongside laser scanning and more traditional techniques, to provide very detailed and precise representations of a range of landscapes at key moments. There are many potential applications for the UAV-MVS technique,

including coastal erosion and accretion monitoring, mine surveying and other environmental monitoring applications. For the generated point clouds to be used in spatial applications they need to be converted to surface models that reduce dataset size without losing too much detail. Triangulated meshes are one option, another is Poisson Surface Reconstruction. This latter option makes use of point normal data and produces a surface representation at greater detail than previously obtainable. This study will visualise and compare the two surface representations by comparing clouds created from terrestrial MVS (T-MVS) and UAV-MVS.

3.1 Introduction

Terrain and Earth surface representations were traditionally derived from imagery using analogue photogrammetric techniques that produced contours and topological maps from stereo pairs. Digital photogrammetry has sought ways to automate the process and improve efficiency. Modern mesh or grid based representations provide relatively efficient storage of terrain data at a wide range of resolutions. The quality of these representations is dependent on the techniques used for data capture and processing. The representation improves with resolution and the data capture technique must be able to accurately determine height points at sufficient density to portray the shape of the surface. The difficulty faced is that the storage and visualisation become increasingly difficult as resolution increases. The surface must therefore be represented by an approximation that resembles reality as closely as possible.

In recent decades photogrammetric techniques have sought to improve surface representation through automated feature extraction and matching. Computer vision uses multi-view stereopsis (MVS) to achieve similar outputs. MVS incorporates Structure-from-Motion (SfM) techniques that match features in multiple views of a scene and derive 3D model coordinates and camera position and orientation. The Scale Invariant Feature Transform (SIFT) operator (Lowe, 2004) provides a robust description of features in a scene and allows features distinguished in other views to be compared and matched. A bundle adjustment can then be used to derive a set of 3D coordinates of matched features. The point density is proportional to the number of matched features and untextured surfaces, occlusions, illumination changes and acquisition geometry can result in fewer matches (Remondino and El-Hakim, 2006). The Bundler software[1] is an open source tool for performing least squares bundle adjustment (Snavely et al., 2006). To reduce computing overheads imagery is often down sampled. Typically the next stage is to densify the point cloud using MVS techniques, such as the patch-based multi-view stereo software PMVS2[2]. Each point in the resulting cloud has an associated normal. The point clouds produced from UAV imagery (referred to as UAV-MVS) acquired at 30–50 m flying height above ground level (AGL) have a density of ~1–3 points per cm^2. There can be in excess of 7 million points in a cloud (file size of ~500 Mb). The point cloud generated can be georeferenced by matching control points in the cloud to surveyed ground control points (GCPs). The resulting accuracy is dependent on the accuracy of the GCP survey or reference datasets and in this case it is approximately 25–40 mm

[1] http://www.cs.cornell.edu/~snavely/bundler/
[2] http://www.di.ens.fr/pmvs/

(Harwin and Lucieer, 2012b). The accuracy can be improved with coregistration to a more accurate base dataset.

To allow these large datasets to be used it is usually necessary to convert them into a more storage efficient data structure so that the data can be used in conventional GIS and 3D visualisation software that rely on a surface for texturing rather than a point cloud. Grid-based (or Raster) and triangular mesh based data models, such as Digital Surface Models (DSMs) and Triangular Irregular Networks (TINs), are commonly used. After processing and classification a Digital Elevation Model (DEM) or a Digital Terrain Model (DTM) representation of the earth's surface, without any vegetation or man-made structures, can be derived. The process of deriving these surface structures from a set of sample points is traditionally done using computational geometry based methods such Delauney triangulation or the Voronoi diagram (Bolitho et al., 2009). The data are assumed to be free from noise and dense enough to allow a realistic surface to be derived (Zhou et al. (2010) in Lim and Haron (2012)). When the point cloud is sparse or noisy the resulting surface is often jagged rather than smooth. The surface reconstruction process interpolates heights between sample points (Bolitho et al., 2009). Each point is considered a moment of height change and between points terrain height change is assumed to be linear or is solved by interpolating a least squares fit. An alternative to computational geometry is function fitting, these approaches define a function for determining a surface at a given location by global and/or local fitting (Bolitho et al., 2009). Kazhdan et al. (2006) developed a Poisson Surface Reconstruction technique that combines both global and local function fitting expressed as a solution to a Poisson equation (Bolitho et al., 2009). The Poisson approach uses the orientation of the point normal to create a surface that changes gradient according to the change in point orientation (Figure 3.1). The algorithm obtains a reconstructed surface with greater detail than previously achievable (Jazayeri et al., 2010).

This paper evaluates the UAV-MVS generated point cloud and surface representations of a natural land form by qualitatively comparing these to a reference dataset generated using close range terrestrial photography based MVS techniques (T-MVS). The aim is to ascertain whether to use point cloud comparison to detect change or whether to convert point cloud datasets to the more memory efficient triangulated mesh data structure prior to comparison. The conversion to a surface representation may introduce artefacts into the data. The objectives of this paper are: i) to visually assess 3D surface generation options as an alternative to point clouds for change detection; ii) to visualise point cloud and surface difference; iii) to compare TIN and Poisson surface representations; iv) to compare T-MVS and UAV-MVS.

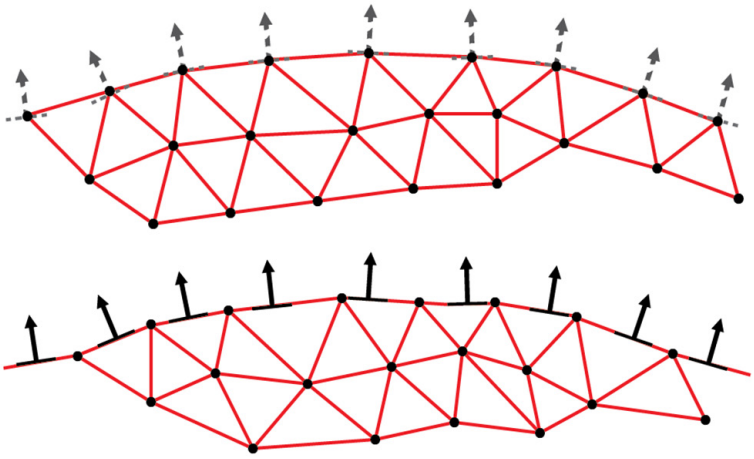

Figure 3.1: A TIN versus a Poisson DSM.

3.2 Methods

3.2.1 Study Area

A dynamic 100 m section of sheltered estuarine coastline in south eastern Tasmania will be monitored for fine scale change (Figure 3.2). The vegetation on the site is grasses and scrub bush along an erosion scarp with salt marsh at the southern end of the study site. For this study a section of the erosion scarp was chosen as the focus area for comparing the close range T-MVS point cloud to the UAV-MVS point cloud (Figure 3.3).

3.2.2 Hardware

The camera chosen to capture photography at sufficient resolution for UAV-MVS point cloud generation is the Canon 550D digital SLR camera. This camera has a light weight camera body and provides control over ISO, aperture and shutter speed settings. The settings are carefully chosen to reduce motion blur when acquiring images at 1 Hz (one photo per second). The resulting image dataset contains around 300 photographs per UAV flight with 70–95% overlap. The OktoKopter micro UAV platform (Mikrokopter, 2012) is the basis for the TerraLuma UAV used for this study. The aircraft is an electric multi-rotor system (eight rotors) capable of carrying a ~2.5 kg payload for approximately six minutes. The system has an on-board GPS (5–10 m positional accuracy) and other sensors that allow it to do waypoint navigation. The camera is attached to a stabilised camera mount. This camera is also used for the hand held terrestrial photography. A Leica 1200 real-time kinematic dual-frequency differential GPS (RTK DGPS) was used

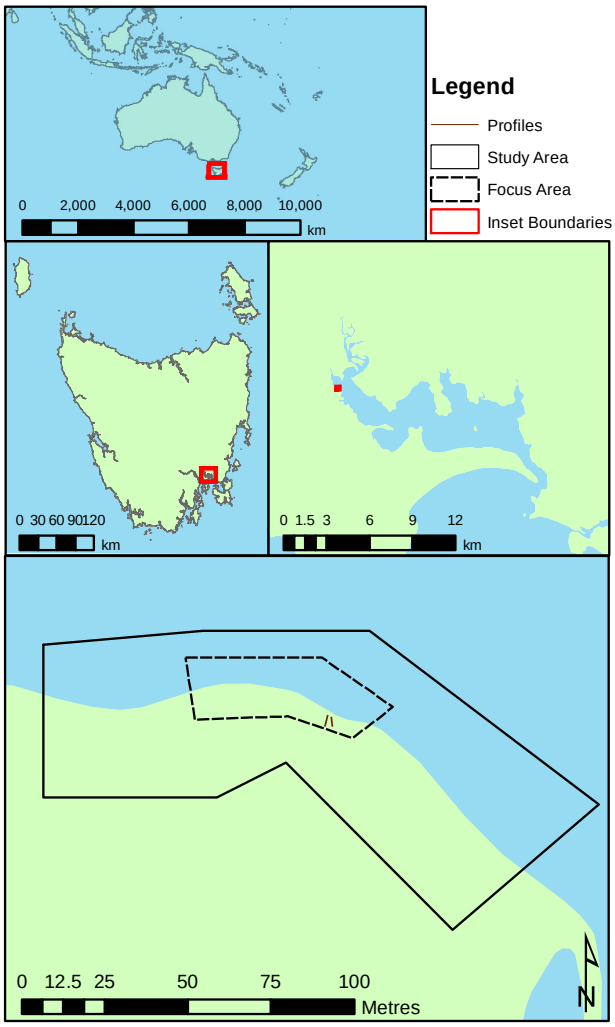

Figure 3.2: Coastal monitoring site.

to capture ground control.

3.2.3 Data Collection

To generate the UAV-MVS point cloud 89 photographs were taken from nadir and 64 oblique photographs were taken from a ~45° angle. The above ground level (AGL) flying height was approximately 30–40 m. Prior to acquiring the UAV imagery 42 small 10 cm orange disks were distributed throughout the focus area. These GCP disks were surveyed using RTK DGPS to an accuracy of ~1.5–2.5 cm. These disks were placed so that they could be seen from above and from the waters edge. The UAV imagery captured these GCPs in ~380 overlapping aerial photographs and then 179 terrestrial photographs were taken of the focus area by hand. The UAV image dataset and the

Figure 3.3: Images of the focus site (the first is taken looking east, the second is taken looking west).

terrestrial dataset were carefully screened and any blurred photographs or photographs beyond the study area were rejected.

3.2.4 Multi-View Stereopsis

The MVS process relies on matching features in multiple photographs of a subject, in this case a section of coastline. The Bundler software is used to perform a least squares bundle adjustment on the matched features. These features are discovered and described using invariant descriptor vectors or SIFT feature vectors. Once defined the SIFT features (or in our version SIFTFast features[3]) can be matched and the SfM process produces a sparse 3D point cloud along with the position and orientation of the camera for each image. Radial distortion parameters are also derived. The imagery used in this first step is down sampled (5184x3456 pixels ⇒ 2000x1333 pixels). The point

[3] `http://sourceforge.net/projects/libsift/`

cloud produced is in an arbitrary coordinate space. The next stage is to densify the point cloud using PMVS2, usually with down sampled images. The improvement made by our UAV-MVS process is that we transform the output from the Bundler bundle adjustment so that PMVS2 can run on the full resolution imagery. The resulting set of 3D coordinates also includes point normals, however it is still in an arbitrary coordinate reference frame.

3.2.5 Georeferencing

The ground control points must identified in the imagery and matched to their GPS positions in the local UTM coordinate system (GDA94 Zone 55). This "semi-automatic GCP georeferencing" is done by analysing the colour attributes of a random selection of orange GCP disks found in the imagery. The point cloud is then filtered based on the derived colour thresholds, i.e. Red, Green, Blue (RGB) range for GCP orange. The filter finds points in the cloud that are close enough in RGB colour space Euclidean distance to the GCP orange. The extracted orange point cloud contains clusters of points for each GCP and the bounding box of those point clusters is used to calculate a cluster centroid for each GCP cluster in the arbitrary coordinate space. To match these cluster centres to the equivalent surveyed GPS positions, the navigation grade on-board GPS positions for the time synchronised camera locations are matched to the Bundler derived camera positions and a Helmert Transformation is derived that, when applied, locates the point cloud in real work scale to an accuracy of ~5–10 m. The cloud is now in real world scale, therefore the GCP cluster centroid can be matched to the GPS positions by manually finding the closest GCP position to each cluster (when GCPs are more dispersed this process is usually automated). The resulting list of GCP disk cluster centres matched to GCP GPS points is then used to derive new Helmert Transformation parameters for transforming from arbitrary coordinate space to the UTM coordinate space.

The terrestrial photography does not have an equivalent set of camera position as the photographs were taken by hand. A "manual GCP georeferencing" technique must therefore be undertaken. This involves to extracting and labelling GCP disk cluster centres from the point cloud and then comparing the distribution to the GPS survey. GPS points can then be matched to their associated cluster centre and a Helmert Transformation can be derived and applied to point clouds and derived surfaces. Once the data was georeferenced it could be clipped into profiles and smaller point clouds using LASTools[4].

[4] `http://www.cs.unc.edu/~isenburg/lastools/`

3.2.6 Surface Generation

Triangulated meshes join the points in the dataset to their nearest neighbours, for this study the focus is on the points (or vertices) before and after Poisson Surface Reconstruction (since the vertex locations will remain the same when a dense triangulated mesh is created). Poisson surface reconstruction was done using Version 3 of the PoissonRecon software[5] provided by Michael Kazhdan and Matthew Bolitho. Default settings were used for all parameters except octree depth and solver divide, for which the values of 12 and 8, respectively, were chosen based on experimentation. MeshLab[6] and Eonfusion[7] were used to visualise point clouds and surfaces and clean the data. Edge face removal using length thresholds were used as well as isolated piece removal (automated and manual). The mesh vertices were then extracted by clipping out the profiles (using LASTools) for comparison with the original MVS derived vertex profiles.

3.2.7 Point Cloud and Surface Comparison

Future studies will investigate the best methods for quantitatively comparing point clouds and derived surfaces. For this study the method chosen was a qualitative comparison of point cloud profiles and strips along lines of interest within the focus area (see Figure 3.4).

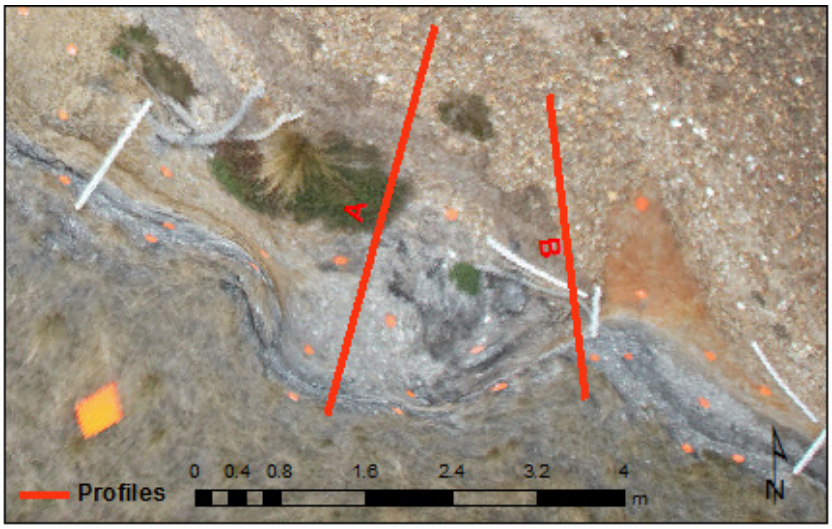

Figure 3.4: The two profiles within the focus area (see Figure 3.2).

Profile strips 1, 2 and 6 cm wide were extracted from the georeferenced MVS point

[5] http://www.cs.jhu.edu/~misha/Code/PoissonRecon/
[6] http://meshlab.sourceforge.net/
[7] http://www.eonfusion.com/

clouds and from the Poisson vertex points clouds. The points and derived surfaces were then overlaid and visually compared to evaluate how well the Poisson vertices represent the surface and how well the UAV-MVS point cloud coincides with the T-MVS point clouds and derived Poisson vertices and surface meshes.

3.3 Results and Discussion

The MVS workflow was applied to the terrestrial and the UAV image datasets. For the UAV-MVS dataset, 151 of 153 images chosen were processed resulting in a point cloud ~175 m by ~60 m containing ~7.3 million points (~1–3 points per cm^2). For the T-MVS dataset, 174 of 179 images chosen were processed resulting in a point cloud ~175 m by ~60 m containing ~6.3 million points (~3–5 points per cm^2). Screen shots of these two clouds and close up views of two 1 m staves are shown in Figure 3.5.

Both point clouds have sparse sections in the woody scrub bush, dead bushes and longer grasses. The UAV-MVS dataset has more points representing vegetation in the central portion of the focus area, this is not surprising due to the occlusion caused by taking the T-MVS photography from the water side of these bushes. Both point clouds have a high density of points on the erosion scarp and for soil and rock in general, even where the scarp is overhanging. The texture of the ground in these areas is ideal for feature identification as there is a lot of rocky gravel and shell grit in the soil and the beach is very pebbly.

To analyse the effect of surface composition on point density profiles were visualised and compared. For illustrative purposes a number of screen shots are provided that show regions or views of interest. The Eonfusion scene is a far better viewing environment than the flat screen shots provided as the view perspective can easily be adjusted to focus on interesting features from various angles.

As can be seen in Figure 3.6(a) and Figure 3.7(a) showing profile A the blue UAV-MVS points are amongst or slightly below the T-MVS points. As the profile crosses the vegetation the sparse T-MVS points on the occluded side of the bush can be seen amongst the relatively dense UAV-MVS points.

On the pebbly beach the UAV-MVS cloud is consistently below the T-MVS cloud (<1 cm) (see Figure 3.6(b) and Figure 3.7(b)). This may simply be due to differences in the Helmert transformation. Coregistration would be required to assess this

(a) The UAV-MVS point cloud.

(b) The T-MVS point cloud.

(c) The close up view of the UAV-MVS point cloud (point size = 2).

(d) The close up view of the T-MVS point cloud (point size = 1).

Figure 3.5: The derived point clouds.

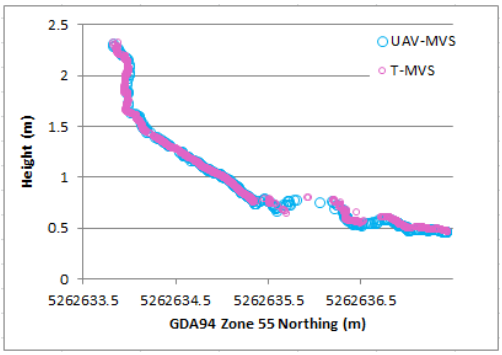

(a) Profile A.

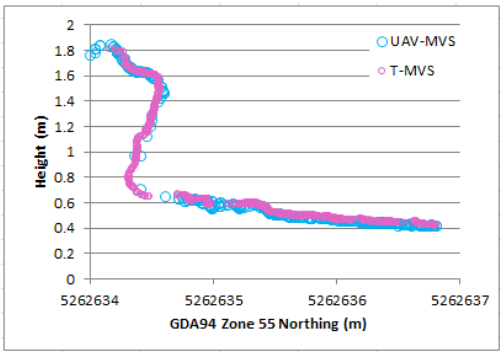

(b) Profile B.

Figure 3.6: A 1 cm wide profiles of the UAV-MVS and T-MVS point clouds.

further in a future study.

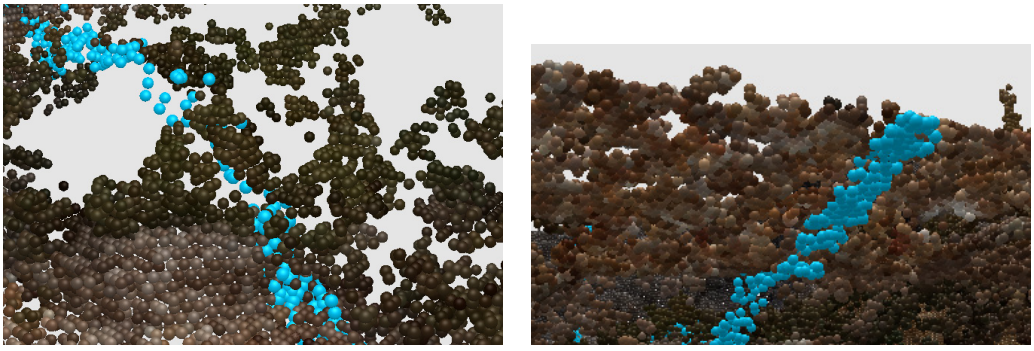

(a) The blue UAV-MVS points amongst the T-MVS points from above.

(b) The blue UAV-MVS points beneath the T-MVS points from below.

Figure 3.7: A 6 cm wide strip (profile A) of the UAV-MVS point cloud viewed with the T-MVS point cloud.

The Poisson surfaces derived from these two clouds produced new point clouds of surface vertices. The UAV-MVS Poisson surface point cloud (referred to as UAV-MVS Poisson) has 2.3 million vertices and the T-MVS Poisson surface point clouds (referred to as T-MVS Poisson) has 1.8 million vertices. After cleaning, the number of vertices were reduced by ~1100 and ~6000 points respectively. To visualise and qualitatively assess the effectiveness of the Poisson reconstruction and compare it to the raw point cloud vertices (which would be used to create a dense triangulated mesh surface), the extracted profiles were overlaid and visualised in Eonfusion.

The wider 6 cm profile strips have been created as surfaces to assess the difference between UAV-MVS Poisson and T-MVS Poisson. Figure 3.8 shows the TIN surface compared to the Poisson surface for T-MVS and UAV-MVS datasets respectively.

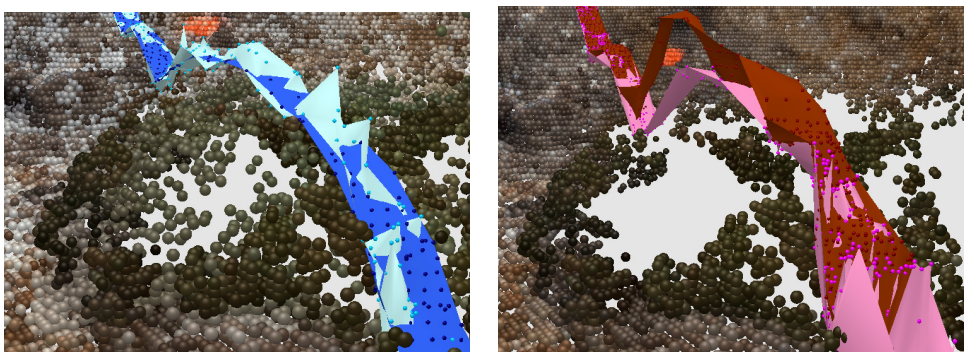

(a) The UAV-MVS point cloud below Poisson (blue) and TIN (light blue) strips.

(b) The T-MVS point cloud below Poisson (brown) and TIN (pink) strips.

Figure 3.8: 6 cm wide strips of Poisson and TIN surfaces viewed over a vegetated section of the points clouds from which they were derived (Z-10 cm), each natural coloured dot has a 14 mm diameter.

In these views the natural coloured point clouds have been offset in the Z dimension

by -10 cm to allow visualisation of the shape of the surface compared to the cloud that it was derived from. The surface covers a vegetated section and in the UAV-MVS dataset the denser section previously mentioned can be seen when comparing this view (Figure 3.8(a)) to the same view of the shrub (Figure 3.8(b)). The T-MVS cloud is sparse here and as a result the Poisson surface seems to have exaggerated the shrub height over the sparse section, probably due to the orientation of the normals varying greatly for those few points, which happens in vegetation. The triangulated mesh is much more jagged than the Poisson surface in both views and the UAV-MVS Poisson is particularly smooth (Figure 3.8(a)). The shrub in reality does have a reasonably smooth shape, in in this instance the UAV-MVS Poisson appears most accurate. To examine this further a section of Profile B that passes through the pebbly beach is visualised. In Figure 3.9(b) the Poisson surface is again smoother and the drop in terrain at this point point is well represented (see Figure 3.6(b)). In Figure 3.9(a) the same seems evident. In Figure 3.9(c) the Poisson surfaces for UAV-MVS and T-MVS are shown on the T-MVS point cloud (Z-10 cm). In this view the UAV-MVS surface is again ~1 cm below the T-MVS surface, but the shape of the terrain is basically the same, where as when two raw MVS based TINs are compared in the same view the outliers in the UAV-MVS data seem to cause the surface to vary suddenly causing spikes or peaks in terrain that are not evident in the equivalent T-MVS TIN.

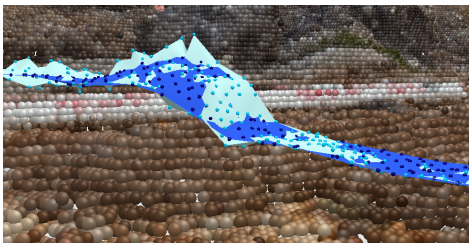

(a) The UAV-MVS point cloud below Poisson (blue) and TIN (light blue) strips.

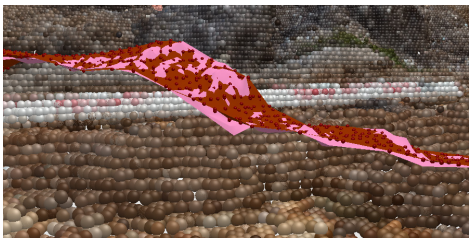

(b) The T-MVS point cloud below Poisson (brown) and TIN (pink) strips.

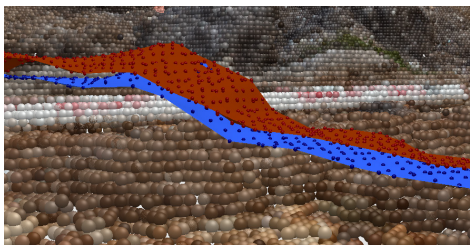

(c) The T-MVS point cloud below UAV-MVS Poisson (blue) and T-MVS Poisson (brown) strips.

Figure 3.9: 6 cm wide strips of Poisson and TIN surfaces viewed over a pebbly beach section of the points clouds from which they were derived (Z-10 cm), each natural coloured dot has a 14 mm diameter.

These visualisations provide insight into the quality of terrain and surface extraction possible using MVS techniques. The use of Poisson surface reconstruction has potential advantages over traditional triangulated mesh creation. Poisson surfaces seem generally smoother and smooth surface representations are often better when undertaking decimation, hydrological analysis, DEM derivative extraction and vegetation and ground filtering. The apparent outliers in the point cloud may not impact on the outputs from these analyses and, provided the point cloud density is carefully monitored and taken into account when mapping surface quality, the result may be more realistic for most surface types. Some vegetated areas have complex geometry (such as complex overlapping branches or tussock grasses) and areas with little or no texture are going to be poorly represented and this may impact on the Poisson reconstruction. The creation of a TIN is still a viable option, particularly when the point cloud can be maintained without decimation. When products with a smaller memory footprint are required there seems to be a strong case for using Poisson surface reconstruction to create a fairly smooth yet detailed representation of the terrain from which lower resolution surfaces can be extracted. The TIN surfaces appear more jagged and these spikes in the terrain can cause erroneous height values in a derived output.

3.4 Conclusions and Future Work

This study presented a qualitative assessment of the accuracy of point clouds derived using multi-view stereo techniques (MVS). Two datasets were derived using the technique, one using terrestrial photography and the other using photography acquired via an unmanned aerial vehicle (UAV). The two point clouds provided dense point coverage of the areas captured in the imagery, the terrestrial MVS dataset had ~3–5 points per cm^2 and the UAV-MVS dataset had ~1–3 points per cm^2. Once georeferenced the two clouds coincided quite well, however in future studies comparison will be between coregistered datasets. Triangulated meshing and Poisson surface reconstruction was used to create surface models and these models were compared and evaluated to assess how well the terrain and surface features were portrayed. The point clouds produced using MVS have point normals associated with each point and this allows detailed surface features to be derived using Poisson surface reconstruction. The derivatives that can be extracted from such a detailed surface representation will benefit from the Poisson algorithm as it combines global and local function fitting and seems to smooth the data and the process is not strongly influenced by outliers in the point cloud. Future studies will undertake quantitative assessment of the differences and evaluate the potential of these techniques

for change detection, in this study area the fine scale coastal erosion that is occurring may be indicative of climate change and, if this technique proves useful, UAVs may be a viable tool for focussed monitoring studies. The issues faced in vegetated areas and areas with complex geometry that result in sparse patches in the point cloud need to be investigated, it may be that the key areas of change are still well represented. The MVS technique has a great deal of potential both in natural and man-made landscapes and there are many potential applications for the use of UAVs for remote sensing data capture, alongside laser scanning and more traditional techniques, to provide very detailed and precise representations of a range of landscapes at key moments. Application areas include landform monitoring, mine surveying and other environmental monitoring. Qualitatively, the outputs from the UAV-MVS process compare very well to the terrestrial MVS results. The UAV can map a greater area faster and from more viewing angles, it is therefore an ideal platform for capturing very high detail 3D snapshots of these environments.

Acknowledgements

The authors would like to thank Darren Turner for his logistical, technical and programming support and UAV training. Thank you to Myriax for the scholarship license for the Eonfusion nD spatial analysis package. In addition, for making their algorithms and software available, we would like to give thanks and appreciation to Noah Snavely and his team for Bundler, David Lowe for SIFT, the libsift team for SIFTFast, Yasutuka Furukawa and Jean Ponce for their multi-view stereopsis algorithms (PMVS2 and CMVS) and Martin Isenburg for LASTools.

Thesis context

Whilst assessing the accuracy of the point clouds produced using UAV-MVS is a fundamental step in the evaluation of the technique for change detection, the point clouds produced tend to contain a large number of points that many common GIS and related software packages are unable to cope with efficiently. The solution is to convert the point clouds to surface models (ideally 3D rather than 2.5D models). This chapter visually assessed two potential surface generation options and found that while they both adequately represent the terrain described by the point cloud, this conversion results in some loss of data and some generalisation, particularly when significant point cloud

decimation is required. Converting point clouds to surfaces can result in artefacts from interpolation and generalisation that may impact change detection. Comparison of surface generation algorithms is beyond the scope of this thesis, instead Chapter 6 will focus on point cloud comparison. The other aspect of this chapter was the comparison of T-MVS (terrestrial MVS) and UAV-MVS. The differences between the datasets also highlighted the likelihood of occlusion and the potential importance of oblique imagery and careful camera network design. In addition, the study undertaken for this chapter has highlighted the need for precise verification points and the usefulness of profiles in visualising point cloud data density and precision. However, for proper comparison more accurate profiles are needed and this lead to the use of reflectorless total station profiling. The need to compare profiles lead to the development of an algorithm for extracting profile terrain lines and calculating point density and accuracy statistics to compare profiles in Chapter 5.

4 | The Impact of the Calibration Method on the Accuracy of Point Clouds Derived Using Unmanned Aerial Vehicle Multi-View Stereopsis (UAV-MVS)

Chapter 4 focuses on assessing the impact of calibration methods and other design decisions on UAV-MVS survey accuracy. The work comprising this chapter is published in the peer-reviewed *Remote Sensing* (Harwin et al., 2015).

Abstract

In unmanned aerial vehicle (UAV) photogrammetric surveys, the camera can be pre-calibrated or can be calibrated "on-the-job" using structure-from-motion and a self-calibrating bundle adjustment. This study investigates the impact on mapping accuracy of UAV photogrammetric survey blocks, the bundle adjustment and the 3D reconstruction process under a range of typical operating scenarios for centimetre-scale natural landform mapping (in this case, a coastal cliff). We demonstrate the sensitivity of the process to calibration procedures and the need for careful accuracy assessment. For this investigation, vertical (nadir or near-nadir) and oblique photography were collected with 80%–90% overlap and with accurately-surveyed ($\sigma \leq 2$ mm) and densely-distributed ground control. This allowed various scenarios to be tested and the impact on mapping accuracy to be assessed. This paper presents the results of that investigation and provides guidelines that will assist with operational decisions regarding camera calibration and ground control for UAV photogrammetry. The results indicate that the use of either a robust pre-calibration or a robust self-calibration results in accurate model creation from vertical-only photography, and additional oblique photography may improve the results. The results indicate that if a dense array of high accuracy ground control points are deployed and the UAV photography includes both vertical and oblique images, then either a pre-calibration or an on-the-job self-calibration will yield reliable models (pre-calibration $\text{RMSE}_{XY} = 7.1$ mm and on-the-job self-calibration $\text{RMSE}_{XY} = 3.2$ mm). When oblique photography was excluded from the on-the-job self-calibration solution, the accuracy of the model deteriorated (by 3.3 mm horizontally and 4.7 mm vertically). When the accuracy of the ground control was then degraded to replicate typical operational practice ($\sigma = 22$ mm), the accuracy of the model further deteriorated (e.g.,

on-the-job self-calibration RMSE_{XY} went from 3.2 mm–7.0 mm). Additionally, when the density of the ground control was reduced, the model accuracy also further deteriorated (e.g., on-the-job self-calibration RMSE_{XY} went from 7.0 mm–7.3 mm). However, our results do indicate that loss of accuracy due to sparse ground control can be mitigated by including oblique imagery.

4.1 Introduction

The optimal workflow for high accuracy three-dimensional (3D) reconstruction using unmanned aerial vehicles (UAVs) (also known as remotely-piloted aircraft systems (RPAS) or drones) is the underlying motivation for much of the current research surrounding the use of photogrammetric, structure-from-motion (SfM) and multi-view stereopsis (MVS) techniques (Snavely et al., 2007; Snavely, 2010; Lowe, 2004; Furukawa and Ponce, 2007; Liu, 2011; Verhoeven et al., 2012; Vu et al., 2012; Turner et al., 2014; Turner et al., 2012; Lucieer et al., 2013; Lucieer et al., 2011b) with UAV imagery (UAV-MVS). This study is part of the research focussing on the application of UAV-MVS for mapping natural landform changes (Harwin and Lucieer, 2012b). UAV-MVS has the potential to produce high accuracy 3D point clouds and digital surface models (DSMs), provided the workflow used in the data capture and processing is robust. Initial research has shown that the technique is capable of producing accuracies in the order of 25–40 mm when flying at 25–50 m above ground level (AGL) (Harwin and Lucieer, 2012b), but these findings do not show how accurate the technique could be under optimal survey design conditions. Quantification of positional accuracy is key to detecting and attributing centimetre-scale landform change.

The study site chosen for this research is a sheltered coastline that is eroding gradually. Prahalad et al. (2014) suggest that although typical erosion rates along sheltered coasts are in the range of 10–20 cm/year the impact of single events contributing to this erosion cannot reliably be measured using satellite imagery or aerial photography and only becomes evident when a number of events have caused cumulative erosion. UAV-MVS may offer the ability to monitor small changes at temporal resolutions suited to the requirement for pre- and post-event mapping and at spatial resolutions of higher than 1–3 cm, allowing researchers to gain new understandings of these processes at the resolution of single events.

Camera network design and the distribution and accuracy of ground control are key determinants of the mapping accuracy that can be achieved from UAV-MVS. A number of studies have compared SfM and MVS derived products to total station surveyed check points (Tahar and Ahmad, 2011; Harwin and Lucieer, 2012b; Neitzel and Klonowski, 2011), to DGPS (Differential Global Positioning System) surveyed check points (Rosnell and Honkavaara, 2012; Carvajal et al., 2011; Mancini et al., 2013) and to LiDAR or terrestrial laser scanning (Strecha et al., 2008; Vallet et al., 2011; James and Robson, 2012; Flener et al., 2013; Westoby et al., 2012). Some have pre-calibrated

the camera (Carvajal et al., 2011; Tahar and Ahmad, 2011), and others have relied on self-calibration (Mancini et al., 2013; Harwin and Lucieer, 2012b; Westoby et al., 2012; D'Oleire-Oltmanns et al., 2012; Neitzel and Klonowski, 2011) or compared the two options (Strecha et al., 2008; Rosnell and Honkavaara, 2012; Vallet et al., 2011). While these studies provided guidance for those making operational decisions during survey design and implementation, our study builds on previous work by quantifying the impact of camera calibration on the accuracy of UAV-MVS point clouds. The assessment of UAV-MVS techniques using a precise total station survey ($\sigma \leq 2$ mm) of ground control and verification points has not been done to date, particularly in the context of natural landform mapping.

The magnitude of systematic and random errors in a point cloud derived from UAV-MVS will be influenced by camera specifications (sensor format, lens focal length, *etc.*), camera calibration accuracy, camera network geometry, the distribution and accuracy of ground control and the precision with which targets can be measured and matched. The majority of cameras used in recent years for UAV surveys have not been designed for photogrammetric accuracy (Fraser, 2013). Non-metric "prosumer" or consumer-grade digital cameras are a popular choice for UAV-MVS, because of their light weight and low cost. These cameras are not manufactured to the same standards as metric cameras, and as a result, they exhibit much greater magnitudes of distortion and instability (Fraser et al., 1995; Fraser, 2013; Remondino and Fraser, 2006; James and Quinton, 2014). These unstable calibration characteristics and potentially large lens distortions, if not reliably modelled, will impact 3D accuracy (Granshaw, 1980; James and Robson, 2014). Some studies have used a zoom lens (Harwin and Lucieer, 2012b); however, a fixed focal length prime lens is likely to be more stable (Fraser, 2013). It is important that a calibration is undertaken that will adequately model a camera and lens at a chosen focus and focal length. It is necessary to fix the focal length and focus for each calibration and, if necessary, to perform a calibration for each setting needed for mapping surveys (Fraser et al., 1995; Fraser, 2013). Camera calibration is therefore an important component of the photogrammetric process.

Pre-calibration using an image set captured from a typical operating distance (flying height) and a convergent camera station network, processed independently of the survey imagery, can be used to derive camera calibration parameters. Alternatively, pre-calibration can be performed more easily using an image set acquired at close range using a calibration array, such as a pattern (e.g., a checker board), a 3D targeted object or a target field. In this case, the calibration is computed from images acquired at camera-to-target distances shorter than those of a typical UAV survey. In the case of

an on-the-job self-calibration, the camera calibration is derived from image coordinates measured in the mapping photography and including the camera calibration parameters as unknowns in a self-calibrating bundle adjustment.

The simplest option for camera calibration is usually to include camera calibration parameters as unknowns in a self-calibrating bundle adjustment. Advances in automated feature identification and matching in recent years have enabled users of consumer-grade cameras to model distortion relatively easily using the self-calibration approach based on a minimal number of overlapping photographs. There is a risk that the camera calibration parameters are derived from a relatively low number of images and a relatively poor camera geometry. In this situation, there is an increased potential for projective coupling between the interior and exterior orientation parameters (Fraser, 2013; Remondino and Fraser, 2006). This means that, while the calibration may be sufficient for the network of images acquired for the particular mapping task, the distortion parameters derived in this way are generally considered specific to the dataset and not necessarily applicable to other image sets. Poorly-modelled camera calibration leads to model deformation, particularly if the camera network is comprised of traditional nadir photography in strips and blocks (Remondino and Fraser, 2006; James and Quinton, 2014; James and Robson, 2014; Rosnell and Honkavaara, 2012).

The accuracy of the measurements directly impacts the repeatability of data capture, and this, in turn, impacts change detection. If the aim of a camera calibration is to reuse the calibration in high accuracy applications, then the calibration must not be specific to a particular camera network. A robust, reusable photogrammetric pre-calibration requires a camera network design and target objects that provide a comprehensive geometric modelling of a camera's image space, independent of the target scene (Fraser et al., 1995; Fryer, 1996). Precisely-coordinated target arrays or engineered 3D target objects, often used in close-range photogrammetric applications, such as engineering metrology, are generally inappropriate for UAV 3D mapping applications, because it is prohibitive to manufacturer arrays that are large enough to accommodate camera fields of view at typical flying heights.

For precise UAV surveys, a deliberate choice needs to be made between the different options. When using the self-calibration approach, the flight plan needs to incorporate design elements that promote effective and robust self-calibration. The inclusion of oblique imagery has the potential to improve the camera model, to reduce model deformation and to improve modelling of complex 3D forms, particularly when coupled with a good control distribution and a target scene that contains objects that result

in reliable image matching (Remondino and Fraser, 2006; James and Quinton, 2014; James and Robson, 2014; Wackrow et al., 2008; Wackrow and Chandler, 2011; Rosnell and Honkavaara, 2012).

Our experience with analysing configuration requirements and assessing the accuracy of UAV-MVS for monitoring centimetre-scale landform change demonstrated a need to assess the sensitivity of the process to camera calibration procedures (Harwin and Lucieer, 2012b). The choices made when incorporating the camera model (in particular lens distortion) into UAV-MVS processing and the impact of camera network design and calibration procedure choices on model accuracy is the focus of this study.

The objectives of this investigation are: (i) to evaluate the impact of the camera calibration method on the model accuracy, specifically comparing self-calibration methods and pre-calibration options; (ii) to ascertain if self-calibration can result in comparable accuracy to pre-calibration if there is an appropriate camera network design, ground control point (GCP) distribution and GCP survey method accuracy; (iii) to assess the impact of additional oblique imagery on a predominantly nadir self-calibration; and (iv) to assess the influence of GCP quality on point cloud accuracy by comparing a precise total station survey and a DGPS survey of GCPs.

4.2 Method

4.2.1 Background Theory

The choices made when endeavouring to balance 3D reconstruction accuracy requirements with camera type and specifications, camera network design, ground control design, and other operational considerations are critical when undertaking UAV-SfM surveys. To evaluate the effect of camera calibration it is necessary to understand the underlying camera model, the bundle adjustment process, GCP uncertainty, image space measurement accuracy and finally the camera network design and target object considerations.

The Camera Model

Lens distortions are departures from collinearity due to imperfections in lens and therefore camera internal geometry (Fraser, 2006). Traditionally, for small format cameras

used in photogrammetry and precision metrology, calibration was achieved by acquiring convergent photography with a range of camera roll angles of a precisely coordinated target array, identifying those targets in the imagery and then using the 3D world coordinates and the 2D images of targets to determine the camera calibration parameters. A camera is considered calibrated if the principal distance, principal point offset and radial distortion have been modelled (Remondino and Fraser, 2006). Additional parameters can also be included such as the Brown (1971) pinhole model that extends the three (or four) coefficient radial distortion polynomial with two coefficients for decentring distortion. A widely adopted model for distortion was first introduced by Brown in the late 1960s (Brown, 1971). This model is employed in the software used for the research reported here (Agisoft Lens[1], Agisoft PhotoScan[2]and ADAM Technology 3DM CalibCam[3]).

[1]Agisoft Lens Version 040.1.1718 beta 64 bit ©2013 Agisoft LLC `http://www.agisoft.com/`

[2]Agisoft PhotoScan Professional Edition Version 1.0.4.1847 64 bit ©2014 Agisoft LLC `http://www.agisoft.com/`

[3]3DM CalibCam Version 2.2a ©December 2006 ADAM Technology `http://www.adamtech.com.au/`

$$x = X/Z$$
$$y = Y/Z$$
$$x' = x(\Delta r) + P_2(r^2 + 2x^2) + 2P_1xy$$
$$y' = y(\Delta r) + P_1(r^2 + 2y^2) + 2P_2xy$$
$$u = c_x + x'f_x + y'skew$$
$$v = c_y + y'f_y$$

where:

$r = \sqrt{x^2 + y^2}$

$\Delta r = K_1^o r^3 + K_2^o r^5 + K_3^o r^7 + K_4^o r^9$(odd form)

$or \Delta r = 1 + K_1^e r^2 + K_2^e r^4 + K_3^e r^6 + K_4^e r^8$(even form)

(X, Y, Z) – point coordinates in the local camera coordinate system

(u, v) – projected point coordinates in the image coordinate system (in pixels)

(f_x, f_y) – focal lengths

(c_x, c_y) – principal point coordinates

$K_1^o, K_2^o, K_3^o, K_4^o$ – radial distortion coefficients (odd form)

$K_1^e, K_2^e, K_3^e, K_4^e$ – radial distortion coefficients (even form)

P_1, P_2 – decentring distortion coefficients

$skew$ – skew coefficient describing non-orthogonality between the x and the $y$axis

This equation models the interior orientation of the camera through the principal point coordinates (c_x, c_y), focal lengths (f_x, f_y) and terms that describe departures from collinearity or image distortion, namely radial distortion (Δr), decentring distortion (P_1, P_2) and optionally skew.

The Bundle Adjustment

For both camera calibration and 3D reconstruction, a bundle adjustment requires a simultaneous least squares adjustment of a set of collinearity condition equations that each represent the relationship between a single point in three-dimensional object space, the image of that point in two-dimensional image space, and the perspective centre of the camera. In UAV photogrammetry, any point in object space may be intersected by

lines (homologous rays) from many photographs.

The certainty of these intersections is bounded by the error estimates on the input parameters and the accuracy with which target features can be located in the imagery (in pixel units). When internal and external constraints are both considered, image and control measurements are weighted based on their estimated precision to balance between the two in the bundle adjustment. Poor *a priori* estimates of GCP or image space coordinate precision can lead to poor estimates of interior or exterior orientation parameters, which in turn can result in systematic distortions in the derived 3D model (James and Quinton, 2014).

With sufficient redundancy it is possible to avoid the need for real-world 3D coordinates in the object space as a bundle adjustment can solve for both the exterior and interior orientation of the camera at each station. The bundle adjustment derives the model (and optionally the coefficients of distortion) in terms of scale independent image space coordinates. The exterior orientation is also part of the solution and can be in an arbitrarily assigned object space coordinate system independent of the scale and orientation of any particular XYZ datum (Fraser et al., 1995). The arbitrary system can then be transformed to a "real-world" system using a Helmert transformation derived from control (Harwin and Lucieer, 2012b). The alternative is to incorporate GCP coordinates or camera station coordinates in the bundle adjustment and solve exterior orientation and model coordinates in the real coordinate system. An evaluation of these alternatives (post bundle adjustment transformation versus incorporating control into the bundle adjustment) is beyond the scope of this paper and the latter option will be used as it is considered more photogrammetrically robust (James and Quinton, 2014).

GCP Uncertainty and Image Space Measurement Accuracy

The bundle adjustment requires the specification of estimated GCP survey precision (when ground control is used) and estimated image space measurement accuracy. Estimated GCP survey precision is related to the survey technique used for GCP coordination and is often expressed in field measurement units as one standard deviation (or one sigma, 1σ). Estimated image space measurement accuracy is a measure of the accuracy of locating the centre of a target in an image and is measured in pixels.

Camera Network Design

Earlier research in the field of UAV-SfM captured imagery using more traditional photogrammetric flight planning (nadir photography captured in strips and blocks with ~60%–80% overlap) (D'Oleire-Oltmanns et al., 2012; Verhoeven, 2011; Verhoeven et al., 2013; Zhang et al., 2011) or by flying more ad-hoc flight paths that include oblique imagery in an effort to completely cover the area of interest and map complex 3D features (Harwin and Lucieer, 2012b; Stal et al., 2014; Verhoeven, 2011; Verhoeven et al., 2013; Niethammer et al., 2010). For these studies, self-calibration was the method of choice.

Calibration will be enhanced by highly convergent camera network geometry and a large number of well distributed object points that result in point features throughout the image frame, all the way to the edges (Fraser, 2013; Remondino and Fraser, 2006). In order to model distortion throughout the full image format it is important to ensure that there are at least 20–30 points per image (the more the better), that each point has at least eight rays per point, and that all regions of image array out to the maximum radial distance are covered multiple times with the network of images (Remondino and Fraser, 2006). To avoid projective coupling between the interior and exterior orientation it is advisable to incorporate orthogonal roll angles into the network design as this ensures object points are "seen" in all parts of the image frame (Fraser, 2013; Remondino and Fraser, 2006).

Target Object Considerations

Ensuring that camera network design produces images with object coordinates throughout the image frame is particularly important when using a 2D or planar target array for pre-calibration. When using a non-coplanar 3D object or target array, Fraser (2013) suggests that the rule of thumb for depth variation is 10% of the camera to object distance. The pre-calibration employed in this study and that uses a 3D target field incorporates this guideline.

Tools and algorithms have evolved that precisely identify the centroids of well-defined targets in multiple images (e.g., CalibCam, Photomodeller, VMS). Automatic centroiding of a well-defined target generally outperforms manual (human) measurement. Automatic centroiding also offers speed advantages. Manual measurement may be required if targets are at highly oblique angles, or if they are partially obscured.

Operational considerations usually mean that targeted arrays are quite small, so small that the camera-target distance is considerably shorter than the normal camera-object distances used in UAV photography. This renders the derived calibration less reliable than using images focused at infinity and with a camera-to-object distance similar to the flying height that will be used in the UAV-SfM survey (Stal et al., 2014; James and Robson, 2012). For completeness, this study will include a checkerboard calibration along with pre-calibration using a 3D target field and "on-the-job" self-calibration in the comparison scenarios.

4.2.2 Study Site

The study site is a 50 m section of Pittwater Estuary, a sheltered estuarine waterway in southeastern Tasmania, Australia (Figure 4.1). For this study, a section of an erosion scarp was chosen as the focus area to evaluate the impact of calibration choices on derived UAV-MVS point clouds. The vegetation is characterised by coastal grasses along an erosion scarp with salt marsh at the southern end of the study site.

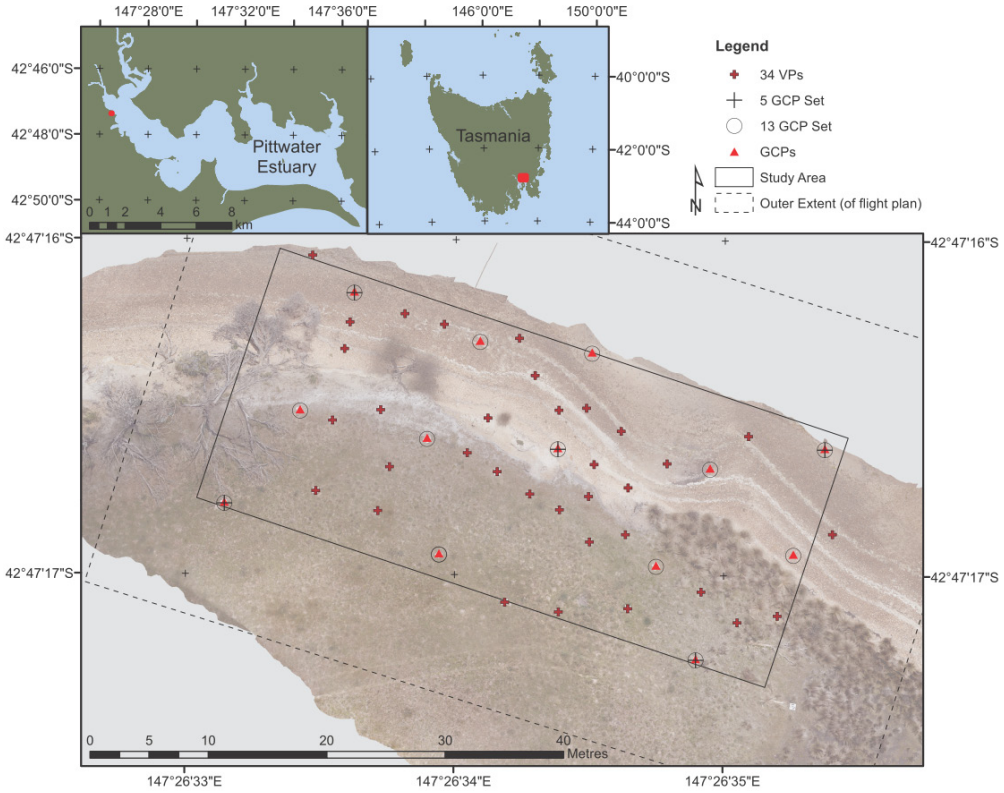

Figure 4.1: The study site is an eroding coastal scarp in a sheltered estuary in southeastern Tasmania, Australia. The map portrays the distribution of ground control and validation points.

4.2.3 Hardware

The UAV used in this study was an OktoKopter UAV platform (Mikrokopter, 2012) with a Droidworx eight rotor airframe. The aircraft has an electric multi-rotor system and is capable of carrying a ~2.5-kg payload for approximately 8–10 min. An on-board navigation-grade GPS (5–10 m positional accuracy), IMU, 3D digital compass and barometric altimeter allow the system to navigate to predefined waypoints. A Canon 550D digital SLR camera with a 20 mm prime lens was attached to a stabilised camera mount that allows camera tilt to be controlled by the UAV operator. This camera has a lightweight body and provides control over ISO, aperture and shutter speed settings. Focus was fixed at infinity, and the camera settings were carefully chosen to reduce motion blur when acquiring images at 1 Hz (one photo per second, 1/1250 shutter speed). A Leica TS06 plus total station theodolite was used to capture ground control using a precise survey (explained below).

4.2.4 Ground Control and Validation Point Distribution

A total of 47 targets was distributed throughout the study area (Figure 4.1). Thirteen of these were used as GCPs and 34 as validation points (VPs). The GCPs were placed along two sides of the study area and through the middle. The targets were coded targets generated by Agisoft PhotoScan Professional (version 1.0.4) (Agisoft LLC) and printed onto 50 × 50 cm matte finish plastic boards with the black centre circle measuring 11 cm in diameter (Figure 4.2).

Figure 4.2: A printed PhotoScan coded target as imaged in one of the UAV photographs from the nadir image set.

To provide for a pre-calibration, a target field adjacent to the study site was established.

It comprised 47 printed PhotoScan targets distributed across an area of approximately 25 × 25 m. Ten targets were placed on top of tripods set up to provide as much variation in height as was practical and to provide a variation in height that was similar to that of the topography on the erosion site. The variation in target height was approximately 10% of the flying height (approximately 17–22 m AGL). In addition, two large measuring tapes were laid out in orthogonal directions to help with target matching and to provide an additional means of obtaining scale if necessary. Five GCPs, one in the centre of the target field and four approximately 5 m from the centre, were accurately surveyed using a total station; the remainder were left as uncoordinated tie points.

4.2.5 Precise Total Station Survey

The GCP and VPs were either theodolite stations or radiated detail points measured from those stations at least 3–4 times facing left and facing right. A short 30 cm prism pole with a staff bullseye bubble was used for all point radiations to reduce errors in vertical alignment of the prism over each point. The final coordinates were determined through a least squares network adjustment using LISCAD[4]. The precision achieved for GCP and VP points was $\sigma_X = 1$ mm, $\sigma_Y = 1.4$ mm and $\sigma_Z = 1.1$ mm. A GCP and VP 3D precision of $\sigma_{XYZ} = 2$ mm was adopted for subsequent calibration and model generation steps.

4.2.6 Degradation of Precise Total Station GCPs to Typical DGPS Accuracy

In most operational situations, a total station survey is too time consuming, and so, the DGPS survey is used to map GCPs. To compare the impact of surveying the GCPs using DGPS instead of a precise total station, the GCP coordinates were degraded using random values from a Gaussian distribution to introduce an error equivalent to typical DGPS. The accuracy setting was chosen based on descriptions in the manufacturer's manual for a typical differential GNSS (Global Navigation Satellite Systems) or DGPS receiver (in this case, the Leica 1200[5]). For surveys carried out in rapid static and static mode after initialization (compliance with ISO17123-8), RMS accuracy is quoted as 5 mm + 0.5 ppm horizontally and 10 mm + 0.5 ppm vertically. For surveys carried out in kinematic (phase) moving mode after initialization, RMS accuracy is quoted as

[4]LISCAD Version 10 `http://www.LISCAD.com`

[5]`http://www.leica-geosystems.com/downloads123/zz/gps/general/brochures-datasheet/GPS1200_TechnicalData_en.pdf`

10 mm + 1 ppm horizontally and 20 mm + 1 ppm vertically. For this study site, the usual GPS base station location is approximately 2 km away, and assuming a lower accuracy in rapid static mode due to the possibility of systematic errors, the accuracy chosen to approximate a DGPS survey was the worst case RMS accuracy of a kinematic survey (20 mm + 1 ppm over 2 km = 22 mm). Each 3D coordinate for the GCPs (not the VPs) therefore had a random error applied constrained by the standard deviation: $1\sigma_{XYZ} = 22$ mm. This was considered a more robust method of comparison than simply surveying the GCPs with DGPS, as the accuracy of the survey can be influenced by a range of factors, including satellite orbit geometry, obstructions, such as over-hanging trees or terrain, and error correlation between stations. Controlling the accuracy of these DGPS equivalent coordinates provides an indication of the impact of less precise GCPs, both on the calibration reliability and 3D reconstruction quality, although not addressing circumstances where the precision of the GPS coordinates is variable across the study site because of, for example, reduced satellite visibility.

4.2.7 UAV Survey

Flights for Pre-Calibration

To obtain convergent imagery of the 3D target field, a circular path was flown three times (Figure 4.3). For the first flight, the camera was mounted normally in landscape orientation. To ensure the targets were distributed throughout the frame of the camera, the camera mount roll angle was set so that the camera was in opposing portrait orientations in the second and third flights, respectively. The camera angle was set at 65° for each flight, and the UAV was flown in a circle (with an approximate radius of 6 m) at an altitude of approximately 18 m (AGL). The UAV was orientated to point at the centre GCP target in the calibration field to ensure convergent photography.

Study Site Flights

A traditional nadir photogrammetric flight path was flown over the main study site with 80%–90% overlap immediately after the calibration flights. The flight dynamics of the aircraft do not allow strict adherence to the flight plan; however, the aircraft usually stays within ~2–3 m of the planned path. The AGL flying height was approximately 20–25 m, and the entire area was covered in two flights. Three additional flight lines were flown with the camera tilted so that a set of oblique images of the erosion could

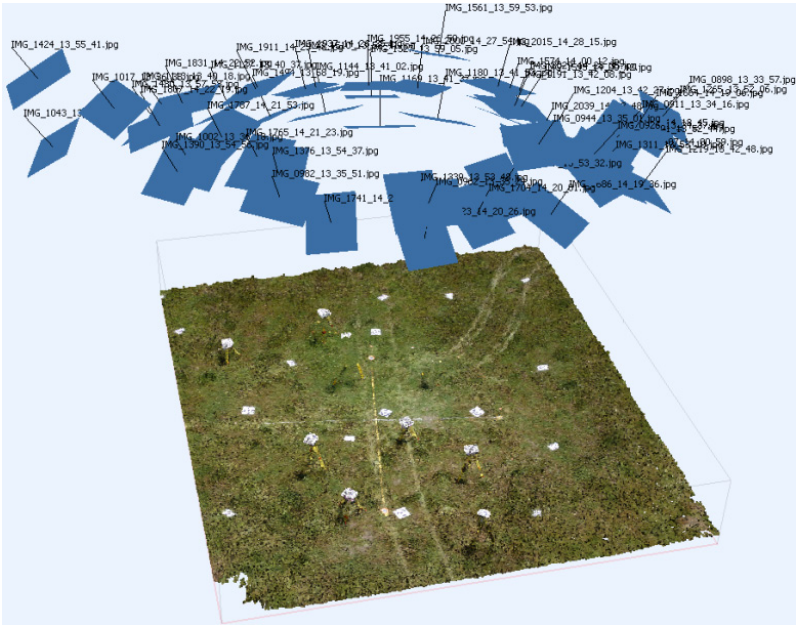

Figure 4.3: Calibration flight point cloud and camera network showing the 50 convergent camera stations and the 3D target array with some targets set up on tripods.

be captured. Again, these were flown so that overlap was approximately 80%–90%.

4.2.8 Scenarios

A total of 28 scenarios were tested. The assessed key variables were: (i) the camera calibration; (ii) the precision of GCPs; (iii) the number of GCPs; and (iv) the inclusion or exclusion of oblique photography. Table 4.1 lists those scenarios and assigns each scenario a code based on the variable settings of each.

4.2.9 Calibration Options

Four calibration options were evaluated:

a) a checkerboard pre-calibration using Lens;

b) a target field pre-calibration using PhotoScan;

c) a target field pre-calibration using CalibCam; and

d) an “on-the-job” self-calibration using PhotoScan.

Table 4.1: Scenarios tested and the codes assigned based on calibration type (checker board, target field, "on-the-job" self-calibration (OTJ self-cal.)), ground control point (GCP) σ, GCP count and whether the oblique imagery set was included.

Scenario Code	Calibration Type	Calibration Software	GCP σ (mm)	GCP Count <N>	Oblique (Yes/No)
Lens13GCP2mm	Checker board	Lens	2	13	No
Lens13GCP2mmObl	Checker board	Lens	2	13	Yes
PS13GCP2mm	Target field	PhotoScan	2	13	No
PS13GCP2mmObl	Target field	PhotoScan	2	13	Yes
Pre<N>GCP0mm (e.g., "*Pre5GCP0mm*")	Target field	CalibCam	0	5,13	No
Pre<N>GCP0mmObl	Target field	CalibCam	0	5, 13	Yes
Pre<N>GCP2mm	Target field	CalibCam	2	5, 13	No
Pre<N>GCP2mmObl	Target field	CalibCam	2	5, 13	Yes
Pre<N>GCP22mm	Target field	CalibCam	22	5, 13	No
Pre<N>GCP22mmObl	Target field	CalibCam	22	5, 13	Yes
Self<N>GCP0mm	OTJ self-cal.	PhotoScan	0	5, 13	No
Self<N>GCP0mmObl	OTJ self-cal.	PhotoScan	0	5, 13	Yes
Self<N>GCP2mm	OTJ self-cal.	PhotoScan	2	5, 13	No
Self<N>GCP2mmObl	OTJ self-cal.	PhotoScan	2	5, 13	Yes
Self<N>GCP22mm	OTJ self-cal.	PhotoScan	22	5, 13	No
Self<N>GCP22mmObl	OTJ self-cal.	PhotoScan	22	5, 13	Yes

Each option is defined in Table 4.1 by the calibration type and the calibration software columns. These options were chosen based on the fact that PhotoScan is the main point cloud generation software package used in this research, and comparing it to a more traditional calibration package (CalibCam) and an automated calibration package (Lens) will allow us to understand the impact of the calibration method on generated point cloud accuracy. Option (a) (Lens) did not require any manual input, whereas the other three options required target centroiding in the imagery. Each calibration results in estimates of focal length, principal point coordinates, three radial distortion coefficients and two decentring lens distortion coefficients (following Brown (1971)). Some conventions regarding calibration parameters in CalibCam differ slightly from those used in Lens and PhotoScan, such as different sign conventions, and these were modified accordingly.

a) Checker Board Pre-Calibration Using Lens

A set of photographs of a checker board pattern on a computer screen was taken from various angles whilst endeavouring to ensure that the pattern filled the field of view and remained in focus (which meant that the camera was not focussed at infinity). The image set was loaded into Lens. The software ran a bundle adjustment based on the matched corners of the checker board pattern to generate camera model parameters and lens distortion coefficients ready for import into PhotoScan. This process was repeated

to ensure that the results were consistent. The residuals for one of the calibrations were marginally better, and the most accurate result was adopted.

b) Target Field Pre-Calibration Using PhotoScan

The set of 50 images from the convergent photography flights over the target field were loaded into PhotoScan, and the markers were detected. In PhotoScan, the marker detection algorithm is proprietary and requires considerable marker point placement verification and adjustment by the human operator. The marker centres were carefully checked and manually adjusted where required. Coordinates for the five GCP were uploaded and an initial alignment executed. The resulting point cloud was cleaned using PhotoScan's "Gradual Selection" tool with the reprojection error filter. This tool allows points in the cloud to be selected and deleted based on a filter option, in this case a reprojection error value greater than approximately one[6]. After each deletion, the solution is optimised using PhotoScan's "Optimize" tool that recalculates the bundle adjustment based on the new point set. The camera calibration coefficients derived via this alignment and self-calibration were exported for later application to the study site project.

Mismatches that occur during the initial alignment result in obviously incorrect points in the sparse point cloud, and leaving these incorrect points in the cloud will degrade the derived camera model. Editing the point cloud to clean it up so that the final optimised point cloud matches the surface as closely as possible is difficult, particularly when the mismatches occur over grassy terrain, as the "true" grass surface is not easily determined. Masking out all of the grass prior to alignment results in a very sparse point cloud, and in practice, it is not possible to reliably clean all erroneous grass points from the alignment-derived sparse point cloud. The first alignment can be cleaned and optimised to improve the derived camera model prior to point cloud densification; however, any remaining image matching errors will influence the derived camera model. The PhotoScan software allows precise placement of markers at the centre of targets in each image; however, it is not possible to align using only those defined target centres. Additionally, when the alignment completes, points corresponding to manually-placed target centres are not represented in the sparse point cloud. If there were a point corresponding to each ground control target, then it would be possible to delete all of the points, except those at marker locations, and to use PhotoScan to perform a more traditional calibration

[6] "Editing point cloud" in User Manual: Agisoft PhotoScan Professional Edition Version 1.0.4.1847 64 bit ©2014 Agisoft LLC `http://www.agisoft.com/`

of the camera that bases the calibration only on the correspondence between target locations defined in the imagery and the marker location in the point cloud.

c) Target Field Pre-Calibration Using CalibCam

We employed another camera calibration software in this project, because of its additional functionality. CalibCam provides target centroiding tools, has the ability to fix calibration coefficients and allows the operator to set GCP XYZ standard deviation estimates and image space measurement accuracy estimates. Automatic and manual target centroid tools were used to place control markers on the 5 GCPs and the remaining uncoordinated targets (termed relative points in CalibCam) in all of the images. CalibCam target identification requires significant human input. The high resolution of the imagery coupled with the low flying height resulted in successful automatic identification of centroids for most GCP and VP targets; however, other targets closer to the edge of the images had significant view angles or were impacted by glare and were more difficult to centroid. Based on examination of the residuals and an assessment of the variance factor (0.9–1.1 is the target range) from the first resection (for interior orientation) and the bundle adjustment, 0.6 pixels were adopted as the image space measurement accuracy setting. The GCP standard deviation estimate was set as 2 mm for each X, Y and Z ordinate. The adjustment resulted in estimates of focal length, principal point coordinates, three radial distortion coefficients and two decentring distortion coefficients, and the result had a variance factor of 1.01 (with 1686 degrees of freedom).

d) "On-The-job" Self-Calibration Using Agisoft PhotoScan

The steps involved in generating a 3D point cloud together with the estimated position and pose of the camera stations and a solution for the camera model parameters are similar regardless of the SfM/MVS software used. For this study, the aim was to ensure that the scenarios were all based on the same PhotoScan project, so that there was minimal difference in the processing steps. This base project contained 172 good-quality, high-resolution images from the nadir and oblique flights that corresponded to 80%–90% overlap (any images that resulted in greater than 95% overlap were avoided). Any water or saturated (reflecting) sand was masked out of each image. The on-board navigation-grade GPS data were used to geocode the images, so that an initial alignment could be done based on these approximate positions. The 13 GCPs and 34 VPs were loaded into the project and detected in the imagery. Each marker was checked and edited when

required to ensure that it was located and centroided in as many images as feasible. Once these markers were placed, the base project was used for the set up, and the following options were varied to produce 28 different operational scenarios:

a) The camera calibration settings were set to either the Lens, PhotoScan or CalibCam pre-calibration parameters and fixed, or these parameters were left unfixed for the self-calibration scenarios;

b) Only the Photoscan markers corresponding to the GCPs (5 or 13) were used for the final bundle adjustment and no VPs nor camera positions were used in this step;

c) The marker coordinates were altered for the DGPS equivalent scenarios;

d) The estimated standard deviation for horizontal and vertical GCP accuracy ($1\sigma_{XYZ}$) was set to either 0 mm, 2 mm or 22 mm; and

e) The oblique images were turned off for the scenarios with that image set excluded.

An alignment was run in each of the 28 projects. Each alignment resulted in a sparse point cloud, which was manually edited to remove any obvious erroneous points (typically where there was tall grass or complex woody vegetation). As described in (a), above, PhotoScan's "Gradual Selection" and "Optimize" tools were used to clean the sparse cloud before generating a dense point cloud. The position and estimated error information were exported. Only the VP positions and their corresponding positions in the derived point clouds were used to calculate error metrics (RMSE, standard deviation, mean, median, maximum and minimum), and boxplots were generated to visualise these results.

4.2.10 GCP Accuracy (GCP σ)

The estimated precision of the total station survey was $\sigma_{XYZ} = 2$ mm. PhotoScan only allows the input of a single estimate of "Marker Accuracy" (rather than an input for X, Y and Z accuracy for each GCP or the GCP set), and therefore, 2 mm was chosen as a reasonable approximation for the 3D GCP accuracy to one standard deviation (1σ). Based on this decision, it was necessary to set the same GCP accuracy value of 2 mm for each X, Y and Z ordinate in the CalibCam pre-calibration and a "Marker Accuracy" of 2 mm in the PhotoScan pre-calibration. In the PhotoScan documentation, it is suggested

that "Marker Accuracy" should be set to zero "if the real marker accuracy is within 0.02 m"[7]. In light of this recommendation, we included an additional scenario set with $\sigma_{XYZ} = 0$ mm. The final standard deviation scenario set is based on the degraded GCP positions that mimic a DGPS survey (Section 4.2.6), with $\sigma_{XYZ} = 22$ mm. Again, the accuracy settings were also set to 22 mm for the CalibCam (e.g., Pre13GCP22mmObl) and PhotoScan (e.g., PS13GCP22mmObl) pre-calibration scenarios (these have their calibrations fixed to the same coefficients as used in the 0 mm and 2 mm scenarios).

4.2.11 GCP Density (GCP Count)

As shown in Figure 4.1, two GCP sets were chosen. The first set can be considered a standard distribution of 13 GCPs, 9 around the periphery of the study area and 4 through the middle. The second set is an example of the sparsest GCP distribution that would be operationally acceptable, a GCP in each corner of the study area and one in the middle.

4.2.12 Inclusion/Exclusion of Oblique Photography

The whole study site was flown with nadir photography. Additional oblique photography was captured with a view toward improving the 3D reconstruction of the main erosion scarp (cracks, overhangs and small caves). For this study, the set of oblique photographs were taken at an AGL flying height of approximately 20–25 m with the camera angled between 45° and 65° oriented to face the erosion scarp. In the scenarios, these oblique images were included/excluded to assess their impact on the accuracy of the self-calibration and the derived model.

4.2.13 Accuracy Assessment Using Verification Points

The method used to assess the accuracy of the derived models in comparison to the total station survey is to report the difference between the precisely-surveyed VPs and their identified location in the derived point cloud. In PhotoScan, this is done by placing a non-ground control marker in the centre of the target in multiple images, and PhotoScan reports the difference between the estimated position of those image marker points in the model to the supplied precise survey coordinate (as X, Y and Z error). In each GCP density scenario, only the chosen set of GCPs were activated as ground control.

[7] Under Optimization at `http://www.agisoft.ru/wiki/PhotoScan/Tips_and_Tricks`

The remaining GCPs were ignored in these scenarios. In each GCP accuracy scenario, the GCP coordinates provided were either the set of precise survey coordinates or the DGPS equivalents. For each scenario, a set of VP errors were exported and used to derive metrics for assessing accuracy in X, Y, Z, XY and XYZ (RMSE, mean, median, standard deviation, minimum and maximum).

4.3 Results and Discussion

The mapping accuracy achieved for each of the scenarios is summarised in the following figures and tables. Refer to Table 4.1 for a summary of the coded scenarios.

4.3.1 Calibration Options

Pre-calibration based on a target field (PS13GCP2mm/PS13GCP2mmObl and Pre13GCP2mm/ Pre13GCP2mmObl), on-the-job self-calibration (Self13GCP2mm/Self13GCP2mmObl) and pre-calibration derived from a checker board pattern (Lens13GCP2mm and Lens13GCP2mmObl) are compared in Figure 4.4 and Table 4.2. The results indicate that the checker board calibration performed the most poorly. This is particularly evident in the vertical accuracy statistics, with substantially lower precision and significant bias. Pre-calibration solutions perform marginally worse than on-the-job self-calibration solutions, particularly in terms of vertical accuracy. The control in these scenarios is very precise, and with the exception of models that employ the checker board pre-calibration (Lens13GCP2mm/Lens13GCP2mmObl), this leads to precise models with no evidence of significant systematic errors. An on-the-job self-calibration that includes oblique photography (Self13GCP2mmObl) results in the most accurate model. That accuracy degrades when the oblique imagery is not included in the solution and results in a model with accuracy comparable to the robust pre-calibration. Measured in terms of achieved precision, the ranking of choices is:

1. On-the-job calibration using a network that includes oblique photography.

2. Either an on-the-job calibration using only nadir photography, or a robust pre-calibration.

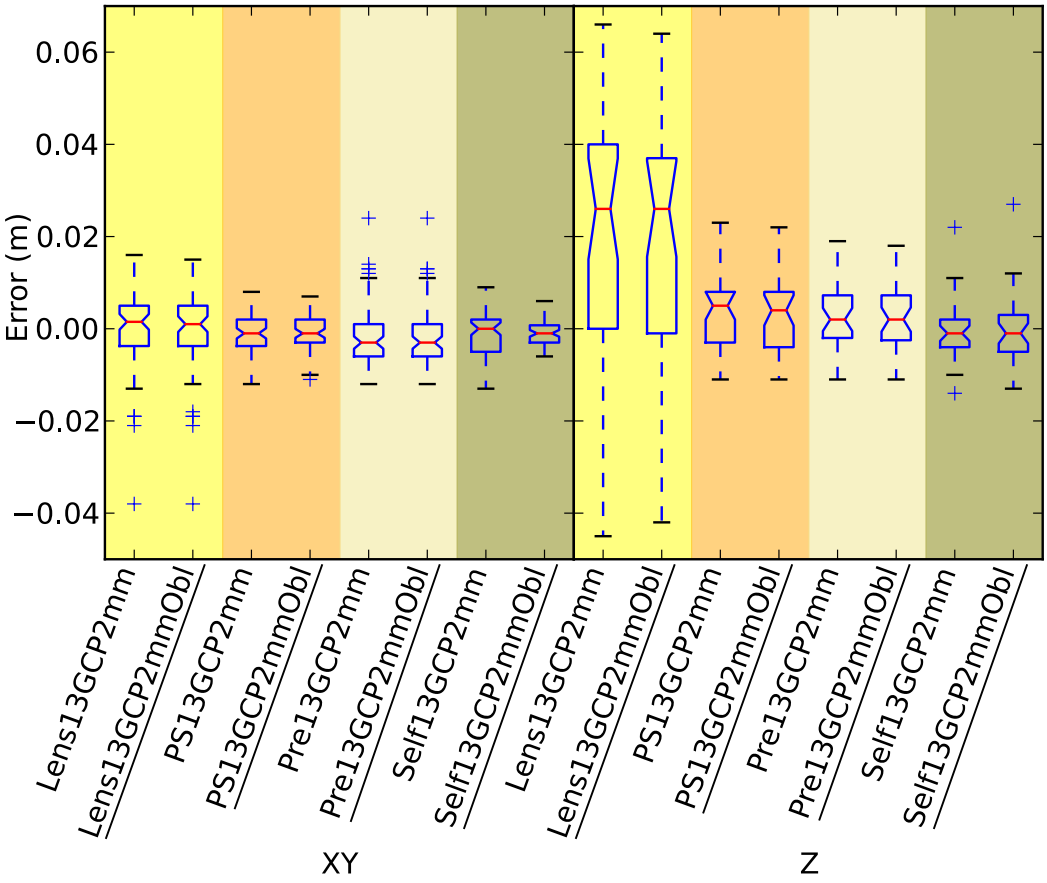

Figure 4.4: Box plots of the four calibration options for $\sigma = 2$ mm and with and without oblique imagery.

Table 4.2: RMSE for each of the four calibration options tested for $\sigma = 2$ mm and with and without oblique imagery.

Scenario	$\mathbf{RMSE}_{XY}$ (mm)	$\mathbf{RMSE}_{Z}$ (mm)
Lens13GCP2mm	8.8	41.0
Lens13GCP2mmObl	8.7	39.3
PS13GCP2mm	4.2	8.3
PS13GCP2mmObl	4.1	8.1
Pre13GCP2mm	7.3	7.1
Pre13GCP2mmObl	7.1	7.2
Self13GCP2mm	5.1	6.4
Self13GCP2mmObl	3.2	7.8

4.3.2 GCP Accuracy (GCP σ)

In assessing the impact of GCP accuracy, we will first consider the 13 GCP scenarios (Figure 4.5) before comparing and examining the impact of reducing the number of GCPs to five in Section 4.3.3 (Figure 4.6). The resulting RMSEs are summarized in Table 4.3.

Table 4.3: RMSE for pre-calibration and on-the-job self-calibration for three different GCP σ scenarios when using a strong control network (13 GCPs) and a sparse control network (5 GCPs).

Scenario	$\mathbf{RMSE}_{XY}$ (mm)	$\mathbf{RMSE}_{Z}$ (mm)	Scenario	$\mathbf{RMSE}_{XY}$ (mm)	$\mathbf{RMSE}_{Z}$ (mm)
Pre13GCP0mm	3.6	5.8	Self13GCP0mm	1.4	5.1
Pre13GCP0mmObl	3.5	5.8	Self13GCP0mmObl	1.3	5.9
Pre5GCP0mm	7.0	7.3	Self5GCP0mm	2.7	5.8
Pre5GCP0mmObl	6.7	7.1	Self5GCP0mmObl	2.1	6.3
Pre13GCP2mm	7.3	7.1	Self13GCP2mm	5.1	6.4
Pre13GCP2mmObl	7.1	7.2	Self13GCP2mmObl	3.2	7.8
Pre5GCP2mm	7.1	7.4	Self5GCP2mm	6.0	13.6
Pre5GCP2mmObl	8.8	7.8	Self5GCP2mmObl	4.3	11.5
Pre13GCP22mm	9.1	12.4	Self13GCP22mm	10.3	16.6
Pre13GCP22mmObl	9.1	12.6	Self13GCP22mmObl	7.0	11.9
Pre5GCP22mm	8.7	20.0	Self5GCP22mm	10.5	19.8
Pre5GCP22mmObl	8.6	20.0	Self5GCP22mmObl	7.3	15.9

Similar to the findings reported in Section 4.3.1, when control is precise ($\sigma \leq 2$ mm), then on-the-job self-calibration (Self13GCP0mm/Self13GCP0mmObl and Self13GCP2mm/Self13GCP2mmObl) and pre-calibration (Pre13GCP0mm/Pre13GCP0mmObl and Pre13GCP2mm/Pre13GCP2mmObl) both produced very accurate models, and including oblique imagery did not significantly impact the results. Fixing the marker accuracy setting in PhotoScan at 0 mm produced more accurate models than those that used the 2 mm setting, particularly for the on-the-job self-calibration scenarios.

When GCP precision was degraded to 22 mm, the positive impact of including oblique imagery became more apparent in the self-calibration scenario (Self13GCP22mmObl), which was shown to be the most accurate 22 mm scenario. The pre-calibration RMSE_{XY} = 9.1 mm, and on-the-job self-calibration RMSE_{XY} = 7.0 mm. There was a 3.3 mm horizontal and 4.7 mm vertical improvement for the on-the-job self-calibration scenario with oblique imagery (Self13GCP22mmObl) *versus* the on-the-job self-calibration scenario without oblique imagery (Self13GCP22mm). The implication is that if the GCP survey is undertaken using DGPS (σ = 22 mm), then on-the-job self-calibration with oblique imagery produces the most accurate model.

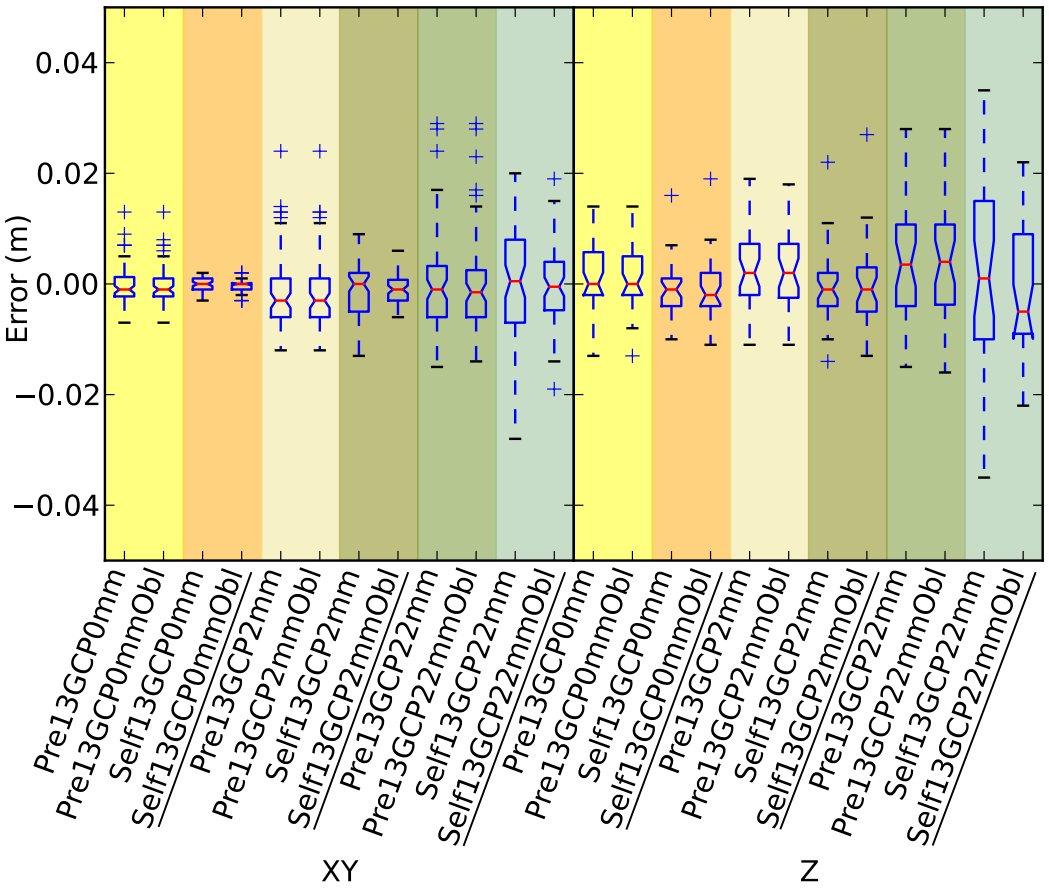

Figure 4.5: Pre-calibration *versus* on-the-job self-calibration scenario comparison using a strong control network (13 GCPs), with and without oblique imagery.

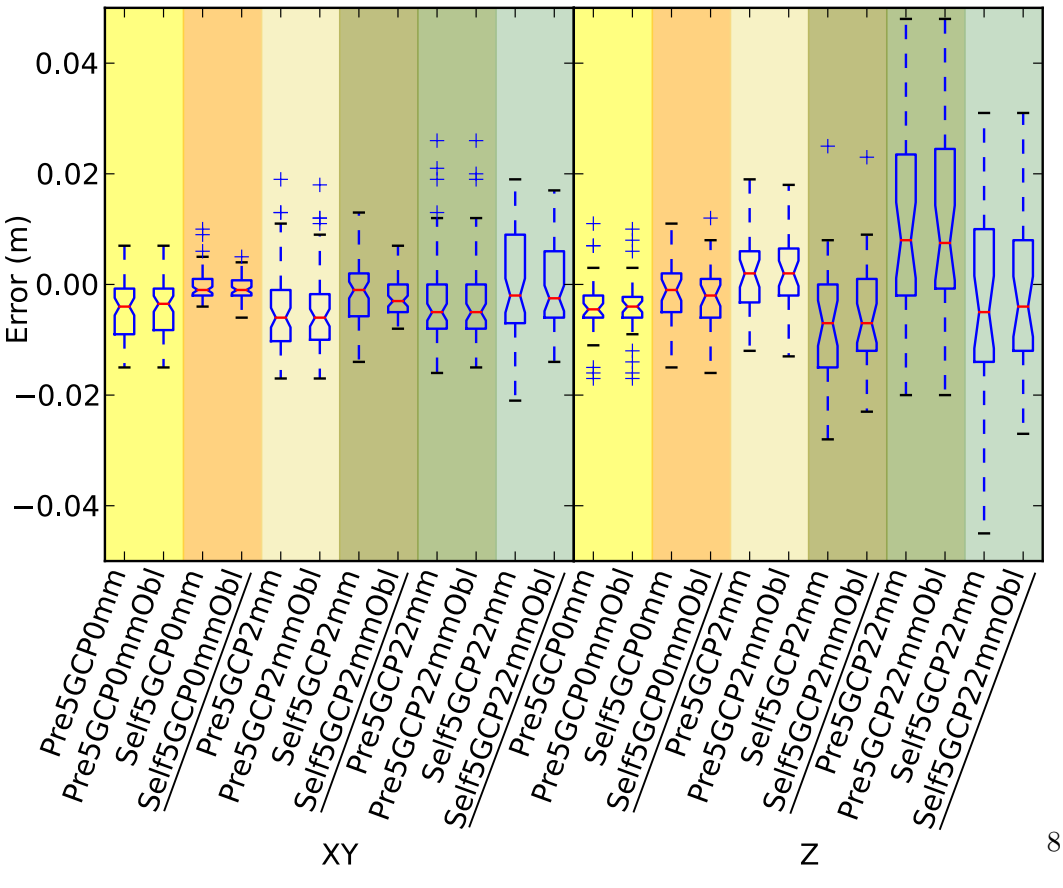

Figure 4.6: Pre-calibration *versus* on-the-job self-calibration scenario comparison using a sparse control network (five GCPs), with and without oblique imagery.

4.3.3 GCP Density (GCP Count)

The impact on model accuracy of reducing the number of GCPs to five will be assessed (Figure 4.6), and then the 13 GCP (dense) and five GCP (sparse) scenarios will be compared (Figure 4.5 *versus* Figure 4.6). Table 4.3 summarises these results.

When the GCP density was sparse (five GCPs), the overall accuracy was degraded, particularly in the vertical, regardless of calibration choice. When control was precise ($\sigma \leq$ 2 mm), the bias in the pre-calibration solutions (particularly in XY) implies that on-the-job self-calibration produced the most accurate models, and including oblique imagery had little impact. When control was less accurate ($\sigma = 22$ mm), all solutions show bias, and on-the-job self-calibration with oblique imagery produced the most accurate model (particularly when comparing vertical accuracy). Once again, on-the-job self-calibration with oblique imagery was the best option when $\sigma = 22$ mm and when control was sparse. As in the dense control scenarios, including oblique imagery provided little or no benefit when the control was precisely surveyed.

When comparing dense (13 GCPs) and sparse (five GCPs) GCP density scenarios, the most accurate models were produced when using a higher number of GCPs. The impact was smaller when control was precise, particularly when using pre-calibration. The vertical accuracy was more greatly influenced than the horizontal accuracy when the number of GCPs was degraded, particularly when $\sigma = 22$ mm and when $\sigma = 2$ mm. When there were only five GCPs, fixing the control (setting $\sigma = 0$ mm) had a significant impact on accuracy in the on-the-job self-calibration case, particularly in the vertical. The same impact was not seen in the 13 GCP scenarios. When GCPs were less accurate ($\sigma = 22$ mm), the addition of oblique imagery improved model accuracy in both the 13 and five GCP cases. Reducing the number of GCPs degraded the vertical accuracy of the models, whereas the horizontal accuracy of the models was not adversely impacted by this reduction in GCP density. In this study, five GCPs represents a practical minimum, since fewer would result in significant areas of terrain without nearby ground control, and 13 is likely to be a practical maximum, since residuals are approaching the limits of measurement precision. The findings of this study do suggest that there is scope for undertaking a similar study over a larger area in order to produce more 'scalable' rules for camera calibration and GCP distribution.

The overarching goal of this research is to better understand the implications of UAV survey design on the capacity to reliably measure topographic change, such as occurs in eroding coastal landscapes.

The precise survey used to validate our model demonstrates that UAV-MVS has provided sub-centimetre accuracy point clouds from 25–30 m AGL, which, in turn, allows change detection at the centimetre level.

The investigation demonstrates that self-calibration is comparable to pre-calibration when the GCP survey is designed with careful consideration of GCP survey accuracy, distribution and density, coupled with a well-designed camera network. Including oblique imagery may improve the accuracy of the results, and for change detection studies, these oblique images better ensure that terrain complexity is mapped.

A future study will investigate further the spatial distribution of errors. In this study, no doming, such as reported by James and Quinton (2014), Javernick et al. (2014), and Woodget et al. (2015), was evident in either the sparse or the dense GCP density scenarios.

This study helps to inform operational decisions in the survey design process and to provide insight into the impact of calibration choices, oblique imagery inclusion, ground control accuracy and ground control density on the accuracy of the resultant photogrammetric model.

4.4 Conclusions

The use of UAV-MVS surveys to generate 3D point clouds for coastal erosion monitoring requires careful survey design to ensure sufficient accuracy for change detection. The influence of calibration methodology, ground control point accuracy, the number of ground control points (GCPs) and the inclusion of oblique imagery was investigated. Accuracy was assessed by comparing precisely-surveyed verification points with their photogrammetrically-derived coordinates. This study is the first to undertake a precise total station field survey with $\sigma \leq 2$ mm for the purposes of assessing the impact of these survey design choices on UAV-MVS 3D models of natural terrain.

Under a range of typical operating scenarios, four calibration options were assessed: on-screen checker board pre-calibration; a pre-calibration using Agisoft PhotoScan; a pre-calibration using 3DM CalibCam; and a self-calibration using Agisoft PhotoScan. The on-screen checker board pre-calibration was shown to be the least accurate method (vertical RMSE was ~5 times less accurate than the other methods), and so, the conclusions here summarise the findings for flown CalibCam pre-calibrations and PhotoScan

on-the-job self-calibrations. The results indicate that when a dense array of precise ground control and no oblique imagery was employed in the solutions, then the differences between a pre-calibration and an on-the-job self-calibration were not substantial (on-the-job self-calibration was marginally more accurate: the horizontal root mean square error (RMSE) differed by ~2 mm ($RMSE_{XY}$ for pre-calibration was 7.3 mm compared to 5.1 mm for self-calibration); the vertical RMSE differed by 0.7 mm ($RMSE_Z$ was 7.1 mm compared to 6.4 mm). When oblique imagery was incorporated into the same solutions, self-calibration remained the more accurate solution for horizontal coordinates (with the difference increasing to 3.9 mm, $RMSE_{XY}$ was 3.2 mm, whereas pre-calibration $RMSE_{XY}$ was 7.1 mm) and still comparable for vertical accuracy (although in this case, 0.6 mm less accurate than the pre-calibration).

The results indicate that when the number of ground control points was reduced (to only five GCPs with $\sigma \leq 2$ mm), the accuracy of the solutions degraded, but more so for the self-calibration solution. However, our results suggest that this degradation of the self-calibration can be mitigated by increasing the accuracy of the ground control. These results indicate that when the ground control accuracy is high, the addition of oblique imagery has little impact on model accuracy.

When the dense array of ground control was geolocated at more common operational survey accuracy ($\sigma = 22$ mm) for both the pre-calibration and on-the-job self-calibration scenarios, then our results show that, with the inclusion of oblique imagery, the self-calibration performed better than a pre-calibration. In this scenario, horizontal accuracy degraded by only 2.0 mm for pre-calibration ($RMSE_{XY}$ went from 7.1–9.1 mm) compared to 3.8 mm for on-the-job self-calibration ($RMSE_{XY}$ went from 3.2–7.0 mm). When comparing on-the-job self-calibration scenarios, then our results show that a solution without oblique photography performed more poorly than one with oblique photography (horizontal accuracy reduced by 3.3 mm ($RMSE_{XY}$ went from 10.3–7.0 mm) and vertical accuracy reduced by 4.7 mm ($RMSE_Z$ went from 16.6–11.9 mm)). When the sparse array, instead of the dense array, of ground control was geolocated at more common operational survey accuracy ($\sigma = 22$ mm) for both the pre-calibration and on-the-job self-calibration scenarios, including oblique imagery significantly improved the on-the-job self-calibration results (in our case, by 3.2 mm horizontally ($RMSE_{XY}$ went from 10.5–7.3 mm) and 3.9 mm vertically ($RMSE_Z$ went from 19.8–15.9 mm)).

Regardless of GCP accuracy, pre-calibration may be operationally expensive, and so, the better option is then to employ on-the-job self-calibration ensuring that there is sufficient overlap and that the imagery extends beyond the focus area. Including oblique imagery

is therefore advised. The GCPs should be distributed across the area to be mapped, particularly around the periphery. The GCP density should be high enough that it will overcome the issues seen in the sparse control scenarios, such as the degradation in overall accuracy. Vertical accuracy is particularly susceptible to poor GCP distribution and density. Questions related to accuracy prediction, configuration considerations, such as GCP distribution, and variations in camera network design will be the focus of Chapter 5. Finally, it is important to understand that the inclusion or exclusion of oblique imagery in the scenarios was focussed on the impact on horizontal and vertical accuracy and does not take into account the improvements to the 3D model that are seen when adding oblique imagery to the camera station network. The influence of oblique imagery on the quality of the 3D model will be investigated in Chapter 5.

Thesis context

The assessment of the impact of design choices is the focus of Chapter 5 and the study described in this chapter evolved as it became clear that calibration methods are an important consideration and required a standalone study/chapter, as a result Chapter 4 and Chapter 5 base their results on the same experiment. The derivation of camera calibration parameters via the set of images used for 3D reconstruction (on-the-job self-calibration) has the potential to cause deformation in the derived 3D model. Camera network design is therefore very important. Pre-calibrating the camera can overcome some of these deformation issues but logistically it is not always possible to calibrate the camera before each data capture mission (which is considered necessary when using non-metric lightweight, consumer-grade cameras). This chapter provides evidence that a well-designed camera network and strong control network can result in an accurate model using an on-the-job self-calibration. The pre-calibration results are also accurate and these, along with simulation results and profile measurements, are used in the Chapter 5 to investigate the impact on accuracy of flight planning and ground control choices.

Acknowledgements

The authors thank Darren Turner (University of Tasmania) for his assistance as the UAV pilot and for his advice on camera network design and Matt Dell for his advice on PhotoScan workflow and settings.

5 | Photogrammetric simulation of flight path configurations for 3D reconstruction of natural landscapes using UAV imagery

Chapter 5 focuses on assessing the impact of camera network design, GCP survey accuracy, and GCP distribution on UAV-MVS survey accuracy and compares simulated achievable precision estimates to empirical results. This chapter will be submitted for publication with one of the following journals: ISPRS Journal of Photogrammetry and Remote Sensing[1]; Photogrammetric Engineering and Remote Sensing[2]; or Remote Sensing[3].

Abstract

The micro-UAV as a mapping tool is gaining popularity worldwide. Computer vision and photogrammetric techniques are widely used to derive surface models from UAV photography. The density of computed point clouds and the accuracy and resolution of the datasets produced is influenced by a number of key variables including camera network geometry, camera specification, camera calibration accuracy, image resolution, ground control point (GCP) distribution and accuracy, surface characteristics (e.g., vegetation cover and surface texture) and the precision with which targets can be measured and matched. This paper discusses these influences on 3D reconstruction accuracy and focuses on three variables, namely camera network design, GCP survey precision, and GCP distribution, in the context of a case study of a natural coastal site. The impact of GCP distribution is assessed alongside the impact of camera network choices such as percentage overlap and the inclusion of oblique photography. A set of terrain profiles are compared to assess point cloud density and accuracy. The results indicate that it was possible to map a section of natural coastal cliff to better than 6 mm (1σ) accuracy at a point density of 1–6 points per cm^2 from 25 m above ground level using precise GCPs ($\sigma \leq 2$ mm) and 10–12 mm (1σ) accuracy using DGPS precision GCPs ($\sigma = 22$ mm). Achievable object space precision predicted by a bundle adjustment simulation is over-estimated when control is precise because the solution will be more strongly

[1] http://www.journals.elsevier.com/isprs-journal-of-photogrammetry-and-remote-sensing/

[2] http://www.asprs.org/Photogrammetric-Engineering-and-Remote-Sensing/PE-RS-Journals.html

[3] http://www.mdpi.com/journal/remotesensing

influenced by unmodelled systematics in the camera distortion estimation. For DGPS precision GCPs simulation is reliable with a good camera calibration as these systematics will not be significant in comparison to measurement precision. The simulation and the experimental work shows that the distribution of ground control impacts on model precision. In our case study, it was found that 12–15 GCPs distributed around the periphery and through the centre of the mapped region provides an optimal solution. The inclusion of oblique imagery improved the object space accuracy, particularly when the number of GCPs used in the solution was reduced and when the terrain to be mapped was complex. This was shown in both the simulation and the experimental work. The similarity between the simulated and empirical results indicates that simulation is a valid method of informing the planning process when endeavouring to achieve high accuracy and resolution. However, this study further demonstrates that the choice of camera station position and pose does not need to be accurately predefined. This suggests that pre-planning using photogrammetric simulation software can be used to optimise photo acquisition and GCP distribution and provide reliable *a priori* estimates of object space precision. However, it also indicates that it is feasible for an experienced UAV survey team to plan a flight in the field so that there is high overlap, minimal occlusion, sufficient redundancy and appropriate oblique imagery of complex 3D terrain to model natural terrain features.

5.1 Introduction

During the last 10 years, UAV remote sensing has been going through a similar transformation to that seen in close-range optical measurement systems in the early 1990's. As described in Shortis and Fraser (1991) those systems had traditionally been in the surveyor's domain, but demand drove the development of more automated and real-time solutions via systems that did not require highly skilled specialist operators with surveying expertise. The then new "off-the-shelf" tools developed for optical measurement could efficiently produce the desired results at sufficient precision to allow an operator with basic training to undertake routine tasks. UAVs are in the midst of a proliferation driven by improved useability and availability (Remondino et al., 2011; Colomina and Molina, 2014; Nex and Remondino, 2013). The miniaturisation of sensors and control/positioning systems, coupled with a significant reduction in cost, have allowed UAVs to move from predominantly military applications into the civil market place. The outcome of this availability of affordable tools is a transformation in the way data can be captured. Computer power coupled with photogrammetric and computer vision algorithms have provided UAV-based data acquisition systems with a workflow that can allow non-specialists to acquire the skills needed to capture data using a UAV carrying appropriate sensors, and to process that data to deliver useful derivatives (Colomina and Molina, 2014). Advances in technology and regulatory changes will see this expansion continue. Research can help fulfil the potential of this field of remote sensing through the delivery of data capture and processing workflows that are both reliable and commercially viable. The accuracy and precision requirements of each application must be carefully assessed so that the work is carried out without over-complicating or over-simplifying data acquisition and therefore reducing the viability and/or reliability of UAV-based surveys.

Manned aircraft provide a means of 3D mapping via photogrammetry and the flying heights chosen will dictate spatial resolution, for example, ~10 cm resolution imagery and DEMs accurate to ~5 cm are common from airborne photogrammetry and 1–3 points per m^2 is standard from LiDAR (up to 10 points per m^2 is possible). UAV mapping systems can fill the scale gap between manned aircraft systems and ground based measurements, such as detail surveys and terrestrial laser scanning (TLS). Hernandez-Lopez et al. (2013) suggests that UAV flight planning needs to be treated differently to traditional photogrammetric flight planning, particularly in terms of greater instability of the platform, less capacity to navigate to precise locations, and greater exposure to the effects of changes in terrain height as a function of flying height. They also note that there

have been few flight planning studies that focus on UAV mapping (e.g. Schmid et al., 2012; Hoppe et al., 2012; Hernandez-Lopez et al., 2013; Sujit et al., 2012; Cheng et al., 2008). The need to move beyond traditional flight planning is particularly valuable for multi-rotor micro-UAVs that have very short flight durations (often <10 min) and can fly complex paths that, when combined with camera rotation, provide six degrees of freedom. The complexity of terrain can be taken into consideration and the fight path can be altered to adapt to that complexity. Optimal flight path planning is a complex task (Olague and Mohr, 2002) and so the adaptability of micro-UAV camera network specification is a key advantage.

In traditional photogrammetric flight planning, when frame cameras are employed, the standard design protocols are based on camera station and flight strip separation to achieve appropriate forward and side overlap constraints. Nadir photography is used so as to create stereo pairs and photogrammetric blocks. In UAV multi-view stereopsis (UAV-MVS), widely used in UAV photogrammetry, this paradigm still holds for nadir photography and can also be useful for more complex flight paths that incorporate oblique photography. The strength of a camera network is defined by the number of camera stations and their spatial layout. The "rule of thumb" used in photogrammetry is to aim for three or four highly convergent rays intersecting each target (Grun, 1980; Fraser, 1984) in (Mason, 1995a). A strong network configuration will have convergence angles in both the XZ and YZ planes of between 60° and 90° or more(Fraser (1992) in Mason (1995a)). Wenzel et al. (2013) point out that while larger intersection angles (such as 90°) lead to optimal geometric conditions for 3D object point extraction in MVS densification, the reduced image similarity impacts image matching in SfM.

The need for sufficient overlap is fundamental to stereovision, whether working with stereo pairs or MVS. In many previous UAV surveys for terrain mapping the design of the camera network is based on desired overlap and in many cases a forward overlap of approximately 80% (sometimes 90%) and a side overlap of 60% is used (e.g. Carvajal et al., 2011; Naumann et al., 2014; Eltner et al., 2013). Other studies have attempted to optimise for forward and side overlap at approximately 80–90% (e.g. Rosnell and Honkavaara, 2012; Lucieer et al., 2011a; Lucieer et al., 2013; Harwin and Lucieer, 2012b). Certainly from an image matching and tie point creation perspective this high overlap goal is sensible as it increases the number of image point measurements for each identifiable target object feature. In our study the impact of reducing overlap from 80% to 60% was assessed.

The low altitude required for high accuracy, high resolution 3D model derivation in-

creases the impact of complex terrain in terms of occlusion and resultant model completeness. Schmid et al. (2012) suggests that nadir photography does not allow for full 3D reconstruction. This is particularly true when surface features include complex man-made structures or terrain that cannot be represented in 2.5D, such as cliffs with overhangs. To overcome this limitation of nadir-only data capture, oblique imagery may be required. Nocerino et al. (2013) and Nocerino et al. (2014) showed that convergent imagery should always be included in flight plans for SfM/MVS surveys. Planning for oblique image capture is more complex than nadir flight planning and the planned camera network can vary considerably from the actual flight path. These differences are caused by a combination of wind conditions and the inaccuracy of UAV position and camera pose due to the majority of UAVs carrying navigation-grade GPS, lightweight IMUs and 3-axis camera mounts or gimbals without fine camera angle definition. Aside from Chapter 4 that assessed the impact of oblique imagery on camera calibration, there has been no study that directly compares the impact of including/excluding oblique imagery from a UAV-MVS survey. Wackrow and Chandler (2011) and James and Robson (2012) have shown that including oblique imagery reduces model distortion and this study builds on that research by assessing the impact on derived model accuracy of including and excluding oblique imagery.

The density and distribution of ground control is important unless direct georeferencing is being used (e.g. Turner et al., 2014). The impact of varying the number of ground control points has been addressed in only two previous studies (Tahar, 2013; Rosnell and Honkavaara, 2012). Both these studies measured the GCP positions with differential GNSS (Global Navigation Satellite Systems) or differential GPS (DGPS) surveys; Tahar (2013) assessed error based on check point comparisons whereas Rosnell and Honkavaara (2012) compared a point cloud from a traditional photogrammetric survey to the UAV survey results. The use of verification points (VPs) (or check points) is a more suitable comparison when survey precision is known. In our study, the high precision of the GCP/VP survey further enhances the comparison metrics.

The precision of ground control directly impacts model accuracy. A total station survey is a robust method for measuring GCPs and has been used in previous studies (Eltner et al., 2013; D'Oleire-Oltmanns et al., 2012; Tahar and Ahmad, 2011). However, there are no previously published studies of UAV accuracy assessment that have fully exploited the high accuracy that can be achieved with a precise total station. The majority of previous studies that have investigated UAVs for terrain mapping have used differential GNSS/DGPS for the control survey (Naumann et al., 2014; Pierzchala et al., 2014; Westoby et al., 2012; Fonstad et al., 2013; Mancini et al., 2013; Flener et al., 2013;

Lucieer et al., 2011a; Lucieer et al., 2013; Rosnell and Honkavaara, 2012; Harwin and Lucieer, 2012b; Niethammer et al., 2010; Niethammer et al., 2012; Carvajal et al., 2011; James et al., 2013). Differential GNSS/DGPS baseline length and satellite geometry influence the accuracy of differential GNSS/DGPS survey measurements and the standard deviation of measurements is usually an approximation. A strong total station network will provide higher precision data than a differential GNSS/DGPS survey.

Mathematical simulation of camera networks can be used to assess the quality of the network design and to predict the precision of the resulting model. Simulation is a powerful pre-analysis tool for assessing a design and predicting achievable precision (Fraser, 1984; Rosnell and Honkavaara, 2012). The entire processing workflow can be evaluated and validated through simulation by examining error propagation and the impact of design changes prior to fieldwork (Rosnell and Honkavaara, 2012). Predictions from simulation can ensure that a flight plan will be sufficient to meet accuracy specifications (Rosnell and Honkavaara, 2012) and can be used to optimise the flight plan by ensuring that no more than the necessary number of photos are acquired. If necessary, the designer can iterate to refine the design by trial and error using expert knowledge to optimise aspects of the design (Fraser, 1984). Mason (1995b) suggests that a camera network design that relies on a trial-and-error approach without simulation is unsatisfactory as there is no guarantee that the whole object will be mapped and/or there may be more images than is optimal.

In close-range UAV mapping the potentially high accuracy and high resolution can be undermined by poor prior knowledge of the target area (leading to an incomplete flight plan and image set) or poor ground control distribution. For terrain mapping the complexity of the terrain must be carefully considered. Avoiding occlusion is desirable but not always practically achievable. The aim should therefore be to minimise the impact of occlusion by ensuring that occlusions are factored into the design, and that the constraints listed above are adhered to. All parts of the target object/surface have to be covered by the images (Hoppe et al., 2012). An object needs to appear in two images in order to derive 3D coordinates, however, three or four is better (Fraser, 1992; Mason, 1995a). The characteristics of target objects within the study area need to be considered. Target features/objects that are complex, repetitive (such as dense woody scrub) and/or homogeneous (such as water bodies) do not provide matching algorithms with distinguishable attributes and therefore the point clouds produced may be sparse or empty in these areas (Rosnell and Honkavaara, 2012; Harwin and Lucieer, 2012b; Scott et al., 2003). In addition, unlike LiDAR, the point cloud produced is a surface model, often missing ground points under dense vegetation. The MVS technique is therefore

most suited to surface model creation and, if precise terrain is needed, there needs to be minimal vegetation in the focus area. Scott et al. (2003) calls these shape and material constraints.

In most UAV studies, expert knowledge rather than simulation has informed "on-the-fly" and ad hoc camera network design and GCP layout. Photogrammetrists expect careful planning and for complex mapping tasks rely on simulation for design validation. The UAV-MVS mapping technique is relatively new and relies on many images of the target with high levels of overlap. This technique may or may not require the level of careful pre-analysis that has been employed in, particularly, high accuracy close-range photogrammetry. This study aims to test whether simulation can be used to predict the accuracy of a UAV-MVS survey.

Simulation has not been used extensively in UAV imaging evaluation and in the assessment of GCP layout scenarios. Rosnell and Honkavaara (2012) used simulation (using the FGIAT bundle block adjustment software[4]) to evaluate control scenarios and to obtain a reference dataset without the influence of systematic deformations. Ahmadabadian et al. (2013) used Vision Measurement System (VMS[5]) to simulate and test camera networks (although not UAV camera networks). James and Robson (2014) also used VMS to simulate camera networks and assess systematic errors in DEMs based on UAV survey simulations. The systematic errors (doming) seen in the (James and Robson, 2014) study were attributed to a combination of the nadir camera network design and distortion modelling inaccuracies due to insufficient control around the periphery and through the centre of the target area. The suggested mitigation for this doming is additional flights with varying flying heights or varying camera angle (oblique or convergent photography) or well distributed control. To some extent this doming is minimised in traditional photogrammetry through the use of metric cameras. Our research builds on those studies by comparing simulations from VMS to actual surveys under different scenarios to assess whether close-range photogrammetric simulation can be validated in the field.

As discussed above, previous research has looked at aspects of UAV survey design and the achievable accuracy of UAV-MVS (Harwin and Lucieer, 2012b; Rosnell and Honkavaara, 2012; Tahar, 2013; Schmid et al., 2012; Hoppe et al., 2012; Hernandez-Lopez et al., 2013; Sujit et al., 2012; Cheng et al., 2008). Many surveys have been ad-hoc without a detailed analysis of the precision and accuracy specifications (Pierzchala et al., 2014;

[4]Developed at the Finnish Geodetic Institute, Masala, `http://www.fgi.fi/fgi/`
[5]Vision Measurement System, `http://www.geomsoft.com`, Robson and Shortis

Fonstad et al., 2013; Mancini et al., 2013; Flener et al., 2013; Lucieer et al., 2011a; Lucieer et al., 2013; Niethammer et al., 2010; Niethammer et al., 2012; Carvajal et al., 2011). This approach results in a 'best-case' accuracy of ~5 cm. For some applications this is not sufficient and it is important to fine-tune the survey parameters to achieve the best accuracy possible. This study aims to address this gap by combining well-established photogrammetry theory with real-world UAV operation within the context of an application that demands sub-centimetre accuracy. Our research seeks to build on those studies using simulation and by comparing precisely surveyed ($\sigma \leq 2$ mm) verification points to their equivalent points in the models derived from a range of scenarios, each defined by a set of design choice differences. The choices relate to image overlap, inclusion of oblique imagery, GCP density and GCP survey precision.

Our efforts to better understand the impact of flight planning and survey configuration choices on the accuracy and completeness of terrain models generated with UAV-MVS highlighted the importance of image overlap and oblique imagery inclusion in UAV camera networks. In photogrammetric workflows, simulation is an important step. Verifying that predictions from simulation are realistic is an aspect of UAV-MVS that has not been studied using real-world data and precise ground control. The distribution and survey precision of ground control also strongly influences accuracy. The focus of this study is therefore on the verification of simulation predictions and the assessment of the impact of UAV survey design choices on model accuracy. The following parameters are assessed: image overlap, inclusion of oblique imagery, GCP density and distribution, and control survey precision.

The objectives of this paper are: i) to investigate whether simulated precision and accuracy can be verified with field observations; ii) to evaluate the impact of flight planning, field setup and processing choices on the accuracy of derived 3D models by comparing 60% and 80% overlap scenarios; the impact of oblique imagery; 5, 9 and 13 GCP scenarios; and precise and differential GNSS/DGPS equivalent GCP quality ($\sigma \leq$ 2 mm and $\sigma = 22$ mm scenarios); ii) to assess the spatial distribution of error; and iv) to compare total station profiles with UAV point clouds (from a number of scenarios) to better understand the impact of design decisions on point cloud density, accuracy, and precision.

5.2 Method

5.2.1 Background Theory

Design choices in UAV photogrammetry must take a range of considerations into account. Considerations relating to quality and operational decisions are described.

Quality Considerations

In examining a mapping technique and the quality of the resulting dataset(s), Fraser (1984) suggests that there are four key aspects to consider: precision, reliability, economy and testability. Precision is driven by the geometric configuration of the measurement sensors and the achievable image space measurement accuracy. The reliability relates to whether or not a technique is self-checking, which in turn relates to optimal levels of redundancy. Economy is driven by the efficiency and affordability of a technique. Very high precision comes at a cost. Testability is driven by network precision and requires some form of comparison to "truth". In UAV flight planning, simulation, data capture and processing there are a number of survey design and processing factors that influence the horizontal and vertical accuracy of the derived point cloud and 3D model. Methods of predicting object space accuracy have been explored by a number of authors, from the 1970s with Abdel-Aziz in close-range applications (Abdel-Aziz and Karara, 1971; Abdel-Aziz, 1974) through to the 1980s (Fraser, 1984; Abdel-Aziz, 1982) and more recently in Structure-from-Motion (SfM), MVS and UAV photogrammetry (Eisenbeiss, 2009; Rosnell and Honkavaara, 2012; James and Robson, 2012; Stefanik et al., 2011) and these use a number of common determinates such as a camera baseline, focal length, image space measurement accuracy, identifiable target size and ground sample distance. In this research we use the VMS software[6] for simulating the bundle adjustment to estimate achievable object space precision.

Convergence angle and incidence angle constraints

A strong camera network geometry will improve the accuracy of object space measurements and the homogeneity of accuracy across the model-space. Highly convergent camera geometry is preferred, with the camera stations arranged so that the optical axes of the cameras (in the case of more than two cameras) do not approach coplanarity (Fraser,

[6]Vision Measurement System version 8.6© `http://www.geomsoft.com`, Robson and Shortis

1984). The benefits of convergent photography can however be reduced if the angle of incidence between the target surface and the camera location becomes highly acute. The greatest coincidence angle that is tolerable before target object measurement and triangulation accuracy exceeds a specified threshold is the maximum convergence angle. Again, the value of this maximum is driven by the physical attributes of the target feature. Fraser (1992) in Mason (1995a) suggests that 60° is a minimum for a strong network and 90°or more is reasonable as a maximum. Verhoeven (2011) suggest that while software such as PhotoScan can handle incidence angles as low as 45° , perpendicular angles (90°) are preferable (Verhoeven, 2011).

The minimum allowable the angle of incidence of the optical axis with the target is dependent on physical attributes of a target feature (geometry and material) and the scene illumination (Ahmadabadian et al., 2013). High angles of incidence negatively affect precision and accuracy of image measurement (Shortis and Hall, 1989). Conversely, the triangulation uncertainty increases as this angle decreases so there needs to be a balance (Ahmadabadian et al., 2013). Camera network geometry strength is improved with highly oblique geometries, but possibly at a cost to viewing angle. These constraints are closely related to forward and side overlap in a traditional 2D photogrammetric flight plan.

Depth of field

The range of sufficiently sharp focus dictates which features in imagery can be precisely measured (Mason, 1995a).

Camera positioning accuracy

Detailed pre-analysis may result in a view point plan that is considered optimal, but the ability of the system to position the camera such that the six degrees of pose are accurately achieved is dependent on the on-board navigation system performance and the constraints in pose defined by the camera mount (Scott et al., 2003). Navigation-grade GNSS/GPS can vary in the range of metres and this dictates camera placement accuracy (Schmid et al., 2012). The planned positions may not be achieved and the recorded position and orientation of those cameras may not be accurate.

Workspace

The workspace is a 3D bounding box defining the potential camera station locations, this may include known obstructions within the target workspace such as buildings or trees (Mason, 1995a).

Time of day

In an ideal situation all photos would be acquired simultaneously resulting in a set of images with the same target illumination and sun angle. In reality, imagery of an area covered in one or two flights may have been acquired over a 5–20 minute period, in which time the illumination may change. In generating time series data over a number of days/weeks/months/years the illumination may be very difficult to control and will almost certainly differ. The sun angle and time of day may also influence the derived terrain model. Shadows are of particular concern when using automated matching (Baltsavias, 1999). For example, shadows can result in false crevasses in the terrain.

Camera choice

High quality lenses and cameras are more stable and more precisely machined, which results in a more robust calibration and improves derived product quality and reliability (Shortis and Hall, 1989). The ability to fix settings such as focus and shutter speed can ensure more predictable image distortions and fewer motion blur artefacts (Rosnell and Honkavaara, 2012). Imaging array resolution and quality play a role in image quality and colour consistency which in turn helps in image matching and GCP target identification. The use of cameras with rolling shutters can reduce image matching accuracy and degrade models, particularly for fast moving aircraft.

Ground control and model registration

GCP target characteristics are an important consideration. The size, contrast and symmetry of targets need to be appropriate to the image resolution and camera network (Shortis and Hall, 1989). Retro-reflective targets may be ideal for accurate surveying but there may be too much reflection in images, which can cause haloing which in turn can reduce target definition in images and in an MVS derived model. The smallest identifiable target size is typically 5–10 times GSD (He et al., 2012).

Early SfM solutions such as Bundler[7] provide the point cloud in an arbitrary coordinate system (Snavely et al., 2007). The arbitrary coordinate system arises from the "free network" bundle adjustment used to process the imagery and obtain approximate camera position and pose, and derive a sparse point cloud. This form of bundle adjustment supports rigorous error propagation and does not require datum information (Mason, 1995b). A free network adjustment was necessary for early SfM/MVS solutions because the intention of much of the early work was to create software that allowed 3D models to be derived of scenes that did not include any known distances of ground control (no exterior constraints). While the free network solution provides this very important flexibility, and if the camera geometry is very well planned can provide high accuracy photogrammetric solutions, the preferred approach in photogrammetric terrain mapping is to include GCPs in the bundle adjustment.

Lens Distortion

Camera lens distortions impact the accuracy of models produced by SfM/MVS (James and Quinton, 2014). The SfM bundle adjustment provides a means of deriving camera calibration parameters via self-calibration and this option produces accurate results (Chapter 4). Many studies have chosen this option (e.g. Naumann et al., 2014; Pierzchala et al., 2014; Fonstad et al., 2013; Mancini et al., 2013; Lucieer et al., 2011a; Lucieer et al., 2013; Rosnell and Honkavaara, 2012; Harwin and Lucieer, 2012b; Niethammer et al., 2010; Niethammer et al., 2012) whilst others have chosen to pre-calibrate the camera either using a target field and a camera to object separation similar to that used in their survey (e.g. Carvajal et al., 2011; Eltner et al., 2013; D'Oleire-Oltmanns et al., 2012) or the checkerboard calibration (e.g. Flener et al., 2013; Stefanik et al., 2011) which is much less reliable (as described in Chapter 4). The pre-calibration is more suited to this study as it removes the set of uncertainties resulting from deriving a camera model via self-calibration. These uncertainties may obscure the impact of the core variables assessed here.

Flight planning/camera network design

The key to generating a complete and accurate 3D model is flight planning. The planner must ensure that the captured image dataset is of sufficient resolution and coverage to enable the production of a complete 3D reconstruction of the target surface, whether

[7]Bundler: Structure from Motion (SfM) for Unordered Image Collections, `http://www.cs.cornell.edu/~snavely/bundler/`

that is a man-made object or natural terrain features. When designing a flight plan for fine-scale terrain mapping with micro UAVs there are a number of options:

1) Fixed AGL nadir photography acquisition

This is the traditional approach and usually begins with the formulation of a detailed flight plan that defines a generic flight path resulting in overlapping nadir strips. The flight path and photograph centres (or camera stations) are defined based on a number of key constraints:

a) Photo scale (GSD)

b) Photo overlap (influenced by parameters such as capacity to accurately navigate the instrument, capacity to acquire photos at high frame rates)

c) Aircraft dynamics (manoeuvrability, platform stability) and regulations (flying height and line of sight restrictions)

d) Camera specifications (e.g., lens quality, maximum image acquisition rate, manual control versus automatic settings)

e) Flight duration (maximum)

f) Airfield to focus area (return) distance

These constraints (particularly the first three) lead to a strip based photo acquisition plan with a strip order driven by the need for efficiency and aircraft dynamics. Object space resolution is dictated by flying height and focal length; these in turn will influence flight line separation. This approach has been used for fixed-wing UAV mapping (e.g. Küng et al., 2011; Xu et al., 2011; D'Oleire-Oltmanns et al., 2012) and for rotary winged UAVs (e.g. Eisenbeiss and Zhang, 2006; Tahar and Ahmad, 2011; Neitzel and Klonowski, 2011). It is a suitable approach for terrain that is reasonably flat/featureless and there is little requirement for detailed *a priori* terrain data (if any). The advantage of the generic nadir approach is that mathematical simulation using the common/traditional photogrammetric formulae (Wolf, 1983) provides pre-flight verification of GSD (resolution), expected accuracy, control point layout and imaging geometry strength (Grun, 1980; Mason, 1995a; Fraser, 1984; Fraser, 1992).

2) Fixed AGL nadir and oblique photography acquisition

The simplest generic camera network is a symmetrically distributed set of camera stations distributed roughly in a 2D planar arrangement (Grun, 1980) in (Mason, 1995a). The choice between nadir and oblique is dictated by object complexity and the camera station network required for ensuring complete coverage. The inclusion of oblique photography is not traditionally done for airborne photogrammetry and is suited to SfM/MVS and close-range photogrammetry when mapping complex 3D objects. The overlap constraints must still hold and the convergence angle should be constrained as well. Occlusion becomes more likely with decreasing flying height and as the flying height to terrain height ration increases, particularly in complex terrain. Adding oblique imagery allows for occluded terrain to be imaged.

3) Variable AGL and variable angle photography acquisition

Beyond the simple approach described in (2), there are three variations generally employed. The simplest is to define a target and fly around and over it in an ad-hoc manner taking photographs at a fixed interval (e.g., 1 Hz). Eisenbeiss and Zhang (2006) used this approach with a helicopter UAV at low altitude. Harwin and Lucieer (2012b), Lucieer et al. (2011a), and Lucieer et al. (2013) used this approach with a multi-rotor UAV from 30-50 m. For oblique imagery, the camera angle can either be adjusted manually, set in the waypoint navigation instructions, or some modern UAVs offer target tracking features that will keep a point of interest in the field of view (FOV) (Mikrokopter, 2012). The set of photographs produced then needs to be carefully analysed to select a subset with sufficient overlap for SfM and MVS. *A priori* data are not needed as the point of interest can be chosen in the field or the operator can choose to fly a path based on their prior experience and a visual evaluation of the site to be mapped. Levels of redundancy need to be built into the design and the appropriate level of redundancy is dictated by the complexity of the terrain, the completeness requirements, and the stability of imaging system. This ensures enough in-focus images can be chosen that adequately frame the target object and meet image point distribution per frame and imaging network strength goals. The key disadvantage of an ad-hoc approach is that there is a high likelihood that a full set of photos will not be acquired in a single flight and the site may need to be re-flown to "fill in the gaps".

The second option is to extend the generic camera network and define a generic flight path that captures photographs on a viewing sphere, this is known as a hemispheric viewpoint plan (Fraser et al., 1995). The radius of this sphere can change to allow for FOV and resolution changes (Olague and Mohr, 2002). The camera stations (XYZ and orientation) are predefined and evenly distributed, and they are not dictated by *a priori*

data. This hemispherical coverage can ensure the object is seen from above and the side whilst ensuring there is sufficient overlap and that a given target point is captured in at least two (Schmid et al., 2012), but preferably three or four photos for SfM/MVS (Fraser, 1992; Mason, 1995a). This approach has the advantage that it is highly likely that a full set of overlapping imagery will be captured and, like a traditional photogrammetric flight plan, the predetermination of the theoretical expectation in terms of accuracy and resolution is a well-defined process. The control point layout can also remain essentially the same for each site. The disadvantage is that if a site contains complex features it is likely that a generic viewing sphere approach will not avoid occlusions and the resulting 3D model will most likely be incomplete. The position and pose accuracy are also a factor. The waypoint navigation capabilities of Micro-UAVs varies and whilst many offer navigation-grade GNSS/GPS positioning (to within 2–10 m) they may not have the ability to control the camera mount tilt via the waypoint navigation system. The position of the camera is programmable but the rotation parameters are not necessarily controllable/programmable during flight. In addition, inaccurate position negates the need for accurate camera angle and therefore specifying a flight plan with six-axis pose and position for each camera stations is potentially unnecessary. The rotation is strongly dependent on position when the captured view must meet overlap constraints. Ensuring there is appropriate redundancy may allow for the inaccuracy of the on-board navigation grade GNSS/GPS and IMU.

This leads to the third, and perhaps most robust, flight planning option for close-range (low altitude) UAV terrain mapping. In this option, the hemispheric viewpoint plan (VPP) consists of camera stations determined based on *a priori* terrain data (not necessarily evenly distributed) and chosen based on the constraint that every point on the target must be visible in at least three photos and fulfil incidence angle, occlusion and redundancy constraints (Mason, 1994; Mason, 1995b; Olague, 2000; Schmid et al., 2012). The camera network design problem or photogrammetric network design (PND) problem (Fraser, 1984) has been tackled in close-range photogrammetry and industrial metrology. A similar problem is also faced in robotics in the field of Simultaneous Localisation and Mapping (SLAM). A robot that is travelling through an unknown terrain or building must choose a path that provides its sensors with the views they need to fill in the gaps in its knowledge of its surroundings. The algorithms that tackle this choice are known as next best view (NBV) algorithms (Hoppe et al., 2012).

The optimal solution to the PND problem has been the focus of a number of previous research efforts. Camera networks defined by these algorithms can vary considerably due to the problem being complex. Chen and Davis (2000) suggests that finding the

absolute global optimum is not necessarily the goal, instead the subset of potential solutions should be derived in a way that allows evaluation and comparison. In Fraser (1984) it is suggested that the best approach to camera network design is a design by simulation strategy that follows the Graferand scheme. Mason (1995b) summarises this scheme as follows:

- Zero Order Design (ZOD): defining the measurement datum
- First Order Design (FOD): configuring the triangulation geometry (camera network geometry design)
- Second Order Design (SOD): measurement precision determination (weighting and observation precision)
- Third Order Design (TOD): network densification

Mason (1995a) suggests that these steps are interrelated and that competing considerations and constraints are not necessarily explicit. Expert knowledge is needed to evaluate the design as it progresses through the stages. Shortis and Hall (1989) suggests that considerations such as datum definition (ZOD) and achievable measurement precision (SOD) are essentially independent of network geometry design whilst being of fundamental importance to the resulting reliability and precision of the network adjustment. Densification (TOD) is usually not applicable for close-range applications (Shortis and Hall, 1989). The geometry of the network (FOD) is the step that will have greatest impact on the final result. Furthermore, Fraser et al. (1995) suggests that the network geometry design stage (FOD) must result in optimal network geometry and convergence angles. The quality of the *a priori* 3D model of the target will dictate initial camera positions and in turn the completeness of the model produced by the camera network. Mason (1995b) suggests that this is the most complex phase requiring decisions relating to the number of cameras and the pose of each camera. Olague and Mohr (2002) discusses the complexity of the problem in terms of the choice between infinite solutions and minimising the number of camera stations whilst maintaining accuracy requirements. The camera network geometry can vary but the accuracy may be the same in each design. There is no single solution and, as Olague (2000) also suggests, the design process is iterative and requires human input (expert knowledge) to evaluate the design criteria at each stage. This hindered early efforts to automate PND and a number of algorithms have been developed that attempt PND automation. Mason (1995b) and Mason (1995a) built on the work of Fraser (1984) to develop CONSENS, an expert systems approach

that uses observational redundancy to generate statistics for network diagnosis when assessing geometry strength and measurement precision for each iteration. Olague and Mohr (2002) built on earlier research (Olague and Mohr, 1997; Olague, 2000) to develop a system that uses an adaptive strategy to tackle the problem of global optimisation design to build on the expert systems approach using genetic algorithms and stochastic optimisation techniques.

Ahmadabadian et al. (2012) and Ahmadabadian et al. (2013) introduced Image Network Designer (IND), a method for image selection for SfM/MVS that seeks to minimise uncertainty and create a 3D model that is geometrically and colourmetrically correct. This method is based on selecting images from a set that has already been captured with high levels of redundancy. They compared their image selection approach to CMVS (Furukawa and Ponce, 2010) and found it performed better in terms of clustering and image selection for complex geometries (Ahmadabadian et al., 2012). They suggest CMVS fails to account for occlusion and range related constraints. Furthermore geometric accuracy cannot be guaranteed by CVMS since the 3D surface coordinate intersection angles are not considered (Ahmadabadian et al., 2012). The incidence angle must be balanced with the triangulation uncertainty which increases as the angle decreases whereas the ability to distinctly recognise a surface point is reduced as the camera approaches the horizon of the surrounding surface (Ahmadabadian et al., 2013).

UAV photogrammetry must tackle the PND problem, particularly when using multi-rotor UAVs that can be programmed to fly the shortest path around a hemispheric view point plan (Schmid et al., 2012; Hoppe et al., 2012). Cheng et al. (2008) approached PND as a UAV trajectory planning and time optimisation problem focussing on complete coverage with photographic acquisition rate set according to overlap and redundancy requirements. The resulting image set needs to have sufficient overlap for SfM whilst allowing for blurred images and camera failures. Saadat-Seresht et al. (2004) proposed an algorithm that uses a fuzzy logic reasoning strategy for camera placement in the absence of an *a priori* 3D model. Xu et al. (2011) used a variant of the Boustrophedon Cellular Decomposition (BCD) algorithm (Choset and Pignon, 1998) to determine optimal terrain coverage taking aircraft dynamics into account, however, they did not consider oblique photography and the PND problem. They focussed on developing a more traditional strip and block flight plan for their fixed-wing UAV. Hoppe et al. (2012) proposed an algorithm that builds on these previous approaches and SLAM. Their approach uses *a priori* knowledge to define a camera network for a UAV-MVS mission that ensures the whole object/target is covered whilst taking overlap and coincidence angles into account. Ahmadabadian et al. (2012) did not focus on UAVs, however, they

suggested that their approach reduces redundant viewpoints and that it can overcome some visibility constraints. The range related constraints were not considered when roughly estimating viewpoint to surface distance. Schmid et al. (2012) also suggested an algorithm for UAV-MVS that calculates a view hull and viewpoint plan for their multi-rotor UAV taking into account the same constraints (coverage, maximum angle of incidence and overlap) to develop a data acquisition system for outdoor scene reconstruction. Hirschmüller (2011) then used this algorithm for their flight planning. Schmid et al. (2012) and Hoppe et al. (2012) appear to be the first studies into view planning for UAV-MVS and both studies concluded that *a priori* data are needed to solve the PND problem. Schmid et al. (2012) incorporated steps in their process to generate an initial DSM used to calculate the network. The requirement for *a priori* knowledge of the structure in the viewpoint planning approach results in a "chicken and egg" problem (Hoppe et al., 2012), where the detail of that input model is crucial for a comprehensive plan to be derived.

The 3D complexity of the target object will dictate the quality of the *a priori* data required to ensure model completeness, however it is not always feasible to obtain high quality *a priori* data. In these situations generating a comprehensive 3D flight plan that includes detailed camera pose specifications may not be necessary, instead a camera network that follows traditional nadir flight planning principles augmented with a minimal number of oblique photos that focus on areas of 3D complexity may be sufficient to allow 3D reconstruction via UAV surveys planned in the field.

5.2.2 Study Site

A fine-scale change monitoring study is being undertaken along a sheltered estuarine coastline known as Pittwater Estuary (Figure 5.1), located in south eastern Tasmania, Australia. The 100 m section of coastline is vegetated with grasses along an erosion scarp with salt marsh at the southern end of the study site. For this study, a section of erosion scarp was chosen as the focus area to evaluate the impact of flight planning and GCP configuration decisions on the accuracy of derived UAV-MVS point clouds.

5.2.3 Hardware

The UAV used for this study is based on the OktoKopter electric multi-rotor micro-UAV platform (Mikrokopter, 2012) with a Droidworx eight rotor airframe. A ~2.5 kg

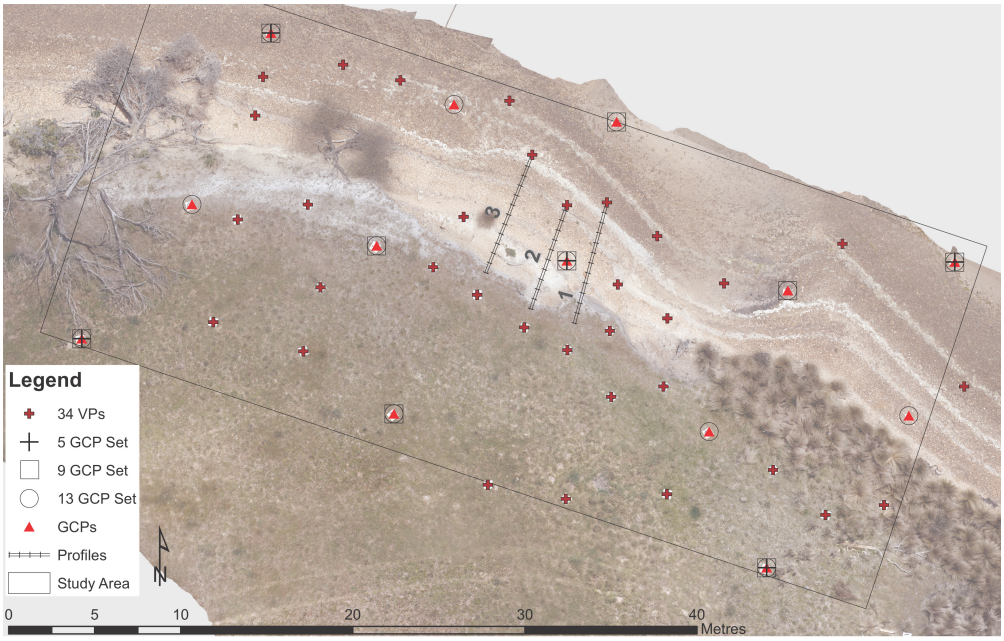

Figure 5.1: Map of study site showing GCP sets, VPs and profile locations

payload can be carried for approximately 8–10 minutes. Waypoint navigation is achieved via the on-board navigation grade GPS (5–10 m positional accuracy), IMU and other sensors. A stabilised camera mount, carrying a Canon 550D digital SLR camera with a 20 mm prime lens, allows camera tilt to be controlled by the remote pilot. This camera provides control over ISO, aperture and shutter speed settings and has a light weight camera body. Focus is fixed at infinity and the remaining settings are carefully chosen to reduce motion blur when images are acquired at 1 Hz (one photo per second, as described in Turner et al. (2014) and Harwin and Lucieer (2012b)). A Leica TS06 plus Total Station Theodolite was used to capture ground control using a precise survey (explained in Chapter 4).

5.2.4 UAV Survey

Flights for Pre-Calibration

Targets were randomly distributed in a 20 m radius with a number of targets placed on top of tripods setup at differing heights to provide depth of field. Three flights were flown to obtain convergent imagery of this 3D target field from a circular flight path. The camera was mounted in landscape orientation for the first flight. The roll angle of the camera was set to opposing portrait orientations in the second and third flight to ensure the targets were distributed throughout the frame of the camera (Figure 5.2).

The UAV was flown in a circle (with an approximate radius of 6 m) at an altitude of approximately 18 m (AGL). The camera angle was set at 65° for each flight. The UAV was orientated to point at the centre GCP target in the calibration field to ensure convergent photography.

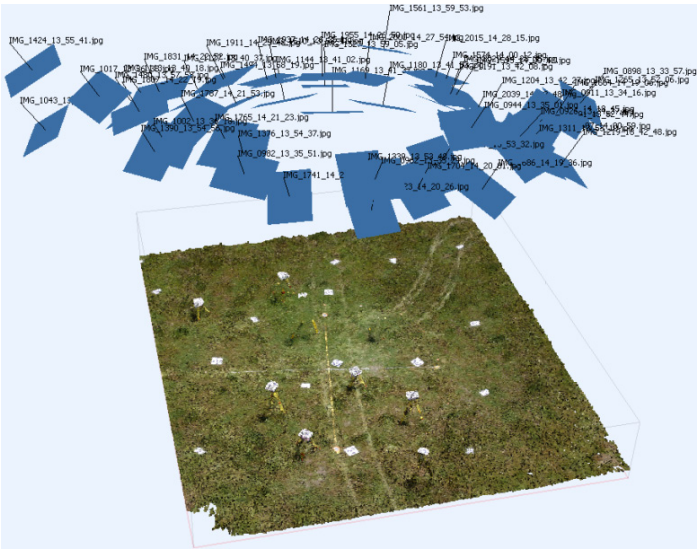

Figure 5.2: Calibration flight point cloud and camera network, a screenshot from PhotoScan showing the 50 convergent camera station locations and the 3D target array with some targets set up on tripods.

Camera Calibration

CalibCam[8] was used to pre-calibrate the camera rather than allowing the chosen 3D reconstruction software, PhotoScan[9], to do a self-calibration. Chapter 4 compared on-the-job self-calibration scenarios to a number of pre-calibration options. PhotoScan on-the-job self-calibration and CalibCam pre-calibration were both found to be accurate means of dealing with imperfections in the consumer grade camera used for photography. Pre-calibration fixes the calibration for all scenarios and this improves comparability. CalibCam's automatic and manual target centroiding tools were used to place control markers in each image on the visible coordinated GCPs in the calibration target field and the remaining uncoordinated targets (termed relative points in CalibCam). CalibCam target identification requires significant human input and 0.6 pixels was adopted as the image space measurement accuracy setting. Each X, Y, and Z coordinate was assigned a GCP standard deviation estimate of 2 mm based on the least squares net-

[8] 3DM CalibCam Version 2.2a © December 2006 ADAM Technology `http://www.adamtech.com.au/`

[9] Agisoft PhotoScan Professional Edition Version 1.0.4.1847 64 bit © 2014 Agisoft LLC `http://www.agisoft.com/`

work adjustment results from the total station survey described below (Section 5.2.6). The adjustment result had a variance factor of 1.01 (with 1686 degrees of freedom) and provided estimates of focal length, principal point coordinates, three radial distortion coefficients and two decentring distortion coefficients. Some conventions regarding calibration parameters in CalibCam differ from those used in PhotoScan, therefore the calibration parameters needed to be modified accordingly. The derived and modified camera model was entered into PhotoScan and fixed as constants in the adjustment.

Study Site Flights

For the coastal study site, a traditional nadir photogrammetric flight path was flown with the flying height above terrain maintained within a range 20 to 25 metres, and a forward overlap of 80%. Two nadir flights were flown immediately after the calibration flights. An additional three flight lines were flown with the camera tilted between 10° and 40° from nadir so that a set of 80% overlap oblique images of the erosion scarp in the focus area could be captured. The 60% overlap image set was extracted from the larger 80% overlap set. The flight dynamics of the aircraft do not allow strict adherence to the flight plan, however the aircraft usually stays within ~2–3 m for the planned path.

5.2.5 Ground Control and Validation Point Distribution

This study and Chapter 4 share the same ground control. As in Chapter 4, of the 47 targets distributed throughout the study area (Figure 5.1) thirteen were used as GCPs and 34 as VPs. Six of these points were also at or near the termination points of three profiles.

GCP Distribution Scenarios

5.2.6 Precise Total Station Survey and Profile Survey

As in Chapter 4, a network of stations and radiation points were measured with a total station 3–4 times using a 30 cm prism pole. Each of the profile termination points was used as a station during the survey and the reflectorless EDM was used to survey profiles between these carefully chosen points. Each profile was measured at least twice from its two termination point stations to avoid any gross errors and ensure a dense coverage of points along each profile line. The final coordinates were determined through a least

squares network adjustment using LISCAD[10] and this resulted in a variance factor of 0.98 with 957 degrees of freedom. The precision achieved for GCP and VP positions was $\sigma_X = 1$ mm, $\sigma_Y = 1.4$ mm and $\sigma_Z = 1.1$ mm. The ground control was accurate to between 1–2 mm. A GCP and VP 3D precision of $\sigma_{XYZ} = 0$ mm was adopted for subsequent calibration and model generation steps as recommended in the PhotoScan documentation when control is very accurate[11]. For the purposes of the experiment the control error is treated as insignificant. The survey control is at a level of precision that we can assume has no significant contribution to the error propagation in the photogrammetry. This choice aligns with the suggested PhotoScan marker accuracy setting (as discussed in Chapter 4).

5.2.7 Degradation of Precise Total Station GCPs to Typical DGPS Accuracy

The accuracy of differential GNSS/DGPS survey measurement is dependent on a number of factors including baseline length and satellite geometry. These influences are difficult to quantify for each measurement and it was considered more appropriate to test the impact of surveying the GCPs using DGPS by degrading precise positions using random values from a Gaussian distribution to introduce an error equivalent to typical differential GNSS/DGPS. This ensures that the standard deviation is known. As described in Chapter 4, the GCPs were degraded to $\sigma_{XYZ} = 22$ mm by applying a standard deviation constrained random error.

5.2.8 Scenarios

A total of 20 scenarios were tested. The following design variables were varied for the investigation: the number of GCPs, accuracy of GCPs, percentage overlap and the inclusion or exclusion of the oblique photography. Table 5.1 lists those scenarios and assigns each scenario a code based on the variable settings of each.

5.2.9 GCP Accuracy (GCP σ)

PhotoScan "Marker Accuracy" GCP accuracy settings were set at $\sigma_{XYZ} = 0$ mm for the precise survey scenarios as described in Chapter 4. Similarly, $\sigma_{XYZ} = 22$ mm was

[10] LISCAD Version 10 `http://www.LISCAD.com`
[11] Under Optimization at `http://www.agisoft.ru/wiki/PhotoScan/Tips_and_Tricks`

Table 5.1: Scenarios tested and codes assigned based on GCP count, GCP σ, overlap percentage and whether the oblique imagery set was included.

Scenario Code	GCP Count <N>	GCP σ <mm>	Overlap <%>	Oblique (Yes/No)
<N>GCP0mm80NoObl *(e.g., "5GCP0mm80NoObl")*	5, 9, 13	0	80	No
<N>GCP0mm80Obl	5, 9, 13	0	80	Yes
<N>GCP22mm80NoObl	5, 9, 13	22	80	No
<N>GCP22mm80Obl	5, 9, 13	22	80	Yes
13GCP0mm<%>NoObl *(e.g., "13GCP0mm60NoObl")*	13	0	60, 80	No
13GCP0mm<%>Obl	13	0	60, 80	Yes
13GCP22mm<%>NoObl	13	22	60, 80	No
13GCP22mm<%>Obl	13	22	60, 80	Yes

set for the differential GNSS/DGPS equivalent scenarios.

5.2.10 GCP Density (GCP Count)

As shown in Figure 5.1, three GCP sets were chosen. The first set could be considered a standard distribution of 13 GCPs, 9 around the periphery of the study area and 4 through the middle. The second set (not used in Chapter 4) is an example of an intermediate distribution of control, 6 around the periphery and 3 through the middle. The third set is an example of the sparsest GCP distribution that would be operationally acceptable, a GCP in each corner of the study area and one in the middle.

5.2.11 Overlap

The simulations were run using both design camera networks and the actual camera networks at 60% and 80% overlap (Figure 5.3 and Figure 5.4). In each case there was an associated oblique camera network that was either included or excluded. Figure 5.5 shows those networks in 3D to show camera pose. A 60% forward overlap and 30% overlap was also attempted but the result was unusable due to large portions of insufficient point matches.

5.2.12 Inclusion/Exclusion of Oblique Photography

As described in Chapter 4, the site was flown with nadir and oblique photography at an AGL flying height of approximately 20–25 m. The additional oblique photography was captured with the camera angled between 45° and 65° oriented to face the erosion

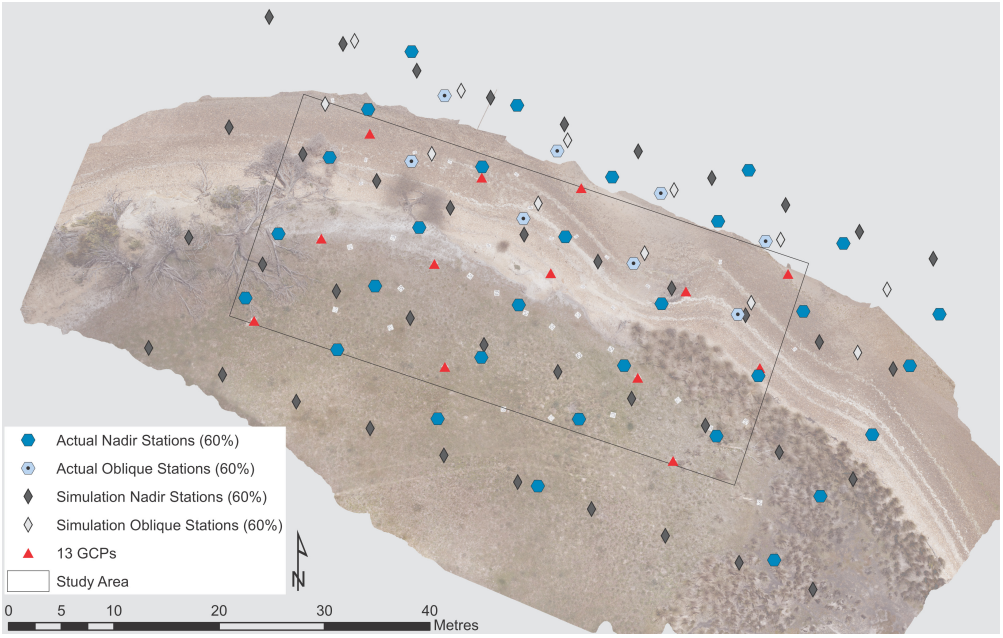

Figure 5.3: 60% overlap camera networks.

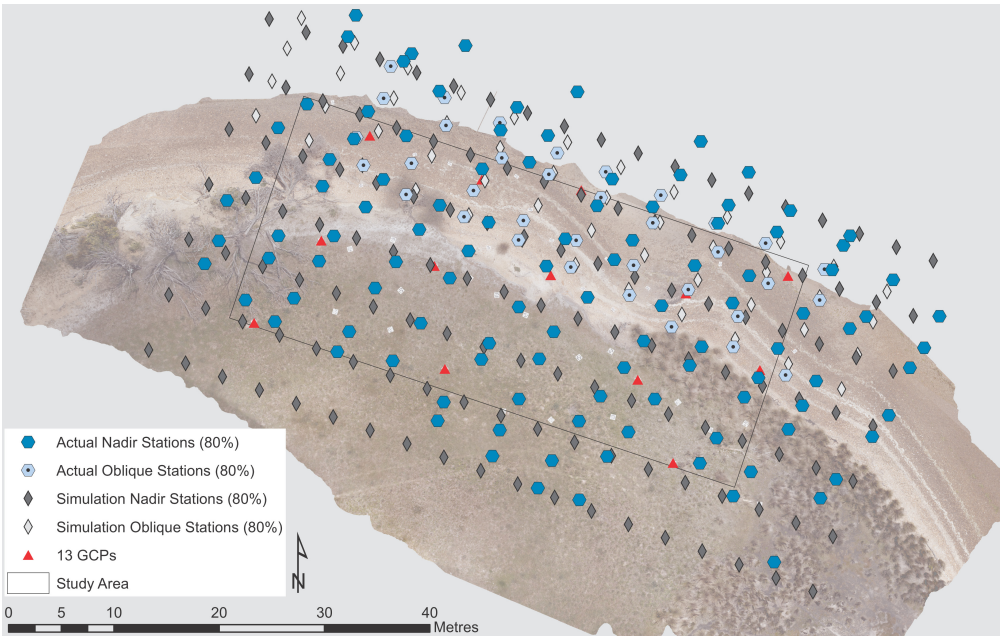

Figure 5.4: 80% overlap camera networks.

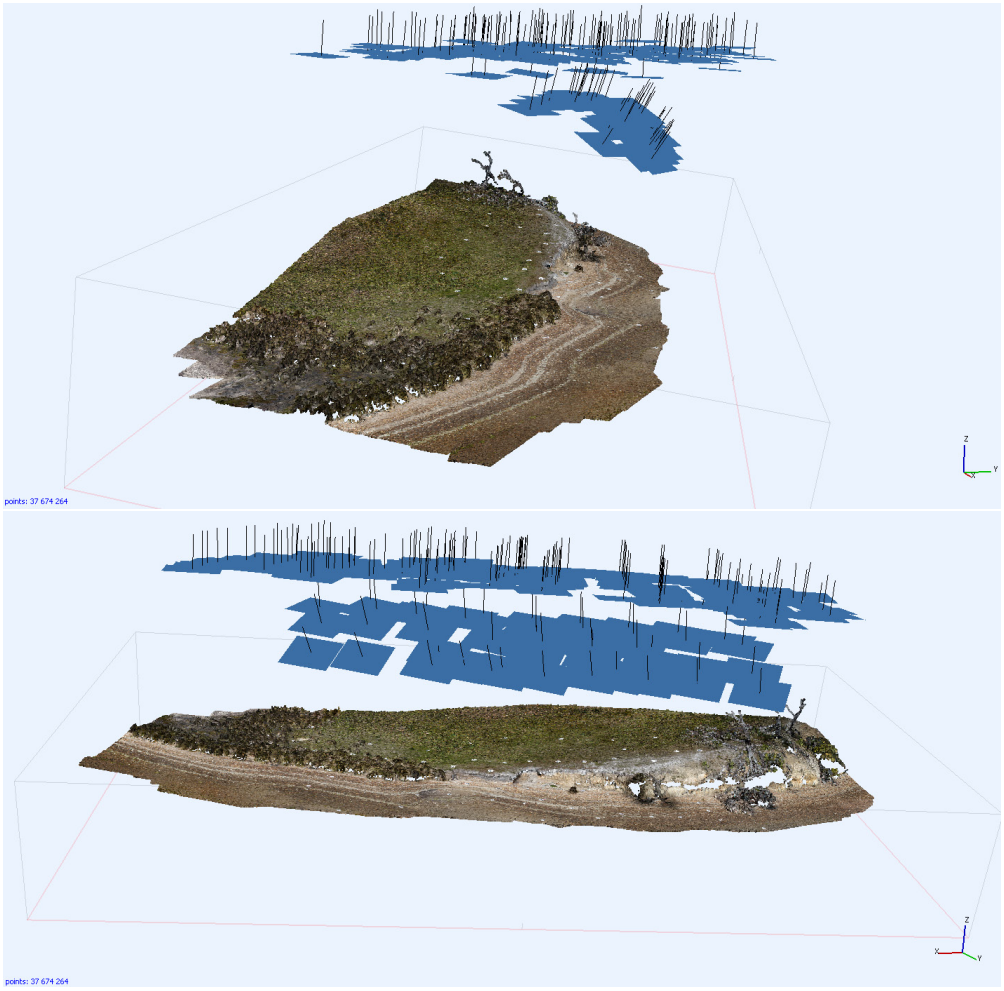

Figure 5.5: Screenshots from PhotoScan showing the camera networks.

scarp. These oblique images were included/excluded from the scenarios to assess their impact on the accuracy of the derived model.

5.2.13 PhotoScan Workflow

The scenarios were all based on the same PhotoScan base project as described in Chapter 4. This base project was then used to set up the 20 projects as follows:

a) the camera calibration settings were left unfixed for the self-calibration;

b) all the photo positions were deactivated/unchecked as ground control and the markers corresponding to each GCPs set were activated/checked (none of the VPs were activated);

c) the photos associated with each overlap percentage were enabled/disabled;

d) the marker coordinates were altered for the DGPS equivalent scenarios;

e) the "Marker Accuracy" setting was set to either 0 mm or 22 mm; and

f) the oblique images were turned off for the scenarios with that image set excluded.

The dense point cloud that was derived in each project was used to create a LAS file. In addition, the position and estimated error information generated by PhotoScan for each marker associated with a VP was exported. The exported error information was then used for:

- the generation of boxplots;
- the generation of maps of the spatial distribution of vertical error;
- simulation verification; and
- overall accuracy assessment.

5.2.14 Simulations versus UAV survey point cloud

When running the simulations, 0.6 pixel image measurement precision (2.6 microns) was chosen and the minimum number of rays per target was set to 2. The camera

was assumed perfect and therefore camera calibration parameters were fixed in the network adjustment simulation. The design and the actual flight paths were used in the simulations. A 50,000 point triangulated mesh was generated and imported into VMS to ensure the terrain complexity influenced the simulation results realistically. The terrain was subsampled to generate a set of over 5000 example target points distributed across the study area with a higher density of random points along the face of the erosion scarp. The VPs were included in this set along with the GCPs (set as control as dictated by each scenario). In order to verify that simulations provide a representative estimation of model accuracy, the standard deviations (1σ) for verification point positions derived in the simulations (in VMS) were compared to the output statistics from PhotoScan models.

5.2.15 Accuracy assessment using verification points

The method used to assess the accuracy of the derived models in comparison to the total station survey is to report the difference between the precisely surveyed VPs and their identified location in the derived point cloud, as described in Chapter 4. For each scenario a set of metrics for assessing accuracy in X, Y, Z, XY and XYZ were derived (RMSE, mean, median, standard deviation, minimum and maximum).

5.2.16 Profile point set comparison

To assess how the shape of terrain impacts point cloud density and accuracy LASTools[12] was used to extract 1 cm wide profile strips from the UAV survey point clouds for comparison with the total station profiles and the profiles from the simulation target point set. The target point set profiles were extracted from UAV survey point clouds and incorporated into the simulation target dataset.

The total station survey profiles were captured in runs starting at one end of the line and taking reflectorless distance measurements and angle readings every few centimetres. This was done from both ends of each profile at least twice per profile. The result is an unordered set of randomly spaced 3D points following the terrain. Similarly, the 3D points extracted from the UAV-MVS point cloud are unordered and non-uniformly spaced. In addition, the point density in the UAV-MVS point cloud varies along the line with some section have a wider vertical distribution (i.e., the cloud is "fatter").

[12] `http://rapidlasso.com/lastools/` © 2007–2015, rapidlasso GmbH, Germany

Point-to-point difference is one way to compare these datasets, and works by measuring the separation between a point in the reference set (the survey profile) and its nearest neighbour in the comparison set (the UAV-MVS point cloud profile or the simulation target point set profile). Point-to-point differencing does not provide information about the comparison points other than the nearest neighbour. The goal of comparing the UAV-MVS profile with the surveyed profile is to calculate density and difference statistics and the nearest neighbour approach will not achieve that. Another problem with this approach is randomness of the point distribution along the terrain. The distance information will be stored at each point and therefore it will be difficult to extract a more general picture of how the distances vary along the terrain. The solution is to generate a generalised version of the survey profile data in the form of an interpolated polyline that represents the profile point set and closely approximates the measured terrain. Creating a polyline is not simply a matter of 'joining the dots' because the profile points are unordered along the profile. The first step required is to order the point set and then to derive a polyline through those ordered points. This polyline can then be used for comparison and statistic derivation based on equal length segments. The outputs include point density, simulation accuracy estimates, and difference metrics describing the separation between the total station profile and the extracted scenario profile or simulation target point set profile.

To sort the points, first the point with the minimum northing was determined and this point is the seed. The nearest neighbour to the seed is the second point. The seed point is removed from the set and the nearest neighbour to the second point is the third point. The second point is removed from the set and the algorithm repeats this as it iterates along the point set to the end. The search radius for the nearest neighbour (NN) is chosen to avoid missing complex terrain shapes during sorting by bridging gaps instead of following the densest portion of the set. In this study, the chosen sort NN search radius was 5 cm.

Once sorted a similar algorithm iterates forwards through the sorted set taking the median of a set of points within a specified radius forward of a search point. In this way a line is created that follows the medians of point subsets contained in the semi-circular search area along the profile. The size of the NN search radius dictates the amount of "smoothing" and must be chosen to match the variability of the data. If the NN search radius is too large there is a higher risk that complexity will be missed, if the search radius is too small then the complexity may dominate the shape of the line and the polyline may become too complex. As above, the smoothing NN search radius was 5 cm.

The total station survey profile polyline was the basis for comparison and the algorithm that performs that comparison is driven by the comparison search radius. This defines the search area in a semi-circle (in two dimensions, Y and Z in this case) from a comparison search point, the first of which is the beginning of the polyline and the next is the comparison search radius along the line. The radius then defines the resulting segment lengths along the line. By moving the search semi-circle along the line a segment length at a time, the comparison algorithm counts how many points in the comparison dataset (the PhotoScan profile point set) are within that search distance and derives the metrics that describe the distances to the points in that subset (RMSE, mean, median, standard deviation, minimum and maximum). The size of the search radius/segment length must be appropriate for the smoothness/roughness of the survey profile line and the distance was chosen so that in the majority of searches at least five points were in a search radius subset. For the UAV survey the search radius was chosen to be 10 cm as this provided statistics per segments based on 5–20 points. It should be noted that the line segments in each search are polylines with vertices where the segment follows the terrain curvature, i.e., they are not straight line segments. For plotting purposes after the statistics are generated, the line segments used to bin the data are flattened to a two vertex line.

5.3 Results and Discussion

5.3.1 Simulations versus UAV survey point cloud

Simulations of both design and actual flight paths were compared to assessed accuracy of the UAV-MVS point cloud. These simulations produced very similar estimates of achievable precision, indicating that the capacity to deliver an accurate model does not depend greatly on precise positioning of the UAV.

Overlap

Two overlap scenarios were tested against GCP accuracy and oblique imagery inclusion. Table 5.2, Table 5.3 and Table 5.4 present the summary statistics derived from the comparison between surveyed verification point coordinates and verification point locations in the UAV-MVS point cloud for each scenario.

When comparing the results from Table 5.2, Table 5.3 and Table 5.4, a reduction in

Table 5.2: Simulation results for design flight paths, 80% and 60% overlap , and $\sigma = 0$ mm and $\sigma = 22$ mm scenarios (Note: The 60% overlap oblique scenarios failed to simulate).

Scenario	σ_{XYZ} (mm)	σ_{XYZ} (mm)	σ_Z (mm)	Scenario	σ_{XYZ} (mm)	σ_{XY} (mm)	σ_Z (mm)
13GCP0mm80NoObl	0.33	0.21	0.56	13GCP22mm80NoObl	9.31	8.92	10.10
13GCP0mm80Obl	0.23	0.16	0.39	13GCP22mm80Obl	9.34	8.95	10.12
13GCP0mm60NoObl	0.61	0.37	1.08	13GCP22mm60NoObl	9.30	8.88	10.16
13GCP0mm60Obl	–	–	–	13GCP22mm60Obl	–	–	–

Table 5.3: Simulation results for actual flight paths, 80% and 60% overlap, and $\sigma = 0$ mm and $\sigma = 22$ mm scenarios.

Scenario	σ_{XYZ} (mm)	σ_{XYZ} (mm)	σ_Z (mm)	Scenario	σ_{XYZ} (mm)	σ_{XY} (mm)	σ_Z (mm)
13GCP0mm80NoObl	0.36	0.23	0.63	13GCP22mm80NoObl	9.06	8.66	9.88
13GCP0mm80Obl	0.26	0.18	0.43	13GCP22mm80Obl	8.79	8.39	9.59
13GCP0mm60NoObl	0.67	0.42	1.18	13GCP22mm60NoObl	9.29	8.87	10.14
13GCP0mm60Obl	0.52	0.35	0.85	13GCP22mm60Obl	8.97	8.57	9.77

overlap percentage produced less accurate models in all cases (better accuracy for 80% versus 60% overlap scenarios). Vertical accuracy was lower than horizontal accuracy in almost all cases. In assessing the impact of oblique imagery the results indicate that including oblique imagery improved precision in the 0 mm scenarios (and this was also seen when we tested for 2 mm GCP accuracy, discussed below). When the GCP precision was modelled as 22 mm in the simulation, the inclusion of oblique imagery did not improve the estimated precision of the solution. However, there is evidence in the empirical tests that precision did improve. These results, combined, indicate that the inclusion of oblique imagery can be expected to improve precision in UAV photogrammetry.

When the GCP precision was 22 mm, the precision achieved in the empirical tests was consistent with the prediction from the simulation. When the GCP precision was 0 mm, the precision achieved in the empirical test was significantly poorer than predicted by the simulation. The image measurement precision setting of 0.6 pixels that was used in the simulation is reasonable and not considered overly optimistic. The variance factors from the simulations and the 22 mm predictions are consistent with this assumption, and so the differences between simulation and empirical precision is not expected to be

Table 5.4: UAV survey results for actual flight paths, 80% and 60% overlap, and $\sigma = 0$ mm and $\sigma = 22$ mm scenarios.

Scenario	σ_{XYZ} (mm)	σ_{XYZ} (mm)	σ_Z (mm)	Scenario	σ_{XYZ} (mm)	σ_{XY} (mm)	σ_Z (mm)
13GCP0mm80NoObl	4.45	3.63	5.62	13GCP22mm80NoObl	10.21	9.06	11.67
13GCP0mm80Obl	4.42	3.56	5.63	13GCP22mm80Obl	10.25	8.97	11.81
13GCP0mm60NoObl	4.47	3.61	5.68	13GCP22mm60NoObl	10.34	9.16	11.75
13GCP0mm60Obl	4.43	3.55	5.66	13GCP22mm60Obl	10.40	9.15	11.91

due to inappropriately high estimates of image measurement precision. This points to the possibility that the residuals seen in the empirical work that employed very high precision ground control are an artefact of systematic errors rather than random errors.

To ensure that these findings were not peculiar to the decision to fix the control precision at 0 mm, a separate set of simulations was run with the precision set to 2 mm (the other end of the estimated error range for the total station GCP survey). The results of that simulation showed a very slight increase in predicted errors (σ_{XYZ} = ~0.9 mm for both the design and the actual flight paths), but not significant.

A likely explanation of this observation is that, when the precision of the ground control is very high, the errors in the model become dominated by those attributable to residual errors in the camera calibration. This suggests that a simulation of achievable accuracy based on distribution and precision of ground control is not reliable when the GCPs are coordinated with very high precision.

As a result, the empirical UAV survey results (Table 5.4) are assumed indicative of the achievable accuracy when using precise control (0 mm), < 4 mm in XY and < 6 mm in Z. There was little difference between the 80%/60% and oblique/no oblique scenarios (10–100 microns). When control was less accurate (22 mm), the accuracy was approximately 9 mm in XY and < 12 mm in Z, which was close to double the accuracy seen in the 0 mm scenarios. The simulated precision estimates (Table 5.2 and Table 5.3) are within 10% of the assessed UAV-MVS model accuracy (Table 5.4).

GCP Density

Three GCP density scenarios (5, 9 and 13 GCPs) were tested against GCP precision and inclusion of oblique imagery. The statistics in Table 5.5, Table 5.6 and Table 5.7 compare GCP density.

Table 5.5: Simulation results for design flight paths, 80% overlap, 13, 9 and 5 GCP and σ = 0 mm and σ = 22 mm scenarios.

Scenario	σ_{XYZ} (mm)	σ_{XYZ} (mm)	σ_Z (mm)	Scenario	σ_{XYZ} (mm)	σ_{XY} (mm)	σ_Z (mm)
13GCP0mm80NoObl	0.33	0.21	0.56	13GCP22mm80NoObl	9.31	8.92	10.10
13GCP0mm80Obl	0.23	0.16	0.39	13GCP22mm80Obl	9.34	8.95	10.12
9GCP0mm80NoObl	0.34	0.22	0.57	9GCP22mm80NoObl	11.73	11.28	12.63
9GCP0mm80Obl	0.25	0.17	0.41	9GCP22mm80Obl	11.77	11.32	12.67
5GCP0mm80NoObl	0.34	0.22	0.58	5GCP22mm80NoObl	13.68	13.20	14.66
5GCP0mm80Obl	0.25	0.17	0.42	5GCP22mm80Obl	13.72	13.23	14.69

Table 5.6: Simulation results for actual flight paths, 80% overlap, 13, 9 and 5 GCP and σ = 0 mm and σ = 22 mm scenarios.

Scenario	σ_{XYZ} (mm)	σ_{XYZ} (mm)	σ_Z (mm)	Scenario	σ_{XYZ} (mm)	σ_{XY} (mm)	σ_Z (mm)
13GCP0mm80NoObl	0.36	0.23	0.63	13GCP22mm80NoObl	9.06	8.66	9.88
13GCP0mm80Obl	0.26	0.18	0.43	13GCP22mm80Obl	8.79	8.39	9.59
9GCP0mm80NoObl	0.36	0.23	0.62	9GCP22mm80NoObl	11.21	10.74	12.16
9GCP0mm80Obl	0.27	0.19	0.45	9GCP22mm80Obl	10.71	10.24	11.65
5GCP0mm80NoObl	0.38	0.24	0.65	5GCP22mm80NoObl	12.73	12.22	13.75
5GCP0mm80Obl	0.29	0.20	0.47	5GCP22mm80Obl	12.73	12.23	13.74

Table 5.7: UAV survey results for actual flight paths, 80% overlap, 13, 9 and 5 GCP and σ = 0 mm and σ = 22 mm scenarios.

Scenario	σ_{XYZ} (mm)	σ_{XYZ} (mm)	σ_Z (mm)	Scenario	σ_{XYZ} (mm)	σ_{XY} (mm)	σ_Z (mm)
13GCP0mm80NoObl	4.45	3.63	5.62	13GCP22mm80NoObl	10.21	9.06	11.67
13GCP0mm80Obl	4.42	3.56	5.63	13GCP22mm80Obl	10.25	8.97	11.81
9GCP0mm80NoObl	4.49	3.63	5.81	9GCP22mm80NoObl	10.67	9.37	12.76
9GCP0mm80Obl	4.39	3.51	5.74	9GCP22mm80Obl	10.72	9.20	13.02
5GCP0mm80NoObl	5.77	5.73	5.84	5GCP22mm80NoObl	13.46	8.31	17.22
5GCP0mm80Obl	5.57	5.41	5.86	5GCP22mm80Obl	13.55	8.18	17.42

As in the overlap assessment, fixing the control (0 mm GCP precision) in the simulations resulted in an overestimation of achievable precision. The simulations were re-run with 2 mm GCP precision and, as expected, the precision decreased marginally but the overestimation was still occurring (for 13 GCPs: σ_{XYZ} = ~0.9 mm; for 9 GCPs: σ_{XYZ} = ~1.0–1.1 mm; and for 5 GCPs σ_{XYZ} = ~1.2 mm for both the design and the actual flight paths). The empirical results from the UAV-MVS survey show that when the control was very precise and fixed in PhotoScan the GCP density had little impact on model accuracy. There was less than 0.2 mm separating the 13 GCP results from the 5 GCP results.

Similar to the results in the overlap assessment, the 22 mm GCP precision results showed good agreement between the simulation and UAV-MVS survey. The estimates of precision derived from the simulation were within 10–20% of the empirical results. There was a significant reduction in horizontal and vertical accuracy for simulated and empirical results as GCP density decreases. Interestingly, the 5 GCP 22 mm scenarios outperformed the 9 GCP 22 mm scenarios horizontally but were much less accurate vertically. Overall, these summary statistics indicate that increasing the number of GCPs improved results. As expected, 13 GCPs resulted in the most accurate model and including oblique imagery marginally improved model accuracy.

Spatial distribution of simulated vertical precision

The verification points used to generate the statistics in the previous two sections were well-placed to ensure minimal occlusion. To more thoroughly assess the impact of overlap and inclusion of oblique imagery, the spatial distribution of simulated vertical precision was investigated. The following 3D views show the estimated achievable precision across the study area represented by the 5000+ sub-sampled target points included in the simulation (Figure 5.6, Figure 5.7, Figure 5.8, Figure 5.9, Figure 5.10, Figure 5.11 and Figure 5.12). These points are colour coded according to their vertical precision estimation as this is the least accurate dimension. Blue points could not be resolved due to occlusion from the terrain.

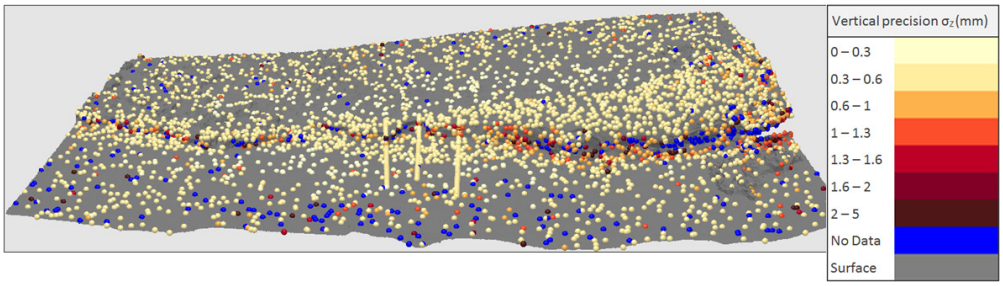

Figure 5.6: Simulated vertical precision for design 80% overlap, 13 GCP, no oblique (13GCP0mm80NoObl).

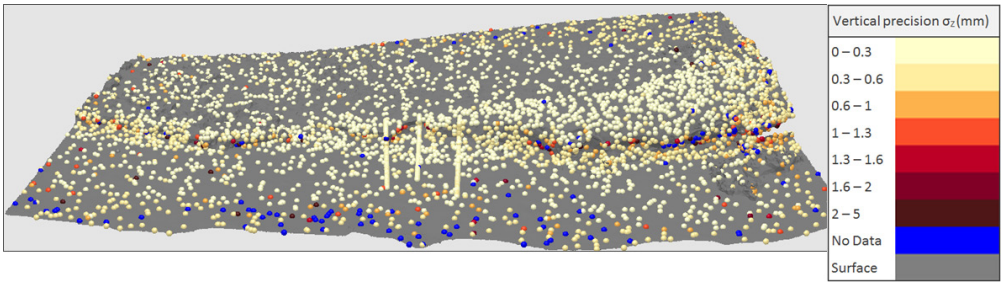

Figure 5.7: Simulated vertical precision for design 80%, 13 GCP, with oblique (13GCP0mm80Obl).

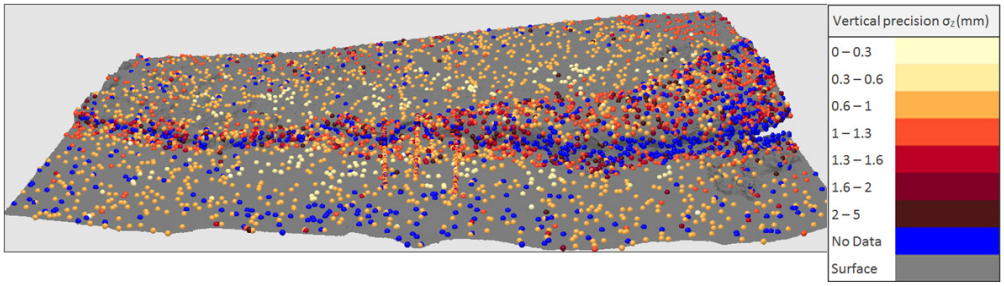

Figure 5.8: Simulated vertical precision for design 60%, 13 GCP, no oblique (13GCP0mm60NoObl).

The portions of the terrain along the erosion scarp were more prone to occlusion and

had lower precision due to fewer matches in the imagery. When oblique imagery was included there were few occlusions along the scarp and precision improved. The 60% overlap without oblique imagery scenario was noticeably less precise than the other scenarios.

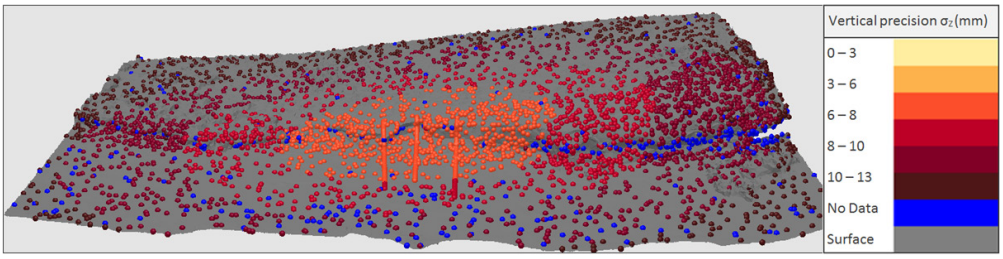

Figure 5.9: Simulated actual 80%, 13 GCP, no oblique (13GCP22mm80NoObl).

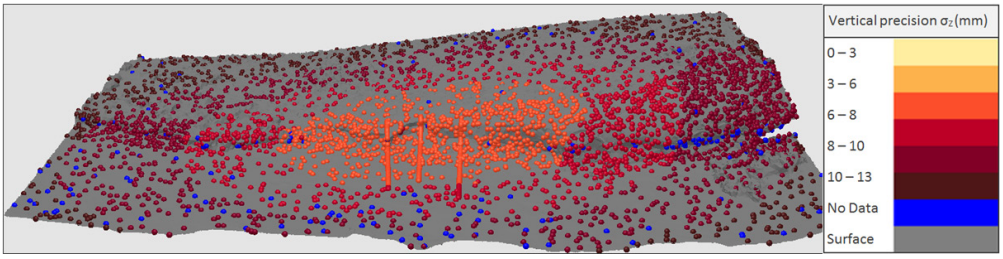

Figure 5.10: Simulated actual 80%, 13 GCP, with oblique (13GCP22mm80Obl).

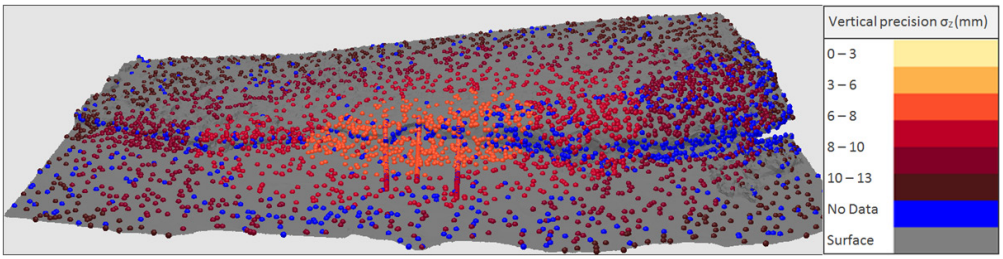

Figure 5.11: Simulated actual 60%, 13 GCP, no oblique (13GCP22mm60NoObl).

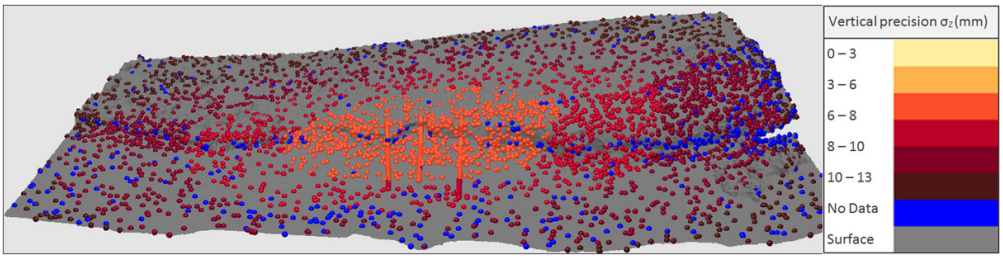

Figure 5.12: Simulated actual 60%, 13 GCP, with oblique (13GCP22mm60Obl).

Reducing the GCP precision had significant impact on estimated achievable precision (Figure 5.9, Figure 5.10, Figure 5.11 and Figure 5.12). In all cases there was a marked decrease in precision, radiating out from the centre of the study area, and with 6–8 mm estimated precision in the centre and as low as 20 mm on the periphery. The precision reduces as the number of photos for each point decreases. There were only a few occluded

points along the scarp in the 80% overlap cases (Figure 5.9 and Figure 5.10) and, as expected, fewer occluded points occurred when oblique image was added (Figure 5.9 and Figure 5.12). Reducing the overlap to 60% increased the number of occluded points.

Simulation shows that when using normal operational GCP precision (22 mm) there was potential for a decrease in precision radially from the centre of the study area, but only in the order of millimetres. This leads to a design guideline recommending to extend the photogrammetric block beyond the area of interest by a buffer of 20–30% the size of the focus area to minimise some of those effects.

Profile analysis comparing simulation results to the UAV-MVS and total station profile comparison

The following profile analysis focusses on the correspondence (or lack thereof) between the estimated achievable precision from the simulations and the assessed accuracy from the comparison between the UAV-MVS survey and total station profile survey. Profile 2 was chosen as it maps a section of the scarp that has a range of terrain characteristics. Along each profile line a set of target points were extracted from the UAV-MVS model and included in the target dataset in the simulation. The mean precision was calculated for 10 cm segments. For comparison with empirical results, profiles extracted from the UAV-MVS model were compared to the total station survey profiles by generating mean differences between the points and 10 cm survey profile segments interpolated from the profile survey points. The mean distance metric for each segment was defined by the mean of the set of distances between the points nearest the segment and the survey profile segment. To aid in the interpretation of these profiles and the density profile analysis photos of key features have been included in Figure 5.13.

Figure 5.14 shows the overestimation of achievable precision from the simulations with the 0 mm GCP accuracy setting. The UAV-MVS survey model comparison in the second profile shows the empirical accuracy for the profile segments. Figure 5.17 shows the achievable precision estimation from the simulations with the 22 mm GCP accuracy setting. In this case the estimation was uniform along the length of the profile whereas the UAV-MVS survey model comparison in the second profile showed higher accuracy along most of the profile. The least accurate portions of the UAV-MVS survey results had similar magnitude to the precision estimates from the simulations. The UAV-MVS survey model comparison in Figure 5.14 and Figure 5.17 showed an increased average distance between the UAV-MVS points and the survey profile. This occurred as a result of the complexity of the rubble at the base of the eroding bank (Figure 5.13(f)) and the cracks at the top of the fresh collapse (Figure 5.13(d)).

All profiles in Figure 5.15, Figure 5.16, Figure 5.17 and Figure 5.18 show very similar trends. Once again, simulation results showed very little variation in precision along the profile and the least accurate portions of the UAV-MVS survey matched the achievable precision from the simulations. The least accurate portions of the UAV-MVS survey profile were at the top of the cliff and in overhangs (Figure 5.13(e)) or cracks (Figure 5.13(d)).

The summary statistics in Tables 5.2–5.7 do not provide information on the spatial distribution of UAV-MVS and simulated achievable precision. Errors in areas of lower UAV-MVS accuracy dominated the summary statistics. The profiles for the 22 mm GCP accuracy UAV-MVS survey (Figures 5.15–5.18) had a realistic worst-case simulated achievable precision and the majority of the profile had better accuracy than the simulation predicted. This was not discernible when looking at summary statistics alone. This profile analysis has provided insight into issues with the simulations that relate to overestimation and uniform precision estimation. The accuracy achieved in the UAV-MVS surveys was not uniform across the profiles. The poorer performing areas illustrate the kinds of terrain that impact on achievable accuracy (and are shown in the photos (Figure 5.13)).

The assessment of simulation as a tool for estimating achievable precision has provided insight into the impact of camera network design, camera distortion estimation, GCP survey accuracy and terrain characteristics.

Figure 5.13: Photos of the site illustrating key terrain features. (a) an overview of the erosion scarp (March, 2012), the shorter staff is 1 metre long and the longer staff is 2 metres long; (b) a view from the top of the scarp overlooking the grass clumps at the top of the scarp and a collapse; (c) an alternate view of the collapse showing the cracked scarp face, sporadic vegetation edge and the rubble at the base of the scarp; (d) a close-up of the rubble at the base of the collapse; (e) the scarp edge showing overhangs, the vegetation edge and the remnants of a previous collapse; (f) one of the many cracks in the scarp, this one is vertical and starts low on the scarp, other cracks exist in amongst the grass back from the scarp edge.

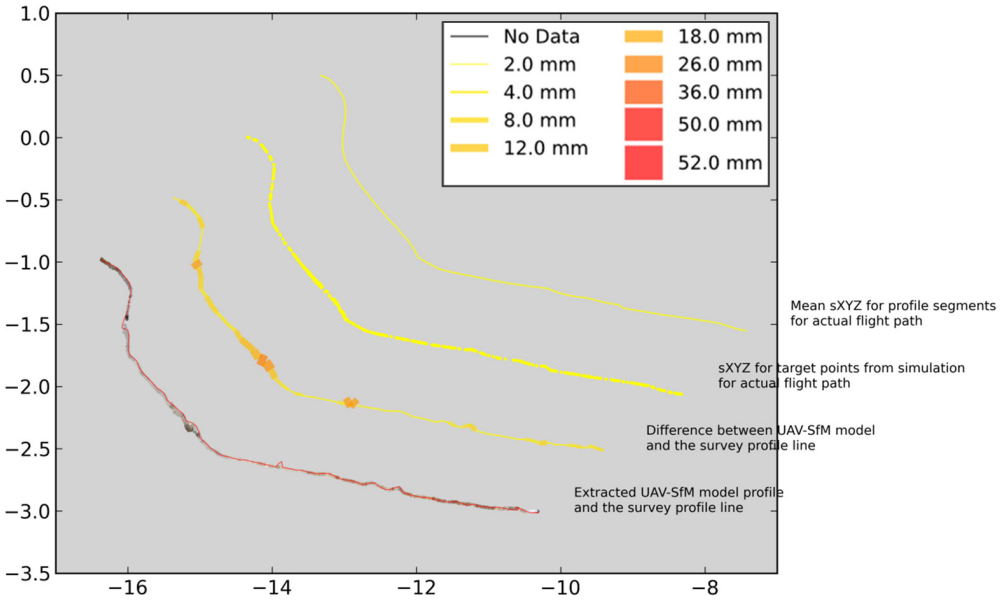

Figure 5.14: Four profile lines of Profile 2 comparing survey data (UAV-MVS profile points overlayed on the survey profile line), the mean distance between the UAV-MVS profile points and the survey line and estimated achievable precision for the actual flight path simulation plotted as points and as mean precision line segments (13GCP0mm80Obl) (axes units are metres).

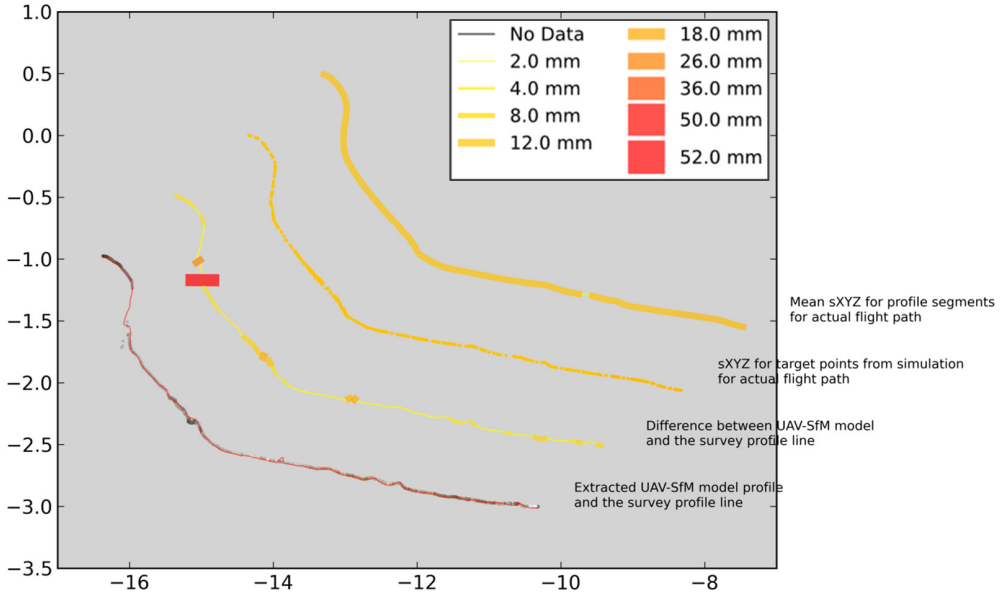

Figure 5.15: Four profile lines of Profile 2 comparing survey data (UAV-MVS profile points overlayed on the survey profile line), the mean distance between the UAV-MVS profile points and the survey line and estimated achievable precision for the actual flight path simulation plotted as points and as mean precision line segments (13GCP22mm80NoObl) (axes units are metres).

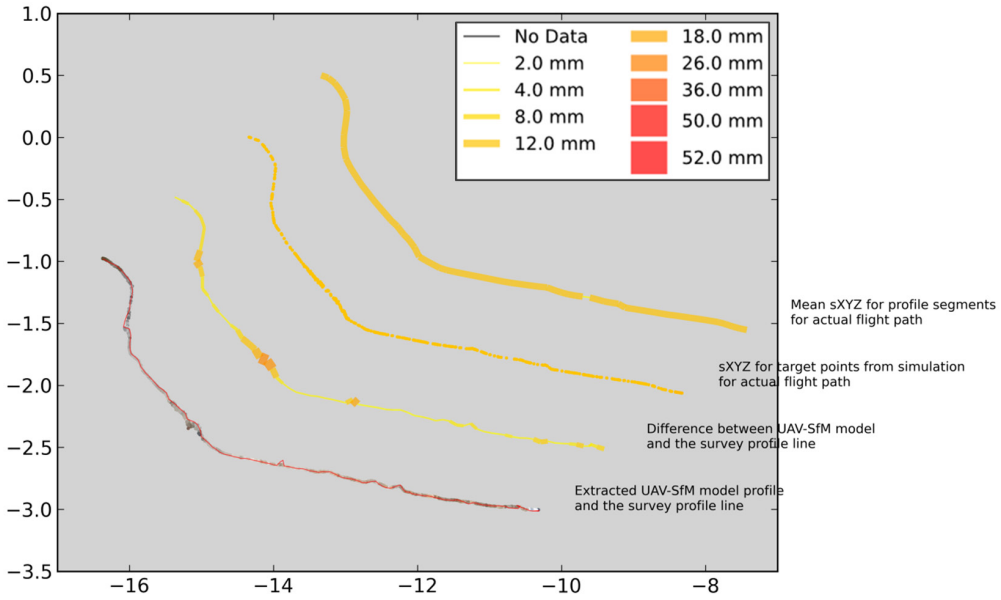

Figure 5.16: Four profile lines of Profile 2 comparing survey data (UAV-MVS profile points overlayed on the survey profile line), the mean distance between the UAV-MVS profile points and the survey line and estimated achievable precision for the actual flight path simulation plotted as points and as mean precision line segments (13GCP22mm60NoObl) (axes units are metres).

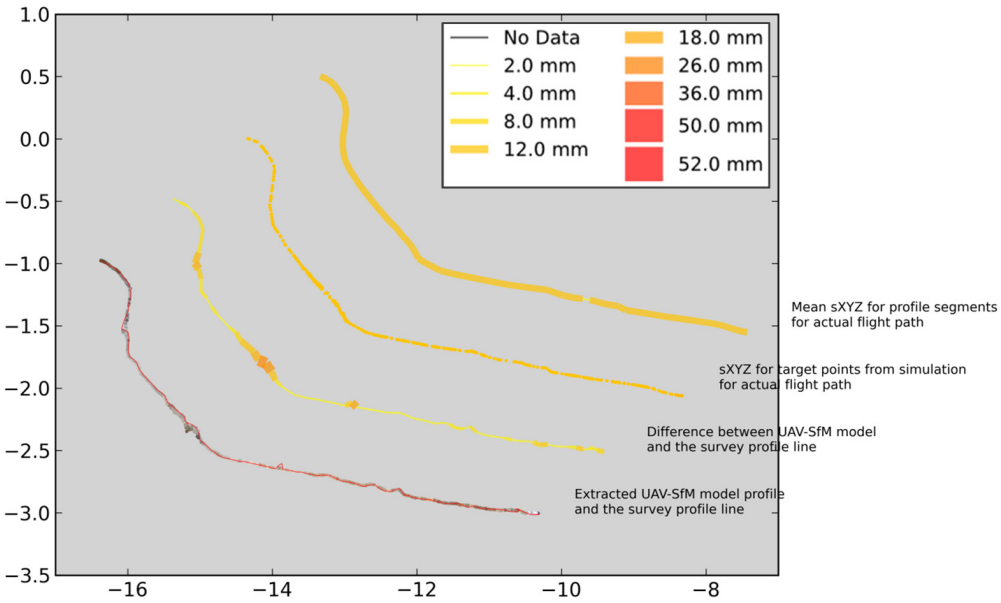

Figure 5.17: Four profile lines of Profile 2 comparing survey data (UAV-MVS profile points overlayed on the survey profile line), the mean distance between the UAV-MVS profile points and the survey line and estimated achievable precision for the actual flight path simulation plotted as points and as mean precision line segments (13GCP22mm80Obl) (axes units are metres).

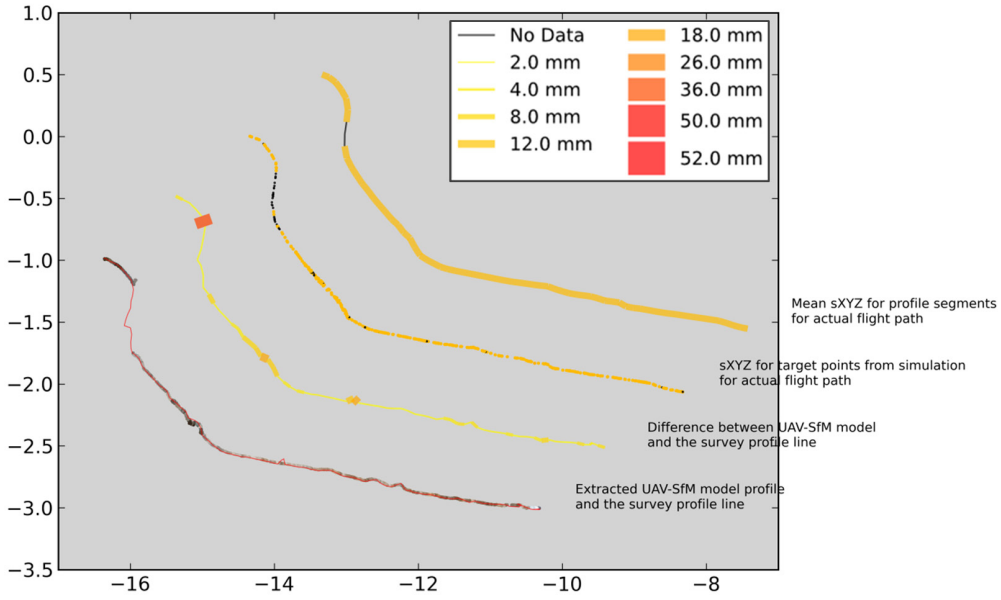

Figure 5.18: Four profile lines of Profile 2 comparing survey data (UAV-MVS profile points overlayed on the survey profile line), the mean distance between the UAV-MVS profile points and the survey line and estimated achievable precision for the actual flight path simulation plotted as points and as mean precision line segments (13GCP22mm60Obl) (axes units are metres).

5.3.2 Scenario accuracy assessment

The scenario accuracy assessment focusses on the results from the comparison between verification point locations from the UAV-MVS model and the verification point coordinates for the total station survey. The simulation results are not included. The impact of overlap, oblique imagery inclusion and GCP density are assessed by interpreting the accuracy statistics summarised in Table 5.4 and Table 5.7 and boxplots are used to summarise horizontal and vertical error (i.e., residuals from the verification point comparison). Horizontal error is shown as XY on the right of each plot and vertical error is shown as Z on the left of each plot. In Figure 5.19, the overlap percentage and inclusion of oblique imagery had little impact on accuracy when GCP precision was fixed at 0 mm. This was also seen in statistics in Table 5.4. When 22 mm GCPs were used, including oblique imagery and using 80% overlap improved model accuracy marginally.

The plots in Figure 5.20 correspond with the findings from Table 5.7. As the number of GCPs increased the UAV-MVS model accuracy improved. The use of 9 GCPs with oblique photography included resulted in a model that was nearly as accurate as the 13 GCPs scenarios, particularly in the horizontal. This was the case for both the 0 mm setting and the 22 mm setting. The implication is that horizontal accuracy can be maintained with fewer GCPs, however, the vertical accuracy was more closely related

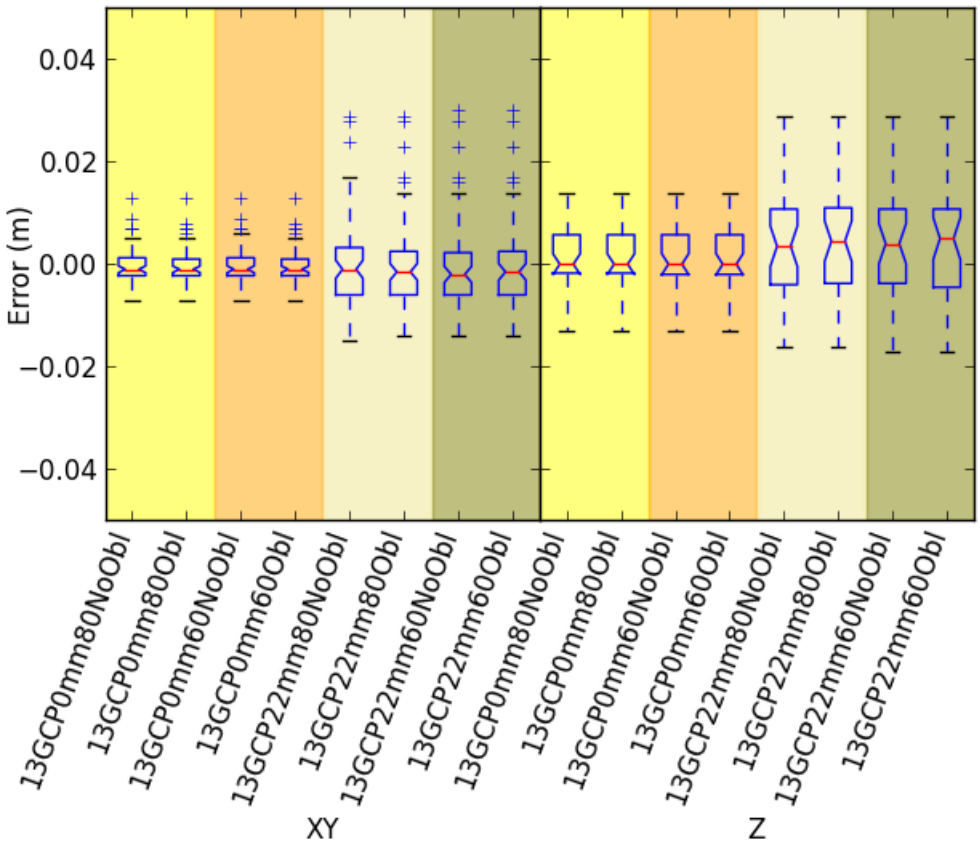

Figure 5.19: Boxplots for overlap scenarios, verification point locations from the UAV-MVS model were compared to total station survey coordinates.

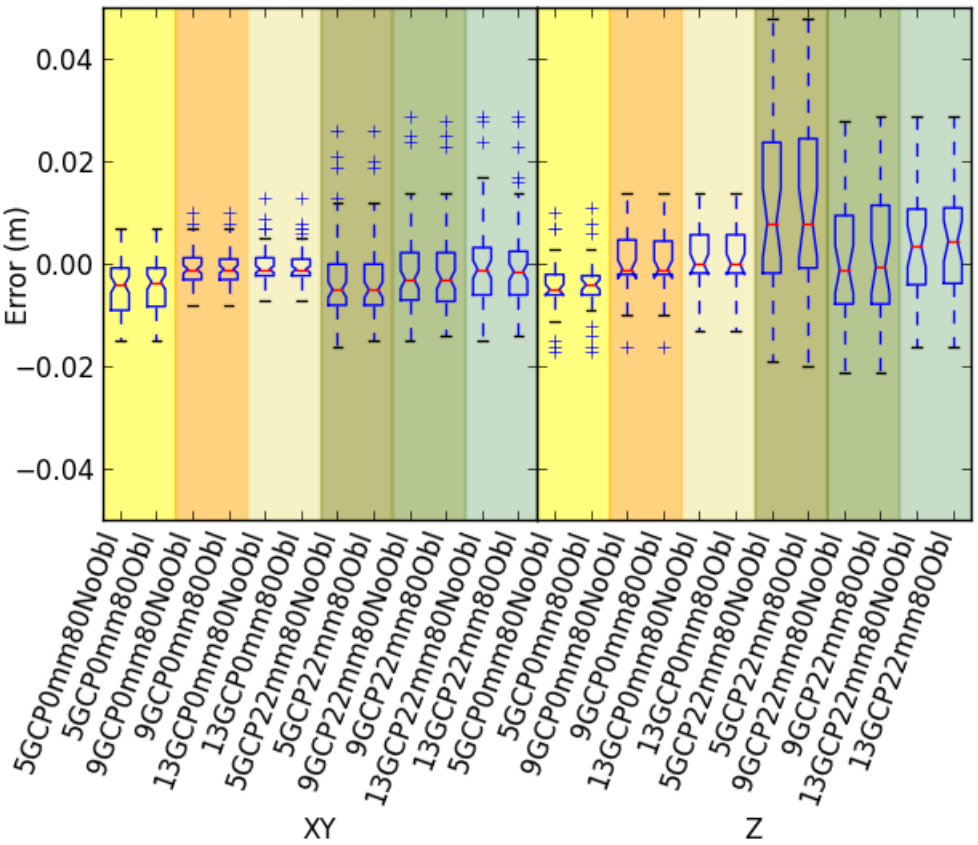

Figure 5.20: Boxplots for GCP density scenarios, verification point locations from the UAV-MVS model were compared to total station survey coordinates.

to GCP density. To better understand this, the following section provides maps of the spatial distribution vertical error for the 5 and 13 GCP scenarios. The inclusion of oblique did not have an obvious impact, however, the impact on point cloud completeness is not portrayed in these results. This will be investigated in a later profile analysis section (Section 5.3.3).

Spatial distribution of vertical accuracy from the UAV-MVS models

The spatial distribution of vertical accuracy varies across the UAV-MVS model. Figure 5.21 and Figure 5.22 portray the impact on accuracy of the design choices in scenarios with 5 and 13 GCPs.

A marked difference in vertical accuracy along the top of the scarp and in the long grass in the southern portion of the study area can be seen in Figure 5.21 and Figure 5.22. This is particularly pronounced when using 22 mm GCPs and when reducing GCP density. Including oblique imagery had no visible impact on the verification points. Again, this is to be expected as the locations of the verification points lead to few occlusions of those points. The effect of occlusion is seen in Section 5.3.1 and Section 5.3.3.

5.3.3 Profile analysis

Assessing the impact of design decisions on the accuracy of UAV-MVS requires analysing profiles to visualise how well the model matches the surveyed profiles and the change in point cloud density. Profile plots for all profiles were generated, and only a subset of those profile plots is presented here. The 13 GCP, 0 mm scenarios were chosen as the key findings that they illustrate are also seen in the 22 mm versions. The profile plots relating to the difference between UAV-MVS survey and the total station profiles in Figure 5.14–5.18 highlight where the UAV-MVS survey points differ from the total station survey profile.

The UAV-MVS survey points were most dense at the top of the scarp and along the grass boundary (Figure 5.23). This is also an area of high mean distance from the survey profile line. There is a clump of grass (pictured in Figure 5.13(b)) that results in a segment with high density in the plot. A similar density bulge is shown in Figure 5.24, which corresponds to the rubble pictured in Figure 5.13(d). The mean separation between the UAV-MVS survey points and the survey profile was also large here (e.g., Figure 5.14). Figure 5.25 also shows a density bulge (corresponding to larger mean separation) re-

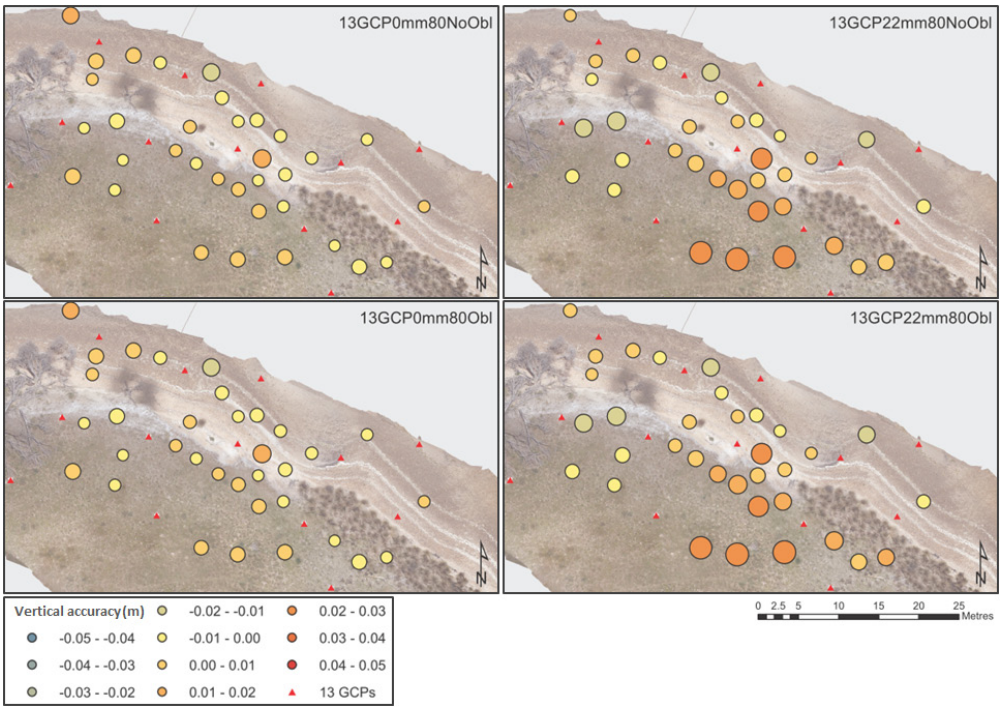

Figure 5.21: Spatial distribution of vertical accuracy for 13 GCP scenarios, with and without oblique and for $\sigma = 0$ mm and $\sigma = 22$ mm scenarios.

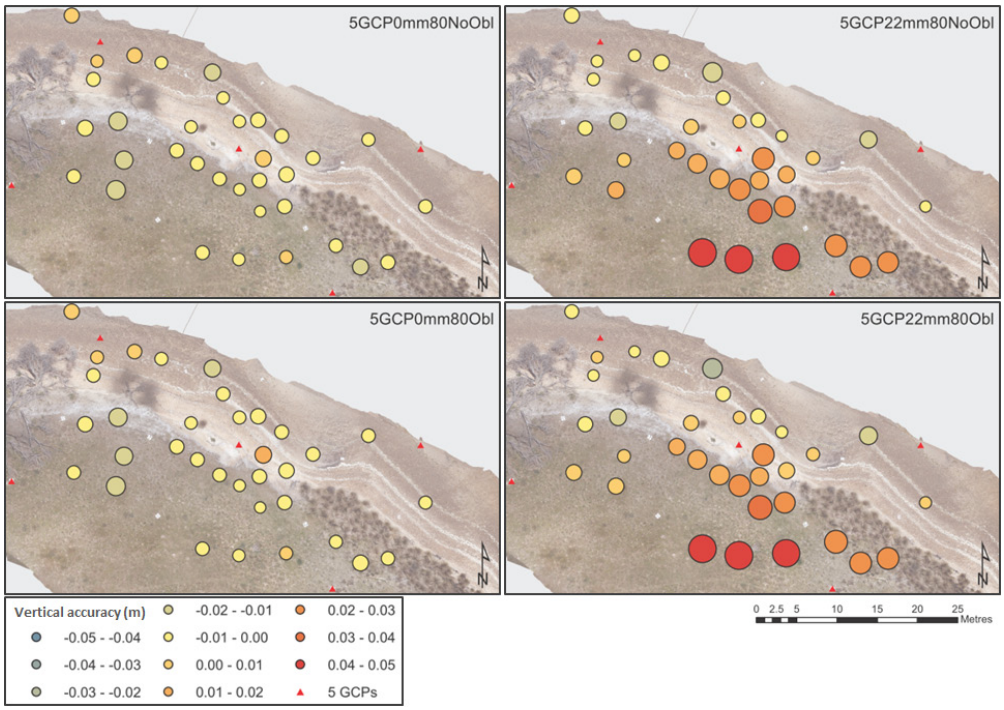

Figure 5.22: Spatial distribution of vertical accuracy for 5 GCP scenarios, with and without oblique and for $\sigma = 0$ mm and $\sigma = 22$ mm scenarios.

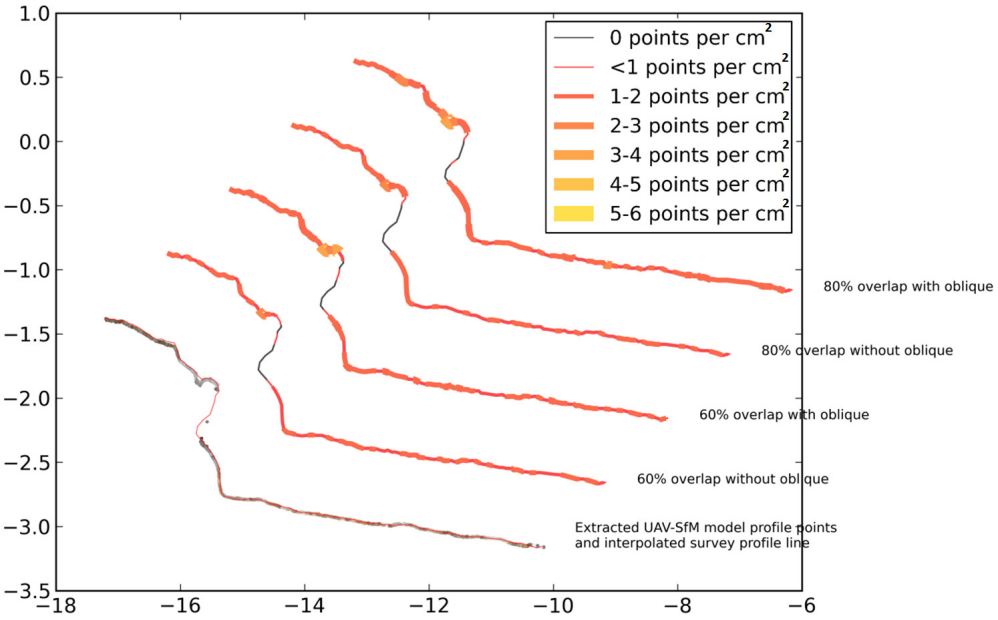

Figure 5.23: Profile 1 density plot for two overlap scenarios, with and without oblique imagery (axes units are metres).

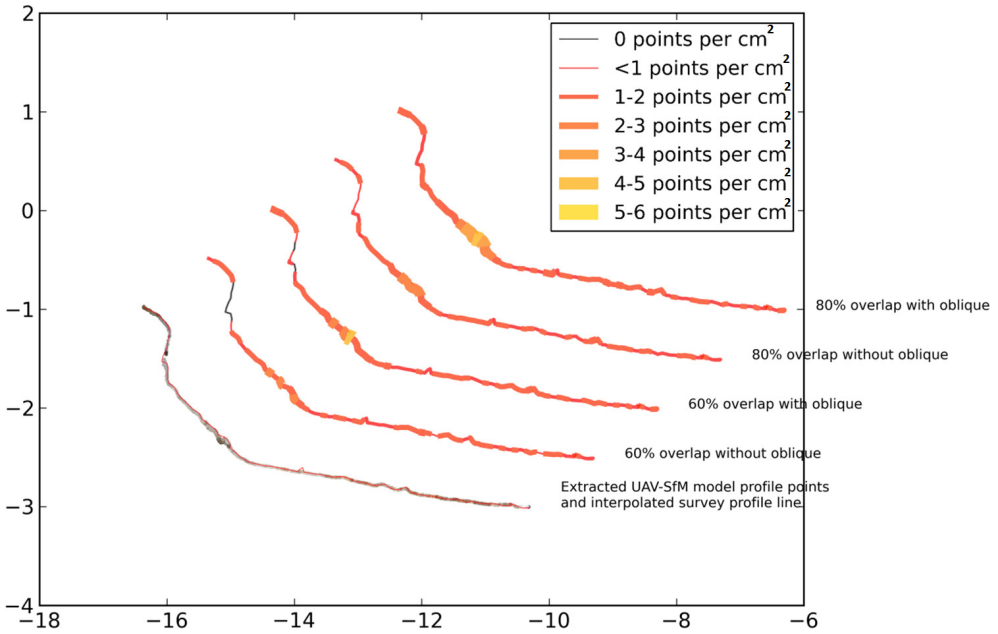

Figure 5.24: Profile 2 density plot for two overlap scenarios, with and without oblique imagery (axes units are metres).

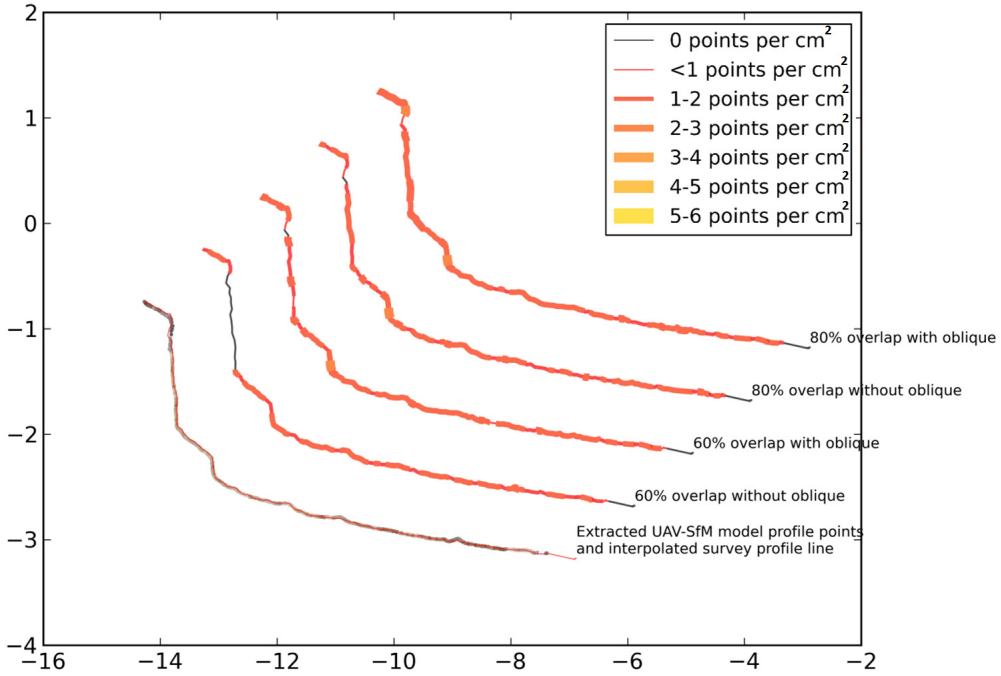

Figure 5.25: Profile 3 density plot for two overlap scenarios, with and without oblique imagery (axes units are metres).

sulting from a section of rubble. The profile in Figure 5.25 was over smoother ground (barely any cracks and no grass) and the point density is more uniform. The subtle overhang in Figure 5.25 and the more obvious overhangs in Figure 5.23 and Figure 5.24 resulted in occlusion. Increased overlap and the inclusion of oblique imagery overcame this occlusion in all except profile 1 (Figure 5.23). The 80% overlap scenarios that included oblique imagery had the most complete coverage and resulted in denser point clusters along the scarp edge. This occlusion in profile 1 was due to the lack of oblique photography capturing this portion of the scarp.

The camera network design included image stations focussed on this portion of the scarp, however, the inaccuracy of UAV position and pose control meant that no clear non-blurry images were captured of this portion. The segments of the profiles that have high density (such as the higher density seen amongst the rubble in Figure 5.24 and pictured in Figure 5.13(c) and (d)) also showed a higher average distance from the survey profile line. This was due to surface characteristics similar to those pictured in the photos in Figure 5.13 such as the cracks and the complexity of the rubble. This terrain complexity resulted in variations in the total station EDM distances that appeared as artefacts in the point cloud. These may, in fact, be real and the UAV-MVS survey may have provided a better representation than the total station survey.

MVS image matching fails to accurately measure terrain beneath vegetation and the

complexity of the vegetation can produce artefacts in the data. The technique also fails to match very reflective surfaces and surfaces with very low optical texture, such as water and wet mudflats. This results in gaps and sparse portions in the point cloud. Areas with optical texture, particularly areas of bare ground, are well matched and the point clouds produced for these areas are dense. The resulting models allow the vegetation line to be extracted. The dense point clouds provide a very accurate representation of the terrain where vegetation is not present and this allows the scarp edge to be accurately determined. In terrain change monitoring it is often the case that the areas of more significant change are also those without vegetation or where the vegetation is no longer present.

The terrain complexity must be taken into account during flight planning and survey design. Overhangs and cracks need to be imaged using a camera network that avoids occlusion and maximises point cloud completeness. This is a complex problem, particularly if using a fixed-wing UAV that does not provide oblique imagery easily. Multi-rotor UAVs provide the manoeuvrability for complex camera networks, however, the inaccuracy of on-board position must be acknowledged by planning for high overlap and high levels of redundancy.

5.3.4 Conclusion

The recent rapid progression in the field of UAV remote sensing has been driven by the proliferation of low-cost systems that take advantage of recent advances in aircraft design, component miniaturisation, battery technology and computing power. In the past, the level of expertise required to plan and execute a successful and efficient photogrammetric mission has been high whereas UAV-based mapping surveys can now be carried out with little or no photogrammetric expertise. This study has focussed on the key considerations that must be evaluated when planning a UAV survey that seeks to create a 3D representation of natural terrain, in this case a coastal erosion site. The study aimed to be consistent with photogrammetric principles and to provide guidance on applying those principles to UAV-MVS survey design. The verification of simulation predictions and the assessment of the impact on model accuracy of UAV survey design choices, particularly image overlap, oblique imagery inclusion, GCP density and distribution and control survey precision were the focus of the investigation.

For the simulation verification component of the study, a set of scenarios were simulated and compared to empirical results. In each case design camera network or an actual

camera network (i.e., comprised of camera stations from the UAV flights flown over the site) were input into the bundle adjustment simulation. These precision estimates were compared to the results of an accuracy assessment of the 3D point cloud generated from the corresponding camera network using UAV-MVS. The GCPs and verification points were surveyed with a precise total station survey ($\sigma \leq 2$ mm). The UAV flying height AGL was between 20 and 25 m and all images were taken with a pre-calibrated consumer-grade camera with a 20 mm prime lens with the focus fixed at infinity. The oblique imagery centred on the erosion scarp with camera angles between 10° and 40° from nadir. The key parameters that defined each scenario were: i) 60% and 80% overlap, ii) the inclusion/exclusion of oblique imagery from each nadir network, iii) GCP density (5, 9 and 13 GCPs), and iv) two control survey accuracies, precise ($\sigma = 0$ mm) and differential GNSS/DGPS equivalent ($\sigma = 22$ mm).

The achievable precision estimates derived using simulation and the assessed accuracy of the actual UAV survey scenarios were affected by design choices. Simulations resulted in accuracy estimates that were overly optimistic when GCP precision was high, whereas simulated accuracy estimations were within 10% of the assessed accuracy when using 13 GCPs coordinated to differential GNSS/DGPS equivalent precision ($\sigma = 22$ mm) and within 10–20% when GCP density was reduced. Simulation using DGPS equivalent precision GCPs produces reliable estimates of achievable precision. It is speculated that this is because the predominant sources of error are the random errors in the observation of ground control and observational image space accuracy.

If control is precise the simulation significantly overestimates achievable precision. The GCP survey precision was set to 0 mm as the precise total station survey achieved $\sigma \leq 2$ mm and thus the control could be treated as error free for the purposes of the experiment. This raised the question of whether fixing the control precision was the cause of the overestimation of precision in the simulation. To assess this, the simulations were re-run with the GCP precision set to 2 mm (the other end of the estimated error range for the total station GCP survey). This resulted in a slight increase in estimated achievable precision values, however, the model precision was still overestimated. The difference was not considered significant enough to suggest that our choice of survey precision setting was the cause. We speculate that the overestimation is caused by residual systematic errors that became dominant at this high precision. These residual systemic errors can almost certainly be attributed to camera calibration modelling errors.

Chapter 4 provides guidance on the impact of calibration choices. The results show that precision cannot be improved by taking lots of photos. The use of convergent photos

and very accurate photo control improves model accuracy to a point, however, model accuracy is fundamentally limited by uncertainty associated with systematic errors in the camera distortion model. As is known in photogrammetry, the derivation of a high quality calibration is crucial when aiming for very high precision. The conclusion is that there is a cut-off for when simulation is useful in UAV-MVS. When object space accuracy to the order of 5 mm is the goal, simulation is less reliable because the achievable accuracy is likely to be limited by residual errors in the camera calibration rather than by the precision of observations in the control survey, or in the image. The cameras and the calibration methods reach their limit at these high accuracies.

The inclusion of oblique imagery has little impact when using precise GCPs, however differential GNSS/DGPS survey precision control combined with oblique imagery results in more accurate models, particularly when GCP density is high. The dense (13 GCP) scenario that included oblique imagery was the most accurate with σ_{XYZ} of ~4.5 mm when GCP survey precision was set at 0 mm (for 1σ). Degrading GCP survey precision to 22 mm (for 1σ) resulted in similar accuracy nadir-only, and nadir and oblique scenarios (with 13 GCPs) with ~10.2 mm. Adverse impacts on accuracy were caused by reducing the number of GCPs and, when GCPs are not precise. Reducing overlap to 60% degraded vertical accuracy radially towards the periphery. Analysis of spatial distribution of error and profiles show improvements in point density, derived point cloud accuracy, and model completeness when camera networks with 80% or higher overlap include oblique imagery. Surface characteristics that increase matched point density such as clumps of grass, cracks in the dirt and areas of coarse rubble influence model accuracy, but it is unclear whether MVS derives more accurate terrain representations than reflectorless total station profiling.

The findings of this study lead to a number of suggested practices. With regard to GCP density, 10–15 GCPs distributed around the periphery and through the centre of the study area are needed for an area that can be covered in one or two flights. Overlap of 80–90% should be used when using differential GNSS/DGPS to survey GCPs, but can be reduced when control is precise. The chosen flying height should result in an image resolution that provides sufficient feature clarity to accurately measure targets and match features. In this study, a flying height of approximately 25 m resulted in accuracies of approximately 5 mm when using precise control and approximately 10 mm for differential GNSS/DGPS control. Including oblique imagery strengthens the camera network, improves model completeness, and improves overall accuracy. Ensuring a high level of redundancy in the camera network avoids the potential for insufficient overlap due to inaccurate UAV positioning and ensures the image set meets overlap specifications

after the removal of poor quality imagery prior to model generation. The inaccuracy of on-board positioning on most UAVs means that carefully defined camera position and pose are not of practical benefit. Instead it is viable to carefully plan a flight in the field based on photogrammetric principles, expert knowledge, and minimal *a priori* data. Simulations are useful for assessing design choices, however, when GCPs are precise the simulation may significantly overestimate accuracy. The camera network should cover around 20–30% more terrain area beyond the study site to reduce the likelihood of degraded vertical accuracy towards the periphery of the study area. This study has verified that bundle adjustment simulation gives realistic estimates of UAV-MVS derived point cloud accuracy when using control with differential GNSS/DGPS equivalent precision.

Thesis context

The use of simulation in photogrammetric mission planning is an important step, particularly when missions involve expensive logistics. The use of simulation in UAV surveys has not been used extensively and this chapter sought to assess how well simulations estimate achievable precision for various survey design scenarios. In addition, design decisions will impact derived model accuracy and this study assesses those impacts in the context of camera network design and ground control survey decisions. Assessing the accuracy of the point clouds derived from UAV-MVS is an essential step in the evaluation of this technique for change detection at the scales needed to monitor sheltered coastline erosion (and for any other applications that seek to detect and quantify fine-scale change). Chapter 6 investigates the comparison of these derived point clouds and uses the knowledge gained in previous chapters to evaluate coastal change monitoring options for UAV-MVS point cloud data, specifically cloud differencing, profile comparison and shoreline definition options

Acknowledgements

The author thanks Dr Christopher Watson (University of Tasmania) for his advice on precise survey design and bundle adjustment intricacies and Professor Mark Shortis (RMIT) for providing the VMS software and advice on simulations.

6 | Detecting coastal change in unmanned aerial vehicle Multi-View Stereopsis (UAV-MVS) point clouds

Chapter 6 focuses on demonstrating that centimetre-scale change can be detected, quantified, and visualised using UAV-MVS point clouds of an eroding coastal site. This chapter will be submitted for publication with one of the following journals: IEEE Journal of Selected Topics in Applied Earth Observations and Remote Sensing (JSTARS[1]; Estuarine, Coastal and Shelf Science[2]; or Estuaries and Coasts[3].

Abstract

High spatial and temporal resolution datasets are important for coastal erosion monitoring and modelling. The focus of much of the research into coastal change and the impacts of sea level rise has been on exposed ocean beaches. The changes that are occurring along sheltered coastlines are also important and the gradual changes may be event driven or the erosion may be an indicator of more subtle long term trends. The traditional methods for monitoring coastal change are either based on coarse-scale monitoring using satellite data, aerial imagery and Airbourne Laser Scanning (ALS), or fine-scale monitoring using profiling or expensive terrestrial laser scanning (TLS). These fine-scale studies are undertaken at key indicator sites that can then provide insight into the changes occurring along a larger section of coast. The emergence of unmanned aerial vehicles (UAVs or drones) as tools for remote sensing and terrain mapping has the potential to revolutionise landscape change monitoring. UAVs can fly on-demand and at low altitude so that the datasets produced can meet spatial and temporal resolution requirements. UAV photogrammetry using multi-view stereopsis (MVS) is known as UAV-MVS and it uses high-resolution image sets to reconstruct the terrain and generate 3D point clouds with very high point density (1–6 points per cm^2) that are georeferenced to better than 2–3 cm. The technique is a cost-effective alternative to other small change monitoring techniques. The point clouds can be compared and the differences detected can be visualised and analysed to gain insight into coastal erosion and accretion at very high resolution. The detail they provide also allows for accurate shoreline proxies to

[1] http://www.grss-ieee.org/publications/jstars/
[2] http://www.journals.elsevier.com/estuarine-coastal-and-shelf-science/
[3] http://www.springer.com/environment/journal/12237

be extracted. This study illustrates cloud to cloud differencing, profile comparison and shoreline proxies to assess the effectiveness of UAV-MVS for monitoring centimetre-level coastal change detection. The resulting absolute difference point clouds show the magnitude of change. Sparse sections of the cloud resulting from occlusion can result in false change. Profile comparison allows change direction to be determined and manual measurement of changes to be made. The comparison of two shoreline proxies, scarp edge and vegetation edge, indicates that, at the scale provided by UAV-MVS, vegetation edge is a poor proxy for shoreline and scarp edge can be more accurately determined.

6.1 Introduction

Coastal change is a natural phenomenon that has been ongoing throughout the earth's history. Anthropomorphic influence in recent centuries has altered our climate and this is changing the way our coasts evolve. Rising sea levels are impacting on the rate of coastal erosion (FitzGerald et al., 2008). The impact on coastal habitats and infrastructure is something that needs to be monitored. Zhang et al. (2004) suggests that the rate of erosion along beaches in the US east coast barrier island system is two orders of magnitude greater than sea level rise. Average sea level rise in Australia was 1.2 mm per year between 1920 and 2000 (Church et al., 2006). This equates to ~120 mm per year of erosion along similar beach systems if sea level rise continues as in the previous century. IPCC (2013) estimated global sea level will likely be rising at a rate of 8 to 16 mm per year (medium confidence) by the end of this century (800–1600 mm per year of erosion on susceptible coastlines). Some studies are seeing annual erosion rates in the 75–125 mm range (Young and Ashford, 2006; Greenwood and Orford, 2008), others are seeing higher annual rates of erosion,~1 m (Smith and Zarillo, 1990a), 2.4–14 m (Middleton et al., 2013), greater than 25 m (Stockdon et al., 2002b; Kuleli, 2010). Most studies have focussed on exposed sandy coastlines (Splinter et al., 2013). The cycle of erosion and accretion along these open ocean beaches is a well-understood phenomenon (Bruun, 1962; Bruun, 1988; Ranasinghe et al., 2011). The impact on more sheltered coasts is less well understood and is likely to be more gradual.

The boundary between land and water is considered the 'coastline' or 'shoreline'. The choice of topological feature used to define shoreline from remote sensing data is a fundamental question faced by coastal geomorphologists, scientists, managers and engineers. In reality this 'line' is not always easy to distinguish due to its dynamic nature. In remote sensing the resolution of the data plays a major role in determining how a coastline is defined and distinguished (Boak and Turner, 2005). The key is to be able to repeatedly and robustly detect the coastline feature from available data sources. Boak and Turner (2005) list and review a large number of coastline indicators and they found that data availability drives the choice of indicator rather than being determined by the context of the specific investigation. They conclude that on coasts where there is a morphological feature such as an erosion scarp, the seaward vegetation line and the scarp edge are two useful shoreline indicators for change detection. The common alternative is to base shoreline on the high water level discernible from imagery (Pajak and Leatherman, 2002). Research has shown that this can be problematic for coastal monitoring due to the tendency for the "line" to be invisible or to appear as a transition zone (e.g. Anders

and Byrnes, 1991; Moore, 2000; Pajak and Leatherman, 2002; Stockdon et al., 2002b). Modelling shorelines and examining how coasts change is a useful tool for examining coastal change. Shoreline modelling is empirical in nature and shoreline calibration requires high quality observational datasets (Splinter et al., 2013). For coastal monitoring the chosen indicator needs to provide robust change analysis to monitor horizontal shoreline retreat and therefore the higher the spatial and temporal resolution the better. Unfortunately, coastal observation datasets tend to have limited resolution. For example, Cowell and Nelson (1991) reports that aerial photography (1:10,000) provides shoreline measurements accurate to approximately +/- 7 m. Not all change is visible at coarse scales, in some areas low-relief landscape features (e.g., beach dunes, berms, scarps) undergo small incremental erosion and accretion. These small changes can be very important in understanding how slow/small phenomena such as mean sea level rise impact on coastal morphology (Mitasova et al., 2004). The rate of change is also important and when that rate is not constant the analysis needs to focus on key events (e.g., storms, king tides) to avoid errors relating to estimations from sparse temporal datasets based on change linearity assumptions (Fenster et al., 2001). Coastal change requires regular monitoring to understand storm-scale response and recovery, seasonal variability, and annual and decadal trends (Splinter et al., 2013). In some areas the extraction of a shoreline feature may not be sufficient. The quantification of sediment displacement requires detailed terrain time series so that volume can be determined and so that the response of specific coastal morphologies and sediments to changes in sea level can be monitored and predicted.

Many studies have mapped coastal change using Landsat satellite imagery at 30 m spatial resolution (Alesheikh et al., 2007; Kuleli, 2010; Ramsey III et al., 2001; Ekercin, 2007; White and El Asmar, 1999; Alhin and Niemeyer, 2009; Marfai et al., 2008; Prabaharan et al., 2010; Azab and Noor, 2007; Rasuly et al., 2010). Aerial photography and photogrammetry can provide more accurate data but pixel sizes are often 10–15cm (Adams and Chandler, 2002). Resolving erosion at the sub-decimetre scale is difficult at these resolutions. Aerial photography remains a common data source for coastal monitoring studies (Al-Hatrushi, 2007; Chalabi et al., 2006; Dolan et al., 1991; Fenster et al., 2001; Makota et al., 2004; Rogers et al., 2004; Shoshany and Degani, 1992; Smith and Zarillo, 1990b; Smith and Bryan, 2007; Thieler and Danforth, 1994). The aim of many of these studies is to document historical coastal change and track more recent change in an effort to foresee the future impacts of climate change (Zhang et al., 2004). These studies are limited to coarse-scale change both temporally and spatially.

Airbourne Laser Scanning (ALS) such as LiDAR can provide point clouds of the coast

and, although the systems and mission costs are high, ALS can offer information-rich datasets for coastal monitoring. ALS can map terrain in greater detail than that provided by traditional beach profiling surveys (Shrestha et al., 2005). Point density is dictated by the sensor and the flying height. Most missions tend to fly at 600–1000 m (Sallenger et al., 2003; Stockdon et al., 2002b; Adams and Chandler, 2002; Carter et al., 1998; Shrestha et al., 2005; Starek et al., 2007). Point density can be as high as ten points per square metre (Mitasova et al., 2009a) (and higher) but is often closer to one point per square metre (Zhou and Xie, 2009; Starek et al., 2007). The accuracy of the georeferenced point clouds can also vary considerably (2 cm to 2 m) (Carter et al., 1998; Middleton et al., 2013; Shrestha et al., 2007; Mitasova et al., 2009a; Stockdon et al., 2002b). ALS point clouds can provide a basis for comparison and change detection based on specific dates of data acquisition, however, fine-scale changes and event-based changes may not be monitored due to the high cost of data acquisition dictating temporal resolution. An alternative is UAV photogrammetry using multi-view stereopsis (MVS) known as UAV-MVS. This technique uses high-resolution overlapping image sets to reconstruct the terrain and generate georeferenced 3D point clouds with very high point density.

The techniques for shoreline feature extraction from ALS point clouds and the change analysis techniques used to compare those ALS point clouds are applicable to UAV-MVS point clouds. Sallenger et al. (2003), Starek et al. (2007), and Stockdon et al. (2002b) used profiles extracted from ALS data to find the shoreline. Lee et al. (2009b) used classification techniques to extract the shoreline. Many have generated raster digital elevation models (DEMs) to extract the shoreline, or used DEMs for differencing to determine change quantities and/or horizontal shoreline retreat (Brock et al., 2002; Deronde et al., 2006; Deronde et al., 2008; Liu et al., 2007; Mitasova et al., 2003; Mitasova et al., 2004; Mitasova et al., 2009b; Overton et al., 2007; Robertson et al., 2004; White and Wang, 2003; Young and Ashford, 2006; Zhou and Xie, 2009). For example, Mitasova et al. (2004) and Mitasova et al. (2009b) interpolated topographic data from ALS and GPS into raster grids to simplify comparison and quantification of change using GIS tools. As discussed in Chapter 3, the point cloud datasets produced in UAV-MVS are large and for some applications it is necessary to first convert the point clouds to surface models. The converted surfaces can then be compared using common GIS tools. Unfortunately, some GIS are constrained to 2.5D DEMs as opposed to true 3D digital surface models (DSMs) or meshes. This constraint can result in the loss of important terrain features such as overhangs and undercuttings. In addition, the conversion from point cloud to DEM (or DSM) can result in artefacts such as peaks and sinks due to outliers in the point cloud data. To avoid these issues this study will

use cloud to cloud differencing. A number of other studies have used this technique for comparing point clouds (Girardeau-Montaut et al., 2005; Eltner et al., 2013; Kaiser et al., 2014; Genchi et al., 2015; Gómez-Gutiérrez et al., 2014).

Profiling along the coast can provide detailed information along each line but it is labour intensive (Smith and Zarillo, 1990a; Smith and Bryan, 2007; Zhang et al., 2004). Terrestrial laser scanning (TLS) is an expensive yet highly effective tool for coastal monitoring offering the ability to resolve erosion rates of less than 5 cm (Lim et al., 2005; Rosser et al., 2005; Eltner et al., 2013). Calligaro et al. (2014) reports point densities of 90 points per m^2, Kang and Lu (2010) reports 500 points per square metre and Schubert et al. (2015) reports 160–240 points per m^2 from a scanning distance of 100 m. Some coastal monitoring has been done by interpreting video (Livingstone, 1999; Smith and Bryan, 2007). In recent years, the use of MVS from terrestrial photography has been investigated (James and Robson, 2012; James et al., 2013; Westoby et al., 2012), from kite aerial photography (KAP) (Bryson et al., 2013) and using UAV-MVS (Mancini et al., 2013; Harwin and Lucieer, 2012b; Rovere et al., 2014; Casella et al., 2014). The point density offered by this technique can reach 1–6 points per cm^2. Such dense datasets can be captured on demand using low-cost equipment. Terrestrial MVS (T-MVS) and UAV-MVS have been used to monitor centimetre-scale change in other applications. For example, Flener et al. (2013) mapped river channels; Room and Ahmad (2013) mapped a river model; D'Oleire-Oltmanns et al. (2012), Eltner et al. (2013), and Frankenberger et al. (2008) mapped soil erosion; Verhoeven (2011), Doneus et al. (2011), Eisenbeiss and Zhang (2006), Eisenbeiss (2009), and Stal et al. (2014) undertook archaeological site mapping; Westoby et al. (2012) mapped a coastal cliff, moraine dam and a geological feature; Genchi et al. (2015) mapped bioerosion; Previtali et al. (2014) mapped mountain slopes; Fonstad et al. (2013) mapped landforms using kite MVS; Hugenholtz et al. (2013) did geomorphological mapping; Niethammer et al. (2012), Lucieer et al. (2013), and Carvajal et al. (2011) mapped landslides; Lucieer et al. (2011a) mapped micro topology in Antarctic moss beds; and Bemis et al. (2014) mapped structural geology.

The UAV-MVS technique is potentially a cost-effective tool for monitoring sections of coast and spatial and temporal resolutions that give indicative insight into coastal change. Much of the research has been on open coast beaches but relatively little research has investigated erosion in sheltered waterways (Prahalad et al., 2014). Erosion along these sheltered coastlines is not driven by ocean swell. Wind waves that coincide with peak tides are the primary driver for erosion of the shores (Prahalad et al., 2014). Housing and infrastructure are common along these waterways and monitoring the changes and the effectiveness of erosion mitigation efforts is a key application of sub-

decimetre coastal change detection. In natural areas, many of these sheltered coasts are fragile saltmarsh ecosystems or soft coastal cliffs. A characteristic of saltmarshes is that they are low-lying and therefore susceptible to inundation and erosion (FitzGerald et al., 2008; Zhang et al., 2004). These coastal ecosystems may be able to cope with a few millimetres of sea level rise per year, however, the plants may not be able to respond rapidly enough to the increasing water level and drown (Zhang et al., 2004). Prahalad et al. (2014) estimated that erosion rates along these sheltered coasts are 10–20 cm per annum. Splinter et al. (2013) suggested that, in order to examine and understand the impact of sea level variations and storm events, monitoring every 30 days or less is needed. Separating seasonal, annual and decadal trends from event-driven erosion is critical if scientists are to understand the degree to which sheltered waterway erosion is a climate change indicator. UAV-MVS provides imagery at very high spatial resolution and the 3D point clouds produced are coloured naturally allowing both the vegetation line and the scarp edge to be extracted. This study aims to assess the effectiveness of UAV-MVS in monitoring centimetre-level coastal for change detection. The objectives of this paper are i) to use point cloud differencing to measure change between 2010, 2012 and 2013 epochs; ii) to visually evaluate the point cloud differences to ascertain whether actual change is represented; and iii) to assess two shoreline definition options for coastal change monitoring, namely vegetation edge and scarp edge.

6.2 Method

6.2.1 Background Theory

Point cloud comparison for accuracy assessment, coregistration and change detection

When evaluating the accuracy of point clouds, determining the similarity of points in two clouds when undertaking coregistration, or evaluating the differences between point clouds for detecting change, the overarching question of point cloud similarity broadly spans all three tasks. Quantifying the difference between one point cloud and another, or a point cloud and some other reference dataset can be done using the following techniques:

- Point-to-point: points are compared to each other, sometimes referred to “cloud-to-cloud”;

- Point-to-surface: points are compared to a reference DSM/DEM/Mesh (also referred as a surface, but in some references they are referred as a mesh, i.e., point-to-mesh comparison), Girardeau-Montaut et al. (2005) calculate the distance from each point to the nearest position on the surface;

- Surface-to-surface: all points clouds are converted into a surface and compared (also known as mesh-to-mesh comparison);

- Point-to-image: compare features in a point cloud that are distinguishable in an orthorectified image to the equivalent feature in the image;

- Surface-to-image: similar to point-to-image comparison, except that the features are in the surface.

The first technique deserves special consideration due to the fact that it uses the original data points for comparison without artefacts that may be introduced during cloud to surface conversion. In undertaking point-to-point comparison Girardeau-Montaut et al. (2005), Knauer and Löffler (2009), and Kang and Lu (2010) encourage the use of the Hausdorff distance for the measurement of point cloud similarity or, in fact any two subsets of metric space. Knauer and Löffler (2009) defined it as "the largest distance from any point in one of the sets, to the closest point in the other set" (see Section 1.3 of Knauer and Löffler (2009) for a more formal mathematical definition). A point cloud pair can be compared as a whole or portions of a cloud can be compared. Currently three software packages that offer point cloud comparison functionality are: MeshLab[4]; Matlab[5]; and CloudCompare[6]. For surface-to-surface comparison simple grid differencing has been used (Young and Ashford, 2006; Zhang et al., 2005a). "Point-to-mesh and mesh-to-mesh" distances have been very well studied and software tools have been included in academic software such as Metro (Cignoni et al., 1998) or Mesh (Aspert et al., 2002) (Girardeau-Montaut et al., 2005).

Assessing the accuracy of registration, coregistration and change detection requires quantifying differences between point clouds. The goal is to find errors, outliers, and missing points. For accuracy assessment of registration and coregistration this requires comparison with a reference dataset that can be considered "truth". For change detection the comparison is between epochs in the time series. As pointed out by Myronenko and Song (2010) point clouds have a large dimensionality, often contain noise and out-

[4] http://meshlab.sourceforge.net/
[5] http://www.mathworks.com/matlabcentral/fileexchange/27905-hausdorff-distance
[6] http://www.cloudcompare.org

liers and may require a non-rigid spatial transformation. They define outliers as points that are incorrectly extracted from an image and have no correspondences in other point clouds, conversely, missing points relate to features that are not comparable to other point clouds or reference data because they cannot be found due to occlusion or inaccurate feature extraction. Similar to the sub-pixel matching in imagery, each point cloud can have a different location of a point on the surface, and it is therefore unlikely there will be exact correspondence between points in a number of clouds (Girardeau-Montaut et al., 2005). These degradations and inconsistencies are to be expected and a number of research efforts have focussed on uncertainty and error modelling for point clouds. Knauer and Löffler (2009) discuss methods for dealing with imprecise point clouds. Zeibak and Filin (2008) discuss uncertainty in terrestrial laser scanner (TLS) data. Mémoli and Sapiro (2004) discuss using the Gromov-Hausdorff distance that allows for slight deformations when comparing two point clouds. Cignoni et al. (1998) investigate comparing surfaces and measuring error in surfaces (i.e., comparing a triangulated mesh to a simplified representation) via Metro, a tool they developed that measures geometric difference between two triangular meshes at different levels of detail by computing the Hausdorff distance and approximation error between corresponding sections of the mesh.

Point cloud coregistration

A point cloud is georeferenced when the point cloud from an arbitrary reference frame is transformed into a real-world coordinate reference frame. Once registered, this point cloud can become the reference for the subsequent coregistration process that assigns correspondences between points in the two point clouds and recovers the transformation that maps one point cloud to the other (Myronenko and Song, 2010). Traditional manual registration and coregistration methods rely on the ability of the human eye to distinguish these key features and tie points explicitly, which limits the number of features that can be matched and can be very slow. Advances in computer vision have allowed automated techniques to emerge which have been a focus of research in this area for the past few decades (Bae and Lichti, 2008; Besl and McKay, 1992; Jaw and Chuang, 2010; Myronenko and Song, 2010). In many automated approaches human input is still required to provide initial clues on the scale and orientation of the point cloud. The process usually relies on iteration and many common approaches are based on the iterative closest point (ICP) model. This model is non-linear and will not converge to a solution without good initial values (Barnea and Filin, 2008). This has also been noted by Besl and McKay (1992), Wendt (2007), Kang et al. (2009), Myronenko and

Song (2010), and Pfeifer and Briese (2007). Variants on the ICP technique have emerged that seek to build upon the model and overcome some of its issues. Rusinkiewicz and Levoy (2001) outline a number of variants on ICP and Myronenko and Song (2010) propose a probabilistic method: Coherent Point Drift (CPD). Pfeifer and Briese (2007) and Böhm and Becker (2007) suggest that the SIFT algorithm (Lowe, 2004) could find homologous points as it is able to identify thousands of features that a human eye would struggle to distinguish. Kang et al. (2009) and Barnea and Filin (2010) extract SIFT features from imagery to coregister 3D point cloud data. Bae and Lichti (2008) find correspondence between point clouds by comparing geometric properties such as change of curvature and estimated point vector normal.

Change detection

All change detection is affected by spatial, temporal, thematic and sometimes spectral constraints. The qualitative and quantitative estimation of change can be profoundly affected by the method chosen (Colwell and Weber, 1981 in Coppin et al., 2004) and by the accuracy of coregistration. There have been many change detection techniques developed and Coppin et al. (2004) concluded that no conclusive superior method exists; each has its own merits and its suitability to a particular application must be evaluated in comparison with other methods. Differencing methods are one of the simplest and best as identified by Yuan and Elvidge (1998) who evaluated a total of 75 methods. Coppin et al. (2004) suggested that whether the method is for bi-temporal or multi-temporal datasets, focussing on pixel-based or object-/feature-based change, any change modelling relies on an initial change extraction procedure (via some change detection algorithm) and then a change separation/labelling procedure (via some change classification routine coupled with expert knowledge). The latter relies on a heuristic understanding of the change event in question in order to derive a set of statistical and/or spatial decision rules that are independent of the detection algorithms. The former, on the other hand, are integral in the characterisation of change as one method of change detection is unlikely to provide the same results as another and so both Lu et al. (2004) and Coppin et al. (2004) suggest using a combination of algorithms as they can complement each other.

Lu et al. (2004) undertook a comprehensive review in which change detection techniques and applications are considered and advantages and disadvantages are summarised. In their review it was suggested that good change detection should provide:

1) Extent of change and rate of change

2) Spatial distribution of change features

3) Change trajectories

4) Accuracy assessment

Change rate and extent (1) and accuracy (4) are seen as key to ensuring the outputs produced are useful in the quest for knowledge on the distribution (2) and trajectory (3) of that change. It could be said that the holy grail of remote sensing is to be able to quantify, map, and monitor biogeophysical parameters in the changing environment. To achieve this, the objective is to focus on measuring changes caused by differences in the variables of interest while controlling variances caused by differences in variables that are not of interest (Green et al, 1994 in Lu et al., 2004). Pre-processing is therefore very important to ensure that the data are corrected as much as possible in an effort to create data layers that are comparable. The key changes can then be detected, identified, mapped and monitored irrespective of the casual agents (Coppin et al., 2004).

Change can be seen as a categorical variable (change/no-change or abrupt changes that can be discretely classified) or as a continuum (changes seen over a period) (Coppin et al., 2004). The former can be classed as conversion while the latter is a more subtle modification, a progressive or incremental change such as gradual boundary change or fragmentation. Detecting change involves accounting for both the characteristics of a static instance and the temporal variability in time series from which the nature of the change can be inferred. "The ability to detect is a function of the 'from' and 'to' classes, the spatial extent, and the context of the change" (Khorram et al., 1999 in Coppin et al., 2004). Some techniques can only provide change/no-change information while others can provide a complete matrix of change directions (i.e., from-to change). Many techniques distinguish change using thresholding to separate real and spurious change. While thresholds are simple to understand, they are difficult to select and assess (Hayes and Sader, 2001). Some suggest the use of fuzzy sets to allow for the non-discrete nature of subtle change (Matternicht, 1999 in Lu et al., 2004). The results can then be assessed based on reference observations across the temporal extent of the data and/or by randomly sampling the data to generate an error matrix that can be compared with those of other techniques.

Appropriately pre-processed time series data provide a means of determining a temporal trajectory and in some cases, such as ecosystem, vegetation, crop and landform monitoring, the trajectory may be cyclic (diurnal, seasonal, annual). Temporal trajectory

analysis can compare those cycles to detect anomalies or deviations from the normal (or average, or optimal as the study dictates) (Coppin et al., 2004). In vegetation monitoring, Coppin et al. (2004) suggest a major hurdle in temporal trajectory analysis using traditional remote sensing systems is the difficulty in acquiring sufficient temporal frequency to capture change through a cycle (a day or a growing season) and compare a number of cycles in order to resolve the issue of differences in phenology affecting change results. The use of a UAV to gather high temporal resolution data has the potential to solve this issue. Similarly, in erosion monitoring, key periods of change need to be closely monitored to quantify the influences of seasonal weather patterns and sea level rise.

Change detection from point clouds

Research in change detection from point clouds has largely been focussed on data provided by ALS. The key is accurate registration or coregistration and once data are registered/coregistered comparison is possible using some of the point cloud comparison techniques described above for quantifying differences between point clouds and/or surfaces. Comparing features or objects post classification (as used in image-based change detection) may also be useful in point cloud change detection (Vosselman et al., 2004; Zeibak and Filin, 2007). The use of ALS to detect urban change for database updating and disaster mapping has been an active research niche (Murakami, 1999; Vosselman et al., 2004; Vögtle and Steinle, 2004; Butkiewicz et al., 2008; Kang and Lu, 2010). Shoreline mapping has also made use of ALS point clouds in monitoring coastal change (Carter et al., 1998; Lee et al., 2009a; Sallenger et al., 2003; Starek et al., 2007; Stockdon et al., 2002a; Young and Ashford, 2006). Other research areas include sand dune change (Woolard and Colby, 2002); rock face change (Scaioni and Alba, 2010); and soil erosion (Afana et al., 2010). The use of UAV-MVS point clouds in terrain monitoring is a new field. One example is presented by Dowling et al. (2009) who looked at long-term erosion on a very fine scale when they created 1 m by 1 m DEMs with a resolution of 2.5 cm from point clouds extracted from PhotoSynth[7].

Some studies have not directly compared point clouds as they have first interpolated the points into raster DSMs and then compared these using pixel-based techniques (Matsuoka and Yamazaki, 2004; Murakami, 1999; Vögtle and Steinle, 2004). Interpolation results in loss of data and can introduce inaccuracy into detected change statistics. Point-based comparison techniques have also been studied (Butkiewicz et al., 2008;

[7] `https://photosynth.net/`

Girardeau-Montaut et al., 2005; Knauer and Löffler, 2009; Mémoli and Sapiro, 2004). These methods use the raw, irregularly spaced ALS points and thus overcome the limitations inherent in a method that relies on interpolation. However, even these cloud-to-cloud comparison algorithms, such as those used in Girardeau-Montaut et al. (2005) may sacrifice precision in exchange for faster data processing. Kang and Lu (2010) assessed Hausdorff distance for change analysis using TLS data and concluded it is an accurate change quantification solution when datasets are accurately registered or coregistered. In studies that are focussed on detecting and quantifying small changes, such as in deformation monitoring (Monserrat and Crosetto, 2008; Dowling et al., 2009; Kang and Lu, 2010; Scaioni and Alba, 2010), the choice of technique plays a critical role, the aim being to avoid any loss of data while managing the comparison of often very large detailed datasets.

6.2.2 Study Site

An erosion monitoring study is being undertaken along a sheltered estuarine coastline in south eastern Tasmania, Australia, known as Pittwater Estuary (Figure 6.1). The 15 m section of coast is an erosion scarp that has been gradually eroding since monitoring began in 2010. The site was mapped using UAV-MVS techniques in November 2010, March 2012 and November 2013 (as described in Chapters 2, 3, 4, and 5).

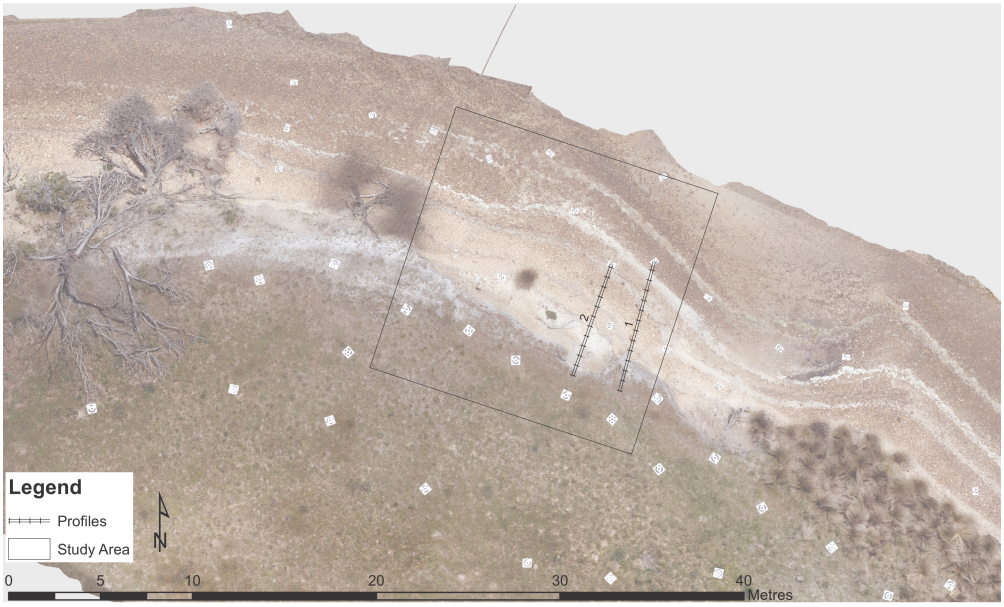

Figure 6.1: Study Site map showing study site boundary and profile locations overlayed on 2014 orthophoto.

6.2.3 Hardware

The UAVs used for this study are based on the OktoKopter electric multi-rotor micro-UAV platform (Mikrokopter, 2012). In 2010, the UAV was capable of carrying a payload of ~1 kg and the larger UAV used in 2012 and 2013 can carry a ~2.5 kg payload for approximately 8–10 minutes. An on-board navigation grade GPS (5–10 m positional accuracy), IMU, 3D digital compass, and barometric altimeter allow the system to navigate to predefined waypoints. A Canon 550D digital SLR camera with a 20 mm prime lens is attached to a stabilised camera mount that allows camera tilt to be controlled by the UAV operator (a zoom lens was used in 2010). This camera has a lightweight body and provides control over ISO, aperture and shutter speed settings. Focus was fixed at infinity and the camera settings were carefully chosen to reduce motion blur when acquiring images at 1 Hz (one photo per second, 1/1250 shutter speed). In 2010 and 2013, a Leica TC407 total station theodolite and a TS06 plus total station theodolite were used to capture ground control points (explained in Chapter 4). In 2012, a Leica 1200 real-time kinematic dual-frequency differential GPS system was used to capture GCP coordinates.

6.2.4 UAV Survey

In 2010 the images were captured from 30–50 m above ground level (AGL) using two nadir flight lines that followed the coastline (as described in Chapter 3). Similarly, in 2012, two nadir flight lines were flown at approximately 25–35 m AGL and, in addition, a number oblique images were captured focussing on the scarp. In 2013, a more rigorous flight plan was designed that incorporated more flight lines of both nadir and oblique imagery (as described in Chapter 4 and Chapter 5) and extended 20–30% beyond the main study area. Imagery was captured from approximately 20–25 m AGL.

The image sets for 3D reconstruction were chosen from the large set of captured images based on overlap and image clarity. In 2010 and 2012 the goal was 70–85% overlap and in 2013 the majority of the area was imaged with 80–90% overlap. These image sets were used to derive three 3D reconstructions of the terrain using Agisoft PhotoScan Professional (version 1.1.2) (Agisoft LLC) and georeferenced by locating the GCP markers in the photographs using the PhotoScan ground control marker tools. The derived point clouds were then exported as LAS files.

6.2.5 Digitising shoreline proxies

The UAV-MVS process results in points that are naturally coloured and the 3D view of the dense cloud has photo realistic qualities. The terrain was examined in detail from a range of perspectives and the shape of the landscape was analysed. The scarp edge was followed closely when digitising in 3D by navigating around the cloud to accurately determine where the terrain fell away at the scarp. The vegetation was also visible and this allowed the vegetation line to be digitised.

6.2.6 Quantifying point cloud differences as distances

2010 was compared to 2012 and 2013, and 2012 was compared to 2013 using CloudCompare. In each case, the older epoch was used as the reference and the more recent as the comparison cloud. Hausdorff distance was calculated for each point in the comparison cloud by measuring the largest distance from a point in the reference point cloud to the closest point in the comparison cloud. Each point in the comparison cloud was assigned attributes describing the absolute Euclidean distance and the distance in X, Y and Z directions. The direction of change and volumetric data could not be calculated. In addition, the shoreline proxies from each epoch were compared visually and the distances between the digitised polylines were measure manually.

6.3 Results and Discussion

6.3.1 Point cloud comparison

The point clouds produced by UAV-MVS are very dense with up to 6 points per cm^2. The estimate absolute accuracy of point cloud 2010, 2013 and 2013 were 1–2 cm, 2–4 cm and 6 mm, respectively (the 2013 dataset was assessed in Chapter 5). The process results in points that are naturally coloured and the 3D view of the dense cloud has photo realistic qualities. Visualising dense point clouds requires software that can render a large number of points and that allows control of symbology to render each point in the average colour from the photography. EonFusion[8] was used to visualise the 3D point cloud models of the study site for the three dates in the figures below.

The dense clouds produced by UAV-MVS provided a means of examining the terrain

[8] `http://www.eonfusion.com/`

Figure 6.2: Naturally coloured UAV-MVS point cloud for 2010.

Figure 6.3: Naturally coloured UAV-MVS point cloud for 2012.

Figure 6.4: Naturally coloured UAV-MVS point cloud for 2013.

in detail from a range of perspectives. The shape of the landscape was analysed to inspect and monitor features such as overhangs and erosion scalloping along the scarp. This ability to navigate around the cloud improved the accuracy of shoreline extraction because the scarp edge could be followed closely when digitising in 3D. The density of the point cloud and the photo realistic qualities meant that the vegetation was clearly visible and this allowed the vegetation line to be digitised. The seasonal difference can be seen in the 2012 (Figure 6.3) which was captured in March (the end of summer) and had much drier grass than the November epochs (Figure 6.2 and Figure 6.4). These seasonal differences can affect vegetation edge delineation.

Point cloud completeness is dictated by the camera network and if portions of the cliff are not visible in sufficient images there will be no points or few points in the resulting cloud. In 2010 (Figure 6.2), sparse areas exist under the eastern overhang and on the steep face on the western end. These occluded areas were a result of sub-optimal flight

planning and UAV positioning inaccuracy. There were similar areas of occlusion in the 2013 dataset (Figure 6.4). This occlusion was problematic for cloud differencing because the nearest neighbour search associated points from a part of the dense cloud in one epoch with the nearest points in the other epoch that are on the edge of the sparse area caused by occlusion. This resulted in a large difference and gave a false impression of change. A solution to this is to exclude sparse sections from the differencing by removing the points in sparse areas from each epoch (which was not done in this study).

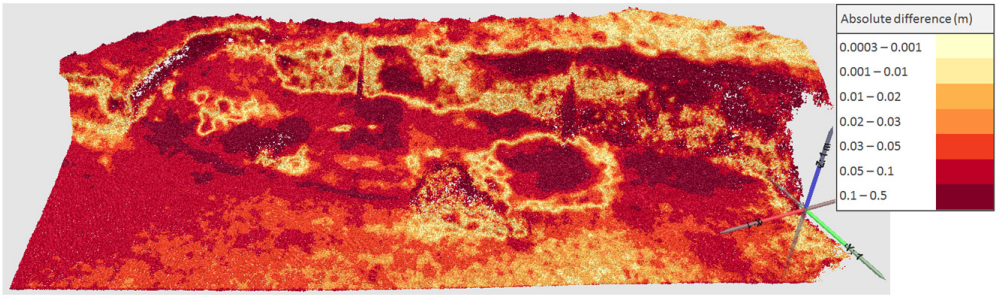

Figure 6.5: Absolute difference for 2010 versus 2012.

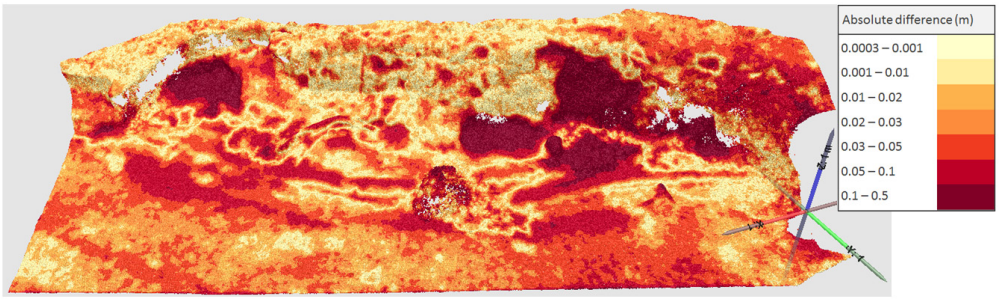

Figure 6.6: Absolute difference for 2012 versus 2013.

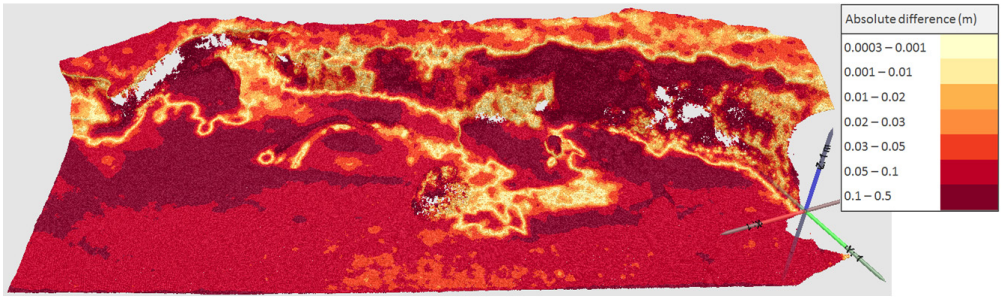

Figure 6.7: Absolute difference for 2010 versus 2013.

CloudCompare compares a more recent cloud to an older epoch (the reference point cloud). The resulting absolute difference measurements are portrayed in (Figure 6.5, Figure 6.6 and Figure 6.7). The majority of the difference was less than 5–10 cm. When comparing the 2010 and 2012 point clouds (Figure 6.5) the majority of erosion apparently occurred to the western end of the scarp with soil collapse resulting in soil build up at the base of the cliff. The sparse areas in the 2010 and 2013 point clouds gave a false

impression of change. This was seen again in the comparison of 2013 to 2010 (Figure 6.7) due to the areas of occlusion in similar areas in the 2013 dataset (Figure 6.4), however, in this case the occluded areas were smaller. Between 2012 and 2013 (Figure 6.6) the differences were generally smaller. In areas where the cloud was uniformly dense in each epoch actual change could be detected. For example, the collapse of the steep section of cliff towards the centre of the scarp is visible (up to 500 mm of the scarp broke away) and the soil build up below it is also clear.

6.3.2 Profile comparisons

An additional visualisation technique for analysing the coastal change to reveal the type of changes that are occurring and give insight into the direction of change was to overlay profiles extracted from the change datasets (Figures 6.5–6.7) on the profiles from the reference datasets (Figures 6.2–6.4), shown in natural colour.

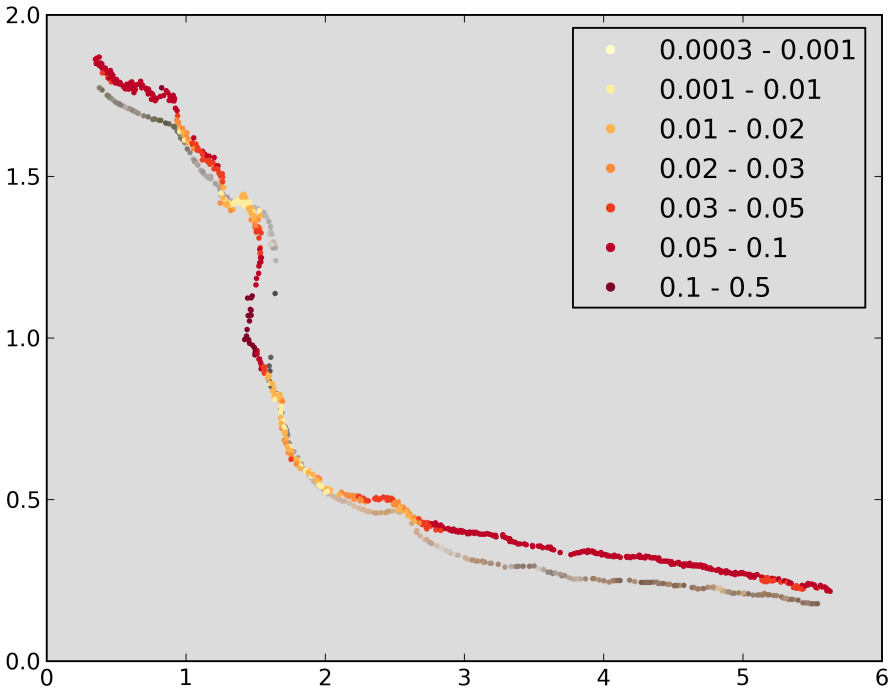

Figure 6.8: Profile 1 extracted from 2010 and absolute difference between 2010 and 2012 shown on the 2012 dataset (axes and legend units are metres).

A number of interesting features were visible in these profiles. In Figure 6.8, the eroded portion of the bank was clearly visible and the greatest change could be measured between the two profiles (17 cm). The grass was longer at the top of the profile and the beach was higher at the base of the profile. In Figure 6.9, the erosion was again

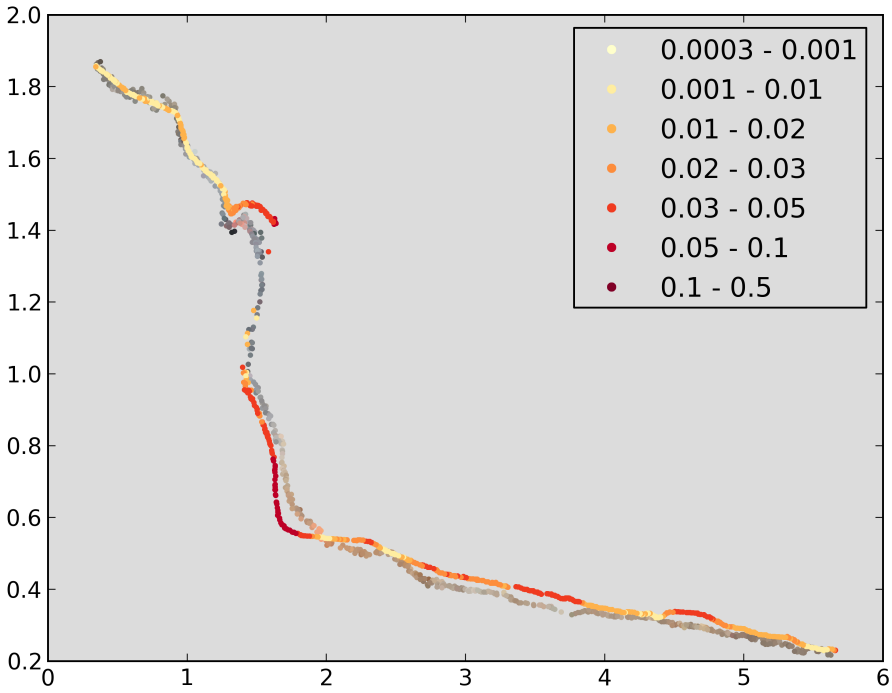

Figure 6.9: Profile 1 extracted from 2012 and absolute difference between 2012 and 2013 shown on the 2013 dataset (axes and legend units are metres).

visible, however, the top of the bank appeared to have grown, this was most likely due to the cracks further up the slope that in places were 3–4 cm wide and the bank was leaning forward prior to collapse. In Figure 6.10, the crack was visible as a depression in the profile and the erosion was again clear (21 cm where the difference is greatest). Profile 2 (Figure 6.11, Figure 6.12 and Figure 6.13) showed that the portion of the scarp that appears to have not eroded between 2010 and 2013 (Figure 6.13) had in fact eroded gradually and the rubble had moved onto the beach. The level of the beach had risen 15 cm. The changes could be analysed by exploring these datasets in this way, however, the analysis was a manual process and therefore time consuming. The direction of change could be determined and the difference between the two profiles give visual insight into volume change.

6.3.3 Extracted shoreline comparisons

Scarp edge and vegetation were digitised from the point cloud data. The scarp edge was clearly visible in the 3D point cloud and this resulted in a very accurate scarp edge from each epoch. The vegetation was more difficult to digitise and the seasonal differences impacted on the extent of the vegetation and the colour. The similarity between the soil colour and the dry grass colour impacted on the accuracy digitising of the vegetation

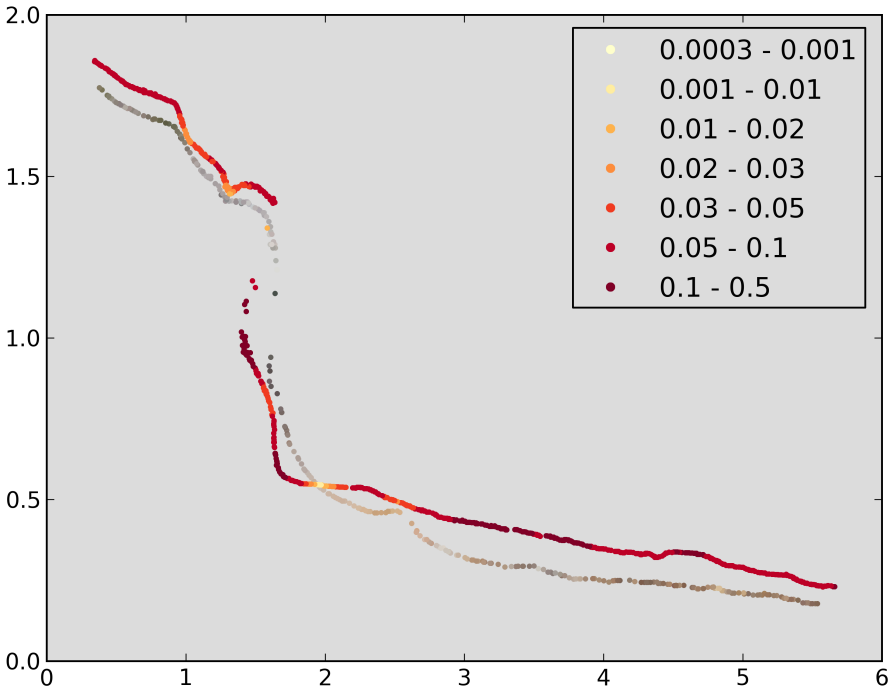

Figure 6.10: Profile 1 extracted from 2010 and absolute difference between 2010 and 2013 shown on the 2013 dataset (axes and legend units are metres).

line.

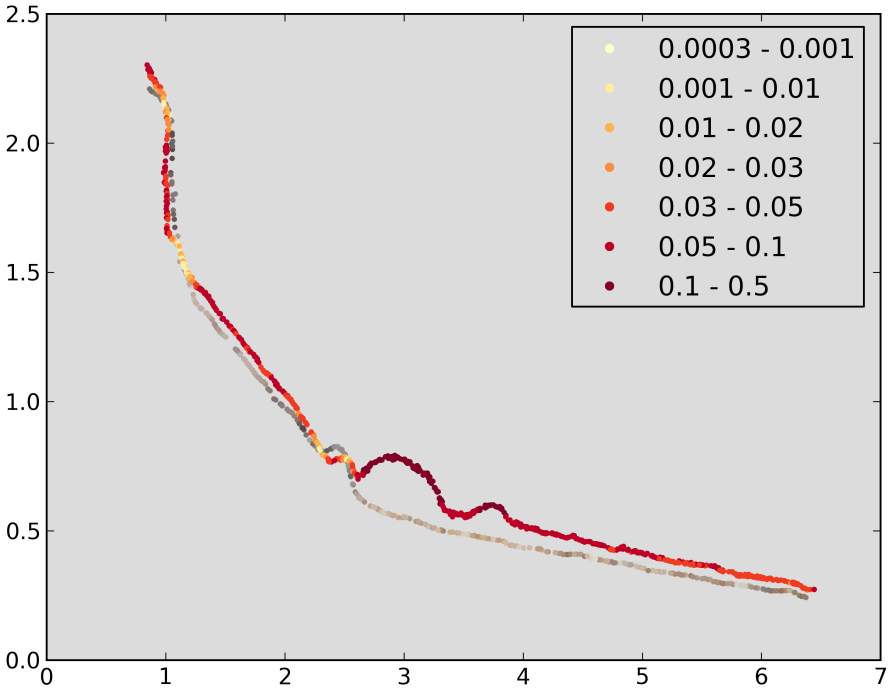

Figure 6.11: Profile 2 extracted from 2010 and absolute difference between 2010 and 2012 shown on the 2012 dataset (axes and legend units are metres).

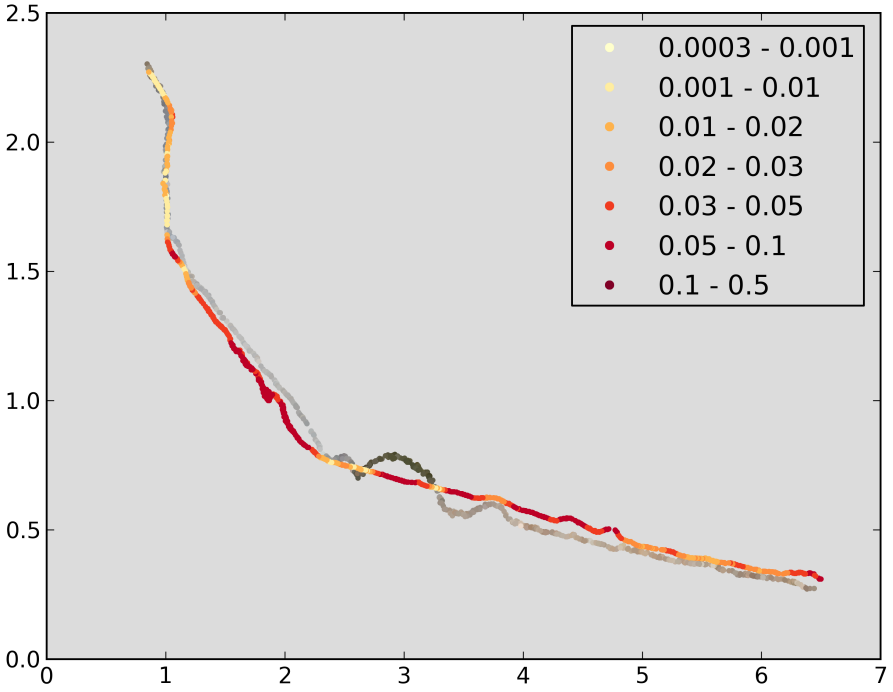

Figure 6.12: Profile 2 extracted from 2012 and absolute difference between 2012 and 2013 shown on the 2013 dataset (axes and legend units are metres).

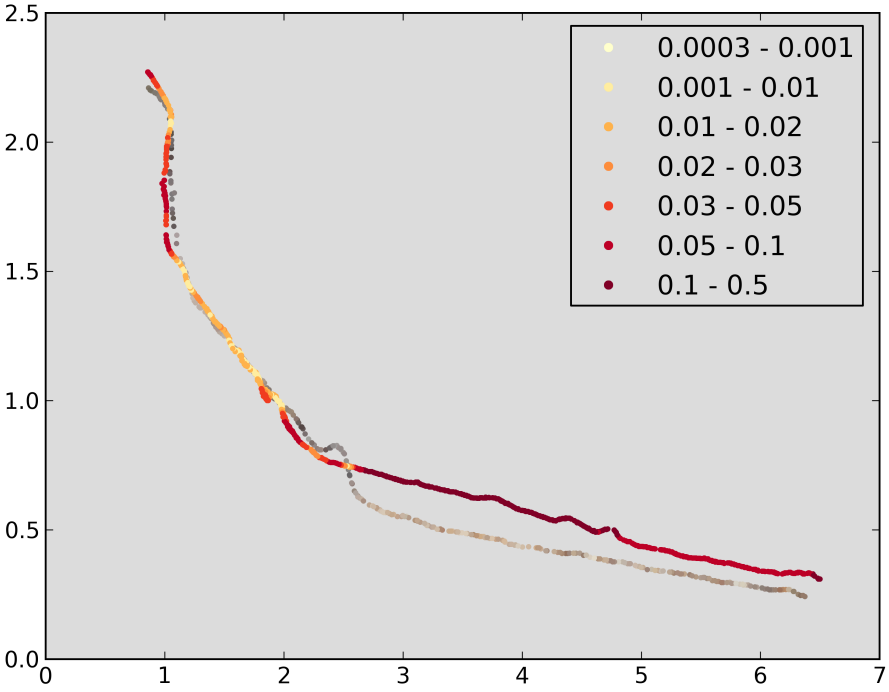

Figure 6.13: Profile 2 extracted from 2010 and absolute difference between 2010 and 2013 shown on the 2013 dataset (axes and legend units are metres).

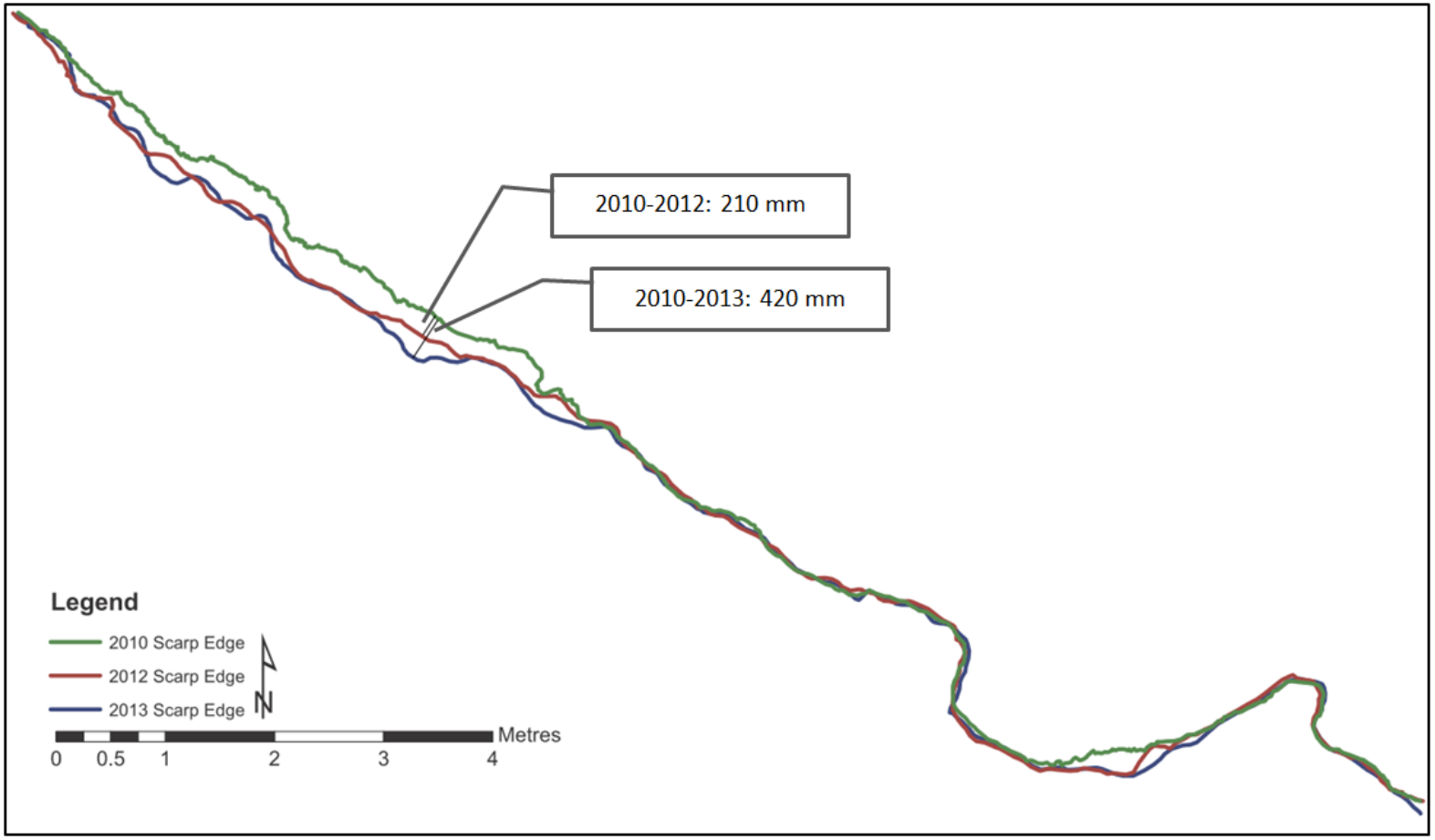

Figure 6.14: Coastline comparison showing 2010, 2012 and 2013 digitised scarps (top edge).

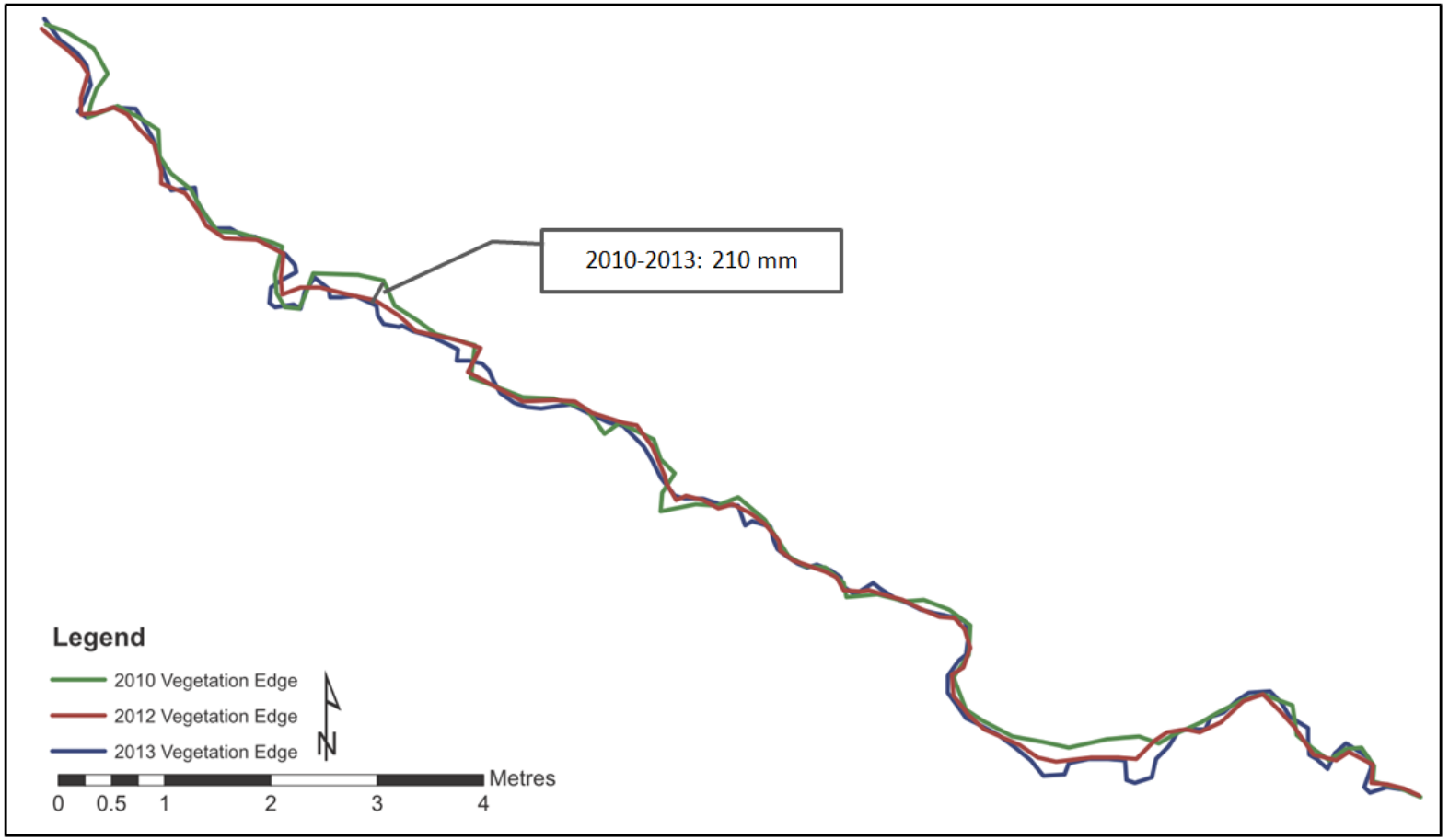

Figure 6.15: Coastline comparison showing 2010, 2012 and 2013 digitised vegetation edge.

The comparison between epochs using the scarp edge (Figure 6.14) provided a good approximation to the change shown in the absolute difference point clouds (Figures 6.5–6.7). Similarly, the areas that saw minimal erosion overlay each other closely, which indicates that the georeferencing was accurate and the section of scarp that did not erode could be delineated accurately. This was not the case when using the digitised vegetation edge (Figure 6.15). The change was not well represented and significantly under-estimated. The cause of this was the pattern of growth along the scarp edge. The vegetation did not extend to the scarp edge, and in most cases the vegetation shoreline proxy was 100–400 mm landward of the scarp edge. Vegetation edge was a poor proxy for shoreline at the scale of data produce in this UAV-MVS survey. Scarp edge was more representative of the shoreline at this scale and provided a reasonable estimation of change.

6.4 Conclusion

UAV-MVS point clouds representing an eroding section of sheltered coastline were created from UAV surveys in 2010, 2012 and 2013. The clouds were registered using surveyed GCPs and not coregistered due to the lack of common features through time in this natural landscape. The change detection therefore relied on the georeferencing accuracy of the individual point clouds to measure absolute difference between the clouds. This illustrates the issues of coregistration in natural landscapes. In these real-world scenarios, common features may not exist naturally that can be used for the coregistration. In a future study, a fourth epoch of this terrain will be measured using the more robust data capture and design guidelines outlined in Chapter 4 and Chapter 5. This should result in a more accurately georeferenced point cloud that will closely match the location of the 2013 dataset (which was captured using the more robust data capture design and registered using more accurate control than the 2010 and 2012 datasets). A second issue faced when comparing these epoch was the occlusion that resulted in sparse portions of the point clouds from 2010 and 2013. These areas resulted in false change. The camera network design needs to be more carefully planned to ensure point cloud completeness. A third issue faced was the absolute difference calculated in the point cloud comparison. This does not give change direction and volumetric change statistics. To understand the direction of change and to calculate volume of erosion and accretion the datasets need to be converted to surfaces and DEM difference used to quantify change. That will be the focus of a future study.

Three methods of visualising coastal change were evaluated. The first technique comprised of spatial views of the absolute distance measurements between points in a reference point cloud to the nearest point in the comparison point cloud. These distances were symbolised on the comparison point cloud in a 3D scene. The second technique consisted of profile comparisons extracted from the point clouds. The third was a comparison of two shoreline proxies, scarp edge and vegetation edge. The spatial views are a comprehensive visualisation of change, however, the differencing tool produced absolute difference, which can lead to difficulties in discerning erosion from accretion. Future research will investigate methods for improving this differencing to provide information on the direction of change. This change direction information will also allow volumetric quantification of change. The profile comparisons overcome some of the issues of absolute difference as the two profiles can be compared in the same plot. This allows the analysis of change direction (erosion versus accretion) and the manual measurement of change. Future research will modify the profile comparison algorithm developed in Chapter 4 and Chapter 5 to provide statistics describing change along a profile. The final method of visualising coastal change was the comparison of shoreline proxies. The scarp edge was far more representative of the coast location in each epoch and provided useful estimates of change. Vegetation edge is not useful at this site but may provide a realistic representative shoreline when the vegetation grows at the edge of the eroding terrain.

The UAV-MVS survey technique is a cost-effective tool for coastal monitoring that can provide very high spatial and temporal resolution datasets. The georeferenced point clouds can be used to detect change. The reliability of change detection is closely linked to point cloud completeness and georeferencing accuracy (particularly when coregistration is not possible). The guidelines offered in Chapter 4 and Chapter 5 have the potential to improve results and allow for more robust change monitoring. This study has demonstrated that centimetre-scale change can be detected, quantified, and visualised. Regular UAV-MVS surveys will provide detailed terrain time series that will give insight into the response of specific coastal morphologies and sediments to changes in sea level.

Thesis context

An overarching aim of this thesis is to prove that UAV-MVS surveys are a viable method for monitoring coastal erosion at scales that are difficult to map using traditional remote

sensing options. The previous chapters assessed the accuracy of the process and with that knowledge this chapter has been able to evaluate centimetre-level coastal change monitoring options for UAV-MVS point cloud data, specifically cloud differencing, profile comparison and shoreline definition options.

Acknowledgements

The author thanks Chris Sharples (University of Tasmania) for his advice on site selection, coastal geomorphology, vulnerability and monitoring and Vishnu Prahalad (University of Tasmania) for his advice on saltmarsh and coastal vulnerability and vegetation types.

7 | Conclusion

There is a need for rigorous assessment of the accuracy unmanned aerial vehicle structure-from motion (UAV-MVS) terrain mapping to evaluate its potential as a high spatial and temporal resolution coastal monitoring tool. This study assessed the accuracy of UAV-MVS in the context of mapping a natural landscape at centimetre resolution. To evaluate the technique, dense point clouds were derived from images captured of an eroding section of sheltered coastline. UAV-MVS surveys at different time epochs were compared and change detected. Survey design decisions relating to camera calibration, flight planning, ground control distribution, and ground control density were investigated. A precise total station survey technique was used to coordinate ground control and verification points in order to assess derived point cloud accuracy. Photogrammetric simulations were undertaken to predict accuracy and these were compared to actual survey results to assess those predictions. The impact of establishing ground control using lower precision differential GPS (DGPS) or differential GNSS (Global Navigation Satellite Systems) was also assessed. Profiles were used to compare datasets and visualise point density, accuracy and precision, and to assess the detected change. In addition, shorelines were digitised and compared to assess their suitability for change monitoring at these scales. This study has demonstrated that the UAV-MVS technique is an effective and accurate method for mapping coastal erosion at the centimetre scale when sufficient ground control is used and the camera network is well-designed.

7.1 UAV-MVS Accuracy Assessment

Objective 1: Assess how accurately an area of natural terrain can be mapped using UAV-MVS.

The initial accuracy assessment compared high precision (total station survey) coordinates of verification points with coordinates of the same verification points derived from UAV-MVS derived point clouds (Chapter 2). The comparison total station survey verification point coordinates were estimated to be accurate to ~1 cm horizontally and ~2 cm vertically. The point clouds were generated using Bundler and PMVS2 and georeferenced via a Helmert transformation. The initial assessment also compared control point density. The results indicated that, when flying at 40–50 m above ground level (AGL) and using a well-placed control network, the technique can deliver accuracies

of ~2.5 cm horizontally and ~4 cm vertically. The resulting assessed accuracy is very similar to the precision of the DGPS survey technique used to coordinate the control. It was decided that this similarity between the ground control point (GCP) survey coordinate precision and the assessed point cloud accuracy combined with the precision of the verification point coordinates were potentially masking the true accuracy of the technique. The experiment used to assess accuracy in Chapter 4 and Chapter 5 ensured that verification point coordinates were very precise (5–10 times more accurate than the hypothesised accuracy of the UAV-MVS survey technique) and that the impact of GCP precision on model accuracy could be assessed.

The point clouds produced by UAV-MVS have 1–6 points per cm^2 when the site is imaged from 25–50 m above ground level (AGL). For such dense datasets to be used in spatial applications they usually need to be converted to surface models that reduce dataset size without losing too much detail. Triangulated meshes are one option for creating a continuous surface from the derived point clouds; another is Poisson surface reconstruction that uses point normal data. Chapter 3 aimed to assess the potential of converting point clouds to surface models prior to change detection by visualising and comparing these two surface representations created from terrestrial MVS (T-MVS) and UAV-MVS. The results indicated that, while these representations were useful for reducing dataset size, the artefacts introduced by the conversion may confuse change detection at the high resolutions possible with UAV-MVS.

Chapter 4 evaluated calibration options in the context of camera network design, GCP survey precision, and GCP density. The results indicate that on-screen checkerboard calibration is the least accurate method. When control is precise (+/- 1–2 mm), the accuracy of results is less sensitive to design choices such as whether or not oblique imagery is included. When control precision is degraded to differential GNSS/DGPS equivalent precision (+/- 22 mm) the sparse control point distribution and poor camera network strength can reduce the object space accuracy of the UAV-MVS model due to poor camera calibration parameter estimation.

Chapter 5 assessed accuracy in the context of ground control survey method and GCP distribution. Verification point locations in the UAV-MVS model were compared to precisely surveyed (+/- 1–2 mm) validation point coordinates to assess whether simulated achievable precision could be verified by an empirical accuracy assessment. When control has differential GNSS/DGPS equivalent precision (+/- 22 mm) the assessed UAV-MVS point cloud accuracy was 10–12 mm (1σ) and the simulated achievable accuracy was ~9 mm (1σ). When control is precise the point cloud produced by the UAV-MVS survey

is accurate to better than 6 mm (1σ). When very precise ground control coordinates (+/- 1–2 mm) are assumed in the simulation, the resulting predicted object space precision is significantly higher than was achieved in the empirical tests. This suggests that the precision achieved in practice is being limited by residual systematic errors, most probably attributable to inaccuracy in the camera calibration.

7.2 UAV-MVS Survey Design

Objective 2: Develop operational guidelines to guide UAV survey design decisions.

Overcoming the issues identified in Chapter 2 involved designing and undertaking an experiment that compares various flight planning and processing configuration choices (camera calibration options, ground control distribution and camera network design). The comparisons required a precise total station survey of ground control and verification points.

The self-calibrating bundle adjustment uses observed GCPs and a large number of conjugate image (tie) points to simultaneously solve for the interior and exterior orientation parameters of all photo stations. The dense point cloud comes from an intersection process following the bundle adjustment solution. The estimated camera distortion was modelled in the photogrammetric solution based on the camera model coefficients derived from the adjustment. The alternative is to pre-calibrate the camera and fix those coefficients in the bundle adjustment. Chapter 4 compared calibration options and Chapter 5 sought to strengthen our understanding of the impacts of survey design choices. The creation of a detailed pre-planned camera network design requires expertise and, in most cases 3D (or 2.5D) *a priori* data, however, "in the field" flight planning may be sufficient to achieve acceptable results. The calibration assessment found that robust pre-calibration or self-calibration can both result in accurate UAV-MVS point clouds when control is well-distributed and sufficiently dense (in this case study: 13 GCPs distributed around the periphery and through the centre of the area). Both studies resulted in a number of design guidelines that can be used to guide UAV-MVS survey design. It was found that vertical accuracy is particularly susceptible to poor GCP distribution and density. When control precision is degraded to the differential GNSS/DGPS equivalent the sensitivity to design choices increases. Including oblique imagery improves the results and is advised. Ensuring image overlap is 70–90% and that the flight plan extends to 20–30% beyond the study area reduces the likelihood of model distortion. The UAV-MVS technique can produce image datasets with high

levels of redundancy and this coupled with high overlap and the inclusion of well-placed oblique imagery focussing on complex terrain features can allow ad-hoc flight planning in the field.

7.3 Coastal Erosion Monitoring

Objective 3: Detect differences between UAV-MVS point clouds and quantify change.

The large datasets generated by UAV-MVS can be converted to surface representations, however, this can result in artefacts in the data that influence the reliable detection of change. Chapter 3 evaluated triangulated mesh and Poisson reconstruction as two surface generation options. Poisson reconstruction uses the point normal in the interpolation and this reduced the likelihood of artefacts, however, the conclusion was that point cloud differencing was the preferable method of change detection for UAV-MVS data. Point cloud differencing provides a measurement of the distance between each point in a reference cloud and its nearest neighbour in the comparison cloud. The method tested in Chapter 6 produced absolute distances and did not provide an indication of change direction, which hinders analysis of erosion and accretion. Profile analysis gave insight into the direction of change and can allow measurement of change. The final method of comparing change was the use of a shoreline proxy. Scarp edge was found to be a more representative feature than vegetation edge as an indicator of shoreline and to allow for change quantification. The change detection is impacted by georeferencing inaccuracy and ideally each epoch would be coregistered to a reference dataset. Unfortunately, common features are often not available in natural landscapes that are undergoing change. This highlights the importance of careful survey design and accurate ground control. The final chapter of this thesis demonstrated the applicability of UAV-MVS to centimetre-scale terrain change monitoring. The detection of coastal erosion at a site that is sheltered from the influence of ocean swell may provide insight into the impact of sea level rise and other influences on the coast.

7.4 Contributions to knowledge

There is rapid growth in the application of UAVs to surveying and mapping. The accuracy assessments and change detection studies undertaken in this thesis have contributed to knowledge in the field of UAV photogrammetry and coastal erosion monitoring in the

following ways:

7.4.1 UAV Photogrammetry

- This is the first study that has undertaken a ground truth survey to +/-1–2 mm precision for the purpose of assessing the accuracy of the UAV-MVS 3D reconstruction techniques for mapping natural landforms.
- This study verified that photogrammetric simulation can predict achievable accuracy when control is mapped using the most common survey technique (differential GNSS/DGPS survey).
- This study developed new profile comparison methods for assessing point cloud accuracy and density.
- This study developed guidelines for the design of UAV-MVS surveys based on careful assessment of choices relating to camera calibration options, camera network design (image overlap and oblique imagery inclusion), ground control density and distribution.

7.4.2 Coastal Erosion Monitoring

- This study evaluated options for converting UAV-MVS point clouds to surface models (TIN and Poisson reconstruction) for coastal change monitoring.
- The chosen study site is indicative of fragile sheltered coastlines and this study demonstrated that the spatial and temporal resolutions offered by UAV-MVS dense point clouds can provide insight into the causes of erosion.
- This study assessed methods for quantifying point cloud change and generated visualisations of coastal change by comparing accurate UAV-MVS point clouds.
- This study compared scarp edge versus vegetation edge derivation as proxies for the shoreline and scarp edge was found to be more representative at the scale offered by UAV-MVS.

7.5 Limitations and future research directions

UAV-MVS provides an effective mapping technique that augments lower resolution remote sensing such as aerial photography or satellite remote sensing. Current limitations on UAV flight duration and payload capacity are linked to battery life, but advances in this field are expected to allow UAVs to fly for longer and/or carry sensor payloads that deliver very high resolution datasets. The study site targeted here was relatively small so that the terrain could be mapped in a small number of flight lines.

The dense point clouds produced are potentially problematic when analysing the data in GIS applications and the common solution is the convert the point cloud to a surface. More research is required into the impact of the interpolation and generalisation that occurs during this conversion. Surface generation methods such a Poisson reconstruction have the potential to minimise these artefacts by incorporating knowledge of the point normal into the interpolation. The software available for point cloud comparison, such as CloudCompare, also provides tools for comparing point clouds to surfaces and classifying features of the terrain. The methods for deriving feature level change, volumetric data and change vectors need to be evaluated and developed so as to maximise the advantage provided by the high density point clouds UAV-MVS offers.

The available software tools for MVS are advancing steadily. Unfortunately, certain steps in the processing chain and assumptions about settings cannot be verified because commercial software often contains little detail on the algorithms used and assumptions made. For example, the marker accuracy setting in PhotoScan is a single number for all markers as opposed to a number for each marker in each dimension (X, Y and Z) (as is offered in VMS).

The thesis has focussed on a coastal site to demonstrate the technique and assess its accuracy. The technique is applicable in a range of other applications. Current and future research will assess that applicability. Other application areas include: other forms of erosion and terrain change (river and gully erosion and landslides); mine mapping (stock pile measurement, deformation monitoring and remediation assessment); precision agriculture and forestry (vegetation height monitoring, drainage and terrain mapping); and archaeology and building monitoring.

This thesis has not assessed the potential accuracy of direct georeferencing with onboard DGPS. The use of sky control can be expected to require careful planning and design, particularly when using self-calibration. For example, the design might require

capturing imagery from multiple heights to avoid issues that can arise when all control is in the same Z plane.

Chapter 6 provided an evaluation of the point cloud differencing and shoreline comparison options. The accuracy of the georeference point clouds produced in the first two epochs was compromised by the flight planning and survey design used. The final epoch was captured using more robust survey design and very accurate control. The next epoch of data captured for this site will adhere to the design guidelines outlined in Chapter 4 and Chapter 5, and so the results should be a more comparable dataset that more closely matches the georeferenced location of the 2013 dataset and will provide better change detection data.

7.6 Final Remarks

UAV photogrammetry is a booming field of spatial science, photogrammetry and remote sensing. A range of issues need to be resolved in order to create accurate time series datasets needed to undertake change detection at the spatial and temporal resolutions possible with this technique. This research chose to focus on coastal change detection as a demonstration of the accuracy of the technique and the suitability of UAV-MVS for sub-decimetre and centimetre-scale terrain mapping and change detection. To understand the detected change it is important to consider the choice of shoreline definition method and, most importantly, the accuracy of the georeferenced point clouds in the time series.

Monitoring of coastal erosion in sheltered waterways is required if scientists are to gauge the impact of sea level rise and other influences on these coasts. Subtle changes that are indicators of long-term trends can be masked by event-driven change. The best way to separate these processes is to regularly monitor at temporal and spatial resolutions that provide sufficient detail to discern changes that are gradual and small from those that are more profound and perhaps exacerbated by the more subtle influences on coastal vulnerability. The scale of change that can be mapped with the UAV-MVS technique is dictated by the accuracy of the derived models. The design of the UAV-MVS survey will dictate the achievable accuracy. This research provides guidelines for that design and a robust assessment of accuracy under different design scenarios.

This thesis has provided guidelines for survey design that will help consolidate the technique as an operationally viable survey and monitoring tool. The assessment of

UAV-MVS accuracy in this study i) provides verification that simulation can aid in survey design, ii) shows that robust calibration of the camera can be undertaken prior to or as part of the UAV-MVS survey, and iii) that camera network design and ground control distribution density are key design considerations. The work presented in this thesis provides guidance for UAV-MVS survey design that will be useful in all UAV-MVS applications.

References

Abdel-Aziz, Y. (1974). Expected accuracy of convergent photos. *Photogrammetric Engineering* 197, pp. 1341–1346.

Abdel-Aziz, Y. (1982). Accuracy of the normal case of close-range photogrammetry. *Photogrammetric Engineering and Remote Sensing* 48 (2), pp. 207–213.

Abdel-Aziz, Y. and Karara, H. (1971). Direct linear transformation from comparator coordinates into object space coordinates in close-range photogrammetry. *American Society for Photogrammetry Symposium on Close-range Photogrammetry, Urbana, Illinois, USA*, pp. 1–18.

Adams, J. and Chandler, J. (2002). Evaluation of Lidar and Medium Scale Photogrammetry for Detecting Soft-Cliff Coastal Change. *The Photogrammetric Record* 17 (99), pp. 405–418.

Afana, A, Solé-Benet, A, Pérez, J., and Gilkes, R. (2010). Determination of soil erosion using laser scanners. *Proceedings of the 19th World Congress of Soil Science*. August, pp. 39–42.

Ahmadabadian, A. H., Serpico, M., and Robson, S. (2012). Automatic Image Selection in Photogrammetric Multi-view Stereo Methods. *VAST International Symposium on Virtual Reality, Archaeology and Cultural Heritage*.

Ahmadabadian, A. H., Robson, S., Boehm, J., Shortis, M., Wenzel, K., and Fritsch, D. (2013). A comparison of dense matching algorithms for scaled surface reconstruction using stereo camera rigs. *ISPRS Journal of Photogrammetry and Remote Sensing* 78, pp. 157–167.

Al-Hatrushi, S. (2007). Shoreline Monitoring at Al Hawasina tidal inlet using remote sensing and GIS techniques. *ACRS2007, The 28th Asian Conference on Remote Sensing,* 1992.

Alesheikh, A., Ghorbanali, A, and Nouri, N (2007). Coastline change detection using remote sensing. *International Journal of Environmental Science Technology* 4 (1), pp. 61–66.

Alhin, K. A. and Niemeyer, I. (2009). Coastal monitoring using remote sensing and geoinformation systems: Estimation of erosion and accretion rates along Gaza coastline. *2009 IEEE International Geoscience and Remote Sensing Symposium*. Ieee, pp. IV–29–IV–32.

Anders, F. J. and Byrnes, M. R. (1991). Accuracy of shoreline change rates as determined from maps and aerial photographs. *Shore and Beach* 59 (1), pp. 17–26.

Anderson, K. and Gaston, K. J. (2013). Lightweight unmanned aerial vehicles will revolutionize spatial ecology. *Frontiers in Ecology and the Environment*, p. 130318104718008.

Aspert, N., Santa-Cruz, D., and Ebrahimi, T. (2002). MESH: measuring errors between surfaces using the Hausdorff distance. *Proceedings. IEEE International Conference on Multimedia and Expo*, pp. 705–708.

Azab, M. and Noor, A. (2007). Change Detection of the North Sinai Coast by Using Remote Sensing and Geographic Information System. *Geographia Technica* 2 (10), pp. 1–10.

Bae, K and Lichti, D (2008). A method for automated registration of unorganised point clouds. *ISPRS Journal of Photogrammetry and Remote Sensing* 63 (1), pp. 36–54.

Baillard, C. and Zisserman, A (2000). A plane-sweep strategy for the 3D reconstruction of buildings from multiple images. *ISPRS Journal of Photogrammetry and Remote Sensing*, pp. 56–62.

Baltsavias, E. (1999). A comparison between photogrammetry and laser scanning. *ISPRS Journal of Photogrammetry and Remote Sensing* 54 (2-3), pp. 83–94.

Barazzetti, L, Remondino, F, and Scaioni, M (2010). Automation in 3D reconstruction: results on different kinds of close-range blocks. *International Archives of Photogrammetry, Remote Sensing and Spatial Information Sciences, Vol. XXXVIII, Part 5 Commission V Symposium*. Vol. XXXVIII. 5. Newcastle upon Tyne, UK.

Barnea, S and Filin, S (2008). Keypoint based autonomous registration of terrestrial laser point-clouds. *ISPRS Journal of Photogrammetry and Remote Sensing* 63 (1), pp. 19–35.

Barnea, S. and Filin, S. (2010). Geometry-image-intensity combined features for registration of terrestrial laser scans. *PCV 2020 IISPRS Commission III Symposium Photogrammetric Computer Vision and Image Analysis*. Vol. XXXVIII. 2008, pp. 145–150.

Bay, H., Tuytelaars, T., and Van Gool, L. (2006). Surf: Speeded up robust features. *Proc. Computer Vision-ECCV 2006, Graz, Austria, May 7-13*. Springer, pp. 404–417.

Bemis, S., Micklethwaite, S., and Turner, D. (2014). Ground-based and UAV-Based photogrammetry: A multi-scale, high-resolution mapping tool for structural geology and paleoseismology. *Journal of Structural Geology* 69, pp. 163–178.

Berni, J., Zarco-Tejada, P., Suarez, L., Gonzalez-Dugo, V., and Fereres, E. (2009a). Remote sensing of vegetation from uav platforms using lightweight multispectral and thermal imaging sensors. *ISPRS Hannover Workshop 2009 HighResolution Earth Imaging for Geospatial Information*.

Berni, J. A. J., Zarco-Tejada, P. J., Suárez, L., and Fereres, E. (2009b). Thermal and Narrowband Multispectral Remote Sensing for Vegetation Monitoring From an Unmanned Aerial Vehicle. *IEEE Transactions on Geoscience and Remote Sensing* 47 (3), pp. 722–738.

Besl, P. and McKay, H. (1992). A method for registration of 3-D shapes. *IEEE Transactions on Pattern Analysis and Machine Intelligence* 14 (2), pp. 239–256.

Boak, E. H. and Turner, I. L. (2005). Shoreline Definition and Detection : A Review. *Journal of Coastal Research* 21 (4), pp. 688–703.

Böhm, J. and Becker, S. (2007). Automatic marker-free registration of terrestrial laser scans using reflectance features. *8th Conf. on O3D, Zurich, Switzerland*, pp. 338–344.

Bolitho, M., Kazhdan, M., and Burns, R. (2009). Parallel poisson surface reconstruction. *Advances in Visual Computing LNCS* 5875, pp. 678–689.

Brock, J., Wright, C., Sallenger, A., Krabill, W., and Swift, R. (2002). Basis and methods of NASA airborne topographic mapper lidar surveys for coastal studies. *Journal of Coastal Research* 18 (1), pp. 1–13.

Brown, D. (1971). Close-range camera calibration. *Photogrammetric Engineering and Remote Sensing* 37 (8), pp. 855–866.

Bruun, P. (1962). Sea level rise as a cause of shore erosion. *American Society Civil Engineers Proceedings, Journal Waterways & Harbors Division*. Vol. 88, pp. 117–130.

Bruun, P. (1988). The Bruun Rule of Erosion by Sea Level Rise: A Discussion on Large Two- and Three-Diminensional Usages. *Journal of Coastal Research* 4 (4), pp. 627–648.

Bryson, M., Johnson-Roberson, M., Murphy, R. J., and Bongiorno, D. (2013). Kite aerial photography for low-cost, ultra-high spatial resolution multi-spectral mapping of intertidal landscapes. *PloS one* 8 (9), e73550.

Butkiewicz, T., Chang, R., Wartell, Z., and Ribarsky, W. (2008). Visual Analysis and Semantic Exploration of Urban LIDAR Change Detection. *Computer Graphics Forum* 27 (3), pp. 903–910.

Calligaro, S., Sofia, G., Prosdocimi, M., Dalla Fontana, G., and Tarolli, P. (2014). Terrestrial Laser Scanner Data To Support Coastal Erosion Analysis: the Conero Case Study. *ISPRS - International Archives of the Photogrammetry, Remote Sensing and Spatial Information Sciences* XL-5/W3 (February), pp. 125–129.

Carter, W., Shrestha, R., and Leatherman, S. (1998). Airborne laser swath mapping: applications to shoreline mapping. *Proceedings of International Symposium on Marine Positioning (INSMAP'98)*, pp. 323–333.

Carvajal, F, Agüera, F, and Pérez, M (2011). Surveying a landslide in a road embankment using unmanned aerial vehicle photogrammetry. *International Archives of Photogrammetry, Remote Sensing and Spatial Information Sciences* XXXVIII (1/C22), pp. 1–6.

Casella, E., Rovere, A., Pedroncini, A., Mucerino, L., Casella, M., Cusati, L. A., Vacchi, M., Ferrari, M., and Firpo, M. (2014). Study of wave runup using numerical models and low-altitude aerial photogrammetry: A tool for coastal management. *Estuarine, Coastal and Shelf Science* 149, pp. 160–167.

Chalabi, A., Mohd-Lokman, H., Mohd-Suffian, I., Karamali, M., Karthigeyan, V., and Masita, M. (2006). Monitoring shoreline change using Ikonos image and aerial photographs: a case study of Kuala Terengganu area, Malaysia. *Proceedings of the ISPRS Mid-term Symposium Proceeding. Enschede, The Netherlands*.

Chao, H., Cao, Y., and Chen, Y. (2010). Autopilots for small unmanned aerial vehicles: A survey. *International Journal of Control, Automation and Systems* 8 (1), pp. 36–44.

Chen, X. and Davis, J. (2000). *Camera Placement Considering Occlusion for Robust Motion Capture*. Tech. rep.

Cheng, P, Keller, J., and Kumar, V. (2008). Time-optimal UAV trajectory planning for 3D urban structure coverage. *IEEE/RSJ International Conference on Intelligent Robots and Systems, Nice, France. Sept 22-26*, pp. 22–26.

Choset, H. and Pignon, P. (1998). Coverage Path Planning: The Boustrophedon Cellular Decomposition. *Field and Service Robotics*. Springer London, pp. 203–209.

Church, J., Hunter, J., McInnes, K., and White, N. (2006). Sea-level rise around the Australian coastline and the changing frequency of extreme sea-level events. *Australian Meteorological Magazine* 55, pp. 253–260.

Cignoni, P., Rocchini, C., and Scopigno, R. (1998). Metro: Measuring Error on Simplified Surfaces. *Computer Graphics Forum* 17 (2), pp. 167–174.

Colomina, I. and Molina, P. (2014). Unmanned aerial systems for photogrammetry and remote sensing: A review. *ISPRS Journal of Photogrammetry and Remote Sensing* 92, pp. 79–97.

Coppin, P, Jonckheere, I, Nackaerts, K, Muys, B, and Lambin, E (2004). Digital change detection methods in ecosystem monitoring: a review. *International Journal of Remote Sensing* 25 (9), pp. 1565–1596.

Coulter, L., Lippitt, C., Stow, D., and McCreight, R. (2011). Near Real-Time Change Detection for Border Monitoring. *Proc. ASPRS annual conference, Milwaukee, USA, May 1-5*, pp. 9–17.

Cowell, P. and Nelson, H (1991). Management of Beach Erosion Due to Low Swell, Inlet and Greenhouse Effects: Case Study with Computer Modelling. *Coastal Engineering: Climate for Change; Proceedings of 10th Australasian Conference on Coastal and Ocean Engineering, 1991*, pp. 311–315.

Cracknell, A. (1998). Review article Synergy in remote sensing-what's in a pixel? *International Journal of Remote Sensing* 19 (11), pp. 2025–2047.

Dandois, J. P. and Ellis, E. C. (2010). Remote Sensing of Vegetation Structure Using Computer Vision. *Remote Sensing* 2 (4), pp. 1157–1176.

Deronde, B, Houthuys, R, Henriet, J., and Lancker, V. (2008). Monitoring of the sediment dynamics along a sandy shoreline by means of airborne hyperspectral remote sensing and LIDAR: a case study in Belgium. *Earth Surface Processes and Landforms* 33 (2), pp. 280–294.

Deronde, B., Houthuys, R., Debruyn, W., Fransaer, D., Lancker, V. V., and Henriet, J.-P. (2006). Use of Airborne Hyperspectral Data and Laserscan Data to Study Beach Morphodynamics along the Belgian Coast. *Journal of Coastal Research* 22 (5), pp. 1108–1117.

Dietrich, J (2014). Applications of Structure-from-Motion Photogrammetry to Fluvial Geomorphology. PhD thesis. University of Oregon.

DigitalGlobe (2015). *30 cm DigitalGlobe imagery.*

Dolan, R., Fenster, M., and Holme, S. (1991). Temporal analysis of shoreline recession and accretion. *Journal of Coastal Research* 7 (3), pp. 723–744.

D'Oleire-Oltmanns, S., Marzolff, I., Peter, K., and Ries, J. (2012). Unmanned Aerial Vehicle (UAV) for Monitoring Soil Erosion in Morocco. *Remote Sensing* 4 (11), pp. 3390–3416.

Doneus, M, Verhoeven, G, Fera, M, and Briese, C (2011). From deposit to point cloud - a study of low-cost computer vision approaches for the straightforward documentation of archaeological excavations. *Sort 100*, pp. 81–88.

Dowling, T., Read, A. M., and Gallant, J. C. (2009). Very high resolution DEM acquisition at low cost using a digital camera and free software. *18th World IMACS / MODSIM Congress*. July, pp. 2479–2485.

Eisenbeiss, H (2009). UAV photogrammetry. PhD thesis. University of Technology Dresden.

Eisenbeiss, H. (2008). The autonomous mini helicopter: a powerful platform for mobile mapping. *Int. Arch. Photogramm. Remote Sens. Spat. Inf. Sci* XXXVII (Part B1), pp. 977–984.

Eisenbeiss, H. and Sauerbier, M. (2011). Investigation of uav systems and flight modes for photogrammetric applications. *The Photogrammetric Record* 26 (136), pp. 400–421.

Eisenbeiss, H. and Zhang, L. (2006). Comparison of DSMs generated from mini UAV imagery and terrestrial laser scanner in a cultural heritage application. *International Archives of the Photogrammetry, Remote Sensing and Spatial Information Science* XXXVI (Part 5), pp. 90–96.

Ekercin, S. (2007). Coastline Change Assessment at the Aegean Sea Coasts in Turkey Using Multitemporal Landsat Imagery. *Journal of Coastal Research* 233, pp. 691–698.

Eltner, A, Mulsow, C, and Maas, H. (2013). Quantitative measurement of soil erosion from TLS and UAV data. *International Archives of Photogrammetry, Remote Sensing and Spatial Information Sciences* XL-1/W2, pp. 119–124.

Farah, A., Talaat, A., and Farrag, F. (2008). Accuracy Assessment of Digital Elevation Models Using GPS. *Artificial Satellites* 43 (4), pp. 151–161.

Farenzena, M., Fusiello, A., and Gherardi, R. (2010). Structure-and-motion pipeline on a hierarchical cluster tree. *Computer Vision Workshops (ICCV Workshops), 2009 IEEE 12th International Conference, Kyoto, Japan, 27 Sept.-4 Oct.* IEEE, pp. 1489–1496.

Fenster, M. S., Dolan, R., Morton, R. A., and Summer, F. (2001). Coastal Storms and Shoreline Change: Signal or Noise? *Journal of Coastal Research* 17 (3), pp. 714–720.

FitzGerald, D. M., Fenster, M. S., Argow, B. a., and Buynevich, I. V. (2008). Coastal Impacts Due to Sea-Level Rise. *Annual Review of Earth and Planetary Sciences* 36 (1), pp. 601–647.

Flener, C., Vaaja, M., Jaakkola, A., Krooks, A., Kaartinen, H., Kukko, A., Kasvi, E., Hyyppä, H., Hyyppä, J., and Alho, P. (2013). Seamless Mapping of River Channels at High Resolution Using Mobile LiDAR and UAV-Photography. *Remote Sensing* 5 (12), pp. 6382–6407.

Fonstad, M. A., Dietrich, J. T., Courville, B. C., Jensen, J. L., and Carbonneau, P. E. (2013). Topographic structure from motion: a new development in photogrammetric measurement. *Earth Surface Processes and Landforms* 38 (4), pp. 421–430.

Frankenberger, J., Huang, C., and Nouwakpo, K. (2008). Low-Altitude Digital Photogrammetry Technique to Assess Ephemeral Gully Erosion. *IGARSS 2008 - 2008 IEEE International Geoscience and Remote Sensing Symposium*, pp. IV –117–IV –120.

Fraser, C. S. (1984). Network design optimization in non-topographic photogrammetry. *IA PRS* 25, pp. 296–308.

Fraser, C. S., Ganci, G, and Shortis, M. (1995). Multi-sensor system self-calibration. *SPIE Conference 2598, Videometrics IV, Philadelphia, USA, October 25-26, 1995.*

Fraser, C. (1992). Photogrammetric measurement to one part in a million. *Photogrammetric Engineering and Remote Sensing* 58 (3), pp. 305–310.

Fraser, C. (2006). Evolution of network orientation procedures. *International Archives of Photogrammetry, Remote Sensing and Spatial Information Sciences* XXXVI (Part 5), pp. 114–120.

Fraser, C. (2013). Automatic camera calibration in close range photogrammetry. *Photogrammetric Engineering & Remote Sensing* 79 (4), pp. 381–388.

Fryer, J. (1996). Camera Calibration. *Close Range Photogrammetry and Machine Vision.* Ed. by K. Atkinson. Caithness, UK: Whittles Publishing, pp. 156–179.

Furukawa, Y. and Ponce, J. (2007). Accurate, Dense, and Robust Multi-View Stereopsis. *Proc. IEEE Conf. Computer Vision and Pattern Recognition, Minneapolis, USA, 18-23 June.* Vol. 1. 1. Ieee.

Furukawa, Y. and Ponce, J. (2010). Accurate, dense, and robust multi-view stereopsis. *IEEE Transactions on Pattern Analysis and Machine Intelligence* 32 (8), pp. 1362 –1376.

Genchi, S. a., Vitale, A. J., Perillo, G. M. E., and Delrieux, C. a. (2015). Structure-from-Motion Approach for Characterization of Bioerosion Patterns Using UAV Imagery. *Sensors (Basel, Switzerland)* 15 (2), pp. 3593–609.

Girardeau-Montaut, D., Roux, M., Marc, R., and Thibault, G. (2005). Change detection on points cloud data acquired with a ground laser scanner. *International Archives of Photogrammetry, Remote Sensing and Spatial Information Sciences* 36 (part 3), pp. 30–35.

Gómez-Gutiérrez, A., Sanjosé-Blasco, J. de, Matías-Bejarano, J. de, and Berenguer-Sempere, F. (2014). Comparing Two Photo-Reconstruction Methods to Produce High Density Point Clouds and DEMs in the Corral del Veleta Rock Glacier (Sierra Nevada, Spain). *Remote Sensing* 6 (6), pp. 5407–5427.

Granshaw, S. I. (1980). Bundle Adjustment Methods in Engineering Photogrammetry. *The Photogrammetric Record* 10 (56), pp. 181–207.

Greenwood, R. and Orford, J. (2008). Temporal patterns and processes of retreat of drumlin coastal cliffs - Strangford Lough, Northern Ireland. *Geomorphology* 94 (1-2), pp. 153–169.

Grun, A (1980). Precision and reliability aspects in close-range photogrammetry. *Photogrammetric Journal of Finland* 8 (2), pp. 117–132.

Hanley, H. (2001). Geopositioning accuracy of IKONOS imagery: Indications from two dimensional transformations. *The Photogrammetric Record* 17 (98), pp. 317–329.

Hartley, R. and Mundy, J. (1993). The relationship between photogrammetry and computer vision. *Proceedings of SPIE*. Vol. 14. 1. Citeseer, pp. 92–105.

Harwin, S. and Lucieer, A. (2012a). An Accuracy Assessment of Georeferenced Point Clounds Produced via Multi-View Stereo Techniques Applied to Imagery Acquired via Unmanned Aerial Vehicle. *ISPRS - International Archives of the Photogrammetry, Remote Sensing and Spatial Information Sciences Conference, Sydney, July, 2012*.

Harwin, S. and Lucieer, A. (2012b). Assessing the Accuracy of Georeferenced Point Clouds Produced via Multi-View Stereopsis from Unmanned Aerial Vehicle (UAV) Imagery. *Remote Sensing* 4, pp. 1573–1599.

Harwin, S., Lucieer, A., and Osborn, J. (2015). The Impact of the Calibration Method on the Accuracy of Point Clouds Derived Using Unmanned Aerial Vehicle Multi-View Stereopsis. *Remote Sensing* 7 (9), pp. 11933–11953.

Hayes, D. and Sader, S. (2001). Comparison of change-detection techniques for monitoring tropical forest clearing and vegetation regrowth in a time series. *Photogrammetric Engineering and Remote Sensing* 67 (9), pp. 1067–1075.

He, J., Li, Y., and Zhang, K. (2012). Research of UAV Flight Planning Parameters. *Positioning* 03 (04), pp. 43–45.

Hernandez-Lopez, D, Felipe-Garcia, B, Gonzalez-Aguilera, D, and Arias-Perez, B (2013). An Automatic Approach to UAV Flight Planning and Control for Photogrammetric Applications: A Test Case in the Asturias Region (Spain). *Photogrammetric Engineering and Remote Sensing* 79 (1), pp. 87–98.

Hirschmüller, H. (2005). Accurate and efficient stereo processing by semi-global matching and mutual information. *IEEE Computer Society Conference on Computer Vision and Pattern Recognition (CVPR'05), San Diego, USA 20-26 June*. Vol. 2, pp. 807–814.

Hirschmüller, H. (2008). Stereo processing by semiglobal matching and mutual information. *IEEE transactions on pattern analysis and machine intelligence* 30 (2), pp. 328–41.

Hirschmüller, H. (2011). Semi-Global Matching - Motivation, Developments and Applications. *Invited Paper at the 54th Photogrammetric Week, Stuttgart, Germany, 5-11 Sept.* Pp. 173–184.

Hodgson, M. and Bresnahan, P. (2004). Accuracy of airborne lidar-derived elevation: empirical assessment and error budget. *Photogrammetric Engineering and Remote Sensing* 70 (3), pp. 331–339.

Hoppe, C., Wendel, A., Zollmann, S., Pirker, K., Irschara, A., Bischof, H., and Kluckner, S. (2012). Photogrammetric Camera Network Design for Micro Aerial Vehicles. *Proc. 17th Computer Vision Winter Workshop, Mala Nedelja, Slovenia, February 1-3, 2012*.

Hugenholtz, C., Whitehead, K, Brown, O., Barchyn, T., Moorman, B., LeClair, A, Riddell, K, and Hamilton, T (2013). Geomorphological mapping with a small unmanned aircraft system (sUAS): feature detection and accuracy assessment of a photogrammetrically-derived digital. *Geomorphology* 194, pp. 16–24.

IPCC (2013). Climate Change 2013: The Physical Science Basis, Summary for Policymakers. *Contribution of Working Group I to the Fifth Assessment Report of the Intergovernmental Panel on Climate Change*. Ed. by Stocker T.F., D. Qin, G.-K. Plattner, M. Tignor, S. Allen, J. Boschung, A. Nauels, Y. Xia, V. Bex, and P. Midgley. Cambridge University Press, Cambridge, United Kingdom and New York, NY, USA.

Irschara, A, Kaufmann, V, and Klopschitz, M (2010). Towards fully automatic photogrammetric reconstruction using digital images taken from UAVs. *Proceedings of the International Society for Photogrammetry and Remote Sensing Symposium*.

James, M. R. and Robson, S. (2014). Mitigating systematic error in topographic models derived from UAV and ground-based image networks. *Earth Surface Processes and Landforms* 39 (10), pp. 1413–1420.

James, M. and Quinton, J. N. (2014). Ultra-rapid topographic surveying for complex environments: the hand-held mobile laser scanner (HMLS). *Earth Surface Processes and Landforms* 39 (1), pp. 138–142.

James, M. and Robson, S. (2012). Straightforward reconstruction of 3D surfaces and topography with a camera: Accuracy and geoscience application. *Journal of Geophysical Research* 117 (F3), pp. 1–17.

James, M., Ilic, S., and Ruzic, I. (2013). Measuring 3D coastal change with a digital camera. *Proc 7th Int Conf Coastal Dynamics*, pp. 893–904.

Javernick, L., Brasington, J., and Caruso, B. (2014). Modeling the topography of shallow braided rivers using Structure-from-Motion photogrammetry. *Geomorphology* 213, pp. 166–182.

Jaw, J. J. and Chuang, T. Y. (2010). On the effectiveness of feature-based lidar point cloud registration. *PCV 2020 IISPRS Commission III Symposium Photogrammetric Computer Vision and Image Analysis*. Vol. XXXVIII, pp. 60–65.

Jazayeri, I, Fraser, C. S., and Cronk, S (2010). Automated 3D Object Reconstruction Via Multi-Image Close-Range Photogrammetry. *International Archives of Photogrammetry, Remote Sensing and Spatial Information Sciences* XXXVIII (2000), pp. 3–8.

Juan, L. and Gwun, O. (2009). A comparison of SIFT, PCA-SIFT and SURF. *International Journal of Image Processing* 3 (4), p. 143.

Kaiser, A., Neugirg, F., Rock, G., Müller, C., Haas, F., Ries, J., and Schmidt, J. (2014). Small-Scale Surface Reconstruction and Volume Calculation of Soil Erosion in Complex Moroccan Gully Morphology Using Structure from Motion. *Remote Sensing* 6 (8), pp. 7050–7080.

Kang, Z. and Lu, Z. (2010). The change detection of building models using epochs of terrestrial point clouds. *International Archives of the Photogrammetry, Remote Sensing and Spatial Information Science*. Vol. XXXVIII. Part 8, pp. 231–236.

Kang, Z., Li, J., Zhang, L., Zhao, Q., and Zlatanova, S. (2009). Automatic Registration of Terrestrial Laser Scanning Point Clouds using Panoramic Reflectance Images. *Sensors* 9 (4), pp. 2621–2646.

Kazhdan, M., Bolitho, M., and Hoppe, H. (2006). Poisson surface reconstruction. *Proceedings of the Eurographics Symposium on Geometry Processing*.

Ke, Y. and Sukthankar, R. (2004). PCA-SIFT: a more distinctive representation for local image descriptors. *Proc. IEEE Computer Society Conf. on Computer Vision and Pattern Recognition, Washington, DC, USA, 27 June-2 July*. IEEE, pp. 506–513.

Kelcey, J. and Lucieer, A. (2012). Sensor Correction of a 6-Band Multispectral Imaging Sensor for UAV Remote Sensing. *Remote Sensing* 4 (12), pp. 1462–1493.

Knauer, C. and Löffler, M. (2009). The directed Hausdorff distance between imprecise point sets. *Algorithms and Computation*, pp. 720–729.

Kocaman, S., Zhang, L., Gruen, A., and Poli, D. (2006). 3D city modeling from high-resolution satellite images. *Proceedings of ISPRS Workshop on Topographic Mapping from Space, Ankara, Turkey, 14-16 Feb.* 1, Volume XXXVI–1/W41.

Kuleli, T. (2010). Quantitative analysis of shoreline changes at the Mediterranean Coast in Turkey. *Environmental monitoring and assessment* 167 (1-4), pp. 387–97.

Küng, O, Strecha, C., Beyeler, A, Zufferey, J.-C., Floreano, D, Fua, P, and Gervaix, F (2011). The Accuracy of Automatic Photogrammetric Techniques on Ultra-Light UAV Imagery. *International Archives of the Photogrammetry, Remote Sensing and Spatial Information Sciences* XXXVIII (1/C22 UAV-g), pp. 125–130.

Laliberte, A. S., Goforth, M. a., Steele, C. M., and Rango, A. (2011). Multispectral Remote Sensing from Unmanned Aircraft: Image Processing Workflows and Applications for Rangeland Environments. *Remote Sensing* 3 (11), pp. 2529–2551.

Laliberte, A., Herrick, J., Rango, A., and Winters, C. (2010). Acquisition, orthorectification, and object-based classification of unmanned aerial vehicle (UAV) imagery for rangeland monitoring. *Photogrammetric Engineering and Remote Sensing* 76 (6), pp. 661–672.

Lee, I.-c., Wu, B., and Li, R. (2009a). Shoreline extraction from the integration or LiDAR point cloud data and aerial orthophotos using Mean Shift Segmentation. *ASPRS 2009 Annual Conference, Baltimore*. Vol. 10. 1.74. Citeseer.

Lee, I. S., Lee, J. O., and Ge, L. (2009b). Comparison of Terrestrial Laser Scanner with Digital Aerial Photogrammetry for Extracting Ridges in the Rice Paddies. *Survey Review* 41 (313), pp. 253–267.

Leuschen, C., Yan, J., Mahmood, A., Rodriguez-Morales, F., Hale, R., Camps-Raga, B., Metz, L., Wang, Z., Paden, J., Bowman, A., Keshmiri, S., and Gogineni, S. (2014). UAV-based Radar Sounding of Antarctic Ice. *EGU General Assembly Conference*. Vol. 16.

Lim, M., Petley, D., Rosser, N., Allison, R., and Long, A. (2005). Combined digital photogrammetry and time-ÂŘof-ÂŘflight laser scanning for monitoring cliff evolution. *The Photogrammetric Record* 20 (110), pp. 109–129.

Lim, S. and Haron, H (2012). Surface reconstruction techniques: a review. *Artificial Intelligence Review*.

Lin, Y., Hyyppa, J, and Jaakkola, A. (2011). Mini-UAV-borne LIDAR for fine-scale mapping. *Geoscience and Remote Sensing Letters* 8 (3), pp. 426–430.

Liu, H. (2011). Algorithmic Foundation and Software Tools for Extracting Shoreline Features from Remote Sensing Imagery and LiDAR Data. *Journal of Geographic Information System* 03 (02), pp. 99–119.

Liu, X., Zhang, Z., Peterson, J., and Chandra, S. (2007). LiDAR-Derived High Quality Ground Control Information and DEM for Image Orthorectification. *GeoInformatica* 11 (1), pp. 37–53.

Livingstone, D (1999). Integrating aerial videography and digital photography with terrain modelling: an application for coastal geomorphology. *Geomorphology* 29 (1-2), pp. 77–92.

Lowe, D. G. (2004). Distinctive Image Features from Scale-Invariant Keypoints. *International Journal of Computer Vision* 60 (2), pp. 91–110.

Lu, D., Mausel, P., Brondízio, E., and Moran, E. (2004). Change detection techniques. *International Journal of Remote Sensing* 25 (12), pp. 2365–2401.

Lu, F., Ji, X., Dai, Q., and Er, G. (2011). Multi-view stereo reconstruction with high dynamic range texture. *Computer Vision - ACCV 2010, Queenstown, New Zealand, 8-12 Nov.* Vol. 6493/2011. Springer, pp. 412–425.

Lucieer, A, Robinson, S., and Turner, D. (2011a). Unmanned Aerial Vehicle (UAV) Remote Sensing for Hyperspatial Terrain Mapping of Antarctic Moss Beds based on Structure from Motion (SfM) point clouds. *Proceedings of the 34th International Symposium on Remote Sensing of Environment (ISRSE34), Sydney, Australia, April 11-15.*

Lucieer, A, Robinson, S., and Turner, D (2011b). Unmanned aerial vehicle (UAV) remote sensing for hyperspatial terrain mapping of Antarctic moss beds based on structure from motion (SfM) point clouds. *International Journal of Applied Earth Observation and Geoinformation* 27(Part A), pp. 53–62.

Lucieer, A, De Jong, S., and Turner, D. (2013). Mapping landslide displacements using Structure from Motion (SfM) and image correlation of multi-temporal UAV photography. *Progress in Physical Geography* 38 (1), pp. 97–116.

Lucieer, A., Malenovský, Z., Veness, T., and Wallace, L. (2014). HyperUAS-Imaging Spectroscopy from a Multirotor Unmanned Aircraft System. *Journal of Field Robotics* 31 (4), pp. 571–590.

Makota, V., Sallema, R., and Mahika, C. (2004). Monitoring shoreline change using remote sensing and GIS: a case study of Kunduchi area, Tanzania. *Western Indian Ocean Journal of Marine Science* 3 (1), pp. 1–10.

Mancini, F., Dubbini, M., Gattelli, M., Stecchi, F., Fabbri, S., and Gabbianelli, G. (2013). Using Unmanned Aerial Vehicles (UAV) for High-Resolution Reconstruction of Topography: The Structure from Motion Approach on Coastal Environments. *Remote Sensing* 5 (12), pp. 6880–6898.

Marfai, M. A., Almohammad, H., Dey, S., Susanto, B., and King, L. (2008). Coastal dynamic and shoreline mapping: multi-sources spatial data analysis in Semarang Indonesia. *Environmental monitoring and assessment* 142 (1-3), pp. 297–308.

Mason, S. O. (1994). Expert System-Based Design of Photogrammertic Networks. PhD thesis.

Mason, S. O. (1995a). Conceptual Model Of The Convergent Multistation Network Configuration Task. *The Photogrammetric Record* 15 (86), pp. 277–299.

Mason, S. O. (1995b). Expert system-based design of close-range photogrammetric networks. *ISPRS Journal of Photogrammetry and Remote Sensing* 50 (5), pp. 13–24.

Matsuoka, M. and Yamazaki, F. (2004). LIDAR-based change detection of buildings in dense urban areas. *IEEE International IEEE International IEEE International Geoscience and Remote Sensing Symposium, 2004. IGARSS '04. Proceedings. 2004* 00 (C), pp. 3413–3416.

Mémoli, F. and Sapiro, G. (2004). Comparing point clouds. *Proceedings of the 2004 Eurographics/ACM SIGGRAPH symposium on Geometry processing - SGP '04*, p. 32.

Middleton, J. H., Cooke, C. G., Kearney, E. T., Mumford, P. J., Mole, M. a., Nippard, G. J., Rizos, C., Splinter, K. D., and Turner, I. L. (2013). Resolution and Accuracy

of an Airborne Scanning Laser System for Beach Surveys. *Journal of Atmospheric and Oceanic Technology* 30 (10), pp. 2452–2464.

Mikolajczyk, K and Schmid, C (2004). Scale & affine invariant interest point detectors. *International Journal of Computer Vision* 60 (1), pp. 63–86.

Mikrokopter (2012). *"MikroKopter WiKI" http://www.mikrokopter.com.*

Mitasova, H., Bernstein, D., Drake, T., Harmon, R., and Miller, C. (2003). Spatio-temporal analysis of beach morphology using LIDAR, RTK-GPS and Open source GRASS GIS. *Proceedings Coastal Sediments.* Vol. 3, pp. 1–13.

Mitasova, H., Drake, T., Bernstein, D., and Harmon, R. (2004). Quantifying Rapid Changes in Coastal Topography using Modern Mapping Techniques and Geographic Information System. *Environmental and Engineering Geoscience* 10 (1), p. 1.

Mitasova, H., Overton, M. F., Recalde, J. J., Bernstein, D. J., and Freeman, C. W. (2009b). Raster-Based Analysis of Coastal Terrain Dynamics from Multitemporal Lidar Data. *Journal of Coastal Research* 25 (2), pp. 507–514.

Mitasova, H., Overton, M. F., Recalde, J. J., Bernstein, D. J., and Freeman, C. W. (2009a). Raster-Based Analysis of Coastal Terrain Dynamics from Multitemporal Lidar Data. *Journal of Coastal Research* 252, pp. 507–514.

Mičušík, B. and Košecká, J. (2010). Multi-view Superpixel Stereo in Urban Environments. *International Journal of Computer Vision* 89 (1), pp. 106–119.

Monserrat, O and Crosetto, M (2008). Deformation measurement using terrestrial laser scanning data and least squares 3D surface matching. *ISPRS Journal of Photogrammetry and Remote Sensing* 63 (1), pp. 142–154.

Moore, L. (2000). Shoreline mapping techniques. *Journal of Coastal Research* 16 (1), pp. 111–124.

Murakami, H (1999). Change detection of buildings using an airborne laser scanner. *ISPRS Journal of Photogrammetry and Remote Sensing* 54 (2-3), pp. 148–152.

Myronenko, A. and Song, X. (2010). Point set registration: coherent point drift. *IEEE Transactions on Pattern Analysis and Machine Intelligence* 32 (12), pp. 2262–2275.

Naumann, M., Bill, R., Niemeyer, F., and Nitschke, E. (2014). Deformation analysis of dikes using unmannaed aerial systems (UAS). *Proceedings of the South Baltic Conference on Dredged Materials in Dike Construction.* April, pp. 10–12.

Neitzel, F and Klonowski, J (2011). Mobile 3D Mapping with a Low-Cost UAV System. *International Archives of the Photogrammetry, Remote Sensing and Spatial Information Sciences* XXXVIII (1/C22 UAV-g, Conf. Unmanned Aerial Vehicle in Geomatics, Zurich, Switzerland), pp. 1–6.

Newby, P. R. T. (2012). Photogrammetric Terminology: Second Edition. *The Photogrammetric Record* 27 (139), pp. 360–386.

Nex, F. and Remondino, F. (2013). UAV for 3D mapping applications: a review. *Applied Geomatics* 6 (1), pp. 1–15.

Niethammer, U, Rothmund, S, and James, M. (2010). UAV-based remote sensing of landslides. *International Archives of Photogrammetry, Remote Sensing and Spatial Information Sciences* XXXVIII (Part 5), pp. 496–501.

Niethammer, U., Rothmund, S., Schwaderer, U., Zeman, J., and Joswig, M. (2012). Open Source Image-Processing Tools for Low-Cost Uav-Based Landslide Investigations. *ISPRS - International Archives of the Photogrammetry, Remote Sensing and Spatial Information Sciences* XXXVIII-1/, pp. 161–166.

Nocerino, E., Menna, F., and Remondino, F. (2014). Accuracy of typical photogrammetric networks in cultural heritage 3D modeling projects. *ISPRS - International*

Archives of the Photogrammetry, Remote Sensing and Spatial Information Sciences XL-5, pp. 465–472.

Nocerino, E., Menna, F., Remondino, F., and Saleri, R. (2013). Accuracy and block deformation analysis in automatic UAV and terrestrial photogrammetry âĂŞ lesson learnt. *ISPRS Annals of Photogrammetry, Remote Sensing and Spatial Information Sciences* II (5/W1), pp. 203–208.

Olague, G. (2000). Design and simulation of photogrammetric networks using genetic algorithms. *ASPRS 2000 Annual Conference Proceedings, Washington DC, USA, American Society for Photogrammetry & Remote Sensing*, p. 12.

Olague, G. and Mohr, R. (1997). Optimal 3D sensor placement to obtain accurate 3D point positions. *Primer Encuentro de Computacion ENC 97: Vision Robotica*, pp. 116–123.

Olague, G. and Mohr, R. (2002). Optimal camera placement for accurate reconstruction. *Pattern Recognition* 35 (4), pp. 927–944.

Overton, M., Mitasova, H., Recalde, J. J., and Vanderbeke, N. (2007). Morphological Evolution of a Shoreline on a Decadal Time Scale. *Coastal Engineering 2006 - Proceedings of the 30th International Conference*, pp. 3851–3861.

Pajak, M. and Leatherman, S. (2002). The high water line as shoreline indicator. *Journal of Coastal Research* 18 (2), pp. 329–337.

Pfeifer, N. and Briese, C. (2007). Geometrical aspects of airborne laser scanning and terrestrial laser scanning. *International Archives of Photogrammetry, Remote Sensing and Spatial Information Sciences* 36 (Part 3), pp. 12–14.

Pierzchala, M., Talbot, B., and Astrup, R. (2014). Estimating Soil Displacement from Timber Extraction Trails in Steep Terrain: Application of an Unmanned Aircraft for 3D Modelling. *Forests* 5 (6), pp. 1212–1223.

Prabaharan, S, Raju, K. S., Lakshumanan. C., and Ramalingam, M. (2010). Remote sensing and GIS applications on change detection study in coastal zone using multi temporal satellite data. *International Journal of Geomatics and Geosciences* 1 (2), pp. 159–166.

Prahalad, V., Sharples, C., Kirkpatrick, J., and Mount, R. (2014). Is wind-wave fetch exposure related to soft shoreline change in swell-sheltered situations with low terrestrial sediment input? *Journal of Coastal Conservation*, pp. 1–11.

Previtali, M., Barazzetti, L., and Scaioni, M. (2014). Accurate 3D surface measurement of mountain slopes through a fully automated image-based technique. *Earth Science Informatics* 7 (2), pp. 109–122.

Ramsey III, E., Nelson, G., and Sapkota, S. (2001). Coastal change analysis program implemented in Louisiana. *Journal of Coastal Research* 17 (1), pp. 53–71.

Ranasinghe, R., Callaghan, D., and Stive, M. J. F. (2011). Estimating coastal recession due to sea level rise: beyond the Bruun rule. *Climatic Change* 110 (3-4), pp. 561–574.

Rasuly, A., Naghdifar, R., and Rasoli, M. (2010). Monitoring of Caspian Sea Coastline Changes Using Object-Oriented Techniques. *Procedia Environmental Sciences* 2, pp. 416–426.

Remondino, F and El-Hakim, S (2009). 3D Virtual Reconstruction and Visualization of Complex Architectures - The "3D-ARCH" Project. *Reconstruction*.

Remondino, F, Barazzetti, L, Nex, F, Scaioni, M, and Sarazzi, D (2011). UAV photogrammetry for mapping and 3d modeling-current status and future perspectives. *International Archives of Photogrammetry, Remote Sensing and Spatial Information Sciences* XXXVIII (1/C22), pp. 25–31.

Remondino, F. and El-Hakim, S. (2006). Image-based 3D Modelling: A Review. *The Photogrammetric Record* 21 (115), pp. 269–291.

Remondino, F. and Fraser, C. S. (2006). Digital camera calibration methods: considerations and comparisons. *ISPRS Commission V Symposium 'Image Engineering and Vision Metrology'*. Vol. WG V/I, pp. 266–272.

Robertson, W., Whitman, D., Zhang, K., and Leatherman, S. (2004). Mapping shoreline position using airborne laser altimetry. *Journal of Coastal Research* 20 (3), pp. 884–892.

Rogers, S., Sandweiss, D., Maasch, K., Belknap, D., and Agouris, P. (2004). Coastal change and beach ridges along the northwest coast of Peru: Image and GIS analysis of the Chira, Piura, and Colan beach-ridge plains. *Journal of Coastal Research* 20 (4), pp. 1102–1125.

Room, M. and Ahmad, A. (2013). Mapping of river model using close range photogrammetry technique and unmanned aerial vehicle system. *8th International Symposium On Digital Earth*.

Rosnell, T, Honkavaara, E, and Nurminen, K (2011). On Geometric Processing of Multi-Temporal Image Data Collected by Light UAV Systems. *International Archives of the Photogrammetry, Remote Sensing and Spatial Information Sciences* XXXVIII (1/C22 UAV-g), pp. 1–6.

Rosnell, T. and Honkavaara, E. (2012). Point cloud generation from aerial image data acquired by a quadrocopter type micro unmanned aerial vehicle and a digital still camera. *Sensors* 12 (1), pp. 453–480.

Rosser, N., Petley, D., Lim, M., Dunning, S., and Allison, R. (2005). Terrestrial laser scanning for monitoring the process of hard rock coastal cliff erosion. *Quarterly Journal of Engineering Geology and Hydrogeology* 38 (4), pp. 363–375.

Rovere, A., Casella, E., Vacchi, M., Mucerino, L., Pedroncini, A., Ferrari, M., and Firpo, M. (2014). Monitoring beach evolution using low-altitude aerial photogrammetry and UAV drones. *Geophysical Research Abstracts* 16 (EGU2014).

Rusinkiewicz, S. and Levoy, M. (2001). Efficient variants of the ICP algorithm. *Proceedings Third International Conference on 3-D Digital Imaging and Modeling*. IEEE Comput. Soc, pp. 145–152.

Saadat-Seresht, M, Samdzadegan, F, Azizi, A, and Hahn, M (2004). Camera placement for network design in vision metrology based on fuzzy inference system. *International Archives of Photogrammetry, Remote Sensing and Spatial Information Sciences*.

Sallenger, A., Krabill, W., Swift, R., Brock, J, List, J, Hansen, M, Holman, R., Manizade, S, Sontag, J, Meredith, A, Morgan, K, Yunkel, J., Frederick, E., and Stockdon, H (2003). Evaluation of airborne topographic lidar for quantifying beach changes. *Journal of Coastal Research* 19 (1), pp. 125–133.

Scaioni, M and Alba, M (2010). Understanding Changes and Deformations on Multi-Temporal Rock Face Point Clouds. *PCV 2020 IISPRS Commission III Symposium Photogrammetric Computer Vision and Image Analysis* XXXVIII, pp. 67–72.

Schmid, K., Hirschmüller, H., Dömel, A., Grixa, I., Suppa, M., and Hirzinger, G. (2012). View Planning for Multi-View Stereo 3D Reconstruction Using an Autonomous Multicopter. *Journal of Intelligent and Robotic Systems* 65, pp. 309–323.

Schubert, J. E., Gallien, T. W., Majd, M. S., and Sanders, B. F. (2015). Terrestrial Laser Scanning of Anthropogenic Beach Berm Erosion and Overtopping. *Journal of Coastal Research* 299, pp. 47–60.

Scott, W., Roth, G., and Rivest, J. (2003). View planning for automated 3D object reconstruction inspection. *ACM Computing Surveys*.

Seitz, S., Curless, B, and Diebel, J. (2006). A comparison and evaluation of multi-view stereo reconstruction algorithms. *IEEE Computer Society Conference on Computer Vision and Pattern Recognition, New York, USA, 17-22 June*. Vol. 1, pp. 519–528.

Shortis, M. and Fraser, C. S. (1991). Current trends in close-range optical 3D measurement for industrial and engineering applications. *Survey Review* 242 (October), pp. 188–200.

Shortis, M. and Hall, C. J. (1989). Network design methods for close range photogrammetry. *Australian Journal of Geodesy, Photogrammetry and Surveying* 50 (June), pp. 51–72.

Shoshany, M. and Degani, A. (1992). Shoreline Detection by Digital Image Processing of Aerial Photography. *Journal of Coastal Research* 8 (1), pp. 29–34.

Shrestha, R, Carter, W, Sartori, M, Luzum, B, and Slatton, K (2005). Airborne Laser Swath Mapping: Quantifying changes in sandy beaches over time scales of weeks to years. *ISPRS Journal of Photogrammetry and Remote Sensing* 59 (4), pp. 222–232.

Shrestha, R., Carter, W., Slatton, C., and Dietrich, W. (2007). *Airborne Laser Swath Mapping: The Defining Factors*. Tech. rep. 510. The National Center for Airborne Laser Mapping.

Shrestha, R. L., Carter, W. E., Lee, M., Finer, P., and Sartori, M. (1999). Airborne Laser Swath Mapping : ALSM. *Civil Engineering* 59 (2), pp. 83–94.

Smith, G. and Zarillo, G. (1990a). Calculating long-term shoreline recession rates using aerial photographic and beach profiling techniques. *Journal of Coastal Research* 6 (1), pp. 111–120.

Smith, G. and Zarillo, G. (1990b). Calculating long-term shoreline recession rates using aerial photographic and beach profiling techniques. *Journal of Coastal Research* 6 (1), pp. 111–120.

Smith, R. K. and Bryan, K. R. (2007). Monitoring Beach Face Volume with a Combination of Intermittent Profiling and Video Imagery. *Journal of Coastal Research* 234, pp. 892–898.

Snavely, N. (2010). *Bundler: Structure from Motion (SfM) for Unordered Image Collections*.

Snavely, N., Seitz, S. M., and Szeliski, R. (2006). Photo Tourism: Exploring image collections in 3D. *ACM Transactions on Graphics* 25 (3), p. 835.

Snavely, N., Seitz, S. M., and Szeliski, R. (2007). Modeling the World from Internet Photo Collections. *International Journal of Computer Vision* 80 (2), pp. 189–210.

Splinter, K., Davidson, M., and Turner, I. (2013). Monitoring data requirements for shoreline prediction: How much, how long, how often. *Journal of Coastal Research* (65), pp. 2179–2184.

Stal, C., Lonneville, B., Nuttens, T., Maeyer, P. D. E., and Wulf, A. D. E. (2014). Highly Detailed 3D Modelling of Mayan Cultural Heritage Using an UAV. *25th FIG Congress*. June.

Starek, M. J., Vemula, R. K., Slatton, K., Shrestha, R. L., and Carter, W. (2007). Automatic feature extraction from airborne lidar measurements to identify cross-shore morphologies indicative of beach erosion. *2007 IEEE International Geoscience and Remote Sensing Symposium*, pp. 2511–2514.

Stefanik, K. V., Gassaway, J. C., Kochersberger, K., and Abbott, a. L. (2011). UAV-Based Stereo Vision for Rapid Aerial Terrain Mapping. *GIScience & Remote Sensing* 48 (1), pp. 24–49.

Stockdon, H., Sallenger Jr, A., List, J., and Holman, R. (2002a). Estimation of shoreline position and change using airborne topographic lidar data. *Journal of Coastal Research* 18 (3), pp. 502–513.

Stockdon, H. F., Sallenger Jr, A. H., List, J. H., and Holman, R. A. (2002b). Estimation of Shoreline Position and Change using Airborne Topographic Lidar Data. *Journal of Coastal Research* 18 (3), pp. 502–513.

Strecha, C., Fransens, R., and Van Gool, L. (2006). Combined Depth and Outlier Estimation in Multi-View Stereo. *IEEE Computer Society Conference on Computer Vision and Pattern Recognition - Volume 2 (CVPR'06), New York, USA, 17-22 June*. Vol. 2. 1, pp. 2394–2401.

Strecha, C., Hansen, C. von, Gool, L. V., Fua, P., and Thoennessen., U. (2008). On benchmarking camera calibration and multi-view stereo for high resolution imagery. *IEEE Computer Society Conference on Computer Vision and Pattern Recognition, Anchorage, USA, 24-26 June*.

Strecha, C. and Fransens, R. (2004). Wide-baseline stereo from multiple views: a probabilistic account. *IEEE Computer Society Conference on Computer Vision and Pattern Recognition, Washington, DC, USA, 27 June-2 July*, pp. I–552 –I–559.

Strecha, C., Bronstein, A., Bronstein, M., and Fua, P. (2011). LDAHash: Improved Matching with Smaller Descriptors. *IEEE transactions on pattern analysis and machine intelligence* 34 (1), pp. 66–78.

Sujit, P. B., Hudzietz, B. P., and Saripalli, S. (2012). Route Planning for Angle Constrained Terrain Mapping Using an Unmanned Aerial Vehicle. *Journal of Intelligent & Robotic Systems* 69 (1-4), pp. 273–283.

Tahar, K. N. and Ahmad, A. (2011). UAV-based stereo vision for photogrammetric survey in aerial terrain mapping. *2011 IEEE International Conference on Computer Applications and Industrial Electronics (ICCAIE)*. Iccaie. Ieee, pp. 443–447.

Tahar, K. (2012). Aerial terrain mapping using unmanned aerial vehicle approach. *International Archives of the Photogrammetry, Remote Sensing and Spatial Information Sciences* XXXIX (September), pp. 493–498.

Tahar, K. (2013). An Evaluation on Different Number of Ground Control Points in Unmanned Aerial Vehicle Photogrammetric Block. *International Archives of the Photogrammetry, Remote Sensing and Spatial Information Sciences* XL (November), pp. 27–29.

Tampubolon, W. and Reinhardt, W. (2014). UAV Data Processing for Large Scale Topographical Mapping. *ISPRS - International Archives of the Photogrammetry, Remote Sensing and Spatial Information Sciences* XL-5 (June), pp. 565–572.

Thieler, E. and Danforth, W. (1994). Historical shoreline mapping (I): improving techniques and reducing positioning errors. *Journal of Coastal Research* 10 (3), pp. 549–563.

Töyrä, J., Pietroniro, A., Hopkinson, C., and Kalbfleisch, W. (2003). Assessment of airborne scanning laser altimetry (lidar) in a deltaic wetland environment. *Canadian Journal of Remote Sensing* 29 (6), pp. 718–728.

Triggs, B., McLauchlan, P., Hartley, R., and Fitzgibbon, A. (1999). Bundle adjustment - a modern synthesis. *ICCV '99 Vision Algorithms: Theory and Practice, Corfu, Greece, 20-21 Sept.* Springer, pp. 153–177.

Turner, D, Lucieer, A, and Watson, C. (2011). Development of an Unmanned Aerial Vehicle (UAV) for hyper resolution vineyard mapping based on visible, multispectral, and thermal imagery. *Proceedings of the 34th International Symposium on Remote Sensing of Environment (ISRSE34), Sydney, Australia, April 11-15*.

Turner, D., Lucieer, A., and Watson, C. (2012). An Automated Technique for Generating Georectified Mosaics from Ultra-High Resolution Unmanned Aerial Vehicle (UAV) Imagery, Based on Structure from Motion (SfM) Point Clouds. *Remote Sensing* 4 (5), pp. 1392–1410.

Turner, D., Lucieer, A., and Wallace, L. (2014). Direct Georeferencing of Ultrahigh-Resolution UAV Imagery. *IEEE Transactions on Geoscience and Remote Sensing* 52 (5), pp. 2738–2745.

Vaaja, M., Hyyppä, J., Kukko, A., Kaartinen, H., Hyyppä, H., and Alho, P. (2011). Mapping Topography Changes and Elevation Accuracies Using a Mobile Laser Scanner. *Remote Sensing* 3 (3), pp. 587–600.

Vallet, J., Panissod, F., Strecha, C., and Tracol, M. (2011). Photogrammetric Performance of an Ultra Light Weight Swinglet "UAV". *ISPRS - International Archives of the Photogrammetry, Remote Sensing and Spatial Information Sciences* XXXVIII (1/C22 UAV-g), pp. 253–258.

Vasuki, Y., Holden, E., Kovesi, P., and Micklethwaite, S. (2013). A geological structure mapping tool using photogrammetric data. *ASEG Extended Abstracts* (August), pp. 11–14.

Verhoeven, G (2011). Taking computer vision aloft - archaeological three-dimensional reconstructions from aerial photographs with photoscan. *Archaeological Prospection* 73 (January), pp. 67–73.

Verhoeven, G, Taelman, D, and Vermeulen, F (2012). Computer Vision-Based Orthophoto Mapping of Complex Archaeological Sites: the Ancient Quarry of Pitaranha (Portugal-Spain). *Archaeometry* 54 (6), pp. 1114–1129.

Verhoeven, G., Sevara, C., Karel, W., Ressl, C., Doneus, M., and Briese, C. (2013). *Good Practice in Archaeological Diagnostics*. Natural Science in Archaeology. Cham: Springer International Publishing.

Vögtle, T and Steinle, E (2004). Detection and recognition of changes in building geometry derived from multitemporal laserscanning data. *The International Archives of the Photogrammetry, Remote Sensing and Spatial Information Sciences* 34, p. 428.

Vosselman, G, Gorte, B., and Sithole, G (2004). Change detection for updating medium scale maps using laser altimetry. *The International Archives of the Photogrammetry, Remote Sensing and Spatial Information Sciences* 35 (B3), pp. 207–212.

Vu, H.-H., Labatut, P., Pons, J.-P., and Keriven, R. (2011). High Accuracy and Visibility-Consistent Dense Multi-view Stereo. *IEEE transactions on pattern analysis and machine intelligence* 34 (5), pp. 889–901.

Vu, H.-H., Labatut, P., Pons, J.-P., and Keriven, R. (2012). High accuracy and visibility-consistent dense multiview stereo. *IEEE transactions on pattern analysis and machine intelligence* 34 (5), pp. 889–901.

Wackrow, R, Chandler, J., and Gardner, T (2008). Minimising systematic errors in DEMs caused by an inaccurate lens model. *Archives of Photogrammetry, Remote Sensing and Spatial Science* XXXVII (Part B5), pp. 1–6.

Wackrow, R. and Chandler, J. H. (2011). Minimising systematic error surfaces in digital elevation models using oblique convergent imagery. *The Photogrammetric Record* 26 (133), pp. 16–31.

Walker, J. P. and Willgoose, G. R. (2006). A Comparative Study of Australian Cartometric and Photogrammetric Digital Elevation Model Accuracy. *Photogrammetric Engineering and Remote Sensing* 72 (7).

Wallace, L., Lucieer, A., Watson, C., and Turner, D. (2012). Development of a UAV-LiDAR System with Application to Forest Inventory. *Remote Sensing* 4 (12), pp. 1519–1543.

Wefelscheid, C., Hansch, R., and Hellwich, O. (2011). Three-dimensional building reconstruction using images obtained by unmanned aerial vehicles. *International Archives of Photogrammetry, Remote Sensing and Spatial Information Sciences* XXXVIII.

Wendt, A (2007). A concept for feature based data registration by simultaneous consideration of laser scanner data and photogrammetric images. *ISPRS Journal of Photogrammetry and Remote Sensing* 62 (2), pp. 122–134.

Wenzel, K, Rothermel, M, Fritsch, D, and Haala, N (2013). Image acquisition and model selection for multi-view stereo. *3D-ARCH 2013: "3D Virtual Reconstruction and Visualization of Complex Architectures". Proceedings of the 5th ISPRS International Workshop, Trento, Italy. 25- 26 February 2013.* Vol. XL. February, pp. 251–258.

Westoby, M., Brasington, J, Glasser, N., Hambrey, M., and Reynolds, J. (2012). 'Structure-from-Motion'photogrammetry: a low-cost, effective tool for geoscience applications. *Geomorphology* 179, pp. 300–314.

White, K. and El Asmar, H. (1999). Monitoring changing position of coastlines using Thematic Mapper imagery, an example from the Nile Delta. *Geomorphology* 29 (1-2), pp. 93–105.

White, S and Wang, Y (2003). Utilizing DEMs derived from LIDAR data to analyze morphologic change in the North Carolina coastline. *Remote Sensing of Environment* 85 (1), pp. 39–47.

Wolf, P. (1983). *Elements of Photogrammetry (2nd Edition)*. McGraw-Hill.

Woodget, a. S., Carbonneau, P. E., Visser, F., and Maddock, I. P. (2015). Quantifying submerged fluvial topography using hyperspatial resolution UAS imagery and structure from motion photogrammetry. *Earth Surface Processes and Landforms* 40 (1), pp. 47–64.

Woolard, J and Colby, J (2002). Spatial characterization, resolution, and volumetric change of coastal dunes using airborne LIDAR: Cape Hatteras, North Carolina. *Geomorphology* 48 (1-3), pp. 269–287.

Wu, C., Hsiao, C., and Hsieh, P. (2013). Using UAV and VBS-RTK for Rapid Reconstruction of En-vironmental 3D Elevation Data of the Typhoon Morakot Disaster Area and Disaster Scale Assessment. *Journal of Chinese Soil and Water Conservation* 44 (1), pp. 23–33.

Xu, A., Viriyasuthee, C., and Rekleitis, I. (2011). Optimal complete terrain coverage using an unmanned aerial vehicle. *IEEE International Conference on Robotics and Automation, Shanghai, China, May 9-13, 2011*, pp. 2513–2519.

Young, A. and Ashford, S. (2006). Application of airborne LIDAR for seacliff volumetric change and beach-sediment budget contributions. *Journal of Coastal Research* 22 (2), pp. 307–318.

Yuan, D. and Elvidge, C. (1998). NALC Land Cover Change Detection Pilot Study: Washington DC Area Experiments. *Remote Sensing of Environment* 66 (2), pp. 166–178.

Zarco-Tejada, P., Berni, J., Suárez, L., Sepulcre-Cantó, G., Morales, F., and Miller, J. (2009). Imaging chlorophyll fluorescence with an airborne narrow-band multispectral camera for vegetation stress detection. *Remote Sensing of Environment* 113 (6), pp. 1262–1275.

Zarco-Tejada, P., González-Dugo, V., and Berni, J. (2012). Fluorescence, temperature and narrow-band indices acquired from a UAV platform for water stress detection

using a micro-hyperspectral imager and a thermal camera. *Remote Sensing of Environment* 117, pp. 322–337.

Zeibak, R. and Filin, S. (2007). Change detection via terrestrial laser scanning. *International Archives of Photogrammetry and Remote Sensing* 36 (3/W52), pp. 430–435.

Zeibak, R. and Filin, S. (2008). Managing uncertainty in the detection of changes from terrestrial laser scanners data. *The International Archives of the Photogrammetry, Remote Sensing and Spatial Information Sciences* XXXVII (B5), pp. 501–506.

Zhang, K., Douglas, B. C., and Leatherman, S. P. (2004). Global Warming and Coastal Erosion. *Climatic Change* 64 (1/2), pp. 41–58.

Zhang, K., Whitman, D., Leatherman, S., and Robertson, W. (2005a). Quantification of beach changes caused by Hurricane Floyd along Florida's Atlantic coast using airborne laser surveys. *Journal of Coastal Research* 21 (1), pp. 123–134.

Zhang, Y., Zhang, Z., Zhang, J., and Wu, J. (2005b). 3D building modelling with digital map, lidar data and video image sequences. *The Photogrammetric Record* 20 (111), pp. 285–302.

Zhang, Y., Xiong, J, and Hao, L (2011). Photogrammetric processing of low-altitude images acquired by unpiloted aerial vehicles. *The Photogrammetric Record* 26 (134), pp. 190–211.

Zhang, Z., Wu, J., Zhang, Y., and Zhang, J. (2003). Multi-view 3D city model generation with image sequences. *International Archives of Photogrammetry, Remote Sensing and Spatial Information Sciences* 34 (5/W12), pp. 351–356.

Zhou, G. and Xie, M. (2009). Coastal 3-D Morphological Change Analysis Using LiDAR Series Data: A Case Study of Assateague Island National Seashore. *Journal of Coastal Research* 25 (2), pp. 435 –447.

Zhou, K., Gong, M., Huang, X., and Guo, B. (2010). Data-Parallel Octrees for Surface Reconstruction. *IEEE transactions on visualization and computer graphics* 17 (5), pp. 669–681.